

UC Berkeley

UC Berkeley Electronic Theses and Dissertations

Title

On the electronic and electrochemical characterization of metal-organic frameworks

Permalink

<https://escholarship.org/uc/item/8sx6611j>

Author

Aubrey, Michael Leonard

Publication Date

2017

Peer reviewed|Thesis/dissertation

On the electronic and electrochemical characterization of metal-organic frameworks

by

Michael Leonard Aubrey

A dissertation submitted in partial satisfaction of the
requirements for the degree of
Doctor of Philosophy in Chemistry

Graduate Division
of the
University of California, Berkeley

Committee in Charge:
Professor Jeffrey R. Long, Chair
Professor Omar M. Yaghi
Professor Nitash P. Balsara

Spring 2017

Abstract

On the electronic and electrochemical characterization of metal-organic frameworks

by

Michael Leonard Aubrey

Doctor of Philosophy in Chemistry

University of California, Berkeley

Professor Jeffrey R. Long, Chair

The conduction of electrons and ions is central to operation of modern technologies. In particular, it is the redistribution of charge within a closed system that enables the production of energy, the storage of information, and the transduction of physicochemical phenomena. Progress on these fronts dictates that underlying component materials also progress towards superior performance and greater specificity in supplying a set of properties tailored to one of an ever growing and nuanced list of applications. Necessarily, new conductive materials must be developed continuously in order to keep up with societal demands for a more electrified and computerized planet.

Historically, functional materials reside with a relatively small set of classes: metals, ceramics, glasses, polymers, zeolites, and carbons. While there have been fantastic advances over the last century among every one of these classes, polymers and zeolites stand out as uniquely modern technologies. Synthetic polymers trace back to 1830, with the development of vulcanized rubbers. The advent of synthetic polymers revolutionized the level of control and tunability possible in materials science by leveraging the near infinite structural diversity possible in organic chemistry. It wasn't until one hundred and twenty years later that synthetic zeolites were commercialized. Zeolites are ceramics that distinguish themselves by their large crystalline void spaces capable of hosting gases and small molecules. Microporous zeolites represented a new competitor to porous carbons, with key advantages of long-range crystalline order and a unique surface chemistry particularly amenable to molecular sieving, gas separations, and the catalytic transformation of commodity chemicals. However, like porous carbons, structural and chemical diversity is limited for zeolites. Today, there are only about 230 known zeolite structures, and the discovery of new zeolite structure types is a notoriously difficult endeavor.

More recently a new set of porous crystals has been discovered, metal-organic frameworks. These hybrid materials are particularly well suited to the task of controlling structure and surface chemistry at the atomic level. With both an inorganic component providing the rich structural diversity unique to transition metal coordination chemistry and a prominent organic linker

component providing near infinite tunability akin to that of organic polymers, the development of metal-organic frameworks has ignited a renaissance in crystal engineering and porous materials chemistry. Over the last twenty years alone, the structures of many thousands of new metal-organic frameworks have been determined, dwarfing zeolites, carbons, and other porous materials. Further, metal-organic frameworks are steadily proving to be vastly superior in performance across many applications, especially for gas storage and separations.

Many obvious implementations of metal-organic frameworks as replacements for zeolites and porous carbons have been widely developed. All the while, the understanding and control of charge transport and electronic communication rested just beyond the horizon. Unlike zeolites and other porous crystals that are exclusively excellent electronic insulators, metal-organic frameworks do not share the same chemical limitations. The possible co-existence of intrinsic porosity, unprecedented structural diversity, intuitive tunability, and long-range electronic communication could fully leverage the potential of this class of materials. That is, the ability to manipulate a bulk electronic structure with precision and dramatic effect may result in new and unpredictable technologies.

Yet, it is not without reason that electronically conductive metal-organic frameworks are rare. Electronic communication is strongly dependent upon the relative distances between interacting valence electrons and vanishes steeply with increasing distance. Likewise, ion mobility in crystalline materials also requires extremely short hopping distances, typically less than half a nanometer. Within a class of materials that routinely boast void fractions in excess of 60%, it is not surprising that finding a high density of valence states or ion hopping sites has proven difficult. As such, it is of fundamental interest to explore how these structures can be coaxed into displaying the bulk transport of charge, and the physical means by which it occurs. By first learning the rules of synthesizing conductive metal-organic frameworks and transporting charge therein, it may then be possible to rationally tailor porous conductors for a targeted property or application.

To this end, *Chapter 1* discusses the nature of ion transport in metal-organic frameworks, its relation to traditional ion conductors, and reviews the prospects of ion conducting frameworks in a number of proposed applications. Surprisingly, though there are many proof-of-concept reports of using metal-organic frameworks in electrochemical devices, the investigation of ion transport is routinely ignored. This is despite it likely being the performance limiting factor in many cases. In fact, many implementations of metal-organic frameworks as component materials in supercapacitor electrodes are predicated on intrinsic porosity translating to fast ion transport. As will be shown, this is decidedly false for many canonical framework materials.

Nonetheless, with considerable optimization and targeted selection of pore structure and surface chemistry, it is possible to obtain ionic conductivities high enough to be useful in electrochemical systems. In fact, with judicious selection of host lattice and host-guest interactions it is possible to conduct ions that have been particularly intransigent to bulk transport in traditional materials like ceramics and polymers. *Chapter 2* highlights the synthesis of several metal-organic framework-based ion conductors capable of conducting magnesium, demonstrating an alternative strategy for multivalent ion conduction. Discussed in detail are the critical factors that dictate ion insertion and bulk transport in metal-organic frameworks and multiple strategies for maximizing ionic conductivity.

With these tools in hand, *Chapter 3* tackles mixed electron-ion conductivity in a similarly structured metal-organic framework. In some respects, the interrogation of ion transport in mixed conductors is made easier by the possibility of probing ion transport over a wide range of concentrations, electrochemically measuring the transport of a single ionic species, and directly observing host-guest interactions by changes in electrochemical potential. While many frameworks have been reported as candidate electrodes, *Chapter 3* represents the first to thoroughly discuss the role of host-guest interactions, and a surprising sensitivity to changes in the included electrolyte.

Finally, *Chapter 4* focuses on the modulation of electronic conductivity with host-guest interactions in a non-ionic metal-organic framework. A new technique for interrogating conductivity in porous solids is presented that is based on *in-situ* gas dosing and the simultaneous determination of conductivity and a gas adsorption isotherm. Unlike previous methods based on vapor exposure at ambient pressure, the measurements reported are referenced to the pure metal-organic framework, which possesses a consistent and well-defined chemical composition. Thus, equilibrium conductivity-composition profiles are directly extracted from the measurement. This is in contrast to the complex and relatively slow exchange reactions that occur by vapor exposure methods, which often lead to results that are difficult to interpret. Thus, a standard method of measuring and reporting the chemresistive response of gaseous and vaporous adsorbates is proposed and demonstrated.

Acknowledgements

First of all, I would like to acknowledge my teachers and mentors. Jeff Long, my advisor, for continually challenging me, for his guidance as I learned to plan, execute and manage a research project, and for giving me the freedom to explore the projects that most interested me. Not only has he taught me how a strong foundation in structural inorganic chemistry translates to a powerful toolbox for designing new materials and understanding their underlying structure-property relationship, but also how to best communicate my research to others. I would like to thank Omar Yaghi for reading this dissertation, chairing my qualifying exam committee. I would also like to thank him for many helpful discussions and his guidance in the development of new project directions and composition of grant proposals. I thank Nitash Balsara for also reading this thesis and allowing me access to his lab and equipment before my research project could support itself enabling me to complete the work presented in Chapter 2. I would also like to thank him for helpful discussions on the prospects for new ion-conducting solids. Richard Andersen and Angelica Stacy served on my qualifying committee and I thank them both for many helpful discussions.

I would like to thank my coauthors and group members that contributed the work presented in this dissertation. I would like to especially thank Brian Weirs for his mentorship and support. His encyclopedic knowledge of chemistry and just about everything else along with his willingness to discuss new and highly speculative project directions helped me to learn how to think through new research projects prior to implementation. Dr. Rob Ameloot joined the group about six months after I did and together with Brian we worked to secure the first funding sources exclusively for the synthesis and characterization of the conductive metal-organic frameworks. I would like to especially thank Rob for sharing his unique approach to research, and empowering me to build and design my own apparatus and instruments which has greatly accelerated my own research and allowed me to think deeply about how electrochemical measurements are made and how to quickly integrate prototyping into a materials chemistry project. With Rob, I was able to import the new electrochemical methods into the lab that are highlighted in Chapters 2 and 3. I would also like to thank Matt Kapelewski and Jo Melville who kindly provided samples for the work presented in a Chapter 4.

I would like to thank my collaborators on many other projects including Samia Hamed and Sebastian Reyes-Lillo for deep discussions on the electronic structure and transport mechanisms in metal-organic frameworks from a DFT perspective. I also thank former visiting student Dr. Kasper Pedersen and Prof. Rodolphe Cl  rac for including me in some of their recent work on making a set of magnetically and electronically interesting coordination solids. Last, I would like to thank Fern Grandjean for her expertise in the analysis and modeling of M  ssbauer spectra.

I would like to thank all of conductivity subgroup, which has quickly expanded over the last few years. Dr. Jeff van Humbeck initiated the single-ion conducting polymer project and it was very informative working closely with him on figuring out how to characterize some rather unique materials. I would also like to thank Jeff for his openness to discuss unconventional project

directions and his ability to imagine strange new materials that might deviate from traditional expectations. Jordan Axelson took over the ion conducting polymer project, and worked towards developing these phases into functional materials. I would like to thank her for including me in this work as we explored potential routes from their basic characterization to potential device integration. Raymond Yu was the first undergraduate to work on conductive metal-organic frameworks. Together we developed the electrochemical characterization techniques of mixed ion- and electron-conducting metal-organic frameworks. Raymond is one of the hardest working students I've ever met and continuously challenged himself to obtain a deeper understanding of materials chemistry. Though Lucy Darago is not officially a member of conductivity subgroup, our close collaboration on transport in mixed-valence coordination solids has led to an intense investigation into the long range electronic communication and magnetic structure in porous materials. The product of this effort now guides much of the conductivity subgroup's future directions.

I would also like to thank the many people in the Long group that have contributed to the conductivity subgroup over the years. In particular, Dr. Aravind Chandiran, who helped to bolster our use of spectroscopic techniques to study transport. I also had the pleasure to work with several talented synthetic chemists pursuing electroactive frameworks including Dr. Keith Keitz, Julia Oktaweic, Dr. Yang Yang, and Dr. Günther Thiele. Finally, I would like to thank all the new students of conductivity, Rodolfo Torres-Gavosto, Jesse Park, Mike Ziebel, Ryan Murphy, and David Jaramillo, for bringing to light a myriad of exciting new porous conductors. Rodolfo is a very thoughtful and careful synthetic chemist poised to shape conductivity into a prosperous subgroup moving forward.

I remain forever indebted to the elder members of the Long Group that made me into the person and scientist I am today. Tom McDonald for many long, intense discussions about carbon capture. Zoey Herm for her unyielding support and showing me that perseverance eventually pays off. I thank Eric Bloch, chief designer of the double chug, for instilling a 'work hard, play hard' attitude into the new student dynamic and leading by example. Katie Meihaus for many ridiculous arguments from constructing a symphony from NMR spectra to the ethics of domesticating squirrels and everything in between. The legendary Xiaowen Feng may be the most interesting person I have ever met, and I am proud to have had the pleasure to work with him. Jarad Mason worked hard to raise the standard of characterization of porous materials in the group and his dedication to quality left a lasting impact on the group. I thank David Zee for many late nights in the lab and for helping me translate the lab's molecular electrochemistry knowledge base to the solid state.

I would like to thank my classmates. I thank Dianne for her focus and drive pushing the rest of us to catch up, her unpredictable snark, and her creative use of a pumpkin. Fellow insomniac Miguel helped me survive my qualifying exam and first few years in the group both by providing lab supervision late into the night and early mornings and by partaking in intense debates on all things chemistry. His ability to mentor new group members in the ways of synthesis and crystallography and his unofficial position of instigator in chief has made the lab an always lively and exciting place to work.

Matt Kapelewski, Douglas ‘Fresh’ Reed, and Phil Bunting joined the lab a year after me. I would like to thank Matt for always being available to break the tension by constantly oversharing. Douglas always kept it chill and was there to remind everyone that we are just mixing chemicals together. Both myself and my doppelgänger Phil managed to survive in the same lab for the last four years without killing each other. Our mutual appreciation for silence and solitude leaves me with many great memories of not talking. The third and fourth years, Julia, Mercedes, Jon, Rebecca, and Kristen were also great additions to the lab and have already made some of the most important advances on the group’s gas sorption and separation projects. The first and second years will mark a shift in the Long group legacy. With them came the first major expansion of the lab in nearly a decade. They represent one of the smartest and most talented crop of students yet, and with hard work, they have the potential to elevate the Long group to new heights. I wait in great anticipation to see their work come to fruition.

Many visiting students and post-docs have come and gone since I began in the lab. Steve Geier taught me that Canada is just a colder version of North Carolina and David Rogow tried to teach me how to be a Californian, but I just wasn’t cool enough. Elizabeth Montalvo and Wendy Queen reminded the group that we are actually a bunch of nerds and yes we can party too hard. I would like to thank Paulina Gomora for her inexhaustible kindness. Michael Nippe’s wisdom and empathy are greatly missed but will serve him well in his new professorship. I cannot thank him enough for putting forth his best effort on converting me to a gentleman scholar. I thank Keith ‘Benji’ Keitz, my Texan brother from another mother, for appreciating all the good things in this world, things like Jurassic Park, Top Gun, The Goonies, space exploration, and the latest 90’s dance hits.

Finally, I would like to thank my family. My two sisters and fellow chemists Marissa and Megan for supporting me and kicking me down a notch when I deserved it. I would like to thank my mom for engendering an intense curiosity for science, nature, and everything else since before I could even read. And I would like to thank my dad for teaching me that the world is much bigger than Mills River, North Carolina, for instilling in me a commitment to doing things the right way, and instilling in me a stern practicality and independence in my research. I could not have asked for a better family to support me in all my academic pursuits.

Table of contents

Front matter	i
Abstract	iii
Acknowledgements.....	vi
Table of contents	ix
List of figures and tables.....	xii
List of supporting figures and tables	xv
1 Ionic conductivity in metal-organic frameworks	1
1.1 Introduction	1
1.2 Ion conduction in traditional materials	4
1.2.1 Liquid and solution phase electrolytes.....	4
1.2.2 Polymer electrolytes.....	5
1.2.3 Solvent included polymer electrolytes	5
1.2.4 Ceramic ion conductors.....	6
1.2.5 Ion conducting proteins.....	6
1.3 Principles of ionic conductivity	7
1.4 Electrochemical characterization of ionic conductors.....	10
1.4.1 Overview	10
1.4.2 Impedance Spectroscopy.....	11
1.4.3 Circuit modeling.....	12
1.4.4 Variable temperature conductivity	14
1.4.5 Alternative methods for measuring ion transport	14
1.4.6 Transference number	14
1.4.7 Electrochemical stability window.....	16
1.5 Ion conducting metal-organic frameworks	17
1.5.1 Overview	17
1.5.2 Proton conductors	17
1.5.3 Ion conducting frameworks by electrolyte impregnation.....	22
1.5.4 Conductivity in ionic metal-organic frameworks.....	25
1.5.5 Single-ion conducting porous organic polymers.....	28
1.6 Status and outlook.....	31
1.6.1 Prospects as battery electrolytes	31
1.6.2 Mixed ion-electron conductors.....	33
1.6.3 Solvent free, ceramic like conduction.....	34
1.7 Conclusions	34
1.8 Acknowledgements	35
1.9 Supporting figures	36

1.10	References.....	39
2	Metal-organic frameworks as solid magnesium electrolytes	52
2.1	Introduction	52
2.2	Results and discussion	52
2.2.1	Ion insertion and electrolyte grafting in Mg ₂ (dobdc)	53
2.2.2	Ionic conductivity of electrolyte grafted Mg ₂ (dobdc)	54
2.2.3	Ion insertion and electrolyte grafting in Mg ₂ (dobpdc).....	56
2.2.4	Ionic conductivity of electrolyte grafted Mg ₂ (dobpdc).....	56
2.2.5	Dependence of ionic conductivity with temperature.....	57
2.2.6	Analysis of magnesium deposition by ac impedance spectroscopy.....	58
2.3	Conclusions	58
2.4	Experimental methods.....	59
2.4.1	General protocols	59
2.4.2	Elemental analysis.....	59
2.4.3	Langmuir surface area measurements.....	59
2.4.4	Thermogravimetric analysis.....	59
2.4.5	Pellet preparation for ac impedance measurements.....	59
2.4.6	AC impedance measurements.....	59
2.4.7	Synthesis of Mg ₂ (dobdc).....	60
2.4.8	Mg ₂ (dobdc) ⊂ [0.05Mg(4-methylphenolate) ₂ • 1.5triglyme].....	60
2.4.9	Mg ₂ (dobdc) ⊂ [0.07Mg(phenolate) ₂ • 1.5triglyme].....	61
2.4.10	Mg ₂ (dobdc) ⊂ [0.06Mg(TFSI) ₂ • 1.4triglyme].....	61
2.4.11	Mg ₂ (dobdc) ⊂ [0.39Mg(OPhCF ₃) ₂ • 6.0triglyme].....	61
2.4.12	Mg ₂ (dobdc) ⊂ [0.31Mg(OPhCF ₃) ₂ • 0.30Mg(TFSI) ₂ • 2.4triglyme].....	62
2.4.13	Synthesis of Mg ₂ (dobpdc).....	62
2.4.14	Mg ₂ (dobpdc) ⊂ [0.22Mg(TFSI) ₂ • 3.3triglyme]	62
2.4.15	Mg ₂ (dobpdc) ⊂ [0.31Mg(OPhCF ₃) ₂ • 3.8triglyme]	62
2.4.16	Mg ₂ (dobpdc) ⊂ [0.21Mg(OPhCF ₃) ₂ • 0.46Mg(TFSI) ₂ • 4.8triglyme]	63
2.5	Acknowledgements	63
2.6	Supporting figures and tables	64
2.7	References.....	70
3	Oxidative insertion of weakly coordinating anions in a metal-organic framework	73
3.1	Introduction	73
3.2	Results and Discussion	74
3.2.1	Topotactic oxidative insertion in Fe ₂ (dobdc)	75
3.2.2	Chemical oxidation of Fe ₂ (dobpdc)	75

3.2.3	Electrochemical oxidation of Fe ₂ (dobpdc)	77
3.2.4	Ligand-centered redox activity	78
3.2.5	Electrolyte dependence on oxidative insertion	80
3.2.6	A prototype sodium half-cell	81
3.3	Conclusions	83
3.4	Experimental methods.....	84
3.4.1	Electrochemical methods	84
3.4.2	Diffuse reflectance UV-visible-NIR spectroscopy	84
3.4.3	FT-IR spectroscopy.....	84
3.4.4	Iron-57 Mössbauer spectroscopy	84
3.4.5	Powder X-ray diffraction.....	85
3.4.6	Chemical oxidation of Fe ₂ (dobpdc)	85
3.4.7	Synthesis of Fe ₂ (dobpdc)(PF ₆) _{0.84}	85
3.4.8	Synthesis of Fe ₂ (dobpdc)(PF ₆) _{1.56}	85
3.4.9	Synthesis of Mg ₂ (dobpdc)(PF ₆) _{0.48}	86
3.4.10	Calculation of Fe-Fe distances in metal-organic frameworks	86
3.4.11	Calculation of anion sizes	86
3.5	Acknowledgements	86
3.6	Supporting schemes, figures, and tables	87
3.7	References.....	102

4 Interrogation of charge transport in metal-organic frameworks by gas sorption107

4.1	Introduction	107
4.2	Results and discussion	109
4.2.1	Hopping transport in Cu[Ni(pdt) ₂]	109
4.2.2	Transport modulation by gas sorption	110
4.2.3	Isothermal response of hydrocarbons at equilibrium	110
4.2.4	Conductivity-composition profiles	112
4.2.5	Kinetic analysis of gas sorption and charge transport upon dosing	113
4.3	Conclusions	114
4.4	Experimental methods.....	114
4.4.1	General procedures and measurements	114
4.4.2	Modified synthesis of Cu[Ni(pdt) ₂]	114
4.4.3	Gas adsorption measurements.....	115
4.4.4	Ac impedance measurements.....	115
4.4.5	Time resolved gas sorption and <i>in situ</i> conductivity measurements.....	115
4.5	Acknowledgements	116
4.6	Supporting figures	117
4.7	References.....	125

List of figures and tables

Chapter 1

Figure 1.1	A typical metal-organic framework that supports electronic and ionic conductivity ...2
Table 1.1	Typical minimum conductivities for proposed applications of conductive frameworks3
Figure 1.2	The four traditional classes of ion conductors.....4
Figure 1.3	Variable temperature conductivity of selected ion conductors by class8
Figure 1.4	Illustration of the ion distribution of an electrolyte at high and low frequencies10
Figure 1.5	Typical 2-electrode cell geometry used to collect ac impedance spectra, a general model circuit for an ion conductor, and an experimentally determined impedance spectrum fit to the model circuit shown.....11
Figure 1.6	Frequency response of the real and imaginary components of $\text{Cu}(\text{Ni}[\text{pdt}]_2)$ showing ideal Debye type relaxation13
Figure 1.7	General experimental sequence for the potentiostatic polarization method15
Figure 1.8	Cyclic Voltammogram of single ion conducting polymer network.....16
Figure 1.9	The Grotthuss mechanism of excess proton conduction in water and 1,2,4-triazole17
Figure 1.10	Crystal structure of $\text{Na}_3(2,4,6\text{-trihydroxy-1,3,5-benzenetrisulfonate})(1\text{H-1,2,4-triazole})_x$18
Figure 1.11	Crystal structure of $\text{D-}[\text{Zn}(3\text{-methyl-2-(pyridin-4-ylmethylamino)-butanoic acid})(\text{Cl})](\text{H}_2\text{O})_2$18
Figure 1.12	Crystal structure of $(\text{NH}_4)_2(\text{adipic acid})[\text{Zn}_2(\text{oxalate})_3] \cdot 3\text{H}_2\text{O}$19
Figure 1.13	Crystal structure of $\text{Zn}(\text{H}_2\text{PO}_4)_2(1,2,4\text{-triazole})_2$20
Table 1.2	Ionic conductivities for metal-organic framework based ion conductors21
Figure 1.14	A portion of the crystal structure of EHU1 and the scandium cluster node.....22
Figure 1.15	Crystal structure of the molecular solid cucurbit[6]uril24
Figure 1.16	Illustration of post-synthetic transmetalation in a metal-organic framework25
Figure 1.17	Illustration of the transmetalation of lithium isopropoxide in $\text{Mg}_2(\text{dobdc})$26
Figure 1.18	The octahedral pore and cluster node of UIO-66 and the ionic conductivity after grafting lithium <i>tert</i> -butoxide.....27

Figure 1.19	A fragment of the $[\text{Ni}_8(\text{OH})_4(\text{H}_2\text{O})_2](1,4\text{-benzene dipyrazolate})_6$ crystal structure	28
Figure 1.20	Lewis structure of the PAF-1 tetraarylmethane node, the PAF-1 dialkynylbenzene linker, the anionic boron based node and the idealized skeletal structure	29
Table 1.3	Ionic conductivities for porous polymer network based ion conductors and related materials	29
Figure 1.21	Teraphthaldehyde condensates of phloroglucinol and melamine.....	30
Figure 1.22	Lewis structure of the lithium ion conductor ICOF-2, a mesoporous lithium spiroborate lattice.....	31
Figure 1.23	Illustration of a metal-organic framework's applications in a lithium battery.....	32
Figure 1.24	Extended inorganic building units that may potentially support solvent free ion conduction	33

Chapter 2

Figure 2.1	Structures of the metal-organic frameworks $\text{Mg}_2(\text{dobdc})$ and $\text{Mg}_2(\text{dobpdc})$ and the open coordination site that interacts with nucleophilic guests	53
Figure 2.2	Single crystal structures of $[\text{Mg}_2\text{Cl}_3(\text{THF})_6]^+ [\text{Cl}_3\text{Al}(\text{p-trifluoromethylphenolate})]^-$ and $\text{Mg}_5\text{Cl}_2\text{O}(\text{THF})_5(\text{cresolate})_6$	54
Table 2.1	Summary of materials synthesized, conductivities and activation energies	55
Figure 2.3	AC impedance spectra for all materials synthesized at room temperature.....	57
Figure 2.4	Nyquist plot of a $\text{Mg} \text{Mg}(\text{OPhCF}_3)_2 \cdot \text{Mg}(\text{TFSI})_2 \subset \mathbf{2} \text{Mg}$ cell	58

Chapter 3

Figure 3.1	Structure of the frameworks $\text{Fe}_2(\text{dobdc})$ and $\text{Fe}_2(\text{dobpdc})$	74
Figure 3.2	Reaction scheme for postsynthetic oxidation of $\text{Fe}_2(\text{dobpdc})$, generalized schematic of how $\text{Fe}_2(\text{dobpdc})$ operates in an electrochemical cell	75
Figure 3.3	NIR- <i>vis</i> -UV absorption spectrum for chemically oxidized samples, unit cell parameters determined by <i>ex situ</i> powder X-ray diffraction for electrochemically oxidized samples of $\text{Fe}_2(\text{dobpdc})(\text{BF}_4)_x$, and <i>ex situ</i> ^{57}Fe Mössbauer spectra for electrochemically oxidized samples of $\text{Fe}_2(\text{dobpdc})(\text{BF}_4)_x$	76
Figure 3.4	Postsynthetic oxidation of $\text{Mg}_2(\text{dobpdc})$ with nitrosonium hexafluorophosphate to yield an organic radical.....	78

Figure 3.5	Infrared spectra and powder X-ray diffraction patterns of $\text{Mg}_2(\text{dobpdc})$ and $\text{Mg}_2(\text{dobpdc})(\text{PF}_6)_{0.48}$	79
Figure 3.6	Charge–discharge dependencies on the electrolyte anion, and cation.....	80
Figure 3.7	Charge–discharge dependencies on the electrolyte solvent	81
Figure 3.8	Half-cell performance of a prototype sodium battery	82
Figure 3.9	Comparison of $\text{Fe}_2(\text{dobpdc})(\text{PF}_6)_x$ discharge profile compared to other electrodes discharged at their maximum capacity	83

Chapter 4

Figure 4.1	A portion of the crystal structure of $\text{Cu}[\text{Ni}(\text{pdt})_2]$ and bond-angle structure of the $\text{Ni}(\text{pdt})_2$ subunit.....	108
Figure 4.2	Nyquist impedance plot of $\text{Cu}[\text{Ni}(\text{pdt})_2]$ fit to a Debye type hopping model	109
Figure 4.3	Schematic of conductivity cell for <i>in situ</i> transport measurements on a gas sorption analyzer.....	110
Figure 4.4	Room temperature gas adsorption isotherms and room temperature conductivity isotherms as a function of absolute pressure for propane, ethane, and ethylene.....	111
Figure 4.5	Conductivity-composition profiles in the phase $(\text{C}_x\text{H}_y)_n\text{Cu}[\text{Ni}(\text{pdt})_2]$ for propane, ethane, and ethylene	112
Figure 4.6	Illustration of a bulk electron path through a pressed pellet conducting through both bulk crystallite and across interparticle contacts, and a one-dimensional model of relative resistivity both through and between neighboring crystals.....	113

List of supporting figures and tables

Chapter 1

Figure S1.1	Nyquist projection of the Kramers-Kronig transform of an impedance spectrum for the electron conductor $\text{Cu}[\text{Ni}(\text{pdt})_2]$36
Figure S1.2	Comparison of Arrhenius and VTF models for a single ion conducting network polymer gel.....36
Figure S1.3	Charge transfer resistance for a UIO-66 solid electrolyte at lithium electrodes ($\text{Li} \text{MOF} \text{Li}$) as determined by circuit modeling the impedance spectra.....37
Figure S1.4	Cyclic voltammogram of a UIO-66 based MOF electrolyte37
Figure S1.5	Current decay curve across a $\text{Li} \text{MOF} \text{Li}$ cell for a UIO-66 based electrolyte38
Figure S1.6	Ac impedance spectra accompanying the current decay curve shown in Figure S1.538

Chapter 2

Figure S2.1	PXRD for materials containing $\text{Mg}_2(\text{dobdc})$64
Figure S2.2	PXRD for materials containing $\text{Mg}_2(\text{dobpdc})$64
Figure S2.3	TGA for materials containing $\text{Mg}_2(\text{dobdc})$65
Figure S2.4	TGA for materials containing $\text{Mg}_2(\text{dobpdc})$65
Figure S2.5	^1H NMR (300 MHz) for materials containing $\text{Mg}_2(\text{dobdc})$66
Figure S2.6	Selected regions of ^1H NMR for materials containing $\text{Mg}_2(\text{dobpdc})$67
Figure S2.7	Room temperature Nyquist plots for the materials given in Table 2.168
Figure S2.8	Temperature dependence on conductivity for electrolytes based on $\text{Mg}_2(\text{dobdc})$ and $\text{Mg}_2(\text{dobpdc})$69
Figure S2.9	SEM images describing morphology of $\text{Mg}_2(\text{dobdc})$ and $\text{Mg}_2(\text{dobpdc})$69

Chapter 3

Scheme S3.1	Schematic of the electrochemical cell.....87
Figure S3.1	Fe-57 Mössbauer of $\text{Fe}_2(\text{dobdc})(\text{PF}_6)(\text{MeCN})_y$88
Figure S3.2	PXRD of $\text{Fe}_2(\text{dobdc})(\text{PF}_6)(\text{MeCN})_y$88

Figure S3.3	Electrochemical oxidation of $\text{Fe}_2(\text{dobdc})$	89
Figure S3.4	Fe-57 Mössbauer spectra before and after chemical oxidation.....	90
Figure S3.5	PXRDs of electrochemically prepared sample of $\text{Fe}_2(\text{dobpdc})(\text{BF}_4)_x$	91
Figure S3.6	PXRD of $\text{Fe}_2(\text{dobpdc})(\text{PF}_6)_x$ before and after 50 charge/discharge cycles.....	91
Figure S3.7	Le Bail refinement of $\text{Fe}_2(\text{dobpdc})$	92
Figure S3.8	Le Bail refinement of electrochemically oxidized $\text{Fe}_2(\text{dobpdc})(\text{BF}_4)_{0.5}$	92
Figure S3.9	Le Bail refinement of electrochemically oxidized $\text{Fe}_2(\text{dobpdc})(\text{BF}_4)$	93
Figure S3.10	Le Bail refinement of electrochemically oxidized $\text{Fe}_2(\text{dobpdc})(\text{BF}_4)_{1.5}$	93
Figure S3.11	Le Bail refinement of electrochemically oxidized $\text{Fe}_2(\text{dobpdc})(\text{BF}_4)_2$	94
Figure S3.12	PXRDs of chemically oxidized samples of $\text{Fe}_2(\text{dobpdc})(\text{PF}_6)_x$	94
Figure S3.13	Le Bail refinement of chemically oxidized $\text{Fe}_2(\text{dobpdc})(\text{PF}_6)$	95
Figure S3.14	Le Bail refinement of chemically oxidized $\text{Fe}_2(\text{dobpdc})(\text{PF}_6)_2$	95
Figure S3.15	Le Bail refinement of $\text{Mg}_2(\text{dobpdc})$	96
Figure S3.16	Le Bail refinement of chemically oxidized $\text{Mg}_2(\text{dobpdc})(\text{PF}_6)_{0.48}(\text{MeCN})_{5.1}$	96
Figure S3.17	Battery summary with all discharge curves labeled	97
Table S3.1	Fe-57 Mössbauer fit parameters for chemically oxidized $\text{Fe}_2(\text{dobdc})(\text{PF}_6)$	97
Table S3.2	Le Bail refined unit cells of $\text{Fe}_2(\text{dobdc})$ oxidized chemically	98
Table S3.3	Fe-Fe distances of selected minerals and iron based metal-organic frameworks with infinite chains of iron polyhedra	98
Table S3.4	Calculated anion volumes from the crystal structures of the binary salts.....	99
Table S3.5	Le Bail refined unit cells of $\text{Fe}_2(\text{dobpdc})$ oxidized electrochemically.....	99
Table S3.6	Le Bail refined unit cells of $\text{Fe}_2(\text{dobpdc})$ oxidized chemically.....	100
Table S3.7	Le Bail refined unit cells of $\text{Mg}_2(\text{dobpdc})$ oxidized chemically	100
Table S3.8	Fe-57 Mössbauer fit parameters for chemically oxidized samples.....	101
Table S3.9	Fe-57 Mössbauer fit parameters for electrochemically oxidized samples.....	101

Chapter 4

Figure S4.1	The powder X-ray diffraction pattern of $\text{Cu}[\text{Ni}(\text{pdt})_2]$	117
Figure S4.2	The 77 K N_2 adsorption isotherm of $\text{Cu}[\text{Ni}(\text{pdt})_2]$ used to calculate the Langmuir surface area.....	117

Figure S4.3	Dc field dependence of Nyquist plots of Cu[Ni(pdt) ₂]	118
Figure S4.4	Ac field invariance of Nyquist plots of Cu[Ni(pdt) ₂]	119
Figure S4.5	Kramers-Kronig transform of Nyquist plot for Cu[Ni(pdt) ₂]	119
Figure S4.6	Bode impedance plot and phase dependence of Cu[Ni(pdt) ₂]	120
Figure S4.7	Real (Z') and imaginary (Z'') bode plots of Cu[Ni(pdt) ₂]	120
Figure S4.8	Time dependent change in current upon pump dose cycles of ethylene at pressures between 0.5 mbar and 8 mbar.....	121
Figure S4.9	Correlation of sensitivity to guest inclusion and gas phase entropy.....	121
Figure S4.10	Kinetic analysis of gas adsorbed and change in conductivity between 19 and 45 mbar.....	122
Figure S4.11	Kinetic analysis of gas adsorbed and change in conductivity between 200 and 300 mbar	122
Figure S4.12	Kinetic analysis of gas adsorbed and change in conductivity between 500 and 600 mbar.....	123
Figure S4.13	Linearized rate of adsorption curve from Figure S4.10.....	123
Figure S4.14	Typical time-resolved conductivity data during the collection of an ethane Isotherm.....	124

Chapter 1

Ionic conductivity in metal-organic frameworks

1.1 Introduction

Metal-organic frameworks are crystalline solids with large, nanometer-scale void spaces akin to those found in zeolites. These three-dimensional network solids are composed of inorganic nodes linked together by organic bridging ligands, and often boast surface areas of 1000 to 5000 m² g⁻¹.^{1,2} Their remarkable gas adsorption properties have led to great interest in potential industrial applications, including gas storage,^{2,4} gas separations,⁵⁻⁸ and heterogeneous catalytic transformations.⁹⁻¹³ Another notable property, common to metal-organic frameworks and zeolites, is that they are typically excellent electronic and ionic insulators.¹⁴⁻¹⁶

From a structural perspective, it is not surprising that zeolites and metal-organic frameworks are usually electronically insulating. They are both crystalline materials held together by strong localized bonds between hard, closed shell metal ions (e.g., Zn²⁺, Al³⁺, Zr⁴⁺, and Si⁴⁺) and hard closed shell organic donors (oxide, carboxylate, phenolate, etc.). Although such materials are remarkably stable, their chemistry is also localized to the sub-nanometer length scale. In the case of metal-organic frameworks, the inherently large distances between atoms contributing to the frontier state make bulk electronic transport impossible. Metal-organic frameworks routinely display porosities greater than 60% of the unit cell, severely limiting the momentum space through which charge mobility is allowed. But unlike aluminosilicate-based zeolite materials, the greater structural diversity of metal-organic frameworks leaves open the possibility for more intriguing electronic structures to be synthesized.¹⁷

The vast majority of metal-organic frameworks also poorly conduct ions, even when saturated with solvent ($\sigma < 10^{-6}$ S/cm).¹⁸ An extremely large unit cell often implies large distances between hopping sites, making the barrier to solvent free ion transport extremely large. Even when solvating guest molecules are introduced, aromatic hydrocarbon based linkers tend to create hydrophobic pore surfaces not conducive to the inclusion of electrolyte salts. Therefore, ion concentrations in metal-organic frameworks are often far too low to yield high conductivities. Additionally, the pores of many metal-organic frameworks are too small, less than two nanometers, to support ion solvation comparable to what is observed in a bulk solution.^{19,20} Further, ions likely prefer to either ion pair or coordinate to the strongest donor on the pore surface (e.g., a carboxylate functionality) rather than solvate as a free ion. Thus, the synthesis of new metal-organic frameworks that do display high ionic conductivity will likely require the development of new structure types and surface chemistries differing from those that have been traditionally focused on for applications centered on gas binding.

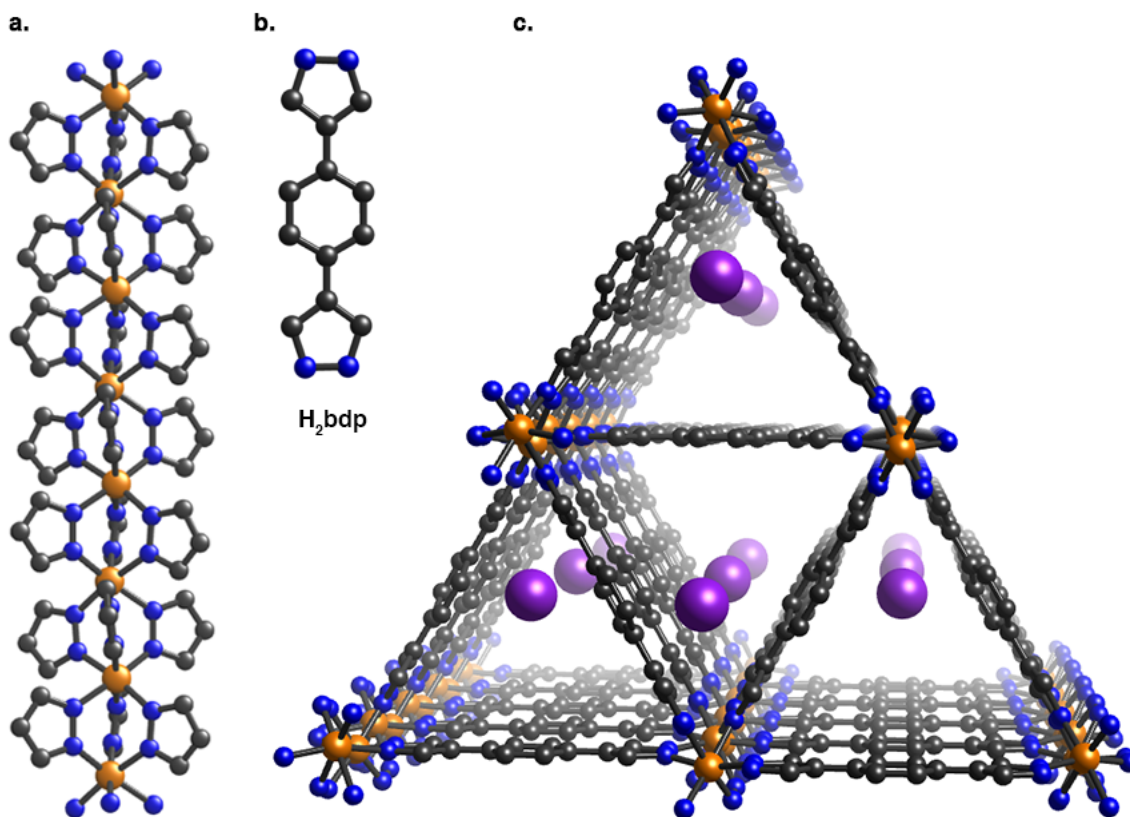


Figure 1.1. (a) A typical metal-organic framework structure, $K_xFe_2(1,4\text{-benzenedipyrazolate})_3$, that can support both electronic and ionic conductivity by allowing electron conduction down 1-D metal chains, (b) an organic linker that can be modified with redox active or ionic functional groups, and (c) an open pore structure allowing facile diffusion of ion solvates (purple spheres).

Yet, the technological prospects of conductive porous crystals are enticing. Amorphous solids, such as activated carbons, are integral to commercial supercapacitors, pseudo-capacitors, supports for electrocatalysts, and component materials in fuel cells and batteries.²¹⁻²⁵ But, like nanoporous metals,^{26,27} they lack the precise definition in pore structure and surface chemistry intrinsic to metal-organic frameworks. In recent years, reports of conductive frameworks have begun to emerge.²⁸⁻³² Unlike porous carbons and metals, electronically conductive metal-organic frameworks can be semiconducting, while ion transport may be precisely controlled by crystal engineering. As such, electronic properties including conductivity, band gap, Fermi level, redox potential, and optical transitions are wonderfully tunable. Consequently, the synthesis of conductive metal-organic frameworks may lead to new applications as battery electrodes,³³⁻³⁶ solid electrolytes,^{18,30} electrocatalysts,³⁷⁻⁴¹ chemical sensors,⁴² thermoelectric materials,⁴³ and electrochromic electrodes.⁴⁴⁻⁴⁷

Despite many examples demonstrating the possible utility of conductive metal-organic frameworks, it is also of primary importance to understand the fundamentals of charge transport through this little-studied class of materials. In doing so, not only do we expect to learn a set of governing design principles for the synthesis of new materials, but also to shed light on both the opportunities and limitations of implementing metal-organic frameworks in practical devices.

Figure 1.1 shows a metal-organic framework that illustrates a variety of opportunities to modify a host lattice to conduct ions, electrons, or both. (1) The intrinsic porosity allows ions to diffuse

such that, if the framework is modified to absorb high concentrations of ions, relatively high conductivities are achievable.

(2) A small subset of MOFs are known with the composite frontier orbitals confined to a small region of the host lattice, yielding 1D or 2D structural motifs with unusually high charge dispersion.⁴⁸⁻⁵² These substructures offer an intuitive and predictable path of electron transport through the bulk solid.

Through post-synthetic redox insertion chemistry, structure types like these may yield mixed ion-electron conducting phases.

(3) One of the most powerful concepts in the design of new metal-organic frameworks is the ease of synthesizing isorecticular phases with different organic linkers.⁵³⁻⁵⁵ With this in mind, the installation of ligand-mediated redox activity can improve exchange between or across metal centers. Additionally, intrinsically charged functional groups can be added to engender or enhance ion or mixed ion-electron transport.

Table 1.1 presents a rough guide to the limiting conductivities required for a variety of applications, as estimated for a multi-cell stack and an allowable polarization of ~ 10 mV, as calculated previously and supplemented here.³³ Lower conductivities are of course feasible, but will likely limit power density. While this list is by no means exhaustive, it is representative of the present body of work on the electrochemical and electronic applications of metal-organic frameworks. With this in mind, it is notable that while charge transport in metal-organic frameworks and related materials is known, and many of the reported phases are likely both ionically and electronically conductive, typically only ionic *or* electronic conductivity is reported. Importantly, nearly all of these prospective applications in **Table 1.1** require the bulk transport of ions.

Yet while the electronic conductivity of metal-organic frameworks and closely related coordination solids have been discussed and reviewed, the topic of ion transport has been unjustifiably neglected.^{17,32,56} Reviews of non-electron based conductivity have focused almost exclusively on proton conductivity,^{30,57} even though ion transport is likely the technologically limiting factor for many of the proposed applications. This conflict may stem from a widespread misconception that because metal-organic frameworks have large pores, ion transport will naturally be fast. As such, the fundamentals of ion transport in these materials will be reviewed in detail here to attempt to better guide the design of electrochemically active frameworks tailored to specific applications.

This review of ion transport in metal-organic frameworks and related materials is organized into five parts. First, ion transport in traditional materials is qualitatively discussed as a point of reference in **Section 1.2**. Second, the fundamentals of ion transport in metal-organic frameworks are detailed, followed by **Section 1.4**, which focuses on the characterization of ion conducting materials. Next, the review of ionic metal-organic frameworks begins with a brief discussion of the special case of proton transport in **Section 1.5.2**. In **Section 1.5.3**, the transport of metal ions and a few anions is

Table 1.1. Typical minimum conductivities for proposed applications of conductive frameworks. Values in parentheses are minimum conductivity estimates if nanostructuring is employed (~ 100 nm scale).

Application	Type	$\text{Log}_{10}(\sigma(\text{S/cm}))$
battery electrode	ion/electron	-7 (-8)
battery solid electrolyte	ion	-3
supercapacitor electrode	ion/electron	-6 to -5
supercapacitor electrolyte	ion	-3 to -2
fuel cell catalytic electrode	ion/electron	-4 to -3 (-5 to -4)
thermoelectric	electron	2 to 3

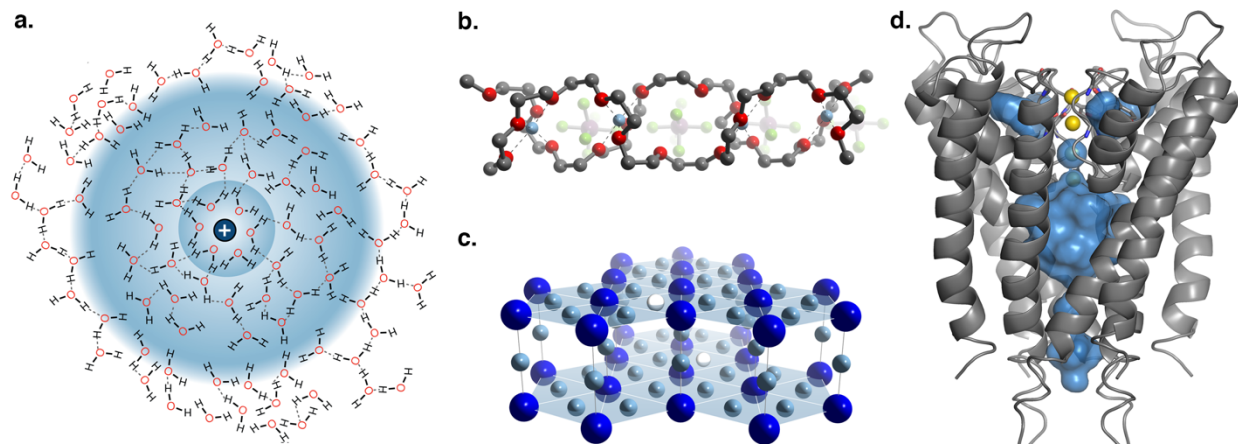


Figure 1.2. The four traditional classes of ion conductors: (a) bulk diffusion of ions through solution that is closely tied to the ion’s solvodynamic radius, (b) polymer electrolytes such as LiPF_6 in polyethylene oxide that follow a transport mechanism crudely estimated as ion hopping followed by reorganization of the polymer matrix, (c) ceramic ion conductors like Li_3N with Li^+ ions (light blue) that hop into site vacancies (white), (d) ion channels in biological cell membranes—with a K^+ channel shown—that are supremely optimized for the rapid and highly selective transport of potassium ions. The volumes surrounded in blue represent large voids in the protein structure that are accessible to water and K^+ (yellow spheres).

comprehensively reviewed for both metal-organic frameworks and closely related organic-based frameworks and polymers. Finally, in **Section 1.6** the overarching status and outlook of these new ion conductors is discussed in relation to their implementation as solid electrolytes and electrode materials, along with their potential to display more exotic properties, leading to new unforeseen applications in the future.

1.2 Ion conduction in traditional materials

1.2.1 Liquid and solution phase electrolytes. Perhaps the best studied systems for ionic conductivity, if not the simplest, are aqueous and solution states. Ionic conductivity in aqueous solutions has been studied intensely since the late 19th century, when Svante Arrhenius completed his dissertation on the conductivity of electrolyte solutions in which he presented his theory of the dissociation of ionic solids in aqueous solutions.⁵⁸ While this original work has been expanded to a vast number of ion conductors over the last century, most of his principles of ion dissociation, diffusion, and conductivity, including his model for the temperature dependence of diffusion, remain largely unchanged.

Ionic conductivity in solution is diffusive, however, the matter is complicated since precise structure of the diffusing ion is often unknown and difficult to determine. **Figure 1.2a** illustrates this complexity by showing water solvation of a cation at very dilute concentrations. In addition to the cation, water molecules coordinate strongly to the ion and must also diffuse through the bulk solution along with the charge carrier for conduction to occur. This inner coordination shell dramatically increases the mass and solvodynamic radius of the ion.²⁰ Additionally, the inner solvation sphere results in a local distortion of the bulk solvent structure that is both partially ordered and loosely bound to the ion; this region, denoted in **Figure 1.2a** as the larger blue circle, is termed the cybotactic region.⁵⁹⁻⁶¹ The solvation number can therefore, in some cases, be much

larger than the coordination number; for example in aqueous solution the coordination number of a Mg^{2+} cation is six, while the solvation number in water is estimated to be as high as thirty-six.¹⁹ Though much weaker in organic and aprotic solvents, solvation effects strongly influence ion activity, conductivity and electrode kinetics.⁶² Then, the manipulation of ion solvation is an important tool in the optimization of devices that use ion solvate conductors, such as batteries and hydrogen fuel cells.

Phenomenologically, solution and liquid phase electrolytes (i.e., ionic liquids) have very high ionic conductivities at room temperature and low activation energies of ~ 0.1 eV. This, along with the ability of liquids to easily deform about and wet rough electrode surfaces, has made liquid-based ion conductors the state-of-the-art in modern batteries, fuel cells, and supercapacitors.⁶³

1.2.2 Polymer electrolytes. Fast ion conduction in polymeric phases was originally reported over 40 years ago by formation of a solid solution of polyethylene oxide (PEO) and lithium binary salts like LiBF_4 .⁶⁴ Given the excellent electrochemical stability of PEO and perfluorinated anions, the vast majority of polymer electrolytes today remain chemically very similar to the original materials.^{65,66}

Pure $\text{PEO}\cdot\text{LiX}$ electrolytes have low ionic conductivities and relatively high activation energies at room temperature, resulting from the low solvation energy of lithium ions in PEO as well as the crystalline packing of PEO chains at room temperature.⁶⁷ A rare example of a $\text{PEO}\cdot n\text{LiPF}_6$ crystal structure is shown in **Figure 1.2b**.⁶⁸⁻⁷⁰ Bulk ion transport in these materials can be imagined to require the partial desolvation of the lithium ion in order to diffuse through a matrix of largely immobile chains of PEO; necessarily, this results in an activation barrier much greater than that observed for liquid electrolytes.

Typically, heating above the glass transition temperature or liquidus (~ 80 to 120 °C) of the PEO-salt complex is required in order to achieve conductivities practical for use in modern batteries, at least $0.1\text{--}1$ mS cm^{-1} . Above the glass transition, the crystallinity of the polymer phase greatly decreases and chain mobility increases, yielding a system more amenable to ion mobility. Heating also increases the solubility of the lithium salt and reduces ion pairing, thus increasing conductivity. In this case, the conductivity of the material behaves more like that of a viscous liquid and follows a Vogel-Tamman-Fulcher type temperature dependence.

1.2.3 Solvent included polymer electrolytes. Alternatively, ionic conductivity through a polymer matrix can be substantially increased at ambient temperatures by the addition of an organic solvent or plasticizer. The distinction between classes of solvent-polymer electrolyte composites is often murky and system dependent. Nevertheless, solvent included polymers can be crudely divided into three regimes based on the polymer-solvent stoichiometry. At low solvent loading, less than 33 wt %, the material largely retains the transport and bulk properties of a solid polymer. Mechanistically, ions in this regime hop by partial dissociation of the inner coordination sphere, followed by a small displacement and reconstitution of the ions' solvation shell. The energy penalty for this process is high, resulting in a strong temperature-dependent conductivity. Above 66 wt % solvent, the electrolyte is normally best described as a gel, with ion solvation and transport properties very similar to liquid electrolytes.⁷¹ Composites within the large regime between these two extremes are

normally considered plastics. In practice, solvent included polymer electrolytes lay on a spectrum of compromise between higher conductivity and lower mechanical stability with increasing solvent content.

1.2.4 Ceramic ion conductors. Ion conducting solids are a very old technology. Modern archeological findings suggest that layered clays have been used to mediate crop fertilization for the last eight millennia.^{72,73} Still, it wasn't until recently, in the mid 19th century, that the exchange mechanism of intercalated ions was formally described.^{74,75} Solid-state ion conductors as a broader class of materials was not fully appreciated until a century later, with discovery of sodium aluminum oxide—misnamed β -alumina.^{76,77} This highly selective and fast sodium ion conductor ($\sim 0.3 \Omega \text{ cm}^{-1}$)⁷⁸ enabled Ford Motor Company to develop the sodium-sulfur battery.⁷⁹ Since then, the study of ion mobility in solids has become critical for the advancement of nearly all modern battery electrode materials, including lithium cobaltate, spinel type lithium manganese oxide, and lithium iron phosphate.⁸⁰⁻⁸³

A mechanistically simple illustrative model, **Figure 1.2c** presents the structure of the fast lithium ion conductor lithium nitride. This ceramic conductor forms as a layered structure of nitride (blue) sheets with lithium ions (light blue) occupying all of the trigonal holes. Between the sheets, the N^{3-} ions are pillared by the remaining lithium ions. By measuring the conductivity of this phase on single crystals, it was found that ionic conductivity through the sample is highly anisotropic. This is a relatively common phenomenon in ceramic ion conductors and distinguishes them from liquid, gel, and most polymer electrolytes. In this case, the lithium ion conductivity was one-hundred times greater parallel to the lithium nitride sheets, with a significantly smaller activation energy.⁸⁴ Careful structural analysis showed a small concentration of lithium ion vacancies (white spheres in **Figure 1.2c**) only within the two-dimensional sheets.⁸⁵ Thus, a hopping mechanism between defect vacancies is expected to account for the observed ionic conductivity. This is a classic explanation for ion conduction in inorganic crystals, and there is a wealth of in-depth analyses on crystal defect classification, modes of ion hopping, and crystal surface effects for this quintessential class of solid electrolytes.^{86,87}

1.2.5 Ion conducting proteins. An alternative lean on the conduction of ions through solids is in the very small yet precision engineered world of protein-based ion channels. The major component of all ATP synthesis in living systems is rooted in the shuttling of ions across a membrane. In fact, nearly a third of all ATP is expended through the active transport of ions across cell membranes.⁸⁸ In doing so, cells routinely maintain fields as high as $200,000 \text{ V cm}^{-1}$ across cell membranes.⁸⁹ Indeed, the selective transport of ions (e.g., Na^+ , K^+ , Ca^{2+} , and H^+) and the resulting concentration gradients produced are central to the existence of complex organisms.

Perhaps the most intensively studied case is that of the ubiquitous potassium ion channel, **Figure 1.2d**. Associated with the 2003 Nobel Prize in chemistry, the $\sim 4.5 \text{ nm}$ long channel is 10,000 times more selective for the conduction of potassium over smaller alkali metals.⁹⁰ Further, ion transport across the membrane approaches the bulk diffusion limit. The protein structure can be considered a nanoporous superstructure with a large central pore of $\sim 10 \text{ \AA}$ in diameter. Ion

transport within the channel is not comparable to that in solid-state conductors (although the selectivity filter at the pore entrance transports a desolvated ion by site hopping), nor to that of a bulk aqueous solution. Instead, conduction through the potassium channel operates via pore confinement effects that prevent an ‘ideal’ bulk solvation state, but still allow ions to diffuse along with some coordinated water molecules.

1.3 Principles of ionic conductivity

The conductivity of a material is a measure of the amount of charge that can be moved for a given electric field gradient and is therefore the multiplicative inverse of resistivity. At the low field limit, conductivity is linear with field and it is an intrinsic material property defined by Ohm’s law normalized to the geometry of the sample. In **Equation 1**, the conductivity, σ , has units of S cm^{-1} , and is the quotient of current flux, j (A cm^{-2}), and electric field E (V cm^{-1}).

$$\sigma = \frac{j}{E} \quad (1)$$

Conductivity is unique among intrinsic materials properties in that it has the greatest range of accessible values, over 28 orders of magnitude, between 10^{-22} and 10^6 S cm^{-1} .⁹¹ Correspondingly, conductivity is remarkably sensitive to relatively small changes in electronic structure. While this bulk material property is a rather crude description of underlying chemical structure, it has proven immensely useful for the classification of materials. Indeed, the demarcation of the elements based on conductivity is the one of the only chemical properties consistently shown on the periodic table.

To the materials chemist a more useful definition of conductivity would be in terms of properties related to individual atoms or ions. As such, the conductivity of a single species can also be defined microscopically as in **Equation 2**, where σ_i is the bulk conductivity of a single ion, n_i is the number density or ion concentration, μ_i is the ion mobility, Z_i is the valence number, and e is the elementary charge constant.

$$\sigma_i = n_i \mu_i Z_i e \quad (2)$$

Naturally it is expected that current flux, and hence the conductivity, should increase with the number of ions. Likewise, conductivity is proportional to ion mobility, which is the ion velocity for a given applied field, E . The final term, $Z_i e$, is the amount of charge passed per ion; divalent ions, such as Mg^{2+} , transport twice as much charge as monovalent ions like Li^+ . Since both cations and anions contribute positively to the total conductivity, the total bulk conductivity observable, as in **Equation 1**, is given as:

$$\sigma = \sum_i |\sigma_i| + \sigma_{el} \quad (3)$$

In **Equation 3**, the summation term is the total ionic conductivity and the second term, σ_{el} , is the electronic conductivity.

It is often the case that only a single type of charge carrier is desirable. For example, in lithium batteries, if the electrolyte separating two reactive electrodes has any significant electronic conductivity, the battery will short circuit, rendering it useless. Further, the conductivity of ions besides Li^+ is also detrimental as these electrochemically inert charge carriers create potential gradients at the electrode surface, ultimately leading to reduced cycle life.⁹² Selective ion conductance

is quantified as the transference number—the fraction of charge transported by a specified ion—expressed by **Equation 4**.

$$t_i = \frac{\sigma_i}{\sum_i |\sigma_i| + \sigma_{el}} \quad (4)$$

Overall, while this description of conductivity is useful as a tool for thinking about the design and synthesis of new ion conductors, in practice it is generally very difficult to determine fundamentally important properties like ion mobility, or even the concentration of free ions. In solids and commercial battery electrolytes, ion concentrations are very high, or ions are in intimate contact with their counter ions. Because of this, the vast majority of potential charge carriers are actually ion paired and do not contribute to the ion concentration in **Equation 2**—more accurately termed the free ion number. Practically, ion number can only accurately be equated to the ion concentration in extremely dilute

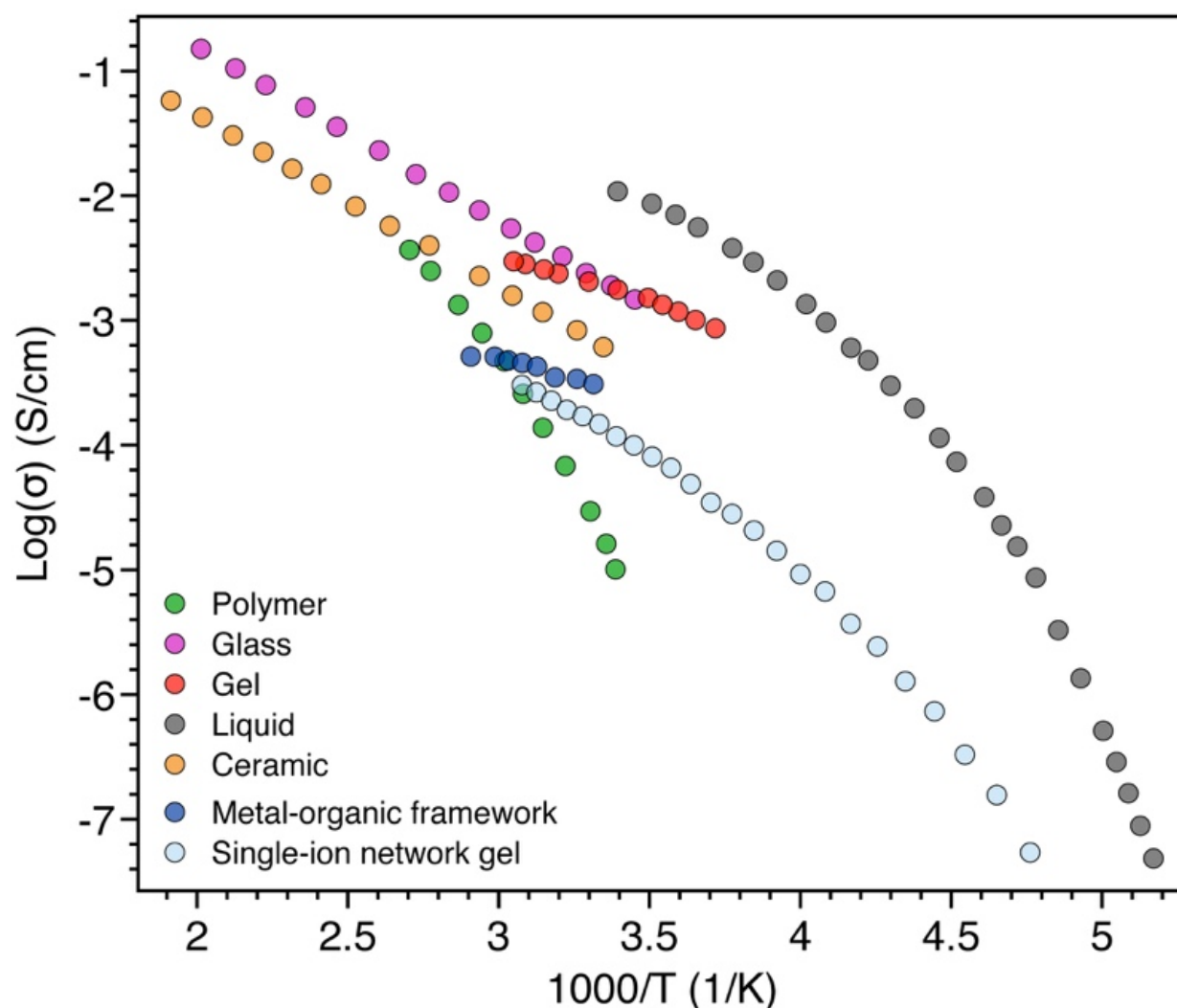


Figure 1.3. Ionic conductivity of selected ion conductors representative of the class. The liquid electrolyte is 1M LiPF₆ in 1:1 ethylene carbonate: propylene carbonate, the gel is poly(vinylidene fluoride-*co*-hexafluoropropylene), the amorphous polymer is PEO · 0.125LiClO₄, 10wt% TiO₂, the glass is Li₂S-SiS₂-Li₃PO₄, the ceramic is Li₃N, the metal-organic framework is Mg₂(dobdc) · 0.35Li⁺Pr⁻ · 0.25LiBF₄ · ethylene carbonate · diethylcarbonate and the single-ion network gel is poly-ethylene glycol-lithium tetrafluoro-tetraphenylborate (68 wt% EC:DEC). Original data and experimental details can be found in references 18,84,101-105.

solutions.⁹³ Ion mobility is similarly difficult to obtain at high concentrations ($> \sim 1$ M), and is especially challenging to determine for multivalent ions that are prone to speciation.

In solutions, polymer gels, and other solvated phases, the conducting ion moves through the electrolyte phase not as a naked M^{n+} or A^{n+} species, but rather within a solvation shell. Ion solvation is especially important for metal cations that coordinate strongly to Lewis basic solvent molecules. **Figure 1.2a** gives a rough illustration of ion solvation in water, wherein a primary solvation shell forms a coordination complex with the metal cation, about which a larger and much more weakly associated secondary solvation shell orders. The radius of an ion plus its effective solvation shell as it tumbles about in solution can be described by the Stokes-Einstein relation given in **Equation 5**.^{94,95}

$$\mu_i = \frac{1}{6\pi\eta r_i} \quad (5)$$

The ion mobility is inversely proportional to the viscosity, η , and the solvodynamic radii, r_s , of the ions. For ions of identical charge, the solvodynamic radius typically decreases as ionic radius increases. This relationship may be anticipated, since solvent molecules associate less strongly with ions of lower charge density, and it is actually the sheer bulk of the solvation shell that defines the effective radius.^{19,20} In comparison, the ionic radius is much smaller.

Ionic conductivity across many types of electrolytes—e.g., liquids, ceramics, and polymers—is diffusive. The Nernst-Einstein relation, **Equation 6**, relates the relative velocity of an ion in an electric field, μ , to its diffusion coefficient, D , where k_B is the Boltzmann constant and T is absolute temperature.

$$D = \mu k_B T \quad (6)$$

Further, the temperature dependence of the diffusion coefficient follows Arrhenius behavior for a hopping-type mechanism, and by implementing **Equations 6** and **2**, the temperature dependence for many ion-conducting systems can be reasonably described by **Equation 7**.^{86,87,96}

$$\sigma T = \sigma_0 e^{\frac{-E_a}{k_B T}} \quad (7)$$

Thus, the product of conductivity and absolute temperature can be related to the activation energy, E_a , and a pre-exponential factor, σ_0 . While the activation energy, formally a reaction enthalpy, can be precisely defined in a model of a potential well in an electric field, it is often difficult to assign to a microscopic charge hopping mechanism, since conductivity is a macroscopic measurement. That is, the true conductivity is usually masked by parasitic resistances, like contact resistance, defect states, grain boundaries, and crystal mosaicity. The pre-exponential factor is a temperature-independent function of the reaction entropy, free ion concentration, symmetry of the conduction mechanism, and the attempt frequency.⁹⁷ Given the difficulty of independent determination, however, the pre-exponential factor is typically not investigated for mechanistic insight and is treated as an empirical constant.

For solid polymers, polymer gels, liquids that glass, and even some liquids that crystallize, the effective viscosity of the electrolyte is often transport limiting rather than a physical hopping barrier. In this scenario, the viscosity will decrease with temperature, as described by the Vogel-Tamman-Fulcher (VTF) relation, **Equation 8**.^{98,99}

$$\eta = A e^{\frac{-B}{T-T_0}} \quad (8)$$

Here A and B are accepted as empirically determined parameters and T_0 is usually correlated with the glass transition temperature of electrolyte. By Walden's Law¹⁰⁰ — $\sigma \propto \eta^{-1}$ — the VTF relation can be expressed in terms of conductivity as in **Equation 9**.

$$\sigma = \sigma_0 e^{\frac{-B}{T-T_0}} \quad (9)$$

Nearly all electrolyte systems follow one of these two models with an occasional discontinuity near phase transitions. Accordingly, the variable temperature conductivity of ion conductors acts as a very clear indicator of transport mechanisms in solids. The Arrhenius plot in **Figure 1.3** illustrates the differences between the Arrhenius and VTF models of transport across different classes of materials.^{18,84,101-105} Note the clear curvature for the canonical liquid, polymer, and gel systems, in contrast to the highly linear trends of glass and ceramic systems.

1.4 Electrochemical characterization of ionic conductors

1.4.1 Overview. Ionic conductivity is ohmic in character; that is, conductance is independent of applied field in the low field limit. However, unlike the electronic conductivity in an ideal resistor, ionic conductivity is frequency dependent and approaches zero at the dc (steady state) limit for a material of finite length. Unlike in an electron conductor, where electrons can migrate through a material and then simply insert into the metallic current collectors, ions are blocked from further migration once they reach the electrode-electrolyte interface. This results in a polarization at the current collectors that effectively shields the bulk sample from the applied field, such that the measured conductance drops to zero. This polarization is described as an electrical double layer capacitance at the electrode-electrolyte interfaces, as depicted in **Figure 1.4**.¹⁰⁶ Due to this effect, it is necessary to measure the impedance of a material as a function of frequency in order to determine the ion transport properties. Here, ac impedance techniques used to characterize ion conductors are reviewed in detail. Aside from conductivity, other critical properties important to the application of new ion conducting materials such as temperature window, transference number, electrochemical stability, and

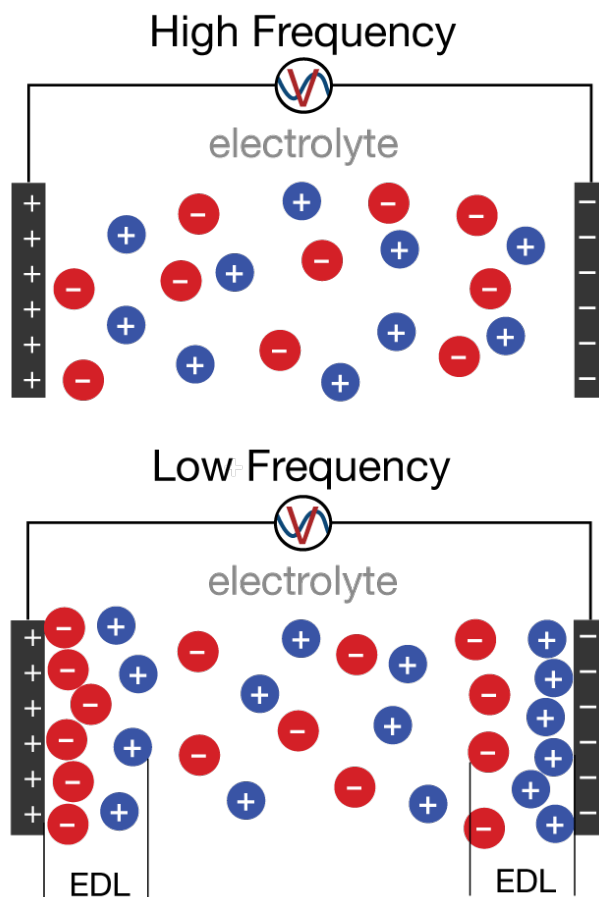


Figure 1.4. Illustration of the ion distribution of an electrolyte at zero field or high frequency (top) and the formation of an electrical double layer capacitance at low frequencies preventing the passage of direct current (bottom).

stability to reactive electrodes are also discussed.

1.4.2 Impedance Spectroscopy. Ac impedance spectroscopy is a particularly powerful technique for the characterization of ion, electron, and mixed conductors, as well as electrochemical reactions.^{107,108} In the simplest terms, this technique allows the charge transport processes within an electrochemical cell to be resolved by their characteristic rate constants. In contrast, dc techniques represent every charge transport process as a single resistance value for a given potential. Ac methods allow much more informative and less ambiguous data to be collected. Further, many modern potentiostats are equipped with frequency domain capabilities making these methods available now more than ever. However, it is important to understand the underlying physics and limitations of ac impedance spectroscopy in order to extract physically meaningful conclusions. Impedance spectra are notoriously misinterpreted or improperly measured.¹⁰⁹⁻¹¹² Provided one is familiar with the basic principles, understands the limitations, and has realistic expectations of what sort of information can be extracted from the data, ac impedance spectroscopy is an indispensable tool for the study of hopping-based transport.

While single crystal and compacted thin films often provide high conductivity values for a material, by far the easiest, most general and most reported method for measuring ionic conductivity is on pressed pellets of microcrystalline powders. For pressed pellets, a simple two-contact cell as shown in **Figure 1.5a** is typically used. Here, the pellet (in orange) is pressed within an insulating washer then pressed between two inert, metallic current collectors. The conductivity for this cell can then be calculated as the geometry normalized dc resistance determined from the impedance spectra.

In the typical experiment, a very small ac voltage or current is applied across two metallic electrodes. The material between the electrodes responds by either polarizing or moving charge, and the resulting impedance is measured as a function of frequency. Impedance is a complex function of frequency, as expressed in **Equation 10**.

$$Z(\omega) = Z'(\omega) + iZ''(\omega) \quad (10)$$

The frequency dependence of any linear, time-invariant system, such as exemplified in **Figure 1.5c**, can be modeled using ideal circuit components. **Figure 1.5b** shows perhaps the most common

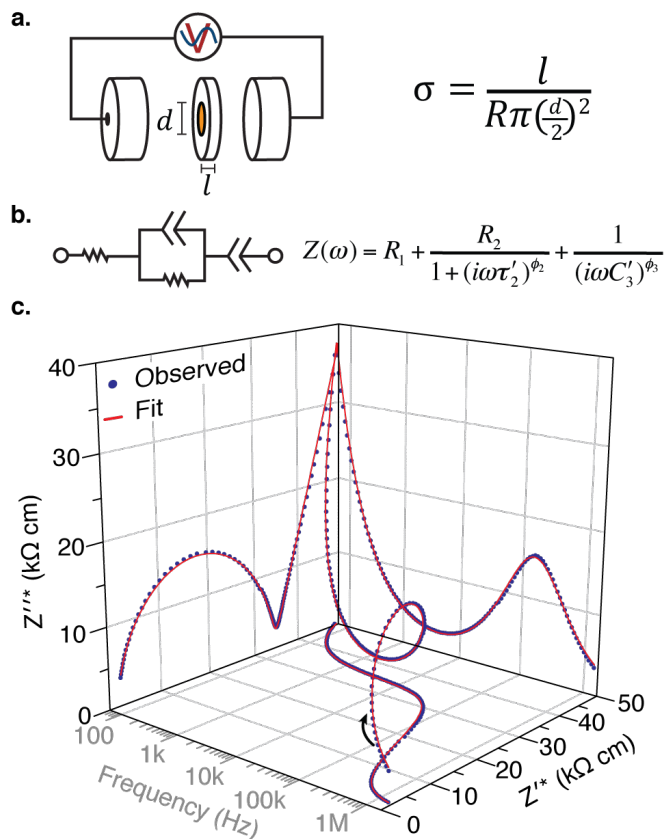


Figure 1.5. Typical 2-electrode cell geometry used to collect ac impedance spectra (a), most general model circuit for an ion conductor on blocking electrodes and the equation it represents (b), and an experimentally determined impedance spectrum for a magnesium ion conductor fit to the model circuit shown (c).

model circuit for an ion conductor on blocking electrodes with a single transport process. This circuit represents an equation for the frequency-dependent impedance of the system, from which an estimate of the ideal dc conductivity can be determined. The equation in **Figure 1.5b** is plotted in **Figure 1.5c** along with the experimentally determined impedance spectra collected for a solid lithium ion conductor.

The typical experiment begins at high frequency (~ 1 MHz) and sweeps to low frequency. The cell response traces a line in three dimensions: resistance, reactance, and frequency. Impedance is a continuous and smooth function of frequency in the 3-D trace. The right wall and the floor of the plot show how the real and imaginary components change with frequency. However, most often, only the complex plane plot is shown since it contains the most useful information about the system in a single representation. The complex plane plot is parametric with respect to frequency and can therefore appear discontinuous. In impedance spectroscopy, the plot of the complex conjugate of **Equation 10** is referred to as a Nyquist Plot.

The impedance spectra for the metal-organic framework $\text{Cu}[\text{Ni}(\text{pdt})_2]$ (pdt = 2,3-pyrazinedithiolate) are shown in **Figure 1.6** and displays a dc hopping conductivity of $2.6 \mu\text{S cm}^{-1}$. This material exhibits the simplest possible spectrum for a hopping conductor, Debye type dielectric relaxation.¹¹³ The equations for impedance response are identical in form to those of dielectric response. Plotted at the left in **Figure 1.6** are the real and imaginary impedances as a function of frequency. The peak in the imaginary impedance spectrum corresponds to the resonance frequency of the cell and is dependent on the dimensions of the sample. The low frequency plateau of the real impedance spectrum corresponds to the low frequency resistance of the cell, and the dc conductivity can be estimated by inspection. **Figure 1.6** at the right shows the Nyquist plot where a single nearly perfect semicircle is observed. A material with a single transport process should only show a single, nearly perfect semicircle in the Nyquist plot. From this graph, we can also determine that the conductivity through the sample is electronic since the impedance is real and frequency independent at low frequencies.

By the Kramers-Kronig transform, a spectrum can be tested for linearity and time invariance without collecting multiple spectra (useful at very low frequencies) or fitting to a model circuit (useful for complicated data). The Kramers-Kronig transform for $\text{Cu}[\text{Ni}(\text{pdt})_2]$ is given in **Figure S1.1**. Variation in the applied dc and ac fields also allows confirmation of ohmic conductance and linearity, respectively. Neither of these features can be determined from single point dc measurements. These analyses and controls are shown in the Supporting Information for $\text{Cu}[\text{Ni}(\text{pdt})_2]$.

1.4.3 Circuit modeling. As previously mentioned, linear, time-invariant impedance spectra can be modeled by functions represented by relatively simple circuit diagrams. A set of a few equations can be combined in complex ways using Kirchoff's circuit laws to model the data. **Equations 11 – 14** are a set of the most common circuit elements used for modeling conductors and electrochemical systems.

$$\text{Capacitor: } Z(\omega) = \frac{1}{i\omega C} \quad (11)$$

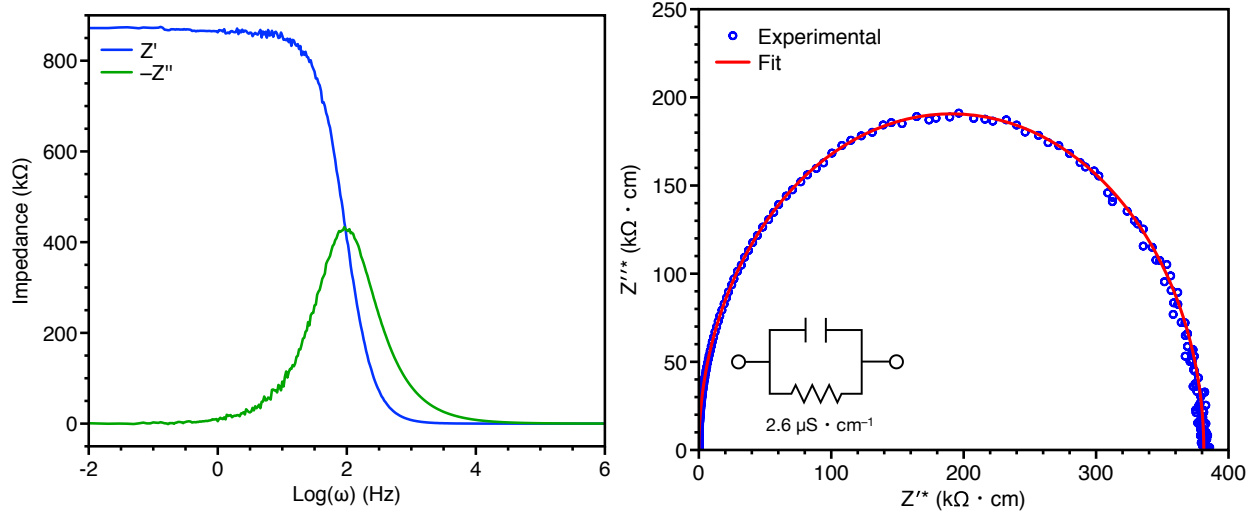


Figure 1.6. (left) Frequency response of the real and imaginary components of $\text{Cu}(\text{Ni}[\text{pdt}]_2)$ shows an ideal Debye type relaxation, and (right) the Nyquist plot from the same experiment fit to an ideal parallel RC circuit is consistent with a single well defined transport process through the bulk of the pellet.

$$\text{Resistor: } Z(\omega) = R \quad (12)$$

$$\text{CPE: } Z(\omega) = \frac{1}{(i\omega)^a Q_0} \quad (13)$$

$$\text{Warburg: } Z(\omega) = \frac{A_W}{\sqrt{\omega}} + \frac{A_W}{i\sqrt{\omega}} \quad (14)$$

Here, Z is the impedance, R , C , Q , a , and A_W are constants, and ω is the frequency. Equations 11 and 12 are the classical ideal circuit elements while the constant phase element (CPE) and Warburg elements can be considered as non-ideal capacitors. The CPE is effectively a Gaussian distribution of capacitances and commonly replaces a capacitor in modeling amorphous or heterogeneous conductors. When $a = 1$, the CPE is equivalent to an ideal capacitor, and as a decreases from unity the distribution of capacitances broadens. The Warburg impedance is essentially CPE with $a = 0.5$ and models infinite diffusion into an electrode or double layer. Warburg behavior is often observed in liquid electrolytes at intermediate frequencies ($\sim 1-0.01$ kHz).

The inset of **Figure 1.6b** shows the model circuit for an ideal Debye type transport process, which nicely models the impedance spectra of $\text{Cu}[\text{Ni}(\text{pdt})_2]$ from 1 MHz to 10 mHz as a parallel RC circuit. The resistor in the circuit represents the bulk dc conductivity of the sample. A single parallel RC circuit represents a single relaxation process in the bulk solid. In this case, it represents bulk electronic to conductivity through the sample. More complex combinations of parallel RC circuits can be drawn represent materials with more than one charge transport process.

Figure 1.5b shows a slightly more complicated model circuit for a typical ion conductor. Very high frequency transport processes (single domain conductivities, ion pairing...) occur above 1 MHz that are not observable as semicircles. Instead, all of these very high frequency processes add together and behave as an ideal resistor. Given the complex nature of this first element, it is normally difficult to assign a single physical process to its value and so it is treated as an empirical fit parameter. The central parallel R-CPE circuit represents bulk charge transport across the measurement cell with a Gaussian distribution of time constants. This element is assigned to the best

guess at the limiting transport process between the two electrodes. For pressed pellets this process is normally an interparticle contact resistance. Since the characteristic frequency of this process is much higher than that of the capacitive tail, it is reasonable to assume it manifests within the sample rather than at the electrode-electrolyte interface. At low frequencies, the right-most CPE in the model circuit models a non-ideal electrical double layer capacitance at the electrode-electrolyte interface. For solid electrolytes, this normally results from rough electrode contacts. Given the inherent roughness of polycrystalline pellets, modeling a capacitive tail with a CPE is quite common.

1.4.4 Variable temperature conductivity. The temperature dependence of ionic conductivity is critically important for the determination of the underlying transport mechanism as well as the determination of the operating temperature of elements in practical devices. For example, the U.S. Department of Energy typically targets an operating range of ± 40 °C for battery electrolytes.¹¹⁴ Data should be collected upon both heating and cooling as a check for thermal equilibration and potential sample decomposition/phase separation. It is rather difficult to isolate a specific temperature model for conductivity by only heating a sample from room temperature to ~ 100 °C. Rather, cryogenic measurements are required to measure conductivity over a much large temperature range. Often, materials that appear to follow a simple Arrhenius law at elevated temperatures can deviate dramatically over a larger temperature range. One exemplary system, given in **Figure S1.3**, is a highly crosslinked polymer gel that appears to be Arrhenius above room temperature.

1.4.5 Alternative methods for measuring ion transport. Other methods for the determination of ion mobility have been reviewed elsewhere.⁸⁷ These include radio tracer diffusion and pulse field gradient where self-diffusion can be determined directly at zero field. While these techniques are ion specific it can be difficult to obtain radioactive isotopes, and not all ions are NMR active. Also, since these techniques measure every ion present, not the conducting species alone, the calculated diffusivities can still be composite. Neither technique can distinguish between ion pairs and free ions. Time domain-based measurements, such as a chronopotentiometry, are very easy to perform and were the standard method before impedance analyzers became common place. Most modern potentiostats are now sold with an on-board impedance analyzer, such that impedance measurements are quickly becoming the preferred method for determination of electrolyte resistance throughout electrochemistry.

1.4.6 Transference number. In most electrochemical devices, it is desirable that the composite ion conductors transport only a single charged species. This ionic selectivity is termed the transference number. Most generally, transference number, t_i , is the fraction of a material's conductivity for which the desired mobile species (cation, anion, electron, or hole) is responsible, as shown in Equation 4. Practically, the determination of transference number has a multitude of complications and ambiguities, especially since different methods to determine transference numbers often do not occur under identical conditions. However, those most commonly used— potentiostatic polarization, galvanostatic polarization, electromotive force, and pulse field gradient NMR— have been shown to typically yield comparable results.¹¹⁵

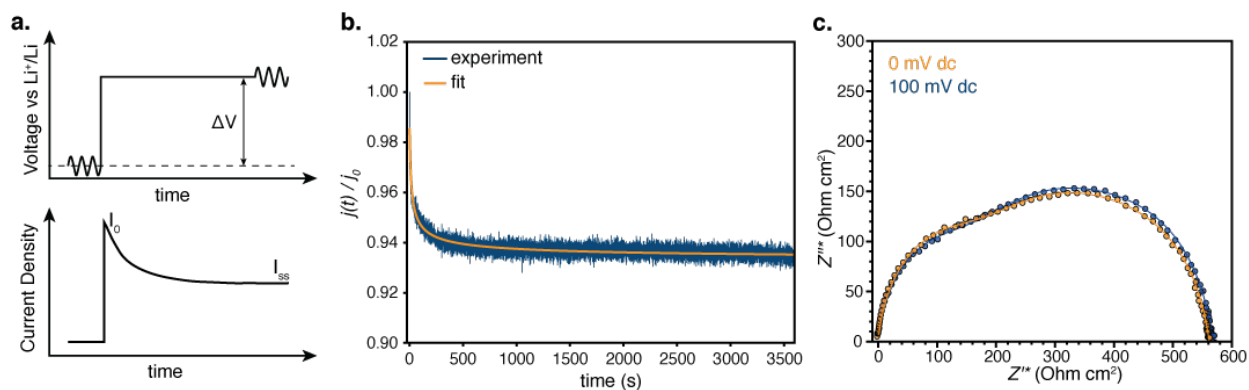


Figure 1.7. General experimental sequence for the potentiostatic polarization method (a). The sine wave indicates an ac impedance technique followed by an applied voltage step then another impedance measurement. Experimental current decay curve fit to a Fickian decay model (b) and ac impedance spectra at zero field and applied field fit with three RC circuits to account for the charge transfer resistance at low frequency (c).

Of these methods, potentiostatic polarization is by far the most practical for the study of materials. In fact, it was originally developed by Evans, Bruce and Vincent as an alternative to the extreme difficulty or impossibility of generating bulk concentration gradients, constructing concentration cells, or using specialized techniques like solid state pulse field gradient NMR on solid ion conductors.¹¹⁶ Although galvanostatic polarization or the electromotive force method are generally considered to be more accurate for liquid electrolytes, for solid ion conductors the potentiostatic polarization methods have become the *de facto* standard, especially for new materials.

A general sequence for the potentiostatic polarization method is given in Figure 1.7a for the determination of lithium ion transference in a lithium electrolyte. In a two-electrode symmetric $Li | electrolyte | Li$ cell, an impedance spectrum is collected at open circuit voltage. This perturbing ac probe voltage should be as small as possible (~ 5 mV) in order to maintain linearity on reactive electrodes. From the known ionic conductivity of the material and the expectation that charge transfer at the electrode-electrolyte interface occurs in the low frequency regime, the resulting spectrum can normally be fitted to a physically meaningful model circuit. In the example given in Figure 1.7c, the spectrum was fit to three RC circuits. The high frequency circuit corresponds to the ionic conductivity of the electrolyte and the low frequency RC circuits correspond to charge transfer at the electrode, i.e. lithium reduction/dissolution.

Prior to measurement the impedance spectrum must be time invariant. For lithium electrodes, the electrode-electrolyte interphase is known to evolve for several days^{117,118} following cell assembly. The temporal stability of the material to reactive electrodes can be a key factor to a device's shelf life and is, on its own, an important performance metric.

The field polarization in Figure 1.7a should also be small, < 100 mV,¹¹⁶ to best maintain electrode symmetry and linearity, and to prevent accelerated electrode-electrolyte interface evolution under applied field. Upon field polarization, the cell responds with a step in current flux that decays with time as an electrical double layer forms at each electrode. In an ideal system, the current decay originates only from ions to which lithium electrodes are blocking. These non-participating ions form an electrical double layer that screens the electric field felt by bulk electrolyte to yield a decay in observed current. After a sufficient amount of time, such a large capacitance from the anions builds up and their contribution to the total current vanishes, so that only the current resulting from

lithium migration remains. Thus, the transference number can be estimated by **Equation 15**, where i_{SS} is the steady state current in **Figure 1.7b**, and i_0 is the initial current before any significant concentration gradient is formed.

$$t_i = \frac{i_{Li}}{i_{total}} \sim \frac{i_{SS}}{i_0} \quad (15)$$

In reality, however, the charge transfer resistance at the electrode is also a function of applied field. Consequently, upon reaching a steady state current, a second impedance spectrum is collected under applied field to determine the shift in charge transfer resistance. To account for this, a correction factor must be applied, yielding the Evans–Bruce–Vincent equation for transference number, **Equation 15**.¹¹⁶ Here R_0 and R_{SS} are the charge transfer resistances before and after application of the step voltage, ΔV .

$$t_i = \frac{i_{SS} \Delta V - I_0 R_0}{i_0 \Delta V - I_{SS} R_{SS}} \quad (16)$$

Solution phase lithium electrolytes normally have transference numbers in the range of 0.3–0.4, solid polymer electrolytes are normally higher though quite variable, 0.3–0.7, and single ion conductors, which display very little, if any, current decay, have transference numbers extremely close to unity. Sample data in **Figures 1.7b** and **1.7c** was collected for a single-ion conducting network polymer impregnated with an organic carbonate solution. This system has a lithium transference number within error of unity, $t_{Li} = 1.01(1)$.

1.4.7 Electrochemical stability window. The electrochemical stability window is defined as the voltage range in which no significant background reactivity is observed on a given electrode. Often times, it is the electrochemical decomposition of electrolyte that limits a device's range of operating voltages by causing electrolyte depletion, electrode passivation, and corrosion. Thus, the stability window is an important property to determine for new electrolyte systems prior to implementation, especially for high voltage batteries and supercapacitors.^{119,120}

The electrochemical stability window is best measured in a three-electrode electrochemical cell with an appropriate working electrode. This is normally a component material in the candidate device (current collector or electrode component). One example is given in **Figure 1.8**, where a porous aromatic framework based electrolyte was found to have an electrochemical stability window of ~ 3.5 V on stainless steel and titanium electrodes.¹²¹ At low potentials, reversible lithium plating and dissolution is observed. The stability window is the distance between this reversible redox process and the onset of

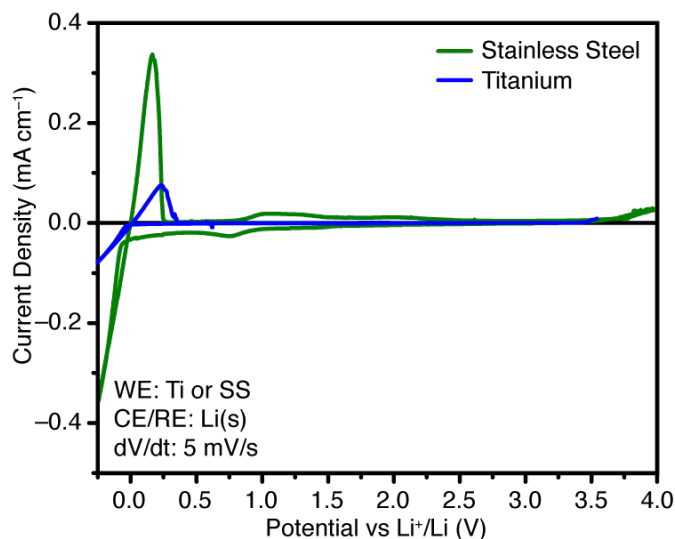


Figure 1.8. Cyclic voltammogram of the single ion conducting polymer network $\text{Li}[\text{B}(\text{F}_4\text{Ph}_4)]$ -1,4-diethynylbenzene on stainless steel and titanium working electrodes. Counter and reference electrodes were both solid lithium. Data was collected as a sweep rate of 5 mV/s (ref. 121).

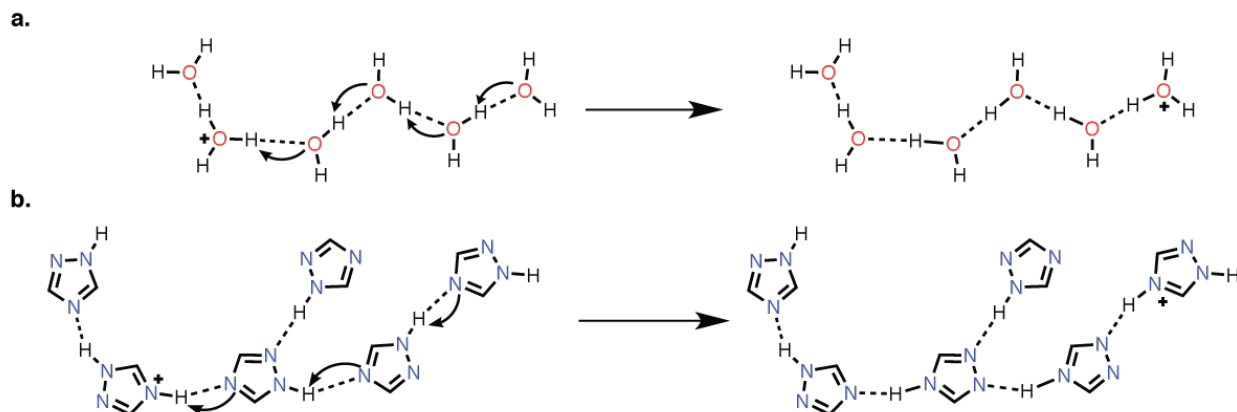


Figure 1.9. The Grotthuss mechanism of excess proton conduction in (a) water and (b) 1,2,4-triazole.

irreversible oxidation. In this case, a small quantity of halide impurities was suspected to provoke the corrosive decomposition at potentials greater than 3.5 V. In the case of systems with lower ionic conductivities, the stability window is determined at low scan rates to avoid kinetic polarization.

1.5 Ion conducting metal-organic frameworks

1.5.1 Overview. Metal-organic frameworks are ideal, model pore structures for the exploration of non-ideal ion solvation states, nano-confined ion mobilities, and the rational engineering of complex heterostructures capable of highly selective ion transport due to their diverse distribution of pore shapes, sizes, and surface chemistries. Here, the discussion will focus on the fundamental transport of metal ions in metal-organic frameworks and related materials, and their implementation in electrochemical devices. However, given the large literature presence of framework-based proton conductors, the unique transport mechanisms of proton conduction also merit discussion.

1.5.2 Proton conductors. While ion transport in metal-organic frameworks remains relatively unstudied, a fairly large number of proton conductors have been reported and reviewed elsewhere.^{30,57,122,123} However, the unique transport mechanism of protons in extended hydrogen bond networks merits a discussion of their properties and design. As proton mobility is easily observed in a large number of water included structures, it is also the best-studied charge transport process in this class of materials.

In electrolytes with extended hydrogen bond networks (e.g. water), protons conduct through a Grotthuss type mechanism.¹²⁴ This is depicted for a variety of molecules used as proton carriers in **Figure 1.9** as a series of hops of a defect or excess proton through the system. In liquid or molten proton conductors, the excess proton is essentially chemically equivalent and thus interchangeable with the other hydrogen bound protons in the cationic complex. Thus, bulk proton transport doesn't require diffusion but local ~ 1 Å hops of many protons in a relay. This transport mode is remarkably efficient and can result in apparent proton diffusivities ten times higher than other cations in aqueous solution.¹²⁵

As shown in **Figure 1.9b**, this mechanism is not unique to aqueous systems. Of technological relevance are molten proton conductors with operating temperatures greater than the boiling point

of water, where higher power densities are obtainable from the rate limiting electrocatalytic reactions at each electrode.^{126,127} Additionally, solid proton conductors that operate at moderate temperatures (300 – 450 K) are also of interest for their ability to effectively separate the anodic and cathodic half-reactions and enable the construction of stable ‘all solid state’ fuel cells. With this in mind, metal-organic frameworks can serve as a robust crystalline host material, with their nanometer scale pores infused with proton conducting liquids and salts. Nearly all reported framework-based proton conductors follow this design principle.

One outstanding example of this strategy is given in **Figure 1.10**. Here the framework $\text{Na}_3(2,4,6\text{-trihydroxy-1,3,5-benzenetrisulfonate})(1\text{H-1,2,4-triazole})_x$ ($x = 0.3\text{--}0.6$) was prepared as a microcrystalline proton conductor with a maximal conductivity of 0.5 mS cm^{-1} at 150°C .^{127,128} This material was also incorporated into a gas separator membrane and implemented in a prototype H_2 -air fuel cell above 100°C —a rare demonstration of a metal-organic framework as a component ion conductor in electrode separators. Although the pore dimensions of the framework without triazole were found to be rather small, $\sim 5.7 \text{ \AA}$, crystallography was unable to resolve the triazole positions in the pores. The apparent lack of large changes in peak intensities suggests the included triazoles are highly disordered.

In some notable cases, the functionalities responsible for proton transport can be crystallographically defined, allowing demonstration of pore- or lattice-constrained Grotthuss-type behavior. For instance, the chiral metal-organic framework $[\text{Zn}(3\text{-methyl-2-(pyridin-4-ylmethylamino)-butanoic acid})(\text{Cl})](\text{H}_2\text{O})_2$ has a helical pore structure, **Figure 1.11**, and undergoes chiral resolution upon the formation of single

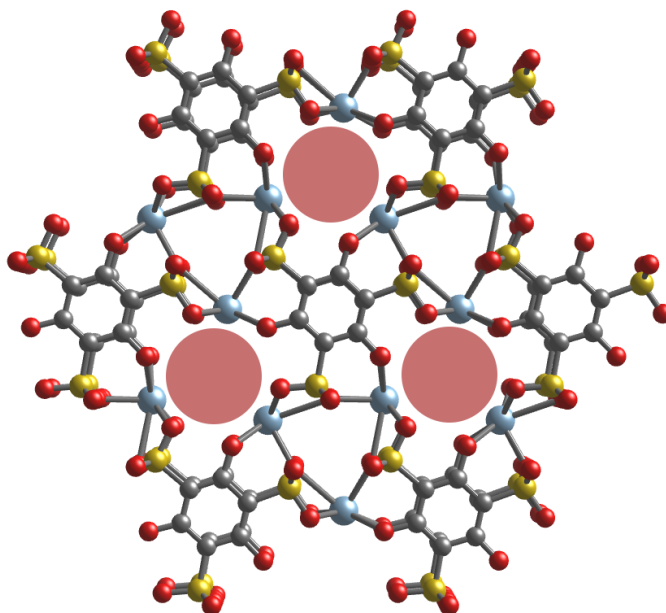


Figure 1.10. Crystal structure of $\text{Na}_3(2,4,6\text{-trihydroxy-1,3,5-benzenetrisulfonate})(1\text{H-1,2,4-triazole})_x$ ($x = 0.3\text{--}0.6$). The light blue, yellow, red and grey spheres indicate Na, S, O and C respectively. The red circles indicate crystallographic voids occupied by included 1,2,4-triazole guests. Sodium atoms are otherwise coordinatively unsaturated as depicted.

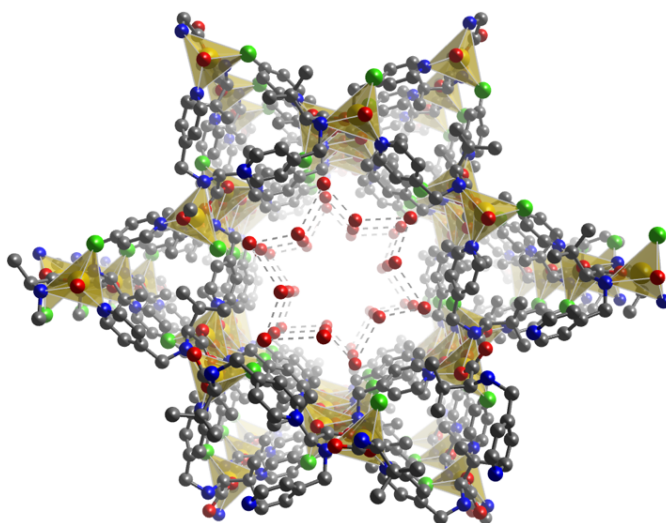


Figure 1.11. Crystal structure of $\text{D-[Zn}(3\text{-methyl-2-(pyridin-4-ylmethylamino)-butanoic acid})(\text{Cl})](\text{H}_2\text{O})_2$. Dashed interactions of the helical water chain in the large pore indicate nearest water contacts close enough to invoke hydrogen bonding interactions ($\sim 2.5\text{--}3.3 \text{ \AA}$).

crystals.¹²⁹ An extended one-dimensional hydrogen bond network was elucidated by single crystal x-ray diffraction, yielding an intuitive pathway for proton conduction through the lattice. The excess protons required to invoke a Grotthuss mechanism likely come from the strong interaction of water molecules with the Zn^{2+} centers lining the pore walls. As with most absorbed-water-based proton conductors, conductivity was strongly dependent on humidity. The water adsorption isotherm displayed cooperative binding and a large step in uptake above 40% R.H. with very little uptake below 20% R.H. A maximal conductivity of $45 \mu\text{S cm}^{-1}$ at room temperature was observed at 98% humidity via two-contact single crystal measurements. While this conductivity is too low to make a

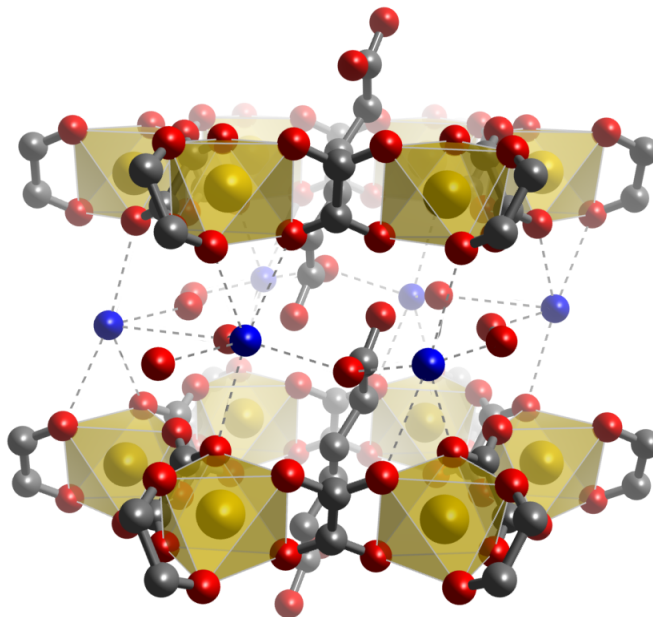


Figure 1.12. Crystal structure of $(\text{NH}_4)_2(\text{adipic acid})[\text{Zn}_2(\text{oxalate})_3] \cdot 3\text{H}_2\text{O}$. Free blue and red spheres indicate ammonium and water molecules; carbon is shown in grey, oxygen in red and zinc in yellow. Potential hydrogen bonding interactions are indicated by dashed lines.

useful device, this stands as a particularly good example of a crystallographically-defined proton channel. Proton mobility can be definitively ascribed to the precise nanometer-scale pore geometry and strong interactions of the absorbed water with the host lattice. Interestingly, the proton channel in **Figure 1.11** is reminiscent of transmembrane ions channels in biological systems.

Another aqueous proton conductor with crystallographically-defined guests is the highly conductive $(\text{NH}_4)_2(\text{adipic acid})[\text{Zn}_2(\text{oxalate})_3] \cdot 3\text{H}_2\text{O}$, **Figure 1.12**.¹³⁰ The $\text{Zn}_2(\text{oxalate})_3$ host lattice forms eclipsed two-dimensional honeycomb sheets charge balanced by interstitial ammonium cations, with a pore structure filled by adipic acid and water. Importantly, all three guests were crystallographically ordered, allowing for an estimate of hydrogen bond distances and then the extended hydrogen bond network topology. Here, both the ammonium and adipic acid behave as excess proton donors, enabling proton transport and a particularly high conductivity of 8 mS cm^{-1} at room temperature (98% R.H). A surprisingly high activation energy was attributed to a possible diffusive, non-Grotthuss mechanism. Alternatively, a non-ideal hydrogen bond network due to crystallographic ordering may result in a higher than expected barrier to the tunneling-assisted hopping, that is still consistent with the expected Grotthuss mode.

Lastly, **Figure 1.13** presents an alternative mode of proton transport in metal-organic frameworks and related materials that does not require the incorporation of guest species within the hosts lattice. The dense, layered coordination solid $\text{Zn}(\text{H}_2\text{PO}_4)_2(1,2,4\text{-triazole})_2$ is a mixed-ligand system with zinc triazole sheets capped by monobasic phosphates.¹³¹ As shown in **Figure 1.13**, this yields alternating layers of proton-rich phosphoric acids that freely rotate about the Zn-O bonds. Secondary participation of the acidic triazole proton is expected. Since both the phosphate and triazole proton donors are tightly bound to the lattice, no significant diffusion is expected. However,

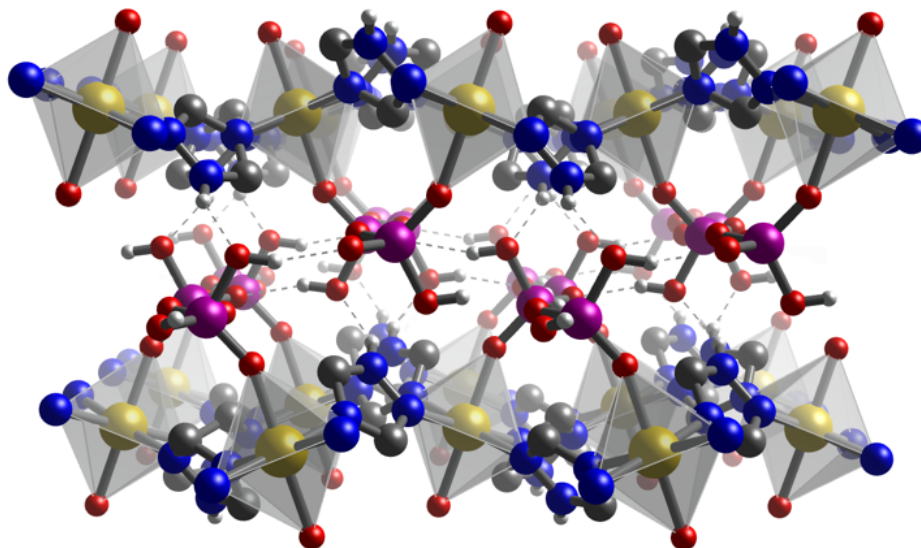


Figure 1.13. Crystal structure of $\text{Zn}(\text{H}_2\text{PO}_4)_2(1,2,4\text{-triazole})_2$. Nitrogen atoms are shown in blue, carbon in grey, oxygen in red, hydrogen in white, phosphorous in fuchsia, and zinc in yellow.

the dense packing of phosphate allows protons to hop between neighboring phosphates and participate in bulk proton transport. With no diffusive guest species, this metal-organic hybrid material is similar to a ceramic ion conductor (e.g. Li_3N in **Figure 1.2c**). However, the presence of an extended contiguous hydrogen bond network suggests a Grotthuss-type mechanism is more likely at play. At elevated temperatures, $> 150\text{ }^\circ\text{C}$, a technologically relevant proton conductivity of 0.12 mS cm^{-1} was obtained. While this material lacks the permanent porosity found in metal-organic frameworks, it remains a rare example of fast ion conduction in a metal-organic coordination solid.

A final note on the conduction of protons in metal-organic frameworks is that much care is required to ensure that observed transport properties are intrinsic to the bulk material before coming to any mechanistic conclusions. It has recently been reported that the conductivity of a $\text{Fe}(\text{oxalate})(\text{H}_2\text{O})_2$ phase as determined by single-crystal measurements is over a million times lower than what was originally reported for pressed pellets of the microcrystalline powder.^{132,133} It was found that small impurity phases of similar composition on the crystallite surfaces were responsible for the originally reported high conductivity at 98% relative humidity. Connectedly, a comparison of Arrhenius parameters also revealed that a large number of metal-organic frameworks behave more like liquids or polymer gels than traditional solid state materials. Ion conductors with Arrhenius energies less than $\sim 0.4\text{ eV}$ and pre-exponential factors less than $10^7\text{ S cm}^{-1}\text{ K}^{-1}$ likely have conduction mechanisms extrinsic to the bulk structure.¹³² Arrhenius energies greater than $\sim 0.5\text{ eV}$ and pre-exponential factors greater than $10^4\text{ S cm}^{-1}\text{ K}^{-1}$ are more consistent with canonical intrinsic proton conductors.

From this analysis, nearly every metal-organic framework with permanent porosity was expected to have conductivity determined by interparticle interfaces, and thus extrinsic to the bulk structure. Of the four specific systems discussed here, all of them displayed activation energies greater than 0.5 eV , except for $[\text{Zn}(3\text{-methyl-2-(pyridin-4-ylmethylamino)-butanoic acid})(\text{Cl})](\text{H}_2\text{O})_2$, which was closer to 0.35 eV .¹²⁹ This may also result from disorder within the particularly large pore structure as

Table 1.2. Ionic conductivities and Arrhenius energies (E_a) for metal-organic framework-based ion conductors.

Ion of Interest	Phase	Solvent	Conductivity (S/cm)	E_a	Measurement Conditions	Ref.
Li ⁺	Cu(BTTri) · <i>n</i> LiBF ₄ ^a	1:1 EC:DEC (sat'd)	1.5·10 ⁻⁹	-	dry, Ar	134
Li ⁺	MOF-177 · <i>n</i> LiBF ₄ ^b	1:1 EC:DEC (sat'd)	4.0·10 ⁻⁷	-	dry, Ar	134
Li ⁺	Mg ₂ (dobdc) · 0.05 LiBF ₄ ^c	1:1 EC:DEC (sat'd)	1.8·10 ⁻⁶	0.31 eV	dry, Ar	18
Li ⁺	Mg ₂ (dobdc) · 0.06 LiO ⁺ Pr ^c	1:1 EC:DEC (sat'd)	1.2·10 ⁻⁵	0.14 eV	dry, Ar	18
Li ⁺	Mg ₂ (dobdc) · 0.35 LiO ⁺ Pr • 0.25 LiBF ₄ ^c	1:1 EC:DEC (sat'd)	3.1·10 ⁻⁴	0.15 eV	dry, Ar	18
Li ⁺	Zr ₆ O ₄ [D] _x Li _x (bdc) _{6-y} ·0.5 (LiO ⁺ Bu) ^{d,e}	14 PC	1.8·10 ⁻⁵	0.18 eV	dry, Ar	135
Li ⁺	Zr ₆ O ₄ (OH) _{1.8} (Oli) _{2.2} [D] _x Li _x (bdc) _{6-y} ^{d,e}	14 PC	3.3·10 ⁻⁶	0.35 eV	dry, Ar	135
Mg ²⁺	Mg ₂ (dobdc) · 0.05 Mg(OPhMe) ₂	1.5 Triglyme	7.9·10 ⁻⁹	-	dry, Ar	136
Mg ²⁺	Mg ₂ (dobdc) · 0.07 Mg(OPh) ₂	1.5 Triglyme	1.0·10 ⁻⁷	-	dry, Ar	136
Mg ²⁺	Mg ₂ (dobdc) · 0.39 Mg(OPhCF ₃) ₂	6.0 Triglyme	1.6·10 ⁻⁶	0.19 eV	dry, Ar	136
Mg ²⁺	Mg ₂ (dobdc) · 0.06 Mg(TFSI) ₂	1.4 Triglyme	1.6·10 ⁻⁶	0.13 eV	dry, Ar	136
Mg ²⁺	Mg ₂ (dobdc) · 0.30 Mg(TFSI) ₂ · 0.31 Mg(OPhCF ₃) ₂	2.4 Triglyme	1.0·10 ⁻⁴	0.15 eV	dry, Ar	136
Mg ²⁺	Mg ₂ (dobpdc) · 0.31 Mg(OphCF ₃) ₂	3.8 Triglyme	6.3·10 ⁻⁷	0.11 eV	dry, Ar	136
Mg ²⁺	Mg ₂ (dobpdc) · 0.22 Mg(TFSI) ₂	3.3 Triglyme	1.3·10 ⁻⁴	0.11 eV	dry, Ar	136
Mg ²⁺	Mg ₂ (dobpdc) · 0.46 Mg(TFSI) ₂ · 0.21 Mg(OPhCF ₃) ₂	4.8 Triglyme	2.5·10 ⁻⁴	0.13 eV	dry, Ar	136
Emim ⁺	[Co ₂ Na(bptc) ₂](Emim) ₃ ^{g,h}	none	2.6·10 ⁻⁵ // 4.8·10 ⁻⁷ ⊥	-	single crystal	137
Li ⁺	[ScLi(μ ₄ -pmdc) ₂ (H ₂ O) ₂] · 2H ₂ O · 0.8 LiBF ₄ ⁱ	DMC	4.2·10 ⁻⁴	0.25 eV	air (hydrated)	138
Na ⁺	[ScLi(μ ₄ -pmdc) ₂ (H ₂ O) ₂] · 2H ₂ O ⁱ	-	3.8·10 ⁻⁷	-		138
Na ⁺	[ScNa(μ ₄ -pmdc) ₂ (H ₂ O) ₂] · 2H ₂ O · 0.7 NaPF ₆ ⁱ	DMC	9.2·10 ⁻⁵	0.64 eV	air (hydrated)	138
Na ⁺	[ScNa(μ ₄ -pmdc) ₂ (H ₂ O) ₂] · 2H ₂ O ⁱ	-	1.1·10 ⁻⁷	-		138
OH ⁻ / H ⁺	La _{1.75} (OH) _{1.25} [Ru(dcpy) ₃] · 16H ₂ O ^j	water	5.5·10 ⁻⁷	-	air, 95% R.H.	139
OH ⁻	[Ni ₈ (OH) ₄ (H ₂ O) ₂ (bdp) ₆] ^k	water	7.6·10 ⁻⁸	0.67 eV	air, 22% R.H.	140
OH ⁻	K[Ni ₈ (OH) ₅ (EtO)(bdp) _{5.5}] ^k	water	3.9·10 ⁻⁶	0.59 eV	air, 22% R.H.	140
OH ⁻	Ni ₈ (OH) ₄ (H ₂ O) ₂ (bdp-OH) ₆ ^k	water	5.8·10 ⁻⁸	0.60 eV	air, 22% R.H.	140
OH ⁻	K ₃ [Ni ₈ (OH) ₃ (EtO)(bdp-O ⁻) ₅] ^k	water	1.8·10 ⁻⁶	-	air, 0% R.H.	140
			2.8·10 ⁻⁵	0.40 eV	air, 22% R.H.	140
			1.2·10 ⁻²	0.21 eV	air, 100% R.H.	140
OH ⁻	Ni ₈ (OH) ₄ (H ₂ O) ₂ (bdp-NH ₂) ₆ ^k	water	7.3·10 ⁻⁸	0.52 eV	air, 22% R.H.	140
OH ⁻	K[Ni ₈ (OH) ₅ (EtO)(bdp-NH ₂) _{5.5}] ^k	water	3.7·10 ⁻⁸	-	air, 0% R.H.	140
			2.8·10 ⁻⁵	0.36 eV	air, 22% R.H.	140
			1.5·10 ⁻³	0.20 eV	air, 100% R.H.	140
Emim ⁺ /TFSI ⁻	100 wt% Emim-TFSI@ZIF-8 ^h	Emim-TFSI	3.1·10 ⁻⁵	-	-	141
EMI ⁺ /TFSI ⁻	125 wt% EMI-TFSA@ZIF-8	EMI-TFSI	1.2·10 ⁻⁴	-	-	141

^aBTTri = 1,3,5-benzene-*tris*-(4-triazolate) ^bMOF-177 = Zn₄O(1,3,5-benzene-tri-benzoate)₂, ^cdobdc⁺ = 2,5-dioxidobenzene-1,4-dicarboxylate, ^dD = defect, ^ebdc²⁻ = benzene-1,4-dicarboxylate, ^fdobpdc²⁻ = 4,4'-dioxido-biphenyl-3,3'-dicarboxylate, ^gbptc = 2,2'-4,4'-biphenyl tetracarboxylate, ^hemim⁺ = 1-Ethyl-3-methyl imidazolium, ⁱpmdc²⁻ = pyrimidine-4,6-dicarboxylate, ^jdcpy = 4,4'-dicarboxy-2,2'-bipyridine, ^kbdp²⁻ = 1,4-benzene-dipyrazolate.

compared to the others and better resembling solution phase transport. In fact, low activation energies may more generally be observed for large pore diameter materials (> 1 nm). Also an extrinsic mechanism is less likely in this case since ionic conductivity was determined using a single crystal.

1.5.3 Ion conducting frameworks by electrolyte impregnation. Metal-organic frameworks' ability to conduct metal ions is especially relevant for their implementation in electrochemical cells. Metal ion conducting frameworks could potentially lead to new solid-state electrolytes, separators, tailored catholytes and anolytes for batteries and supercapacitors, as well as ion selective membranes for fuel cells and flow batteries.¹⁴² Fundamentally, the nanoconfinement of electrolytes within porous structures can lead to unusual or non-classical behavior including fast ion conduction, enhanced transference numbers, and, in extreme cases, wave-like charge delocalization.^{143,144}

To date, metal ion conducting metal-organic frameworks have been prepared, broadly, by three methods: absorption of electrochemically stable electrolyte solutions, post-synthetic grafting of reactive metal salts, and modular synthesis of intrinsically charged frameworks and related organic scaffolds. These are each discussed in turn.

One important property of metal-organic frameworks compared to other porous crystals is their unique surface chemistry. Zeolites, the most classic porous crystalline materials, are replete with anionic oxygens facing the internal pore structure. These polar donor groups are available to bind extra framework cations and lead to an overall hydrophilic surface chemistry.¹⁴⁵ The lattice enthalpy of metal-organic frameworks is similarly dominated by ionic interactions between metal cations and organic anions forming the nodes. However, these groups are often masked by the conjugated

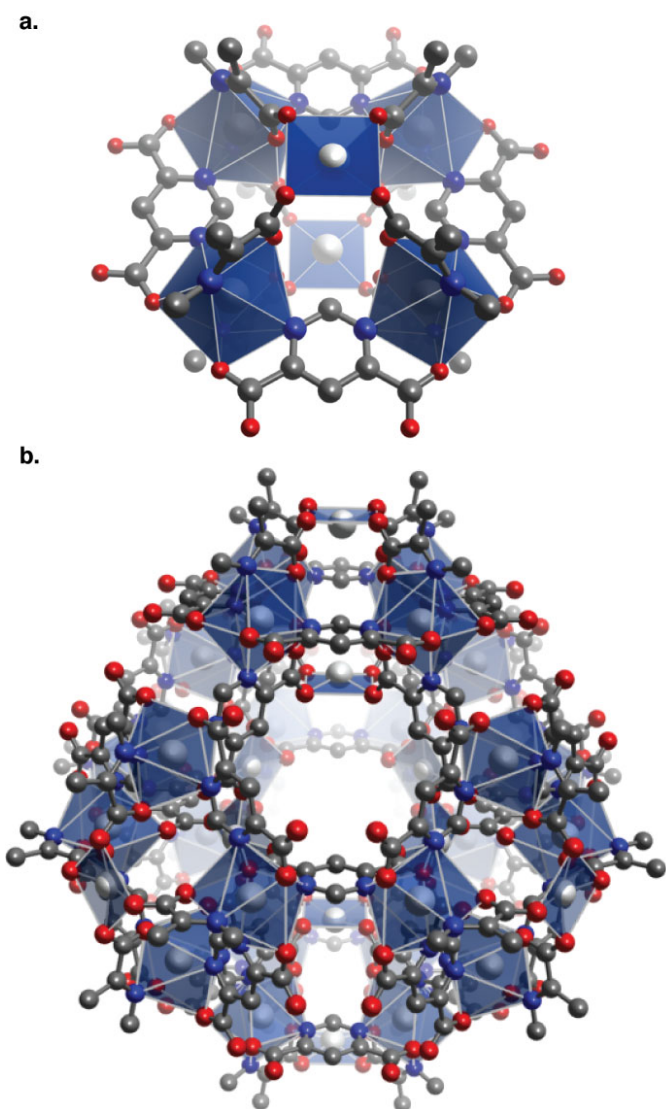


Figure 1.14. (a) A portion of the crystal structure of EHU1 including the scandium cluster node containing four eight-coordinate metal sites and two likely five-coordinate square sites with a square pyramidal geometry. Extra framework cations were not located by diffraction and are not shown. (b) The pore geometry can be approximated as a truncated tetrahedron. Scandium is represented in white, oxygen in red, nitrogen in blue and carbon in grey.

hydrocarbon-based substructures that represent the large majority of the total surface area. For this reason, most metal-organic frameworks are considered to be hydrophobic.¹⁴⁶

For this reason, early attempts at using metal-organic frameworks with ~1 nm diameter pores as electrolyte separator materials yielded materials with very low carrier concentrations.¹³⁴ The frameworks, Cu₃(1,3,5-tris(5-triazol)-benzene),¹⁴⁷ ZnO(1,3,5-benzenetribenzoate) (MOF-177)¹⁴⁸ and Mg₂(dobdc) (dobdc⁴⁻ = 2,5-dioxidobenzene-1,4-dicarboxylate),^{149,150} were soaked in a 1 M LiBF₄ solution in 1:1 (v:v) EC:DEC solvent mixture and, upon equilibration, filtered to afford a free-flowing powder. In each case, very little lithium salt was absorbed, and the observed ionic conductivities were consequently very low: 1.5·10⁻⁹ S/cm, 4·10⁻⁷ S/cm, and 1.8·10⁻⁶ S/cm respectively. These results, along with those for every other ion conductor discussed herein, are summarized in **Table 1.2**.

More recently an intrinsically charged scandium-based framework with extra-framework cations was reported to display a low intrinsic conductivity.¹³⁸ In the phase, ScM(μ_4 -pmdc)₂ (H₂O)₂]·2H₂O (M = Li, Na), named EHU1 (**Figure 1.14**), only the charge balancing sodium or lithium cations in the pore can formally account for the observed conductivity of about 1·10⁻⁷ S/cm, making this possibly the first report of a single ion conductivity in a metal-organic framework. In an attempt to boost the conductivity, EHU1-Li and EHU1-Na were soaked in 1M carbonate solutions of LiBF₄ and NaPF₆, respectively. In both cases, a large amount of alkali salt was absorbed to yield the compositions EHU1-Li·0.8(LiBF₄) and EHU1-Na·0.7(NaPF₆). Surprisingly, neither phase appeared to absorb any carbonate solvent by elemental analysis. Instead, the frameworks retain a significant quantity of disordered water as confirmed by infrared spectroscopy. A large increase in conductivity was observed, up to roughly 1·10⁻⁴ S/cm for the impregnated materials. These are among the highest reported in metal-organic frameworks filled with electrolyte.

While a precise mechanism for conduction was not proposed, the authors point out the presence of decrepitation at the crystallite surface in the scanning electron micrographs. With this in mind, high surface diffusivities of hydrated alkali ions cannot be ruled out as an extrinsic mode of transport in this system. However, even though sodium has a smaller hydrodynamic radius than lithium, the sodium electrolyte displayed a much stronger temperature dependence, **Table 1.2**.²⁰ This suggested either a more solid state conduction mechanism of alkali metals or a pore window size constraint on the mobility of hexafluorophosphate versus the smaller tetrafluoroborate anion of the lithium salt. Unfortunately, measurement of this phase over a much large temperature range than that reported is required to definitively classify the mode of ion conduction.

An alternative way to obtain high electrolyte concentrations is by the absorption of ionic liquids. Ionic liquid inclusion by incipient wetness (and lower loadings) has the advantage that electrolyte uptake occurs via a very large enthalpic driving force.¹⁵¹ Incipient wetness is when an amount liquid phase that is added to a porous solid is exactly equal to the total pore volume. Since the exchange of the initially gas-filled pores for solvent or electrolyte is very favorable (compared to the equilibrium between solutions and MOF-guest-solution phases as discussed above), nearly all of the ionic liquid can be assumed to enter the host lattice. This is also confirmed by a loss in gas-accessible surface area. A strong freezing point depression compared to the bulk ionic liquid 1-ethyl-3-methylimidazolium bis(trifluoromethylsulfonyl)imide (EMI-TFSI) indicates a clear nanoconfinement

effect is imposed on the included guests. Importantly this is the first framework to show such an effect by electrical conductance. The 100 mol% impregnated phase, the most impregnated phase that maintained phase purity, was also more conductive below the freezing point transition at ~ 265 K than bulk EMI-TFSI.¹⁴¹ Similar lithium ion conducting phases have also been reported.¹⁵² Recently, the structure analysis and applications of ionic liquid impregnated metal-organic frameworks has been reviewed; additional details of these and similar materials can be found therein.^{153,154}

While lacking the extended structure and hybrid composition of a metal-organic framework, porous molecular crystals may display very similar ion transport properties. Recently a ‘pumpkin’ shape compound, cucurbit[6]uril, was found to be permanently porous via a single-crystal-to-single-crystal desolvation, **Figure 1.15**, and selective for carbon dioxide adsorption.^{155,156}

In other reports, cucurbit[6]uril was found to conduct protons¹⁵⁷ and battery electrolytes, such as lithium hexafluorophosphate solutions.¹⁵⁸ Again, soaking of the desolvated crystals in 1M solutions of LiPF_6 or LiClO_4 in propylene carbonate or dimethyl carbonate resulted in a significant uptake of the electrolyte solution. For LiPF_6 in both propylene carbonate and dimethyl carbonate, electrolyte absorption was near one equivalent per cage molecule, along with co-insertion of 2–3 equivalents of carbonate solvent (see **Table 1.3** for the precise stoichiometries).

For all reported electrolyte included phases, ionic conductivities on the order of 10^{-4} S cm^{-1} were observed, compared to a background conductivity of 10^{-8} S cm^{-1} for the pristine cucurbit[6]uril phase. Surprisingly high transference numbers were also reported for both perchlorate and hexafluorophosphate based electrolytes, $t_+ = 0.7\text{--}0.8$, compared to the transference numbers of 0.5–0.3 that are normally observed in bulk solution.^{62,115,159,160} The authors explain the high value by invoking a pore confinement hindering of the mobility of the larger anions relative to the ionic radius of a lithium ion analogous to a sieving effect. This explanation inherently assumes an ion hopping model and excludes solvent participation in lithium transport. Unfortunately, it is difficult to confirm a hopping-based conductivity for the material since variable temperature conductivity was only measured over a relatively small range. One possible explanation is the selective inclusion

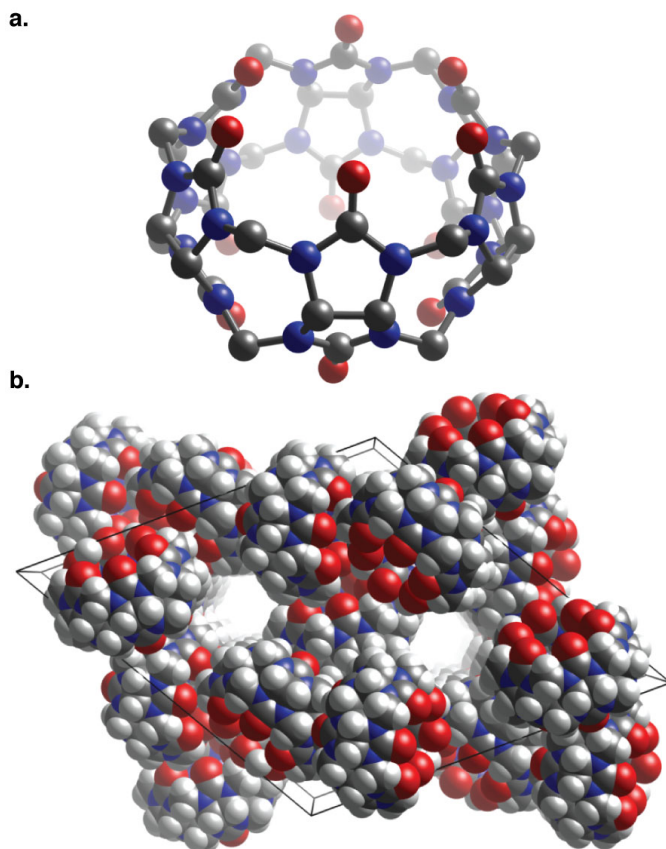


Figure 1.15. (a) Crystal structure of the molecular solid cucurbit[6]uril. (b) The crystal displays an intermolecular 1-D pore structure along the c-axis that is filled with water molecules (removed for clarity). Large voids also exist within the molecular ‘pumpkin’ but no guests were resolved by single-crystal x-ray diffraction. The white, red, blue and grey spheres represent hydrogen, oxygen, nitrogen and carbon respectively.

of the anion within the molecular cage, effectively trapping it and thus limiting anion diffusion, as is the case for gibbsite • LiCl. Interestingly, even the dimethyl carbonate phase maintained a stable conductivity at 100 °C, suggesting either that the included solvent was non-volatile or that the desolvated structure is also conductive—both exciting prospects for ion transport in porous materials.

1.5.4 Conductivity in ionic metal-organic frameworks. The direct absorption of electrochemically useful electrolytes into a porous framework is certainly the simplest method of making a metal-organic framework-based ion conductor. However, as mentioned in **Section 1.5.3**, this absorption is not always favorable. One solution to this problem is to consider systems where a very strong host-guest interaction can drive electrolyte inclusion. For example, through grafting of anionic bases to coordinatively unsaturated metal clusters, neutral frameworks can be charged post-synthetically to potentially afford single ion conductors. **Figure 1.16** illustrates the general scheme of taking a neutral metal-organic framework and converting it to an ionic host post-synthetically to provoke selective ion transport.

One unique aspect of the $\text{Mg}_2(\text{dobdc})$ framework is that it has an extremely high density of oxophilic, coordinatively unsaturated metal sites exposed to the honeycomb pore structure, **Figure 1.17**. It is this polar surface chemistry that likely yielded greater electrolyte uptake and thus a higher ionic conductivity than other canonical frameworks soaked in electrolyte solutions.¹³⁴ Even in this case, however, the included electrolyte was much too dilute to afford an applicable conductivity. In an attempt increase the electrolyte concentration, a nucleophilic anion was added that could interact strongly with the open metal sites lining the pore walls, **Figure 1.17**.¹⁸ Lithium isopropoxide was found to be ideally suited for the $\text{Mg}_2(\text{dobdc})$ pore structure and may be expected, at least in part, to transmetalate from the charge balancing lithium cation in the pore to the oxophilic magnesium ions imbedded in the pore wall. In doing so, the alkoxide charge was efficiently screened by the bulk of the host lattice, leaving the now free lithium ions to easily transport charge. This effect was evidenced by the reduction of the Arrhenius energy to 0.14 eV.

Importantly, even at the same low concentration as the lithium tetrafluoroborate inclusion compound, the ionic conductivity of the lithium isopropoxide-grafted $\text{Mg}_2(\text{dobdc})$ was an order of magnitude greater, $\sim 10^{-5} \text{ S cm}^{-1}$. In order to improve upon this value, the concentration of lithium alkoxide in the framework was maximized, and then the material was soaked in a lithium tetrafluoroborate solution. With the pores filled with lithium isopropoxide, the host lattice was much more favorable to the

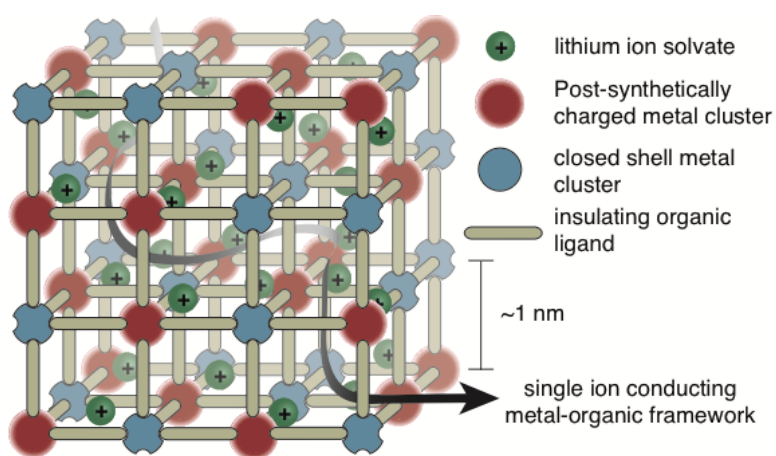


Figure 1.16. Schematic illustrating the post-synthetic introduction of excess metal ion solvates as potential charge carriers in metal-organic frameworks.

absorption of the electrolyte solution compared to the pristine host lattice. A maximal room temperature conductivity of $3 \cdot 10^{-4} \text{ S cm}^{-1}$ was observed, representing the first metal-organic framework-based material to express a lithium ion conductivity at the practical limit for implementation in a lithium-ion battery.^{161,162} Typically, minimum conductivities at least three or four fold higher are desirable in commercial cells.⁶²

Subsequently, the conductance of ions that have been notoriously difficult to transport in the solid state (e.g. Zn^{2+} , Mg^{2+} , Ca^{2+} and Al^{3+}) became of interest. The challenging nature of multivalent cation transport is typically ascribed to their strong preference to form stable, charge neutral clusters and gels in solution.¹⁶³ Confinement of multivalent ions in nanoporous structures may prompt adoption of unusual, less stable ion configurations not observed in bulk solution, or in ceramic/glassy phases, both of which may enable improved charge transport. By the absorption of magnesium bis-phenolate complexes into $\text{Mg}_2(\text{dobdc})$ and a larger pore analog $\text{Mg}_2(4,4'$ -dioxidobiphenyl-3,3'-dicarboxylate) along with the weakly coordinating $\text{Mg}(\text{TFSI})_2$, metal-organic framework based electrolytes

with conductivities a hundred time higher than any other solid magnesium ion conductor at room temperature were observed.¹³⁶ Further, these magnesium electrolytes represent the only solid magnesium ion conductors with conductivities high enough for practical use in an electrochemical cell at ambient conditions. This work is the focus of **Chapter 2**, where it is discussed in detail.

Another interesting metal-organic framework with exposed oxophilic metal sites is the zirconium(IV)-based material UiO-66 or $\text{Zr}_6\text{O}_4(\text{OH})_4(1,4\text{-benzenedicarboxylate})_6$.^{164,165} This framework is also one of the most stable metal-organic frameworks known, with a thermal decomposition temperature of nearly 500 °C, excellent stability in the presence of water, and a calculated minimal shear modulus greater than 13 GPa.¹⁶⁶ This shear modulus is three times that of lithium metal and could therefore feasibly block dendrite growth.¹⁶⁷ A portion of the structure is shown in **Figure 1.18**, highlighting the coordinatively unsaturated Zr^{4+} sites in the cluster node. In

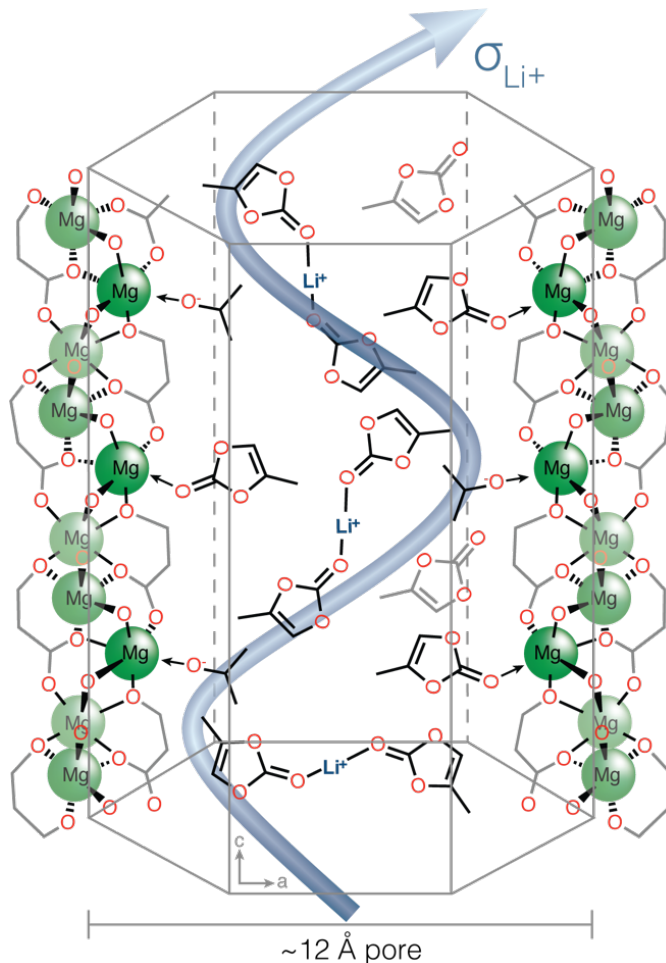


Figure 1.17. Illustration of the transmetalation of lithium isopropoxide in $\text{Mg}_2(\text{dobdc})$. The hexagonal pores are about 12 Å in diameter with coordinatively unsaturated five-coordinate magnesium ions lining the vertices of the pore. Only two of the six 1-D metal chains for this pore are shown for clarity. Only one in three magnesium ions point into the pore shown here, while the two adjacent ions point into the adjoining pores of the infinite honeycomb lattice.

this structure, there are three open metal sites poised to coordinate hydroxides or alkoxides in a μ^3 fashion. The transmetalation reaction was found to be highly favorable, since the counterion binds to three metal centers instead of just one.¹⁶⁸ High electrolyte concentrations and a conductivity of $\sim 10^{-5}$ S cm^{-1} were observed for the alkoxide grafted samples. With the additional inclusion of LiBF_4 in propylene carbonate, conductivities greater than 10^{-4} S cm^{-1} were also observed.

More recent electrochemical characterization of this phase demonstrated a stability to lithium metal for at least two weeks, and an electrochemical stability window in excess of five volts, **Figures S1.3** and **S1.4**. However, since it was still necessary to include the weakly coordinating LiBF_4 supporting electrolyte to obtain a functional conductivity, the measured transference number was an expectedly low 0.35, as shown in **Figure S1.5** and **S1.6**. In fact, it was found to be extremely similar to that of bulk solutions of LiBF_4 in carbonate solutions measured by the same potentiostatic polarization procedure.¹¹⁵

A remarkably stable nickel pyrazolate framework has recently been reported with an inorganic building unit similar to that of $\text{Zr}_6\text{O}_6(1,4\text{-benzenedicarboxylate})_6$, as shown in **Figure 1.19**.¹⁶⁹⁻¹⁷¹ In $[\text{Ni}_8(\text{OH})_4(\text{H}_2\text{O})_2](1,4\text{-benzene dipyrazolate}_X)_6$ ($X = \text{H}, \text{OH}, \text{NH}_2$), the $[\text{Ni}_8(\text{OH})_4(\text{H}_2\text{O})_2]^{12+}$ cluster was shown to react directly with an ethoxide that exchanges for a μ^4 -hydroxide. In the presence of water, the now very basic cluster readily deprotonates adsorbed water to yield an extra-framework hydroxide that is free to conduct charge.¹⁴⁰ The conductivities of the resulting phases are summarized in **Table 1.2**. A roughly thousand-fold enhancement in conductivity was observed when comparing the pristine framework's conductivity with that of the base-treated structures at 22 % R.H. Increasing the relative humidity to nearly 100 %, the conductivity typically increased by another factor of one thousand. This was consistent with the step position of the water isotherms, which were all above 22 % R.H. The framework composed of the benzene dipyrazolate linker functionalized with a phenolic oxygen was found to produce the high conductivity of 0.01 S cm^{-1} , which is the highest ionic conductivity reported in a metal-organic

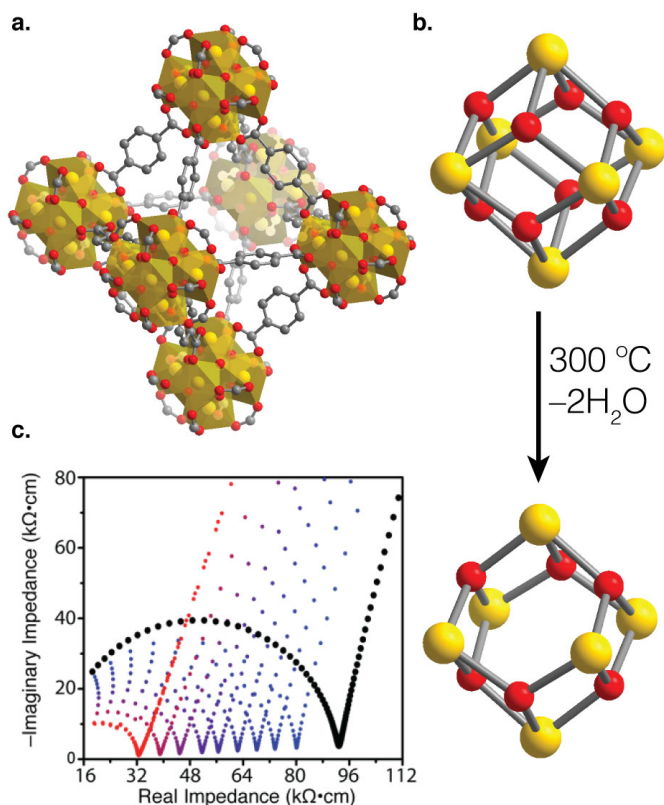


Figure 1.18. (a) The octahedral pore of UiO-66 forms an infinite tiling with complementary tetrahedral pores joined at the faces to form an FCU lattice. Zirconium is shown in yellow, oxygen in red and carbon in grey. (b) The $\text{Zr}_6\text{O}_4(\text{OH})_4$ cluster node dehydrates at elevated temperature to yield the Zr_6O_6 cluster (with six open Zr^{4+} sites capable of coordinating two alkoxides). The hydroxyl protons are disordered across all eight of the oxygen atoms shown. Last, (c) displays the room temperature Nyquist plot for the framework grafted with lithium *tert*-butoxide in black and for increasing temperatures up to $120\text{ }^\circ\text{C}$ in the blue to red spectrum.

framework in which the charge carriers are not protons.

Importantly, the authors note that in the as-synthesized material about 15% of the organic linkers are missing, yielding defect vacancies that are expected to significantly modulate the observed conductivities. This is due to the replacement of the missing ligands by additional water and hydroxide ligands bound to the metal clusters. Thus, these groups lead to additional ionic charge carriers upon treatment with potassium ethoxide. The large Arrhenius energies observed for all phases also suggest that the conductivities do not stem from extrinsic proton conduction at low humidity. However, the activation barriers for the most conductive samples (100 % R.H.) were rather low, preventing a surface-based conduction mechanism from being ruled out.

1.5.5 Single-ion conducting porous organic polymers. Porous organic polymers' permanent porosity, synthetic tunability, and modular design make this diverse class of materials kin to metal-organic frameworks in function and design. The large majority of materials reported are for charge neutral structures with an all-hydrocarbon skeletal structure.¹⁷²⁻¹⁷⁴ One

notable property of these phases, especially the porous aromatic frameworks, is their incredible stability and well defined pore structures.¹⁷⁵ For this reason, they are all attractive candidates as single-ion battery electrolytes with potentially very large electrochemical stability windows.

The first report of a ion conducting phase with high conductivity was prepared by simple atom substitution of the tetrahedral carbon node in PAF-1 with a boron to yield an anionic framework with tetraphenylborate nodes, **Figure 1.20**.¹²¹ Several other lithium ion conducting polymers based on borate nodes have also been reported as lithium electrolytes.^{176,177} Tetraphenylborates and especially their perfluorinated congeners are well known weakly coordinating anions in coordination chemistry, but are less commonly used as battery electrolytes. Several different lithium tetraphenylborate-based PAF's were prepared by a variety of different synthetic conditions. A few of

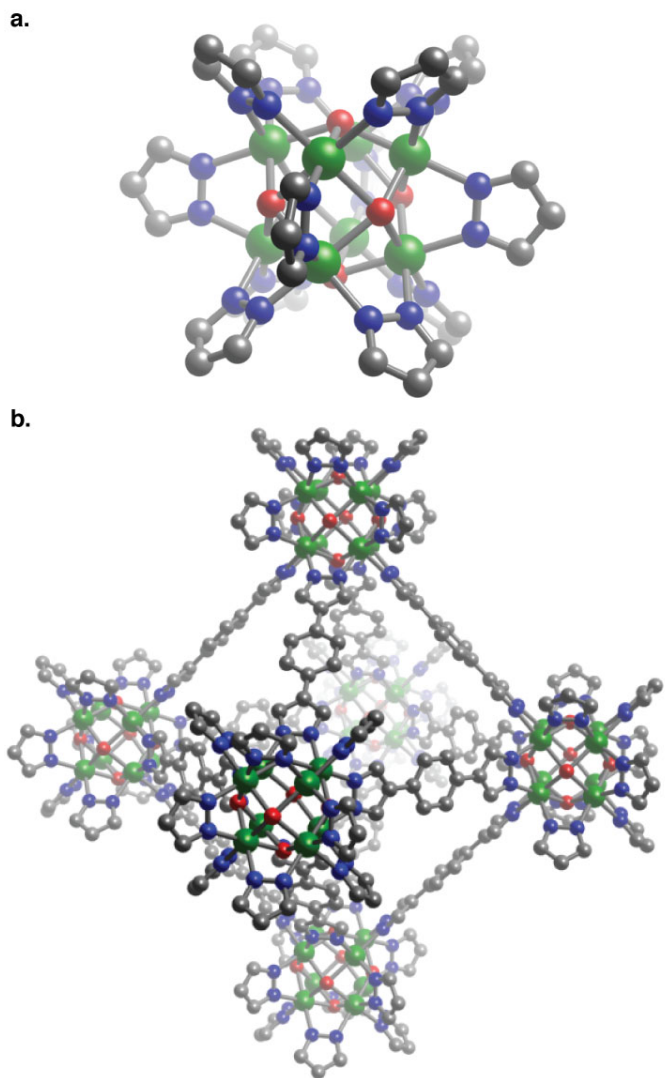


Figure 1.19. (a) A fragment of $[\text{Ni}_8(\text{OH})_4(\text{H}_2\text{O})_2](1,4\text{-benzene dipyrazolate})_6$ highlighting the octanuclear nickel cluster node and (b) the octahedral pore network that is topologically equivalent to UiO-66. Nickel sites are shown in green, oxygen in red, nitrogen in blue and carbon in grey.

the standout materials as summarized in **Table 1.3**. In contrast to the parent PAF-1 structure, most of these materials were non-porous.

Nonetheless upon adding ~10 wt% propylene carbonate to the synthesized powders, rather high conductivities were observed for single ion conductors. In the best case, using a lithium perfluorotetraphenylborate node, conductivity was maximized at slightly above 10^{-4} S cm⁻¹. Curiously, materials identical in composition, but synthesized using different reaction solvents, resulted in noticeable changes in particle packing and morphology and were 10,000 times less conductive. This, along with the low activation energies and low solvent content, are most consistent with a surface-based

conduction mechanism. The solids formed in the system were universally amorphous, and scanning electron microscopy revealed that the most conductive materials were agglomerations of densely packed sub-100 nm particles. Taking this into consideration, conduction in these tetraphenylborate-based frameworks may be described as a nanoionic effect.¹⁷⁸

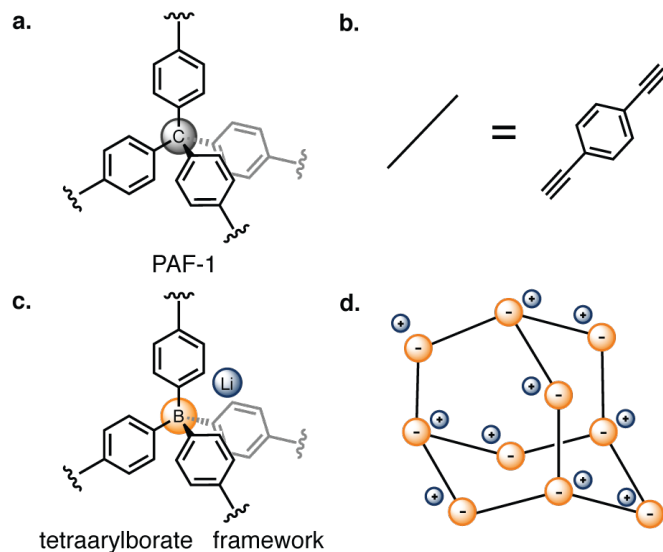


Figure 1.20. (a) Lewis structure of the PAF-1 tetraarylmethane node and the PAF-1 dialkynylbenzene linker (b). Substitution of the carbon node for boron yields an anionic framework that can be charge balanced by lithium cations (c). (d) The idealized skeletal structure for these porous aromatic frameworks, that are actually brittle, amorphous solids.

Table 1.3. Ionic conductivities and Arrhenius energies (E_a) for porous-polymer-network-based ion conductors and related materials.

Ion of Interest	Phase	Solvent	Conductivity (S/cm)	E_a	Measurement Conditions	Ref.
Li ⁺	ICOF-2 ^a	PC (55 wt%)	$3.0 \cdot 10^{-5}$	0.24 eV	-	181
Li ⁺	Cucurbit[6]uril 0.8LiPF ₆ 3PC	PC	$9.0 \cdot 10^{-5}$	0.38 eV	-	158
Li ⁺	Cucurbit[6]uril 0.4LiClO ₄ 3.4PC	PC	$8.0 \cdot 10^{-5}$	0.32 eV	-	158
Li ⁺	Cucurbit[6]uril 1.1LiPF ₆ 2.2DMC	DMC	$1.0 \cdot 10^{-4}$	0.34 eV	-	158
Li ⁺	PVDF-HFP/melamine-terephthaldehyde-lithium salt ^b	1:1 EC:PC	$6.0 \cdot 10^{-4}$	-	dry, Ar	180
Li ⁺	PVDF-HFP / phluoroglucinol-terephthaldehyde lithium salt ^b	1:1 EC:PC	$6.3 \cdot 10^{-4}$	-	-	179
Li ⁺	Li[B(Ph ₄)]-1,4-diethynylbenzene PAF ^c	PC	$3.6 \cdot 10^{-5}$	0.28 eV	dry, Ar	121
Li ⁺	Li[B(F ₄ Ph ₄)]-1,4-diethynylbenzene PAF ^c	PC	$2.7 \cdot 10^{-4}$	0.25 eV	dry, Ar	121
Li ⁺	Li[B(F ₄ Ph ₄)]-1,4-diethynyl-2,5-bis-OTEG-benzene PAF ^{c,d}	PC	$3.0 \cdot 10^{-5}$	-	dry, Ar	121

^aICOF-2 is a spiroborate coordination polymer of (3,6-di(prop-1-yn-1-yl)-9H-fluorene-9,9-diyl)bis(methylene)diol, ^bPVDF-HFP = Poly(vinylidene fluoride-*co*-hexafluoropropylene) ^cPAF = porous aromatic framework, ^dOTEG = [2-[2-(2-methoxyethoxy) ethoxy] ethoxide]

Other performance characteristics of the lithium tetraphenylborate-based PAF's were also investigated for possible implementation into lithium batteries. Lithium transference numbers between 0.89 and 0.93 were consistent with the expectation that these materials are single ion conductors. The deviation from unity is mostly the result of either continued SEI evolution at the electrode surface interfering with the measurement, or small amounts of mobile ammonium or iodide not detected by elemental analysis. Nonetheless, by ac impedance spectroscopy, the charge transfer resistance across the cell was found to be stable for over a week. Finally, by three-electrode cyclic voltammetry, an electrochemical stability window of ~ 3.5 V was observed with stainless steel and titanium working electrodes. This was also lower than initially expected and can possibly be explained by residual aryl iodide from the polymerization corroding the electrode.

Recently, two new ionic polymers have been prepared by condensation of polytopic nucleophiles and terephthalaldehyde, **Figure 1.21**.^{179,180} Although in this case the resulting polymer strongly coordinates charge balancing lithium ions, the extremely high concentration of lithium included is sufficient, upon forming a gel with organic carbonates, to afford conductivities around $6 \cdot 10^{-4}$ S cm^{-1} (**Table 1.3**). Importantly, all of the electrochemical measurements were performed after imbedding the polymer nanopowders in a PVDF-HFP mixed-matrix membrane. This represents a rare example of producing an easily processable ion conductor with this class of materials compatible with state of the art device fabrications methods. While these materials display high transference numbers, between 0.86 and 0.88, no explanation for the deviation from unity is proposed. Broad infrared absorbance above 3000 cm^{-1} seems to be consistent with the presence of residual water; perhaps trace hydroxide is responsible for lowered transference numbers in these basic materials. Since cell integration was made possible by the preparation of a membrane-type material, a prototype LiFePO_4 cell was also prepared and demonstrated stable cycling for least 30 cycles at room temperature and at temperatures as high as 80°C .

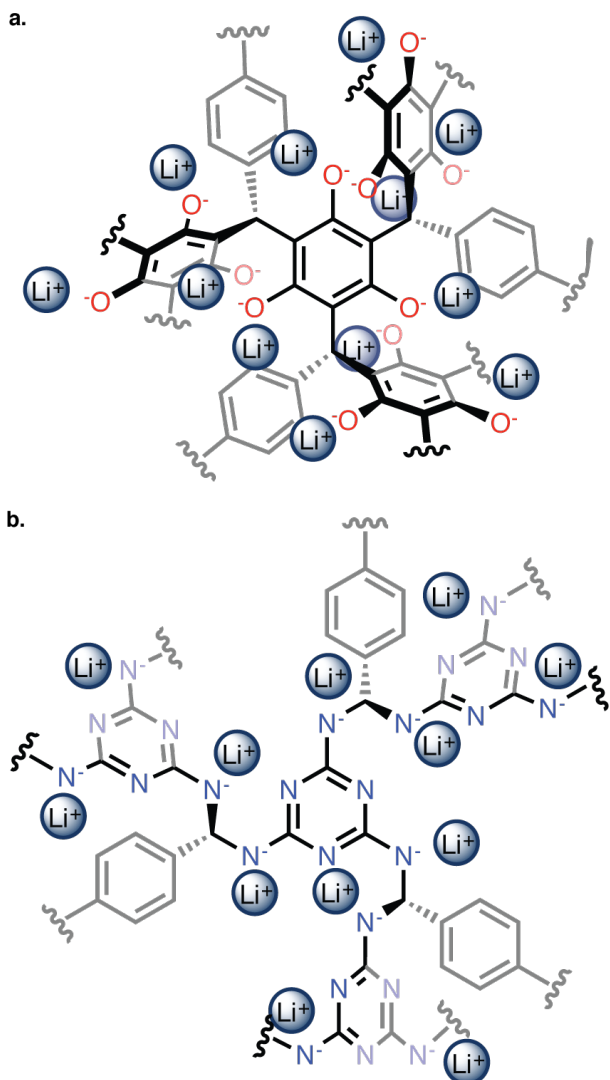


Figure 1.21. (a) Terephthalaldehyde condensates of phloroglucinol and (b) melamine are lithium ion conducting polymers with high transference numbers.

A 2-D single ion conducting covalent organic framework based on a spiroborate node was also reported recently, and a portion of the proposed structure is shown in **Figure 1.22**.¹⁸¹ While the lithium concentration in the material was comparatively low, this structure displayed a very high BET surface area ($\sim 1200 \text{ m}^2 \text{ g}^{-1}$). Ionic conductivities on the order of $10^{-5} \text{ S cm}^{-1}$ were reported, likely lower than the other organic frameworks discussed here due to the low density of lithium. The high activation energy of 0.24 eV was consistent with these materials primarily conducting a single ion. A reasonably high lithium transference number of 0.8 was observed, though the deviation from unity was not investigated. While the measured conductivities were low, the large mesopores in this lattice should enable excellent mass transport in the solution phase, and may therefore be of interest as catalyst supports or separator materials.

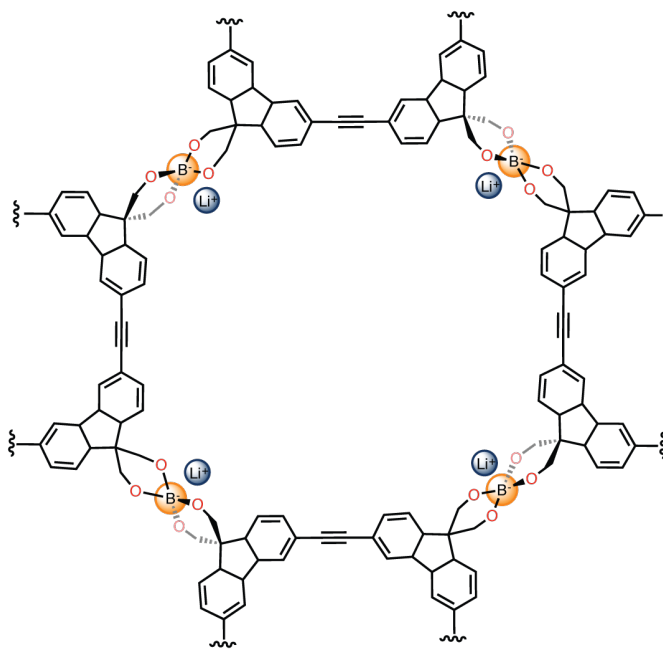


Figure 1.22. Lewis structure of the lithium ion conductor ICOF-2 formed by chelation of boron with fluorene-based diols to yield a mesoporous lithium spiroborate lattice.

1.6 Status and outlook

To date, ion conducting metal-organic frameworks remain a relative new and underdeveloped class of materials. Thus far, only solvent-assisted transport has been observed, limiting their implementation in mixed solid-liquid phase device architectures. Further, their conductivities, while technically permitting framework use as bulk electrolyte materials in battery and possibly fuel cell devices, remains ten to one-hundred times lower than the values desirable for high power applications. Nonetheless, these early reports only begin to approach the potential scope of unique transport phenomena that metal-organic frameworks could demonstrate. With this in mind, what follows is a brief discussion of the potential and the limitations of metal-organic frameworks in traditional and emerging technologies. A few potential applications of metal-organic frameworks as component materials in batteries and capacitors are illustrated in **Figure 1.23**.

1.6.1 Prospects as battery electrolytes. As discussed in **Section 1.5**, the ionic conductivities of a variety of battery-relevant metal cations have been demonstrated to be high enough for potential implementation as separator materials, catholytes or anolytes. While the requisite solvation does limit their use to liquid-containing battery architectures, such architectures remain the most prevalent for even state-of-the-art lithium batteries, as well as new devices in development. Moving forward, though achieving higher conductivities ($> 0.1 \text{ mS cm}^{-1}$) remains an important goal, investigation of other performance factors competes for priority.⁶² Of utmost importance is more thorough

assessment of electrochemical stability, along with the processing of metal-organic framework materials into mechanically stable, large format structures.

In terms of electrochemical stability, there are strict limitations on the allowable chemistries that are worth investigating. Across liquid electrolyte and polymer chemistry, there are a few obvious structure types with proven stability to both reducing electrodes like lithium, sodium, and lithium graphite, as well as acceptable oxidative stability to many cathode materials. Polyethylene oxides have been particularly successful.⁶⁶ Organic carbonate solutions are

the state of the art, but like many electrolyte materials are not stable to lithium or lithium graphite. Instead, their functionality at these strongly reducing potentials stems from a serendipitous decomposition into an ionically conductive passivation layer. However, results such as these are very difficult to predict.⁶²

Considering metal-organic framework chemistry specifically, the choice of metals is limited to those with very low reduction potentials that are kinetically inaccessible to reduction. With this in mind, Zr^{4+} , Ti^{4+} , Y^{3+} , Al^{3+} , and to a lesser extent Mg^{2+} are optimal choices. The more common divalent, late transition metals will plate out at low potentials and are therefore not suitable.^{182,183} Ligand choice is also problematic since most metal-organic frameworks are made from aromatic hydrocarbon and terephthalate backbones that can form reactive radical anions at very reducing potentials.^{45,46,184-186} In addition to direct chemical reaction and decomposition of the ion conductor, single electron ligand reduction may also result in bulk electron conduction and self-discharge of the cell by essentially short circuiting the anode and cathode.¹⁸⁷ With this in mind, non-conjugated ligand scaffolds may be of primary interest. In terms of oxidative stability, however, metal-terephthalates are quite stable, and material performance is likely limited only by the presence of conductive anions within the framework pores. **Figure S1.4** shows an electrochemical stability window determined by cyclic voltammetry for a metal-organic framework electrolyte based on the canonical framework UiO-66. While this phase does indeed show excellent oxidative stability, the faradaic efficiency for deposition of lithium on the titanium working electrode was significantly less than unity.

Materials processing is another major hurdle for ion conducting metal-organic frameworks. In many aspects metal-organic frameworks are closely related to ceramic ion conductors. They are both crystalline materials with significant ionicity in bonding interactions that limit their lattice enthalpy. However, unlike ceramics that can be annealed or sintered to yield mechanically robust monoliths approaching the shear modulus of single crystals, techniques to achieve mechanically stable metal-organic framework components have yet to be developed.^{9,188-191} As such, making mechanically robust films or self-supporting sheets of pure metal-organic framework remains a persistent

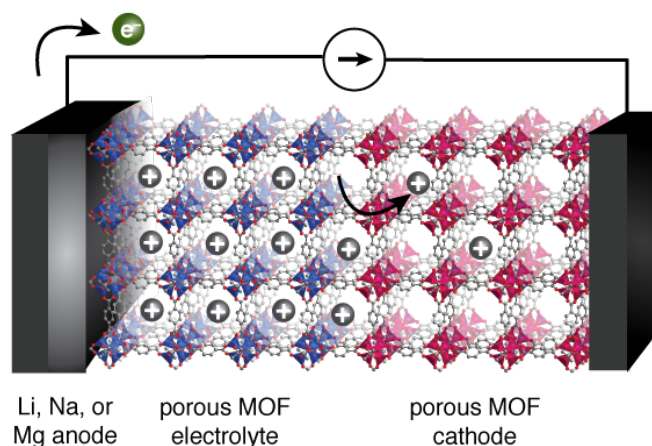


Figure 1.23. Illustration of a metal-organic framework's potential applications as an electrolyte/separator and electrode material for mixed ion-electron conductors. Shown explicitly here is an example of their implementation in a lithium battery.

challenge. A few of the framework-like ion conducting organic polymers discussed were dispersed in a polymer phase to yield a contiguous mixed-matrix membrane.^{179,180} Though this option is by far the simplest and most promising technique demonstrated thus far, the mechanical properties of mixed-matrix membranes are still inferior to those expected for a pure monolith. Also, since all of the framework-based ion conductors reported require solvent, these materials cannot be used as conductive filler in dry polymer cells to boost conductivity. More recently, a mixed-matrix membrane containing a metal-organic framework was used for the selective transport of lithium over polysulfides and was simply not used to provide structural support.¹⁹² In this scenario, mechanical stability of the separator was less of a necessity in achieving the desired performance, such that this may be a more realizable application for framework-based separators moving forward. In conclusion, in order for metal-organic frameworks to be realistically considered for implementation as component materials in batteries, supercapacitors, or fuel cells, much progress must be made towards acceptable mechanical properties and shape factors.

1.6.2 Mixed ion-electron conductors.

One promising class of ionically conductive metal-organic frameworks is the subset of mixed ion-electron conductors. Unfortunately, though to date there have been a number of proof-of-concept reports of applications for metal-organic framework-based mixed conductors, in nearly every case bulk charge transport was assumed but not directly demonstrated.^{193,194} This oversight is in spite of the fact that when considering the application of metal-organic frameworks as electrocatalysts, battery electrodes, or supercapacitor electrodes, the transport of charge that will most likely be the performance-limiting metric.

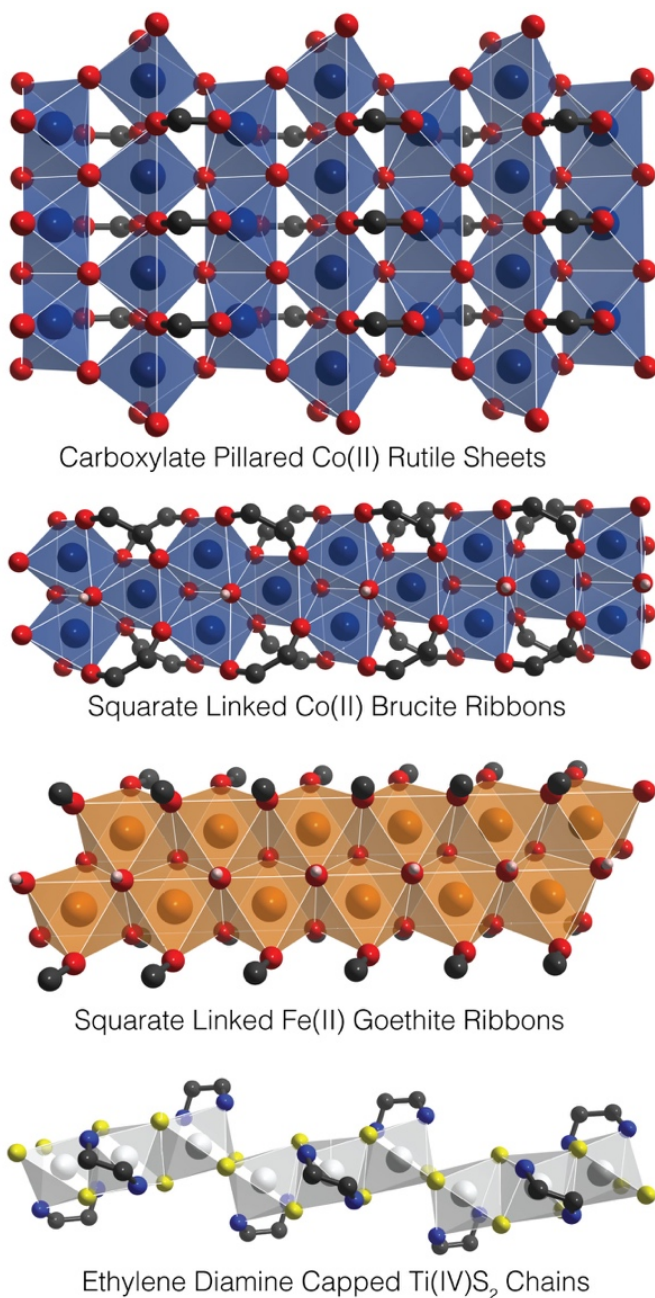


Figure 1.24. Extended inorganic building units that may be incorporated as substructures in metal-organic frameworks and potentially support solvent-free ion conduction.

Nonetheless, in many cases mixed conducting metal-organic frameworks are likely very promising as component materials in electrodes. There are several reports of sulfur impregnated metal-organic frameworks with superior cycling stability compared to sulfur-carbon composite electrodes.¹⁹⁵⁻¹⁹⁸ However, for these phases, neither electron nor ion transport through the bulk solid was investigated, and the sulfur reduction mechanism remains largely unknown. The application of metal-organic frameworks as secondary lithium insertion electrodes has also garnered interest.^{35,36,199,200} There have been multiple reports of a large number of insulating frameworks that have predictably shown very poor cycling.²⁰¹⁻²⁰³ A few cases have taken a rational design approach where charge transport was considered when targeting a specifically structure though the ionic and electronic conductivities were not experimentally determined or discussed.³⁶ **Chapter 3** discusses one of the first metal-organic framework insertion electrode reports that investigates critical factors governing ion transport and electrode kinetics in this class of materials. There is also an in-depth comparison to state-of-the-art non-porous ceramic electrodes. Thus, the principles of ion transport in mixed conducting phases will not be discussed in detail here.

1.6.3 Solvent-free, ceramic-like conduction. Future prospects for ion transport in metal-organic frameworks are numerous and may result in new materials with properties that can't be achieved in traditional materials. One intriguing case is solvent-free ion conduction in a porous crystal. The coexistence of gas-accessible microporosity and facile ion mobility has never been observed in a crystalline material. Metal-organic frameworks are often derived from structural motifs recognizable as analogs of dense ceramic phases like brookite, gibbsite, CdCl₂, cubic-zirconia, anatase, and perovskite. We may expect certain inorganic substructures that are derived from bulk solid electrolytes to also conduct ions under the right circumstances. There are a large number of reported frameworks (many from the very early years of the field) that contain metal-dense substructures likely to better support the short hopping distance required for significant ion mobility.^{48,49,204-207} **Figure 1.24** gives a few examples of inorganic substructures known in metal-organic frameworks that also have some similarity to known, dense ceramic ion conductors. The coexistence of ion conduction and permanent porosity may enable new technologies like superior dielectric materials, new gas sensors, novel gas sorption phenomena, nanoionic devices, and new component materials for gaseous fuel cells.

1.7 Conclusions

Though metal-organic framework-based ion conduction is still a new field, the establishment of transport mechanisms and best practices for characterization is critical in order to facilitate the efficient manifestation of rationally designed materials and technologies. Even in this early stage of development, several basic principles and expectations have emerged as guidelines for the synthesis and performance of metal-organic framework-based ion conductors. Importantly, since all ion conducting metal-organic frameworks reported thus far require solvent to facilitate conduction, ion conduction in these materials appears most similar to that of liquids and polymers, and best matches a Vogel-Tamman-Fulcher model, where conduction is viscosity limited. However, in certain cases nanoconfinement effects have been observed where transport can differ greatly from what is

observed in bulk solution. These scenarios may open the door to new technological opportunities for these materials. Excitingly, the structural functionalization unique to metal-organic frameworks may enable control of ion transport at the atomic level, akin to the specificity observed in biological ion channels.

Practically, ionic conductivity is best characterized by ac impedance spectroscopy in a temperature controlled cell down to cryogenic temperatures. The measurement of conductivities with temperature change between room temperature and 100 °C, though commonly reported, has simply too small a temperature range to accurately distinguish transport mechanisms. For many proposed applications, such as separator materials, active electrodes, and electrocatalysts, metal-organic frameworks are soaked in electrolyte solutions. In contrast to what is often assumed, despite their porosity, the bulk conductivity of metal-organic frameworks under these conditions can be expected to be less than 10^{-6} S cm⁻¹. Mesoporous structures with continuous pore diameters in excess of 2 nm do not suffer from the same mass and ion transport limitations since they can better accommodate solvation states approximating those in bulk solutions. Nonetheless, with significant optimization of surface chemistry and ion concentration, sub-2-nm pores can display conductivities greater than 10^{-6} S cm⁻¹, and have been shown to approach 10^{-3} S cm⁻¹.

Moving beyond conductivity, other performance characteristics such as transference number, electrochemical stability, mechanical stability, and cell integration become high priorities for development of metal-organic framework-based electrolytes. Similarly, for framework-based battery electrodes and active materials in pseudo-capacitors, once ionic and electronic conductivities are no longer limiting, energy density, specific capacity, and cycling stability must be prioritized. Finally, the field of ion conducting metal-organic frameworks remains very new, and the first reports are still appearing. We may expect large advances over the next few years as researchers leverage the full toolbox of synthetic design principles available to this class of materials to make truly unique and exotic ion conductors.

1.8 Acknowledgements

This research was supported by the National Science Foundation under award no. DMR-1309066 and the Bosch Energy Research Network. Arkema is also thanked for fellowship support for the author.

1.9 Supporting figures

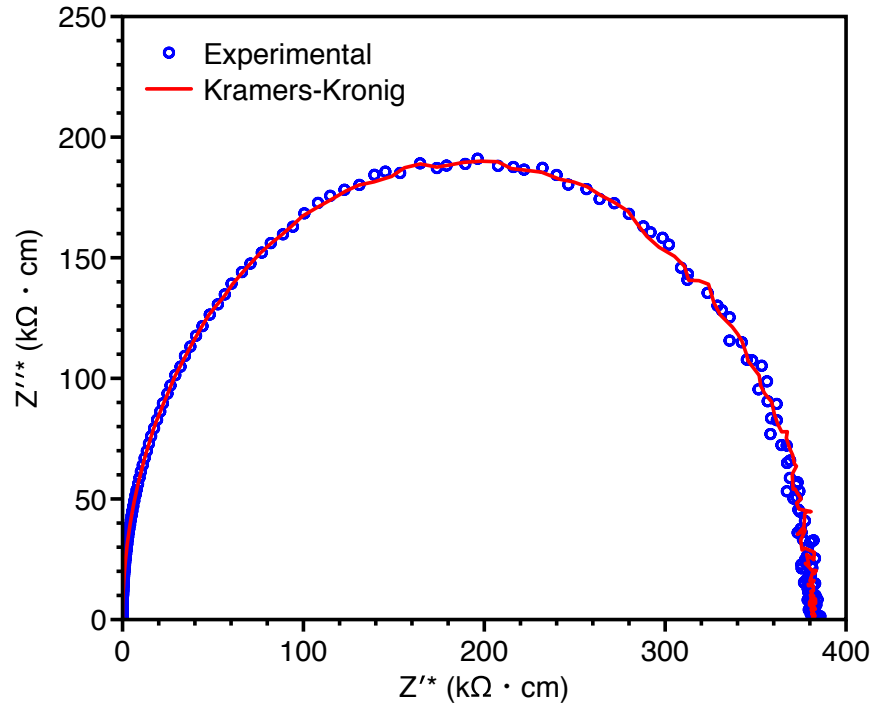


Figure S1.1. Nyquist projection of the Kramers-Kronig transform of an impedance spectrum for the electron conductor $\text{Cu}[\text{Ni}(\text{pdtd})_2]$.

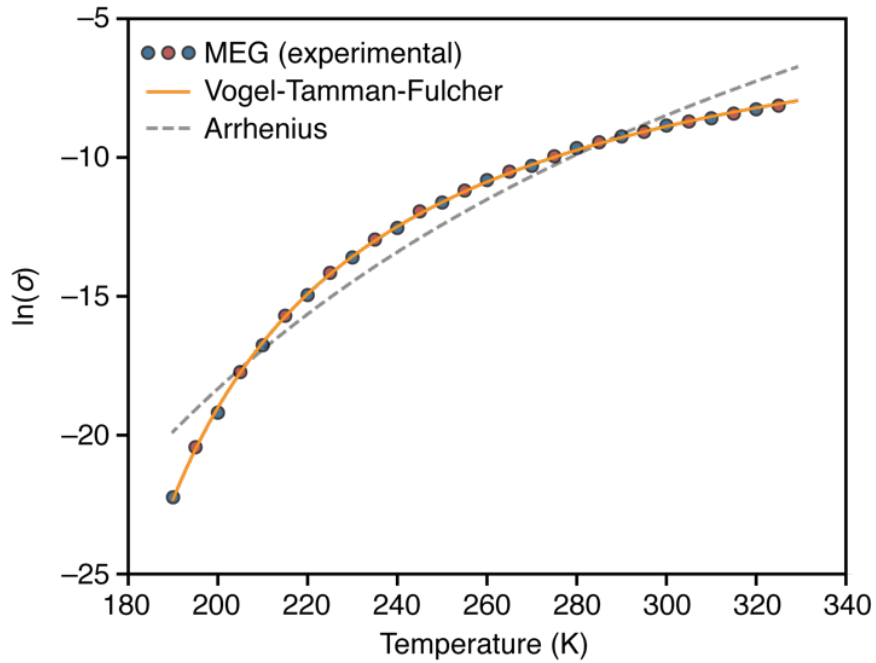


Figure S1.2. Comparison of Arrhenius and VTF models for a single ion conducting network polymer gel. For data collected from room temperature to $\sim 100^\circ\text{C}$ the two models are indistinguishable based on the quality of the fit and a wider temperature range is clearly required in order to propose an underlying mechanism for ion conduction.

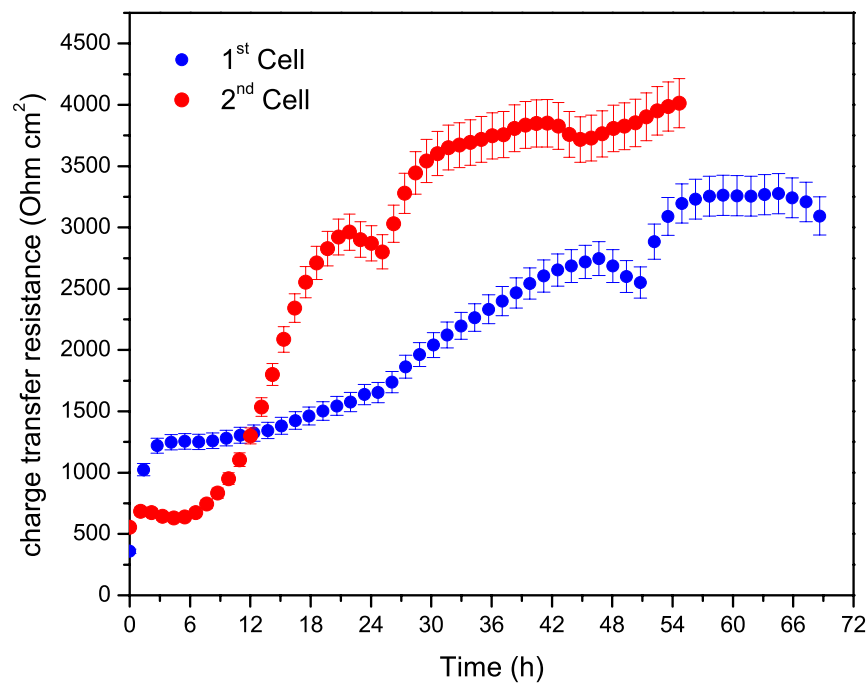


Figure S1.3. Charge transfer resistance for a UiO-66 solid electrolyte at lithium electrodes (Li|MOF|Li) as determined by circuit modeling as impedance spectroscopy data to two parallel-RC circuits connected in series. Exemplary data is shown in **Figure 1.6**. SEI evolution begins to stabilize after about 60 hours.

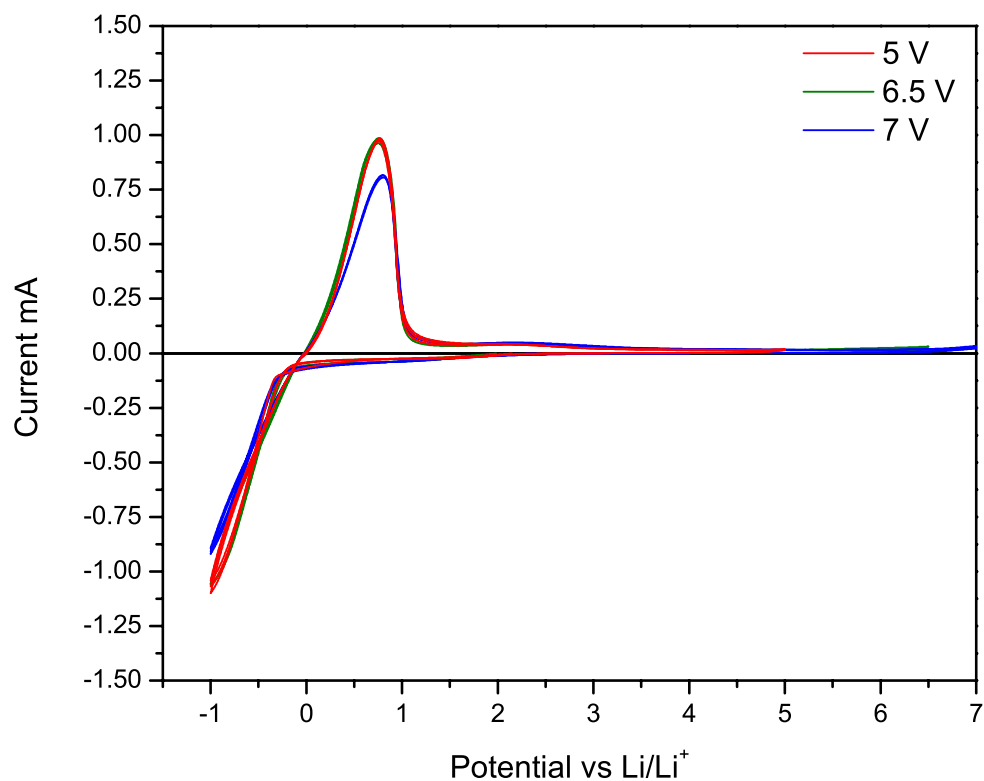


Figure S1.4. Cyclic voltammogram of a UiO-66 based MOF electrolyte on a titanium working electrode using lithium counter and reference electrodes that shows reversible lithium deposition at low potentials and very little background oxidation even out to 7 V vs Li/Li⁺.

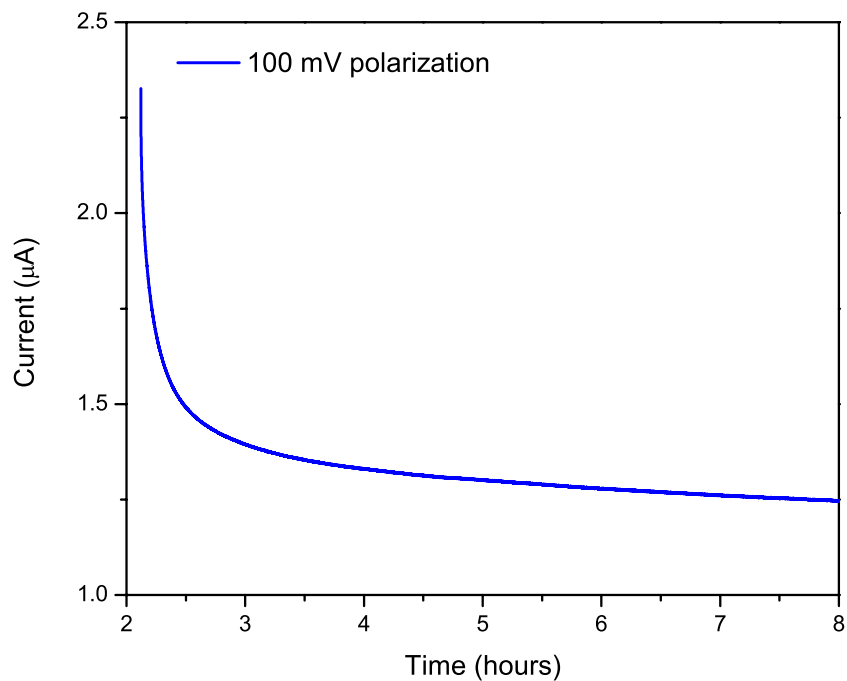


Figure S1.5. Current decay curve following a 0 mV to 100 mV step across a Li|MOF|Li cell for a UiO-66 based electrolyte. Impedance spectra were collected before and after the step and used to determine the transference number of the bulk electrolyte phase, Figure 1.7.

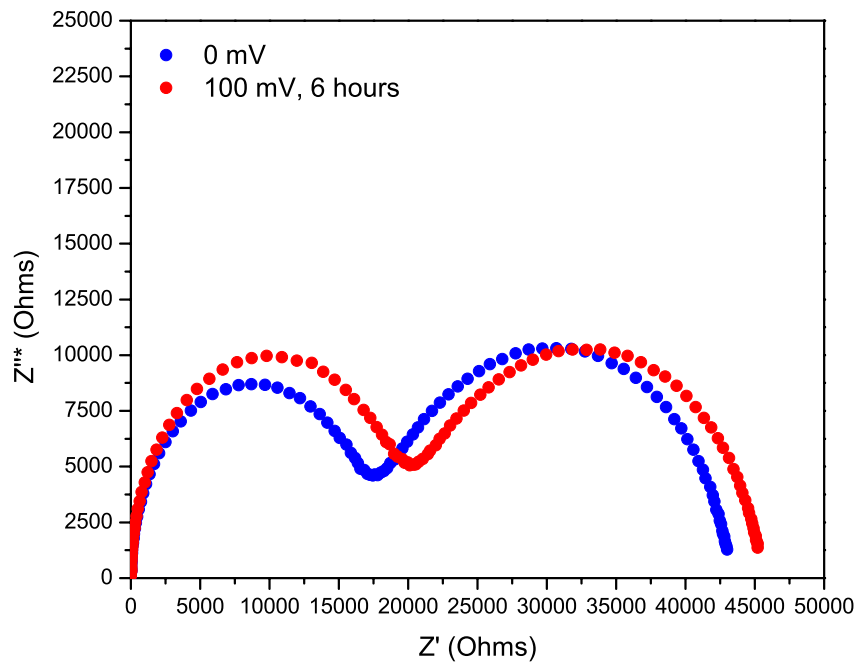


Figure S1.6. Ac impedance spectra accompanying the current decay curve shown in **Figure 1.6**. Data was collected from 1 MHz to 1 Hz with a 10-mV sinus amplitude.

1.10 References

- (1) “The pervasive chemistry of metal-organic frameworks” Long, J. R. and Yaghi, O. M. *Chem. Soc. Rev.* **2009**, *38*, 1213–1214.
- (2) “The chemistry and applications of metal-organic frameworks” Furukawa, H.; Cordova, K. E.; O’Keeffe, M.; and Yaghi, O. M. *Science* **2013**, *341*, 1230444.
- (3) “Hydrogen storage in metal-organic frameworks” Murray, L. J.; Dincă, M.; and Long, J. R. *Chem. Soc. Rev.* **2009**, *38*, 1294–1314.
- (4) “Methane storage in flexible metal-organic frameworks with intrinsic thermal management” Mason, J. A.; Oktawiec, J.; Taylor, M. K.; Hudson, M. R.; Rodriguez, J.; Bachman, J. E.; Gonzalez, M. I.; Cervellino, A.; Guagliardi, A.; Brown, C. M.; Llewellyn, P. L.; Masciocchi, N.; and Long, J. R. *Nature* **2015**, *527*, 357–361.
- (5) “Selective gas adsorption and separation in metal-organic frameworks” Li, J.-R.; Kuppler, R. J.; and Zhou, H.-C. *Chem. Soc. Rev.* **2009**, *38*, 1477–1504.
- (6) “Metal-organic frameworks for separations” Li, J. R.; Sculley, J.; and Zhou, H. C. *Chem. Rev.* **2011**, *112*, 869–932.
- (7) “Carbon dioxide capture in metal-organic frameworks.” Sumida, K.; Rogow, D. L.; Mason, J. A.; McDonald, T. M.; Bloch, E. D.; Herm, Z. R.; Bae, T.-H.; and Long, J. R. *Chem. Rev.* **2012**, *112*, 724–781.
- (8) “Cooperative insertion of CO₂ in diamine-appended metal-organic frameworks” McDonald, T. M.; Mason, J. A.; Kong, X.; Bloch, E. D.; Gygi, D.; Dani, A.; Crocellà, V.; Giordanino, F.; Odoh, S. O.; Drisdell, W. S.; Vlasisavljevich, B.; Dzubak, A. L.; Poloni, R.; Schnell, S. K.; Planas, N.; Lee, K.; Pascal, T.; Wan, L. F.; Prendergast, D.; Neaton, J. B.; Smit, B.; Kortright, J. B.; Gagliardi, L.; Bordiga, S.; Reimer, J. A.; and Long, J. R. *Nature* **2015**, *519*, 303–308.
- (9) “Industrial applications of metal-organic frameworks” Czaja, A. U.; Trukhan, N.; and Müller, U. *Chem. Soc. Rev.* **2009**, *38*, 1284–1293.
- (10) “Metal-organic framework materials as catalysts” Lee, J.; Farha, O. K.; Roberts, J.; Scheidt, K. A.; Nguyen, S. T.; and Hupp, J. T. *Chem. Soc. Rev.* **2009**, *38*, 1450–1459.
- (11) “Engineering metal organic frameworks for heterogeneous catalysis” Corma, A.; García, H.; and Xamena, F. L. I. *Chem. Rev.* **2010**, *110*, 4606–4655.
- (12) “Homochiral metal-organic frameworks for asymmetric heterogeneous catalysis” Yoon, M.; Srirambalaji, R.; and Kim, K. *Chem. Rev.* **2011**, *112*, 1196–1231.
- (13) “A homochiral metal-organic porous material for enantioselective separation and catalysis” Seo, J.; Whang, D.; Lee, H.; Jun, S.; Oh, J.; Jeon, Y.; and Kim, K. *Nature* **2000**, *404*, 982–986.
- (14) “Tunability of band gaps in metal-organic frameworks” Lin, C.-K.; Zhao, D.; Gao, W.-Y.; Yang, Z.; Ye, J.; Xu, T.; Ge, Q.; Ma, S.; and Liu, D.-J. **2012**, *51*, 9039–9044.
- (15) “Dielectric properties of selected metal-organic frameworks” Warmbier, R.; Quandt, A.; and Seifert, G. *J. Phys. Chem. C* **2014**, *118*, 11799–11805.
- (16) “Metal-organic frameworks: new interlayer dielectric materials” Usman, M.; Mendiratta, S.; and Lu, K.-L. *ChemElectroChem* **2015**, *2*, 786–788.
- (17) “Electrical conductive coordination polymers.” Givaja, G.; Amo-Ochoa, P.; Gómez-García, C. J.; and Zamora, F. *Chem. Soc. Rev.* **2012**, *41*, 115–147.

- (18) “A solid lithium electrolyte via addition of lithium isopropoxide to a metal-organic framework with open metal sites” Wiers, B. M.; Foo, M.-L.; Balsara, N. P.; and Long, J. R. *J. Am. Chem. Soc.* **2011**, *133*, 14522–14525.
- (19) “Solvation numbers of ions” Hinton, J. F. and Amis, E. S. *Chem. Rev.* **1971**, *71*, 627–674.
- (20) “Phenomenological theory of ion solvation. effective radii of hydrated ions” Nightingale, E. R., Jr *J. Phys. Chem.* **1959**, *63*, 1381–1387.
- (21) “Carbon materials for the electrochemical storage of energy in capacitors” Frackowiak, E. and Beguin, F. *Carbon* **2001**, *39*, 937–950.
- (22) “Fabrication of ordered uniform porous carbon networks and their application to a catalyst supporter” Yu, J.-S.; Kang, S.; Yoon, S. B.; and Chai, G. *J. Am. Chem. Soc.* **2002**, *124*, 9382–9383.
- (23) “A review of anode catalysis in the direct methanol fuel cell” Liu, H.; Song, C.; Zhang, L.; Zhang, J.; Wang, H.; and Wilkinson, D. P. *J. Power Sources* **2006**, *155*, 95–110.
- (24) “Carbon materials for supercapacitor application” Frackowiak, E. *Phys. Chem. Chem. Phys.* **2007**, *9*, 1774–13.
- (25) “Carbon supports for low-temperature fuel cell catalysts” Antolini, E. *Appl. Catal. B* **2009**, *88*, 1–24.
- (26) “Nanoporous metals for catalytic and optical applications” Ding, Y. and Chen, M. *MRS Bulletin* **2009**, *34*, 569–576.
- (27) “Nanoporous metals: fabrication strategies and advanced electrochemical applications in catalysis, sensing and energy systems” Zhang, J. and Li, C. M. *Chem. Soc. Rev.* **2012**, *41*, 7016–16.
- (28) “Towards conducting metal-organic frameworks” D'Alessandro, D. M.; Kanga, J. R. R.; and Caddy, J. S. *Aust. J. Chem.* **2011**, *64*, 718–722.
- (29) “Conductive metal-organic frameworks and networks: fact or fantasy?” Hendon, C. H.; Tiana, D.; and Walsh, A. *Phys. Chem. Chem. Phys.* **2012**, *14*, 13120–13132.
- (30) “Ion conductivity and transport by porous coordination polymers and metal-organic frameworks.” Horike, S.; Umeyama, D.; and Kitagawa, S. *Acc. Chem. Res.* **2013**, *46*, 2376–2384.
- (31) “Metal-organic frameworks: semiconducting frameworks” *Encyclopedia of Inorganic and Bioinorganic Chemistry* Xu, Z. *John Wiley and Sons Ltd.* **2014**, 1–13. DOI: 10.1002/9781119951438.eibc2212
- (32) “Electrically conductive porous metal-organic frameworks” Sun, L.; Campbell, M. G.; and Dincă, M. *Angew. Chem. Int. Edit. Engl.* **2016**, *55*, 3566–3579.
- (33) “Metal-organic frameworks for electrochemical applications” Morozan, A. and Jaouen, F. *Energy Environ. Sci.* **2012**, *5*, 9269–9290.
- (34) “Exploration of vanadium benzenedicarboxylate as a cathode for rechargeable lithium batteries” Kaveevivitchai, W. and Jacobson, A. J. *J. Power Sources* **2015**, *278*, 265–273.
- (35) “Two distinct redox intercalation reactions of hydroquinone with porous vanadium benzenedicarboxylate MIL-47” Kaveevivitchai, W.; Wang, X.; Liu, L.; and Jacobson, A. J. *Inorg. Chem.* **2015**, *54*, 1822–1828.

- (36) “Mixed-valence Li/Fe-based metal-organic frameworks with both reversible redox and sorption properties” Férey, G.; Millange, F.; Morcrette, M.; Serre, C.; Doublet, M.-L.; Grenèche, J.-M.; and Tarascon, J.-M. *Angew. Chem. Int. Ed.* **2007**, *46*, 3259–3263.
- (37) “A metal-organic framework as an electrocatalyst for ethanol oxidation” Yang, L.; Kinoshita, S.; Yamada, T.; Kanda, S.; Kitagawa, H.; Tokunaga, M.; Ishimoto, T.; Ogura, T.; Nagumo, R.; Miyamoto, A.; et al. *Angew. Chem.* **2010**, *122*, 5476–5479.
- (38) “Octamolybdate-based metal-organic framework with unsaturated coordinated metal center as electrocatalyst for generating hydrogen from water” Gong, Y.; Wu, T.; Jiang, P. G.; Lin, J. H.; and Yang, Y. X. *Inorg. Chem.* **2012**, *52*, 777–784.
- (39) “Electrocatalytic four-electron reduction of oxygen with copper(II)-based metal-organic frameworks” Mao, J.; Yang, L.; Yu, P.; Wei, X.; and Mao, L. *Electrochem. Commun.* **2012**, *19*, 29–31.
- (40) “Highly selective electrochemical reduction of carbon dioxide using Cu based metal-organic framework as an electrocatalyst” Senthil Kumar, R.; Senthil Kumar, S.; and Anbu Kulandainathan, M. *Electrochem. Commun.* **2012**, *25*, 70–73.
- (41) “A graphene oxide and copper-centered metal-organic framework composite as a tri-functional catalyst for HER, OER, and ORR” Jahan, M.; Liu, Z.; and Loh, K. P. *Adv. Funct. Mater.* **2013**, *23*, 5363–5372.
- (42) “Metal-organic framework materials as chemical sensors” Kreno, L. E.; Leong, K.; Farha, O. K.; Allendorf, M.; Van Duyne, R. P.; and Hupp, J. T. *Chem. Rev.* **2011**, *112*, 1105–1125.
- (43) “Thin film thermoelectric metal-organic framework with high seebeck coefficient and low thermal conductivity” Erickson, K. J.; Léonard, F.; Stavila, V.; Foster, M. E.; Spataru, C. D.; Jones, R. E.; Foley, B. M.; Hopkins, P. E.; Allendorf, M. D.; and Talin, A. A. *Adv. Mater.* **2015**, *27*, 3453–3459.
- (44) “Rapid determination of the optical and redox properties of a metal-organic framework via in situ solid state spectroelectrochemistry” Usov, P. M.; Fabian, C.; and D'Alessandro, D. M. *Chem. Commun.* **2012**, *48*, 3945–3947.
- (45) “Facile deposition of multicolored electrochromic metal-organic framework thin films” Wade, C. R.; Li, M.; and Dincă, M. *Angew. Chem.* **2013**, *125*, 13619–13623.
- (46) “Metal-organic framework thin films composed of free-standing acicular nanorods exhibiting reversible electrochromism” Kung, C.-W.; Wang, T. C.; Mondloch, J. E.; Fairen-Jimenez, D.; Gardner, D. M.; Bury, W.; Klingsporn, J. M.; Barnes, J. C.; Van Duyne, R.; Stoddart, J. F.; Waslewski, M. R.; Farha, O. K.; and Hupp, J. T. *Chem. Mater.* **2013**, *25*, 5012–5017.
- (47) “Directed growth of electroactive metal-organic framework thin films using electrophoretic deposition” Hod, I.; Bury, W.; Karlin, D. M.; Deria, P.; Kung, C.-W.; Katz, M. J.; So, M.; Klahr, B.; Jin, D.; Chung, Y. W.; et al. *Adv. Mater.* **2014**, *26*, 6295–6300.
- (48) “Hydrothermal syntheses, structures and magnetic properties of coordination frameworks of divalent transition metals” Kumagai, H.; Sobukawa, H.; and Kurmoo, M. *J. Mater. Sci.* **2007**, *43*, 2123–2130.

- (49) “Hydrothermal synthesis of brucite type copper hydroxide squarate $[\text{Cu}_3(\text{OH})_2(\text{C}_4\text{O}_4)] \cdot 4\text{H}_2\text{O}$ ” Sharma, S. and Jansen, M. Z. *Z. Anorg. Allg. Chem.* **2008**, *634*, 1911–1914.
- (50) “Porous, conductive metal-triazolates and their structural elucidation by the charge-flipping method.” Gándara, F.; Uribe-Romo, F. J.; Britt, D. K.; Furukawa, H.; Lei, L.; Cheng, R.; Duan, X.; O’Keeffe, M.; and Yaghi, O. M. *Chem. Eur. J.* **2012**, *18*, 10595–10601.
- (51) “Separation of Hexane Isomers in a Metal-Organic Framework with Triangular Channels.” Herm, Z. R.; Wiers, B. M.; Mason, J. A.; van Baten, J. M.; Hudson, M. R.; Zajdel, P.; Brown, C. M.; Masciocchi, N.; Krishna, R.; and Long, J. R. *Science* **2013**, *340*, 960–964.
- (52) “High electrical conductivity in $\text{Ni}_3(2,3,6,7,10,11\text{-hexaminotriphenylene})_2$, a semiconducting metal-organic graphene analogue.” Sheberla, D.; Sun, L.; Blood-Forsythe, M. A.; Er, S.; Wade, C. R.; Brozek, C. K.; Aspuru-Guzik, A.; and Dincă, M. *J. Am. Chem. Soc.* **2014**, *136*, 8859–8862.
- (53) “Large-pore apertures in a series of metal-organic frameworks” Deng, H.; Grunder, S.; Cordova, K. E.; Valente, C.; Furukawa, H.; Hmadeh, M.; Gandara, F.; Whalley, A. C.; Liu, Z.; Asahina, S.; Kazumori H.; O’Keeffe M.; Terasaki O.; Stoddart J. F.; and Yaghi O. M. *Science* **2012**, *336*, 1018–1023.
- (54) “Hydrogen storage in microporous metal-organic frameworks” Rosi, N. L.; Eckert, J.; Eddaoudi, M.; Vodak, D. T.; Kim, J.; O’Keeffe, M.; and Yaghi, O. M. *Science* **2003**, *300*, 1127–1129.
- (55) “Systematic design of pore size and functionality in isorecticular MOFs and their application in methane storage” Eddaoudi, M.; Kim, J.; Rosi, N.; Vodak, D.; Wachter, J.; O’Keeffe, M.; and Yaghi, O. M. *Science* **2002**, *295*, 469–472.
- (56) “Exploiting redox activity in metal-organic frameworks: concepts, trends and perspectives” D’Alessandro, D. M. *Chem. Commun.* **2016**, *52*, 8957–8971.
- (57) “Proton conduction in metal-organic frameworks and related modularly built porous solids.” Yoon, M.; Suh, K.; Natarajan, S.; and Kim, K. *Angew. Chem. Int. Edit. Engl.* **2013**, *52*, 2688–2700.
- (58) “Development of the theory of electrolytic dissociation” Arrhenius, S. *Nobel Lecture in Chemistry* **11 December 1903**.
- (59) “Solvents and solvent effects in organic chemistry” Reichardt, C. *John Wiley and Sons* **2005**, *3rd Ed.*, 1–646.
- (60) “The structure of water and aqueous solutions” Horne, R. A. *Survey Prog. Chem.* **1968**, *4*, 1–43.
- (61) “Effect of ions on the structure of water: structure making and breaking” Marcus, Y. *Chem. Rev.* **2009**, *109*, 1346–1370.
- (62) “Nonaqueous liquid electrolytes for lithium-based rechargeable batteries” Xu, K. **2004**, *104*, 4303–4418.
- (63) “Energy storage” Huggins, R. A. *Springer Science and Business Media* **2010**, 1–28.
- (64) “Fast ion transport in solids” Armand, M. B.; Chabagno, J. M.; Duclot, M. J.; and Vashishta, P. **1979**, P. Vashista, J. N. Mundy, and G. K. Shenoy, Ed., North-Holland, Amsterdam, p 131.

- (65) “Ceramic and polymeric solid electrolytes for lithium-ion batteries” Fergus, J. W. *J. Power Sources* **2010**, *195*, 4554–4569.
- (66) “Polymer electrolytes for lithium-ion batteries” Meyer, W. H. *Adv. Mater.* **1998**, *10*, 439–448.
- (67) “Solid polymer electrolytes: materials designing and all-solid-state battery applications: an overview” Agrawal, R. C. and Pandey, G. P. *J. Phys. D: Appl. Phys.* **2008**, *41*, 223001.
- (68) “Increasing the conductivity of crystalline polymer electrolytes” Christie, A. M.; Lilley, S. J.; Staunton, E.; Andreev, Y. G.; and Bruce, P. G. *Nature* **2005**, *433*, 50–53.
- (69) “Ionic conductivity in crystalline polymer electrolytes” Gadjourova, Z.; Andreev, Y. G.; Tunstall, D. P.; and Bruce, P. G. *Nature*, **2001**, *412*, 520–523.
- (70) “Alkali metal crystalline polymer electrolytes” Zhang, C.; Gamble, S.; Ainsworth, D.; Slawin, A. M. Z.; Andreev, Y. G.; and Bruce, P. G. *Nature Materials* **2009**, *8*, 580–584.
- (71) “Performance of Bellcore's plastic rechargeable Li-ion batteries” Tarascon, J. M.; Gozdz, A. S.; Schmutz, C.; Shokoohi, F.; and Warren, P. C. *Solid State Ionics* **1996**, *86-88*, 49–54.
- (72) “Crop manuring and intensive land management by Europe's first farmers.” Bogaard, A.; Fraser, R.; Heaton, T. H. E.; Wallace, M.; Vaiglova, P.; Charles, M.; Jones, G.; Evershed, R. P.; Styring, A. K.; Andersen, N. H.; Arbogast, R.-M.; Bartosiewicz, L.; Gardeisen, A.; Kanstrup, M.; Maier, U.; Marinova, E.; Ninov, L.; Schäfer, M.; and Stephan, E. *Proc. Natl. Acad. Sci. U.S.A.* **2013**, *110*, 12589–12594.
- (73) “Inorganic intercalation compounds” O'Hare, D. *Inorganic Materials* Bruce, D. W. and O'Hare, D Ed. *John Wiley and Sons* **1992**, *4*, 171–244.
- (74) “On the Power of Soils to Absorb Manure” Way, J. T. *J. R. Agri. Soc. Engl.* **1850**, *11*, 13.
- (75) “On the Absorbent Power of Soils” Thompson, H. S. *J. R. Agri. Soc. Engl.* **1850**, *11*, 68-74
- (76) “Ion exchange properties of and rates of ionic diffusion in beta-alumina” Yao, Y.-F. Y. and Kummer, J. T. *J. Inorg. Nucl. Chem.* **1967**, *29*, 2453–2475.
- (77) “Dielectric loss of beta alumina and of ion-exchanged beta alumina” Radzilowski, R. H.; Yao, Y. F.; and Kummer, J. T. *J. Appl. Phys.* **1969**, *40*, 4716–4725. doi:10.1063/1.1657279.
- (78) “Beta-alumina electrolytes” Kummer, J. T. *Prog. Solid State Chem.* **1972**, *7*, 141–175.
- (79) “Battery having a molten alkali metal anode and a molten sulfur cathode” Kummer, J. T.; Neill, W.; and Co, F. M. **1968**, US 3413150 A.
- (80) “ Li_xCoO_2 ($0 < x < -1$): a new cathode material for batteries of high energy density” Mizushima, K.; Jones, P. C.; Wiseman, P. J.; and Goodenough, J. B. *Mater. Res. Bull.* **1980**, *15*, 783–789.
- (81) “Electrochemistry of manganese dioxide in lithium nonaqueous cell III. X-ray diffraction study on the reduction of spinel-related manganese dioxide” Ohzuku, T.; Kitagawa, M.; and Hirai, T. *J. Electrochem. Soc.* **1990**, *137*, 769–775.
- (82) “The spinel phase of LiMn_2O_4 as a cathode in secondary lithium cells” Tarascon, J. M.; Wang, E.; Shokoohi, F. K.; McKinnon, W. R.; and Colson, S. J. *Electrochem. Soc.* **1991**, *138*, 2859–2864.
- (83) “Phospho-olivines as positive-electrode materials for rechargeable lithium batteries” Padhi, A. K.; Nanjundaswamy, K. S.; and Goodenough, J. B. *J. Electrochem. Soc.* **1997**, *144*, 1188–1194.

- (84) “Ionic conductivity in Li_3N single crystals” Alpen, von, U.; Rabenau, A.; and Talat, G. H. *Appl. Phys. Lett.* **1977**, *30*, 621–623.
- (85) “Ionic conductivity of pure and doped Li_3N ” Lapp, T.; Skaarup, S.; and Hooper, A. *Solid State Ionics* **1983**, *11*, 97–103.
- (86) “Proton transfer and superionic conductivity in solids and gels” Colomban, P. and Novak, A. **1988**, *177*, 277–308.
- (87) “Physical techniques for the study of solid electrolytes” Linford, R. G. and Hackwood, S. **1981**, *81*, 327–364.
- (88) “A family of membrane proteins uses ATP hydrolysis to pump ions across membranes” Berg, J. M.; Tymoczko, J. L.; and Stryer, L. *Biochemistry* New York: W H Freeman, **2002**, 5th Ed., 13.2, <https://www.ncbi.nlm.nih.gov/books/NBK22464>.
- (89) “Intracellular ion environment and membrane electric potential” Lodish, H.; Berk, A.; Zipursky, S. L.; Matsudaira, P.; Baltimore, D.; and Darnell, J. *Molecular Cell Biology*, New York: W H Freeman, **2000**, 4th Ed., 15.4, <https://www.ncbi.nlm.nih.gov/books/NBK21627/>
- (90) “The structure of the potassium channel: molecular basis of K^+ conduction and selectivity” Doyle, D. A.; Cabral, J. M.; Pfuetzner, R. A.; Kuo, A.; Gulbis, J. M.; Cohen, S. L.; Chait, B. T.; and MacKinnon, R. *Science* **1998**, *280*, 69–77.
- (91) “One-dimensional metals: Conjugated Polymers, Organic Crystals, Carbon Nanotubes and Graphene” Roth, S.; and Carroll, D. *John Wiley & Sons* **2015**, 1–49.
- (92) “Single-ion BAB triblock copolymers as highly efficient electrolytes for lithium-metal batteries” Bouchet, R.; Maria, S.; Meziane, R.; Aboulaich, A.; Lienafa, L.; Bonnet, J.-P.; Phan, T. N.; Bertin, D.; Gigmes, D.; and Devaux, D. *Nat. Mater.* **2013**, *12*, 452–457.
- (93) “Ion pairing” Yizhak Marcus, A. and Hefter, G. *Chem. Rev.* **2006**, *106*, 4585–4621.
- (94) “Ionization, ionic velocities, and atomic sizes” Sutherland, W. *Phil. Mag. S. 6* **1902**, *3*, 161–177.
- (95) “A dynamical theory of diffusion for non-electrolytes and the molecular mass of albumin” Sutherland, W. *Phil. Mag. S. 6*, **1905**, *9*, 781–785.
- (96) “A lithium superionic conductor” Kamaya, N.; Homma, K.; Yamakawa, Y.; Hirayama, M.; Kanno, R.; Yonemura, M.; Kamiyama, T.; Kato, Y.; Hama, S.; Kawamoto, K.; and Mitsui, A. *Nat. Mater.* **2011**, *10*, 682–686.
- (97) “Advanced batteries: materials science aspects” Huggins, R. A. *Springer Sciences and Business Media* **2010**, 1–491.
- (98) “Analysis of recent measurements of the viscosity of glasses” Fulcher, G. S. *J. Am. Ceram. Soc.* **1925**, *8*, 339–355.
- (99) “Die Abhängigkeit der Viscosität von der Temperatur bei Unterkühlten Flüssigkeiten” Tammann, G. and Hesse, W. *Z. Anorg. Allg. Chem.* **1926**, *156*, 245–257.
- (100) “Application of Walden’s rule to the electrical conduction of sea water” Horne, R. A. and Courant, R. A. *J. Geophys. Res.* **1964**, *69*, 1971–1977.
- (101) “NMR, DSC and high pressure electrical conductivity studies of liquid and hybrid electrolytes” Stallworth, P. E.; Fontanella, J. J.; Wintersgill, M. C.; Scheidler, C. D.; Immel, J. J.; Greenbaum, S. G.; and Gozdz, A. S. *J. Power Sources* **1999**, *81-82*, 739–747.

- (102) “Conductivity study of porous plasticized polymer electrolytes based on poly(vinylidene fluoride) a comparison with polypropylene separators” Song, J. Y.; Wang, Y. Y.; and Wan, C. C. *J. Electrochem. Soc.* **2000**, *147*, 3219–3225.
- (103) “Nanocomposite polymer electrolytes for lithium batteries” Croce, F.; Appetecchi, G. B.; Persi, L.; and Scrosati, B. *Nature* **1998**, *394*, 456–458.
- (104) “New lithium ion conductors based on $\text{Li}_2\text{S-SiS}_2$ system” Kondo, S.; Takada, K.; and Yamamura, Y. *Solid State Ionics* **1992**, *53-56*, 1183–1186.
- (105) “Single-Ion Conducting Polymer Networks with Borate Anions and Flexible Linkers” Axelson, J.; Aubrey, M. L.; and Long, J. R. **2016** *Manuscript in Preparation*.
- (106) “Electrochemical methods: fundamentals and applications” Bard, A. J.; Faulkner, L. R.; Leddy, J.; and Zoski, C. G. *New York: Wiley* **1980**, 2.
- (107) “Experimental methods to evaluate the critical properties of electrodes and electrolytes” Huggins, R. A. *Advanced batteries: materials science aspects*. Springer Sciences and Business Media **2010**, 393–430.
- (108) “Fundamentals of impedance spectroscopy” Macdonald, J. R. and Johnson, W. B. *Impedance Spectroscopy* John Wiley and Sons, **2005**, 1–26.
- (109) “Impedance spectroscopy on solids: the limits of serial equivalent circuit models” Fleig, J. *J. Electroceram.* **2004**, *13*, 637–644.
- (110) “The impedance of imperfect electrode contacts on solid electrolytes” Fleig, J. and Maier, J. *Solid State Ionics* **1996**, *85*, 17–24.
- (111) “Analysis of three-electrode setups for ac-impedance measurements on lithium-ion cells by FEM simulations” Ender, M.; Weber, A.; and Ellen, I.-T. *J. Electrochem. Soc.* **2011**, *159*, A128–A136.
- (112) “On impedance spectroscopy analysis of nonideal heterojunctions” Brus, V. V. *Semicond. Sci. Technol.* **2012**, *27*, 035024.
- (113) “Dispersion and absorption in dielectrics I. alternating current characteristics” Cole, K. S. and Cole, R. H. *J. Chem. Phys.* **1941**, *9*, 341–351.
- (114) “Financial assistance funding opportunity announcement: integration and optimization of novel ion conducting solids” ARPA-E, U.S. D.O.E. **2016**, <https://arpa-e-foa.energy.gov/FileContent.aspx?FileID=92b0a016-687b-475a-9884-3201512f1037>.
- (115) “Measurement of transference numbers for lithium ion electrolytes via four different methods, a comparative study” Zugmann, S.; Fleischmann, M.; and Amereller, M. *Electrochim. Acta* **2011**, *56*, 3926–3933.
- (116) “Electrochemical measurement of transference numbers in polymer electrolytes” Evans, J.; Vincent, C. A.; and Bruce, P. G. **1987**, *28*, 2324–2328.
- (117) “Ageing mechanisms in lithium-ion batteries” Vetter, J.; Novák, P.; Wagner, M. R.; Veit, C.; and Möller, K. C. *J. Power Sources* **2005**, *147*, 269–281.
- (118) “Impedance spectroscopy of lithium electrodes: part 1. general behavior in propylene carbonate solutions and the correlation to surface chemistry and cycling efficiency” Aurbach, D. and Zaban, A. *J. Electroanal. Chem.* **1993**, *348*, 155–179.

- (119) “Design and preparation of materials for advanced electrochemical storage” Melot, B. C. and Tarascon, J. M. *Acc. Chem. Res.* **2013**, *46*, 1226–1238.
- (120) “Evolution of strategies for modern rechargeable batteries” Goodenough, J. B. *Acc. Chem. Res.* **2012**, *46*, 1053–1061.
- (121) “Tetraarylborate polymer networks as single-ion conducting solid electrolytes” Van Humbeck, J. F.; Aubrey, M. L.; Alsbaiee, A.; Ameloot, R.; Coates, G. W.; Dichtel, W. R.; and Long, J. R. **2015**, *6*, 5499–5505.
- (122) “MOFs as proton conductors – challenges and opportunities” Ramaswamy, P.; Wong, N. E.; and Shimizu, G. K. H. *Chem. Soc. Rev.* **2014**, *43*, 5913–5932.
- (123) “Hydrated proton-conductive metal–organic frameworks” Sadakiyo, M.; Yamada, T.; and Kitagawa, H. *ChemPlusChem* **2016**, *81*, 691–701.
- (124) “Theory of decomposition of liquids by electrical currents” de Grotthuss, C. *Ann. Chim. Paris* **1806**, *58*, 54–74.
- (125) “CRC handbook of chemistry and physics” Lide, D. D. ed. *CRC Press* **2011**, *92*, 1–34.
- (126) “Anhydrous proton-conducting polymers” Schuster, M. F. H.; and Meyer, W. H. *Ann. Rev. Mat. Res.* **2003**, *33*, 233–261.
- (127) “Anhydrous proton conduction at 150 °C in a crystalline metal-organic framework” Hurd, J. A.; Vaidhyanathan, R.; Thangadurai, V.; Ratcliffe, C. I.; Moudrakovski, I. L.; and Shimizu, G. K. H. *Nat. Chem.* **2009**, *1*, 705–710.
- (128) “Proton conduction with metal-organic frameworks.” Shimizu, G. K. H.; Taylor, J. M.; and Kim, S. *Science* **2013**, *341*, 354–355.
- (129) “Helical water chain mediated proton conductivity in homochiral metal-organic frameworks with unprecedented zeolitic unh-topology” Sahoo, S. C.; Kundu, T.; and Banerjee, R. *J. Am. Chem. Soc.* **2011**, *133*, 17950–17958.
- (130) “Rational designs for highly proton-conductive metal-organic frameworks” Sadakiyo, M.; Yamada, T.; and Kitagawa, H. **2009**, *131*, 9906–9907.
- (131) “Inherent proton conduction in a 2D coordination framework” Umeyama, D.; Horike, S.; Inukai, M.; Itakura, T.; and Kitagawa, S. *J. Am. Chem. Soc.* **2012**, *134*, 12780–12785.
- (132) “Intrinsic and extrinsic proton conductivity in metal-organic frameworks” Tominaka, S. and Cheetham, A. K. *RSC Advances* **2014**, *4*, 54382–54387.
- (133) “High proton conductivity of one-dimensional ferrous oxalate dihydrate” Yamada, T.; Sadakiyo, M.; and Kitagawa, H. *J. Am. Chem. Soc.* **2009**, *131*, 3144–3145.
- (134) “Charge transport in metal-organic frameworks” Wiers, B. M. *Ph.D. dissertation* **2015**, 1–130.
- (135) “Ionic conductivity in the metal-organic framework UiO-66 by dehydration and insertion of lithium *tert*-butoxide” Ameloot, R.; Aubrey, M.; Wiers, B. M.; Gómora-Figueroa, A. P.; Patel, S. N.; Balsara, N. P.; and Long, J. R. *Chem. Eur. J.* **2013**, *19*, 5533–5536.
- (136) “Metal-organic frameworks as solid magnesium electrolytes” Aubrey, M. L.; Ameloot, R.; Wiers, B. M.; and Long, J. R. *Energy Environ. Sci.* **2014**, *7*, 667–671.
- (137) “Temperature-dependent conductivity of emim⁺ (emim⁺ = 1-ethyl-3-methyl imidazolium) confined in channels of a metal-organic framework” Chen, W.-X.; Xu, H.-R.; Zhuang, G.-L.; Long, L.-S.; Huang, R.-B.; and Zheng, L.-S. **2011**, *47*, 11933–11933.

- (138) “Scandium/alkaline metal-organic frameworks: adsorptive properties and ionic conductivity” Cepeda, J.; Pérez-Yáñez, S.; Beobide, G.; Castillo, O.; Goikolea, E.; Aguesse, F.; Garrido, L.; Luque, A.; and Wright, P. A. *Chem. Mater.* **2016**, *28*, 2519–2528.
- (139) “Visualization of ion conductivity: vapo-chromic luminescence of an ion-conductive ruthenium(II) metalloligand-based porous coordination polymer” Watanabe, A.; Kobayashi, A.; Saitoh, E.; Nagao, Y.; Yoshida, M.; and Kato, M. *Inorg. Chem.* **2015**, *54*, 11058–11060.
- (140) “Metal-organic frameworks containing missing-linker defects leading to high hydroxide-ion conductivity” Montoro, C.; Ocón, P.; Zamora, F.; and Navarro, J. A. R. *Chem. Eur. J.* **2016**, *22*, 1646–1651.
- (141) “Low temperature ionic conductor: ionic liquid incorporated within a metal-organic framework” Fujie, K.; Otsubo, K.; Ikeda, R.; Yamada, T.; and Kitagawa, H. *Chem. Sci.* **2015**, *6*, 4306–4310.
- (142) “Inorganic and organic hybrid solid electrolytes for lithium-ion batteries” Fu, X.; Yu, D.; Zhou, J.; Li, S.; Gao, X.; Han, Y.; Qi, P.; Feng, X.; and Wang, B. *Cryst. Eng. Commun.* **2016**, *18*, 4236–4258.
- (143) “Superior conductive solid-like electrolytes: nanoconfining liquids within the hollow structures” Zhang, J.; Bai, Y.; Sun, X. G.; Li, Y.; Guo, B.; Chen, J.; Veith, G. M.; Hensley, D. K.; Paranthaman, M. P.; Goodenough, J. B.; and Dai, S. *Nano Lett.* **2015**, *15*, 3398–3402.
- (144) “Quantum tunneling of water in beryl: a new state of the water molecule” Kolesnikov, A. I.; Reiter, G. F.; Choudhury, N.; and Prisk, T. R. *Phys. Rev.* **2016**, *116*, 167802.
- (145) “Studies of the water adsorption on zeolites and modified mesoporous materials for seasonal storage of solar heat” Jänchen, J.; Ackermann, D.; Stach, H.; and Brösicke, W. *Solar Energy* **2004**, *76*, 339–344.
- (146) “Characterization of metal-organic frameworks by water adsorption” Küsgens, P.; Rose, M.; Senkovska, I.; and Fröde, H. *Microporous Mesoporous Mater.* **2009**, *120*, 325–330.
- (147) “Strong CO₂ binding in a water-stable, triazolate-bridged metal-organic framework functionalized with ethylenediamine” Demessence, A.; D'Alessandro, D. M.; Foo, M. L.; and Long, J. R. *J. Am. Chem. Soc.* **2009**, *131*, 8784–8786.
- (148) “A route to high surface area, porosity and inclusion of large molecules in crystals” Chae, H. K.; Siberio-Pérez, D. Y.; Kim, J.; Go, Y. B.; and Eddaoudi, M. *Nature* **2004**, *427*, 523–527.
- (149) “Dramatic tuning of carbon dioxide uptake via metal substitution in a coordination polymer with cylindrical pores” Caskey, S. R.; Wong-Foy, A. G.; and Matzger, A. J. **2008**, *130*, 10870–10871.
- (150) “Base-induced formation of two magnesium metal-organic framework compounds with a bifunctional tetratopic ligand” Dietzel, P. D. C.; Blom, R.; and Fjellvåg, H. *Eur. J. Inorg. Chem.* **2008**, *2008*, 3624–3632.
- (151) “Inclusion and dynamics of a polymer–Li salt complex in coordination nanochannels” Yanai, N.; Uemura, T.; Horike, S.; Shimomura, S.; and Kitagawa, S. *Chem. Commun.* **2011**, *47*, 1722–1724.
- (152) “Lithium ion diffusion in a metal–organic framework mediated by an ionic liquid” Fujie, K.; Ikeda, R.; Otsubo, K.; Yamada, T.; and Kitagawa, H. *Chem. Mater.* **2015**, *27*, 7355–7361.

- (153) “Ionic liquid transported into metal-organic frameworks” Fujie, K. and Kitagawa, H. *Coordin. Chem. Rev.* **2016**, *307*, 382–390.
- (154) “Ionic metal-organic frameworks (iMOFs): design principles and applications” Karmakar, A.; Desai, A. V.; and Ghosh, S. K. *Coordin. Chem. Rev.* **2016**, *307*, 313–341.
- (155) “Cucurbit[6]uril: organic molecular porous material with permanent porosity, exceptional stability, and acetylene sorption properties” Lim, S.; Kim, H.; Selvapalam, N.; and Kim, K. J. *Angew. Chem. Int. Edit. Engl.* **2008**, *120*, 3400–3403.
- (156) “Highly selective carbon dioxide sorption in an organic molecular porous material” Kim, H.; Kim, Y.; Yoon, M.; Lim, S.; Park, S. M.; Seo, G.; and Kim, K. J. *Am. Chem. Soc.* **2010**, *132*, 12200–12202.
- (157) “Functionalized cucurbiturils and their applications” Kim, K.; Selvapalam, N.; Ko, Y. H.; Park, K. M.; Kim, D.; and Kim, J. *Chem. Soc. Rev.* **2007**, *36*, 267–279.
- (158) “Solid lithium electrolytes based on an organic molecular porous solid” Park, J. H.; Suh, K.; Rohman, M. R.; Hwang, W.; Yoon, M.; and Kim, K. *Chem. Commun.* **2015**, *51*, 9313–9316.
- (159) “Determination of lithium-ion transference numbers in LiPF₆-PC solutions based on electrochemical polarization and NMR measurements” Zhao, J.; Wang, L.; He, X.; Wan, C.; and Jiang, C. J. *Electrochem. Soc.* **2008**, *155*, A292–A296.
- (160) “Importance of donor number in determining solvating ability of polymers and transport properties in gel-type polymer electrolytes” Kim, C. S. and Oh, S. M. *Electrochim. Acta* **2000**, *45*, 2101–2109.
- (161) “All solid battery with phosphate compounds made through sintering process” Nagata, K. and Nanno, T. *J. Power Sources* **2007**, *174*, 832–837.
- (162) “Challenges for rechargeable Li batteries” Goodenough, J. B. and Kim, Y. *Chem. Mater.* **2009**, *22*, 587–603.
- (163) “Synthesis and structural study of a tetranuclear magnesium alkoxide: [Mg₄(M₃, η²-OR)₂ (μ², η²-OR)₄(OR)₂] with OR-OCH(CH₃)CH₂OCH₃” Albaric, L.; Hovnanian, N.; Julbe, A.; Guizard, C.; Alvarez-Larena, A.; and Piniella, J. F. *Polyhedron* **1997**, *16*, 587–592.
- (164) “A new zirconium inorganic building brick forming metal-organic frameworks with exceptional stability” Cavka, J. H.; Jakobsen, S.; Olsbye, U.; Guillou, N.; Lamberti, C.; Bordiga, S.; and Lillerud, K. P. *J. Am. Chem. Soc.* **2008**, *130*, 13850–13851.
- (165) “Disclosing the complex structure of UiO-66 metal-organic framework: a synergic combination of experiment and theory” Valenzano, L.; Civalleri, B.; Chavan, S.; Bordiga, S.; Nilsen, M. H.; Jakobsen, S.; Lillerud, K. P.; and Lamberti, C. *Chem. Mater.* **2011**, *23*, 1700–1718.
- (166) “Exceptional mechanical stability of highly porous zirconium metal-organic framework UiO-66 and its important implications” Wu, H.; Yildirim, T.; and Zhou, W. *J. Phys. Chem. Lett.* **2013**, *4*, 925–930.
- (167) “The impact of elastic deformation on deposition kinetics at lithium/polymer interfaces” Monroe, C. and Newman, J. J. *Electrochem. Soc.* **2005**, *152*, A396–A404.

- (168) “Ionic conductivity in the metal-organic framework UiO-66 by dehydration and insertion of lithium *tert*-Butoxide” Ameloot, R.; Aubrey, M.; Wiers, B. M.; Gómora-Figueroa, A. P.; Patel, S. N.; Balsara, N. P.; and Long, J. R. *Chem. Eur. J.* **2013**, *19*, 5533–5536.
- (169) “Cubic octanuclear Ni(II) clusters in highly porous polypyrazolyl-based materials” Masciocchi, N.; Galli, S.; Colombo, V.; Maspero, A.; Palmisano, G.; Seyyedi, B.; Lamberti, C.; and Bordiga, S. *J. Am. Chem. Soc.* **2010**, *132*, 7902–7904.
- (170) “Study of the incorporation and release of the non-conventional half-sandwich ruthenium(II) metallodrug RAPTA-C on a robust MOF” Procopio, E. Q.; Rojas, S.; Padial, N. M.; Galli, S.; Masciocchi, N.; Linares, F.; Miguel, D.; Oltra, J. E.; Navarro, J. A. R.; and Barea, E. *Chem. Commun.* **2011**, *47*, 11751–11753.
- (171) “Highly hydrophobic isoreticular porous metal-organic frameworks for the capture of harmful volatile organic compounds” Padial, N. M.; Quartapelle Procopio, E.; Montoro, C.; López, E.; Oltra, J. E.; Colombo, V.; Maspero, A.; Masciocchi, N.; Galli, S.; Senkovska, I.; Kaskel, S.; Barea, E.; and Navarro, J. A. R. *Angew. Chem. Int. Ed. Engl.* **2013**, *52*, 8290–8294.
- (172) “Conjugated microporous polymers: design, synthesis and application.” Xu, Y.; Jin, S.; Xu, H.; Nagai, A.; and Jiang, D. *Chem. Soc. Rev.* **2013**, *42*, 8012–8031.
- (173) “Functional porous organic polymers for heterogeneous catalysis.” Zhang, Y. and Riduan, S. N. *Chem. Soc. Rev.* **2012**, *41*, 2083–2094.
- (174) “Nanoporous organic polymer networks” Dawson, R.; Cooper, A. I.; and Adams, D. J. *Prog. Polymer Sci.* **2012**, *37*, 530–563.
- (175) “Porous aromatic frameworks: synthesis, structure and functions” Ben, T. and Qiu, S. *CrystEngComm* **2013**, *15*, 17–26.
- (176) “Lithium-ion batteries with a wide temperature range operability enabled by highly conductive sp³ boron-based single ion polymer electrolytes” Sun, Y.; Xu, G.; Cai, W.; Rohan, R.; and Lin, A. *Energy Technol.* **2014**, *2*, 643–650.
- (177) “A class of sp³ boron-based single-ion polymeric electrolytes for lithium ion batteries” Zhang, Y.; Xu, G.; Sun, Y.; Han, B.; Chen, Z.; and Rohan, R. *RSC Adv.* **2013**, *3*, 14934–14937.
- (178) “Nanoionics: ion transport and electrochemical storage in confined systems” Maier, J. *Nat. Mater.* **2005**, *4*, 805–815.
- (179) “A pre-lithiated phloroglucinol based 3D porous framework as a single ion conducting electrolyte for lithium ion batteries” Rohan, R.; Pareek, K.; Chen, Z.; and Cheng, H. *RSC Adv.* **2016**, *6*, 53140–53147.
- (180) “Melamine–terephthalaldehyde–lithium complex: a porous organic network based single ion electrolyte for lithium ion batteries” Rohan, R.; Pareek, K.; Cai, W.; Zhang, Y.; Xu, G.; Chen, Z.; Gao, Z.; Dan, Z.; and Cheng, H. *J. Mater. Chem. A* **2015**, *3*, 5132–5139.
- (181) “Ionic-covalent organic frameworks with spiroborate linkage.” Du, Y.; Yang, H.; Whiteley, J. M.; Wan, S.; Jin, Y.; Lee, S.-H.; and Zhang, W. *Angew. Chem. Int. Edit. Engl.* **2016**, *55*, 1737–1741.

- (182) “Shape-controlled synthesis and lithium-storage study of metal-organic frameworks $Zn_4O(1,3,5\text{-benzenetribenzoate})_2$ ” Li, X.; Cheng, F.; Zhang, S.; and Chen, J. *J. Power Sources* **2006**, *160*, 542–547.
- (183) “Lithium storage in a metal-organic framework with diamondoid topology – a case study on metal formates” Saravanan, K.; Nagarathinam, M.; Balaya, P.; and Vittal, J. J. *J. Mater. Chem.* **2010**, *20*, 8329–8335.
- (184) “Conjugated dicarboxylate anodes for Li-ion batteries” Armand, M.; Grugeon, S.; Vezin, H.; Laruelle, S.; Ribière, P.; Poizot, P.; and Tarascon, J. M. *Nat. Mater.* **2009**, *8*, 120–125.
- (185) “Radicals in metal-organic frameworks” Faust, T. B. and D'Alessandro, D. M. *RSC Adv.* **2014**, *4*, 17498–17512.
- (186) “Reactions of the Radical Anions and Dianions of Aromatic Hydrocarbons” Holy, N. L. *Chem. Rev.* **1974**, *74*, 243–277.
- (187) “Organic dicarboxylate negative electrode materials with remarkably small strain for high-voltage bipolar batteries.” Ogihara, N.; Yasuda, T.; Kishida, Y.; Ohsuna, T.; Miyamoto, K.; and Ohba, N. *Angew. Chem. Int. Edit. Engl.* **2014**, *53*, 11467–11472.
- (188) “Metal-organic frameworks—prospective industrial applications” Mueller, U.; Schubert, M.; Teich, F.; Puetter, H.; Schierle-Arndt, K.; and Pastré, J. *J. Mater. Chem.* **2006**, *16*, 626–636.
- (189) “Shaped bodies containing metal-organic frameworks” Hesse, M.; Mueller, U.; and Yaghi, O. **2011**, US 7931960.
- (190) “Shaped bodies containing metal-organic frameworks” Mueller, U.; Lobree, L.; Hesse, M.; and Yaghi, O. **2005**, US 7524444.
- (191) “Polymer electrolyte membrane comprising coordination polymer” De Figueiredo Gomes, D.; Nunes, S.; Peinemann, K.-V.; Kaskel, S.; Abetz, V.; Gkss-Forshungszentrum Geesthacht GmbH; and Dresden, T. U. **2012**, US 8124660.
- (192) “Metal-organic framework-based separator for lithium-sulfur batteries” Bai, S.; Liu, X.; Zhu, K.; Wu, S.; and Zhou, H. *Nat. Energy* **2016**, *1*, 16094.
- (193) “Metal-organic frameworks for lithium ion batteries and supercapacitors” Ke, F.-S.; Wu, Y.-S.; and Deng, H. *J. Solid State Chem.* **2015**, *223*, 109–121.
- (194) “Metal-organic frameworks as platforms for clean energy” Li, S.-L. and Xu, Q. *Energy Environ. Sci.* **2013**, *6*, 1656–1683.
- (195) “Lewis acid-base interactions between polysulfides and metal-organic framework in lithium sulfur batteries” Zheng, J.; Tian, J.; Wu, D.; Gu, M.; Xu, W.; Wang, C.; Gao, F.; Engelhard, M. H.; Zhang, J.-G.; Liu, J.; Xiao, J. *Nano Lett.* **2014**, *14*, 2345–2352.
- (196) “Rational design of a metal-organic framework host for sulfur storage in fast, long-cycle Li-S batteries” Zhou, J.; Li, R.; Fan, X.; Chen, Y.; Han, R.; Li, W.; Zheng, J.; Wang, B.; and Li, X. *Energy Environ. Sci.* **2014**, *7*, 2715–2724.
- (197) “A metal-organic framework with open metal sites for enhanced confinement of sulfur and lithium-sulfur battery of long cycling life” Wang, Z.; Li, X.; Cui, Y.; Yang, Y.; Pan, H.; Wang, Z.; Wang, Z.; Wu, C.; Chen, B.; and Qian, G. *Cryst. Growth Design* **2013**, *13*, 5116–5120.

- (198) “Sulfur embedded in metal-organic framework-derived hierarchically porous carbon nanoplates for high performance lithium-sulfur battery” Xu, G.; Ding, B.; Shen, L.; Nie, P.; Han, J.; and Zhang, X. *J. Mater. Chem. A* **2013**, *1*, 4490–7.
- (199) “Synthesis, structure, characterization, and redox properties of the porous MIL-68(Fe) solid” Fateeva, A.; Horcajada, P.; Devic, T.; Serre, C.; Marrot, J.; Grenèche, J.-M.; Morcrette, M.; Tarascon, J.-M.; Maurin, G.; and Férey, G. *Eur. J. Inorg. Chem.* **2010**, *2010*, 3789–3794.
- (200) “Discovery of a ‘bipolar charging’ mechanism in the solid-state electrochemical process of a flexible metal-organic framework” Zhang, Z.; Yoshikawa, H.; and Awaga, K. *Chem. Mater.* **2016**, *28*, 1298–1303.
- (201) “Monitoring the solid-state electrochemistry of Cu(2,7-aqdc) (aqdc = anthraquinone dicarboxylate) in a lithium battery: coexistence of metal and ligand redox activities in a metal-organic framework” Zhang, Z.; Yoshikawa, H.; and Awaga, K. *J. Am. Chem. Soc.* **2014**, *136*, 16112–16115.
- (202) “MIL-101(Fe) as a lithium-ion battery electrode material: a relaxation and intercalation mechanism during lithium insertion” Shin, J.; Kim, M.; Cirera, J.; Chen, S.; Halder, G. J.; Yersak, T. A.; Paesani, F.; Cohen, S. M.; and Meng, Y. S. *J. Mater. Chem. A* **2015**, *3*, 4738–4744.
- (203) “3-D coordination polymers based on the tetrathiafulvalenetetracarboxylate (TTF-TC) derivative: synthesis, characterization, and oxidation issues” Nguyen, T. L. A.; Demir-Cakan, R.; Devic, T.; Morcrette, M.; Ahnfeldt, T.; Auban-Senzier, P.; Stock, N.; Goncalves, A.-M.; Filinchuk, Y.; Tarascon, J.-M.; and Férey, G. *Inorg. Chem.* **2010**, *49*, 7135–7143.
- (204) “Hydrothermal synthesis of microporous transition metal squarates: preparation and structure of $[\text{Co}_3(\mu^3\text{-OH})_2(\text{C}_4\text{O}_4)_2] \cdot 3\text{H}_2\text{O}$ ” Gutschke, S. O. H.; Molinier, M.; Powell, A. K.; and Wood, P. T. *Angew. Chem. Int. Edit. Engl.* **1997**, *36*, 991–992.
- (205) “Microporous magnets” Dechambenoit, P. and Long, J. R. *Chem. Soc. Rev.* **2011**, *40*, 3249–3265.
- (206) “Magnetic metal-organic frameworks” Kurmoo, M. *Chem. Soc. Rev.* **2009**, *38*, 1353–1379.
- (207) “Organic-inorganic hybrid materials: from ‘simple’ coordination polymers to organodiamine-templated molybdenum oxides” Hagrman, P. J.; Hagrman, D.; and Zubieta, J. *Angew. Chem. Int. Ed.* **1999**, *38*, 2638–2684.

Chapter 2

Metal-organic frameworks as solid magnesium electrolytes

2.1 Introduction

Metal-organic frameworks, are a class of porous crystalline solids composed of metal ions connected via multifunctional organic ligands to form a robust three-dimensional architecture that is permanently porous.^{1,2} The modular nature of these materials allows their framework composition and pore dimensions to be tuned via judicious selection of the metal ion and organic ligand.^{3,4} Further, alteration of the internal surfaces through post-synthetic modification has been widely developed, and presents opportunities for manipulating the properties of a crystalline solid to a degree not possible in purely inorganic solid electrolytes.^{5,6}

The diffusion of selected guest species, both in solution and in the gas phase, within the pores of MOFs has been studied extensively. Notably, some studies have demonstrated significantly greater diffusivities in MOFs compared to other microporous materials.⁷ For structures with relatively small pores, confinement effects have further been shown to impose a highly disordered structure upon polymer guest species, resulting in ionic diffusivities more similar to those found in a molten state.⁸⁻¹⁰ However, the transport of charged species within MOFs and their electrochemical applications remains a nascent field.^{11,12} To date, work on ionically conductive MOFs has been almost exclusively focused on proton transport, which is mechanistically very different from the transport of metal cations.¹³⁻¹⁵ Nevertheless, a number of Na⁺ and Li⁺ conducting MOFs have been reported, and these have exhibited conductivities as high as 0.3 mS cm⁻¹ at room temperature.^{8,10,16-19} In contrast to polymer electrolytes, intrinsically porous MOF electrolytes have the distinct advantage that conductivity and mechanical properties are not inversely related. This is because ionic movement relies on through-the-pore diffusion instead of polymer chain mobility.

Considering ions of larger size and greater charge density than Li⁺ using solid electrolytes with pores large enough to easily accommodate the guest species may enable fast conduction of such ions, a difficult task in polymer or inorganic electrolytes. This is especially true in the case of Mg²⁺, because materials that have previously been reported either degrade when ion exchange is attempted, conduct only at very high temperatures (e.g., 600 °C), or conduct only in a hydrated state and never above 1 mS cm⁻¹ at room temperature.²⁰⁻²⁵ Here, we present the preparation and characterization of a series of solid Mg²⁺ electrolytes in which a host metal-organic framework can mediate remarkably facile ion transport, achieving rates unprecedented in other classes of crystalline materials.

2.2 Results and discussion

We hypothesized that MOFs with a high density of open metal sites capable of coordinating

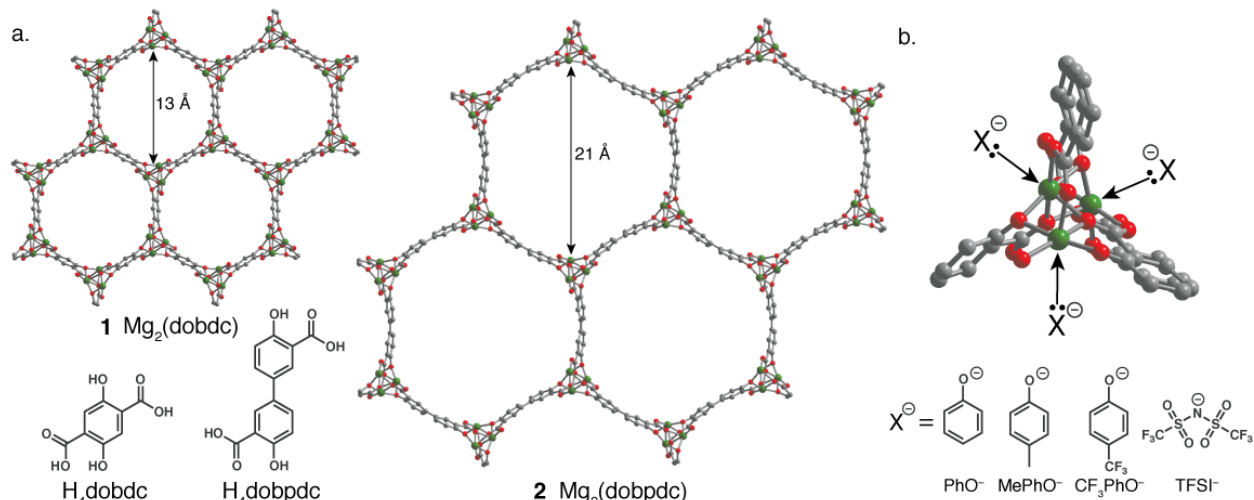


Figure 2.1. (a) Structures of the metal-organic frameworks $\text{Mg}_2(\text{dobdc})$ (**1**) and $\text{Mg}_2(\text{dobpdc})$ (**2**), as viewed along the c-axis. The vertices of the one-dimensional channels are formed by 1-D chains of Mg^{2+} ions linked together by the respective ligands (bottom left) that form the pore walls (b) a close-up of the open coordination sites at the vertices of the pore that interact with nucleophilic guest species: PhO^- = phenolate, MePhO^- = 4-methylphenolate, CF_3PhO^- = 4-trifluoromethylphenolate, and TFSI^- = bis(trifluoromethanesulfonyl)imide.

nucleophilic anions could provide an enthalpic driving force for the insertion of appropriate magnesium salts within the pores. A similar approach was taken previously for lithium electrolytes.¹⁰ This may result in a material with electrolyte concentrations greater than what is achievable in the bulk solutions. Further, the open metal sites may also inhibit the migration of nucleophilic anions, potentially favouring cation mobility. We therefore chose to investigate $\text{Mg}_2(\text{dobdc})$, **1**, (dobdc^{4-} = 2,5-dioxidobenzene-1,4-dicarboxylate),²⁶ and its expanded analogue $\text{Mg}_2(\text{dobpdc})$, **2**, (dobpdc^{4-} = 4,4'-dioxidobiphenyl-3,3'-dicarboxylate).^{27,28} As depicted in **Figure 2.1**, frameworks **1** and **2** have an identical inorganic building unit consisting of one-dimensional chains of coordinatively-unsaturated Mg^{2+} cations linked via oxido and carboxylato bridging moieties. In this particular series of isorecticular frameworks the pore size can be increased systematically.²⁹

2.2.1 Ion insertion and electrolyte grafting in $\text{Mg}_2(\text{dobdc})$. The two frameworks were soaked at 80 °C for one week in solutions consisting of a magnesium salt, either a magnesium phenolate or magnesium bis(trifluoromethanesulfonyl)imide ($\text{Mg}(\text{TFSI})_2$), dissolved in triglyme. Similar or lower electrolyte loadings were observed with shorter reaction times for electrolyte incorporation in $\text{Mg}_2(\text{dobdc})$. The reaction was attempted with $\text{Ni}_2(\text{dobdc})$ as well but lower electrolyte loadings were observed under identical reaction conditions. Note that some magnesium phenolates have recently been proposed as a component in non-pyrophoric electrolytes for magnesium batteries.³⁰⁻³³ The resulting solids were washed with triglyme to remove excess electrolyte solution from the crystallite surfaces. The materials were then filtered to yield free-flowing microcrystalline powders. Although previous electrolytes tested in magnesium batteries have typically been based on THF, triglyme offered a greater solubility of the magnesium phenolate salts, together with lower volatility.³⁴⁻³⁶ The use of such oligoether solvents has been previously reported in pioneering work on prototype magnesium batteries, as well as in MOF-based lithium electrolytes.^{8,37}

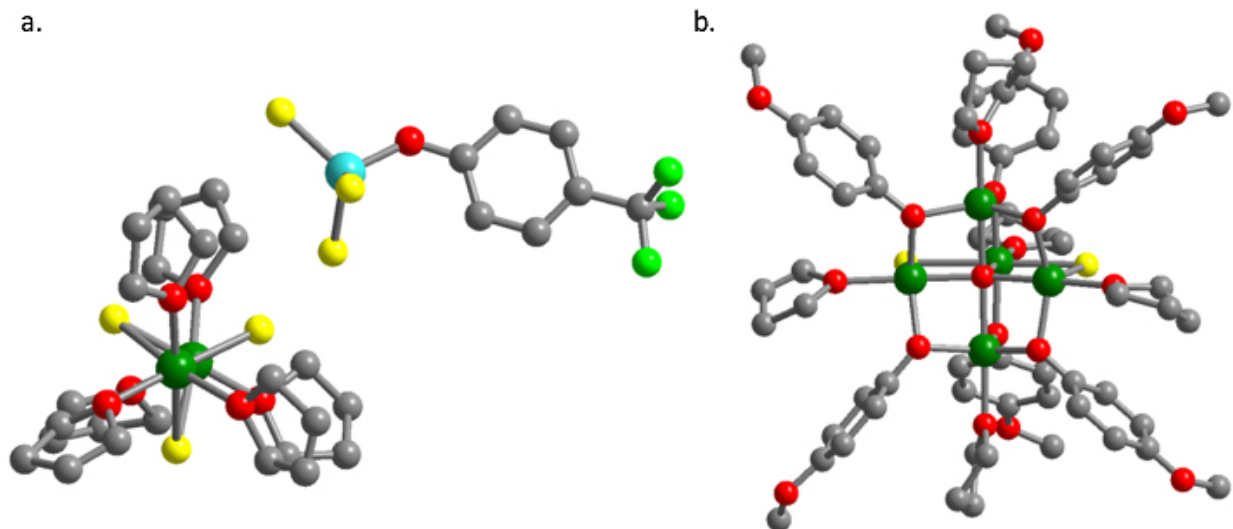


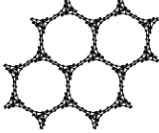
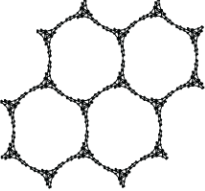
Figure 2.2. Single crystal structures of $[\text{Mg}_2\text{Cl}_3(\text{THF})_6]^+ [\text{Cl}_3\text{Al}(\text{p-trifluoromethylphenolate})]^-$ (a) and $\text{Mg}_5\text{Cl}_2\text{O}(\text{THF})_5(\text{p-methoxyphenolate})_6$. Carbon is shown in grey, oxygen in red, chlorine in yellow, magnesium in dark green, fluorine in green, and aluminum in light blue. Both were crystallized from a THF solution of trichloroaluminum and their respective phenoxy magnesium chloride salt. Atom coordinates were taken from ref. 31.

Inclusion of a magnesium phenolate salt within the MOF pores is expected to compete with the reversible formation of multinuclear magnesium phenolate complexes in the bulk solution that could potentially be too large to enter the framework structure.^{31,38} As such, magnesium salts with less electron donating phenolates, and thus larger dissociation constants, were anticipated to yield materials with higher magnesium phenolate loadings and thus an electrolyte loading shifted towards the framework-magnesium salt host-guest complex. Indeed, this hypothesis was recently supported by single crystal X-ray diffraction of the trichloroaluminum salt adducts, **Figure 2.2**.³¹ As expected, the more electron withdrawing OPhCF_3^- crystallized as a mononuclear anion transmetallated to the more Lewis acidic aluminum cation while OPhOMe^- crystallized as a much larger tetranuclear cluster that likely would not fit in the pores of **1**. The magnesium phenolates $\text{Mg}(\text{OPhMe})_2$ and $\text{Mg}(\text{OPh})_2$ exhibited a preference for the bulk solution phase, whereas $\text{Mg}(\text{OPhCF}_3)_2$, featuring a less coordinating anion, exhibited much higher concentration within the framework. It is possible that the more strongly coordinating phenolates are diffusion limited over the time scale of the experiment; no change in concentration was observed with shorter reaction times. As summarized in **Table 2.1**, the observed concentration ratios and salt loading capacities reflect the strength of the interaction between the Mg^{2+} ions and the counteranion.

The salt $\text{Mg}(\text{TFSI})_2$, which is not expected to form aggregates in solution since the TFSI^- anion is a very poor nucleophile, is also not expected to coordinate to the open metal sites lining the MOF pores. Therefore, the enthalpy gradient that drives electrolyte insertion is much smaller for $\text{Mg}(\text{TFSI})_2$ than for the magnesium phenolates, and indeed the observed loading was less than for $\text{Mg}(\text{OPhCF}_3)_2$. Here, the host-guest equilibrium does not favor inclusion within the MOF, since entropic factors are more significant in determining the equilibrium.

2.2.2 Ionic conductivity of electrolyte grafted $\text{Mg}_2(\text{dobdc})$. Ionic conductivities of the salt-included MOFs were measured using AC impedance spectroscopy. Samples were pressed into

Table 2.1. Summary of materials synthesized, conductivities and activation energies. Electrolyte concentrations were approximated from the unit cell volume. Concentration ratios were determined from the electrolyte concentration per unit cell as determined by elemental analysis and $^1\text{H-NMR}$ and the concentration of the solution that the framework was in contact with.

framework	guest salt(s) per mole of framework	equivalents triglyme	electrolyte concentration (M)	K_{eq}	conductivity $\log_{10}(\text{S/cm})$	molar conductivity $\log_{10}(\text{S/M}\cdot\text{cm})$
 $\text{Mg}_2(\text{dobdc})$	$0.05\text{Mg}(\text{OPhMe})_2$	1.5	0.19	0.63	-8.1	-7.4
	$0.07\text{Mg}(\text{OPh})_2$	1.5	0.26	0.86	-7.0	-6.4
	$0.39\text{Mg}(\text{OPhCF}_3)_2$	6.0	1.5	5.0	-5.8	-6.0
	$0.06\text{Mg}(\text{TFSI})_2$	1.4	0.22	0.73	-5.8	-5.2
	$0.31\text{Mg}(\text{OPhCF}_3)_2$ and $0.30\text{Mg}(\text{TFSI})_2$	2.4	2.3	2.6 ($\text{Mg}(\text{TFSI})_2$)	-4.0	-4.4
 $\text{Mg}_2(\text{dobpdc})$	$0.31\text{Mg}(\text{OPhCF}_3)_2$	3.8	0.63	2.1	-6.2	-6.0
	$0.22\text{Mg}(\text{TFSI})_2$	3.3	0.45	1.0	-3.9	-3.6
	$0.21\text{Mg}(\text{OPhCF}_3)_2$ and $0.46\text{Mg}(\text{TFSI})_2$	4.8	1.37	2.4 ($\text{Mg}(\text{TFSI})_2$)	-3.6	-3.7

pellets and sandwiched between two stainless steel electrodes in a temperature-controlled cell. The frequency responses of the materials at room temperature are presented in the Nyquist and Bode plots shown in **Figure 2.3**. The Nyquist plots all display a single semicircle at high frequency, indicating ionic conductivity through the bulk material, followed by a positively sloping capacitive tail at lower frequencies.³⁹ For more conductive samples, a significant fraction of the semicircular region is shifted beyond the high frequency limit of the instrument. The bulk conductivity for each sample was determined from the right-hand minimum of the semicircle, which represents the total contribution to the impedance from ion transport through the crystal structure, grain boundaries, and interparticle interfaces.

Depending on the nature of the guest salt, ionic conductivities in **1** vary over four orders of magnitude, as reflected in the Bode plots in **Figure 2.3** and the conductivity values listed in **Table 2.1**. Materials containing only phenolate derivatives exhibit trends in conductivity consistent with electrolyte concentration and the expected proclivity of the guest salt for ion pairing. Thus, conductivity increases with decreasing electron-donating character of the anion. The contrast in loading and conductivity between $\text{Mg}(\text{OPhMe})_2 \subset \mathbf{1}$ and $\text{Mg}(\text{OPhCF}_3)_2 \subset \mathbf{1}$, underscores the importance that the donor ability of the anion has on the interaction with the framework, given their similarity in steric bulk. Interestingly, the conductivities of $\text{Mg}(\text{OPhCF}_3)_2 \subset \mathbf{1}$ and $\text{Mg}(\text{TFSI})_2 \subset \mathbf{1}$ are very similar, even though the electrolyte content differs dramatically. Triglyme absorbed into $\text{Mg}_2(\text{dobdc})$ has a conductivity of 10 nS cm^{-1} , significantly smaller than the electrolyte loaded samples except in the case of $\text{Mg}(\text{OPhMe})_2$ that demonstrated exceptionally low loading. This residual ionic conductivity was attributed to charge balancing defect sites within the framework that were observed by $^1\text{H-NMR}$, as discussed in the supporting information.

2.2.3 Ion insertion and electrolyte grafting in Mg₂(dobpdc). The expanded structure of **2** has a pore diameter of 21 Å and a unit cell volume of 7279 Å³, nearly double the values of 13 Å and 4005 Å³ observed for **1**. While the one-dimensional Mg²⁺ chains at the vertices of the hexagonal channels are the same, the larger organic linker decreases the polarity of the framework surface.¹⁹ This of course alters the propensity of the material for incorporating magnesium salts. In line with the increase in pore volume, the number of mole equivalents of Mg(TFSI)₂ included more than triples, the concentration, as determined from the unit cell volume, doubles, and the calculated equilibrium constant is consistent with what would be expected for a weakly interacting guest salt (see **Table 2.1**). Remarkably, the observed ionic conductivity upon pore expansion approaches 0.1 mS cm⁻¹, representing a more than 100-fold enhancement in ionic conductivity with respect to Mg(TFSI)₂⊂**1**.

The host-guest interaction is weaker in Mg(OPhCF₃)₂⊂**2** than in Mg(OPhCF₃)₂⊂**1**, as evidenced by the decrease in the amount of Mg(OPhCF₃)₂ taken up from 0.39 to 0.31 equivalents under identical conditions. In a less polarizing pore environment, ion pairing is expected to be more favored, and, accordingly, the ionic conductivity of Mg(OPhCF₃)₂⊂**2** is less than that observed in **1**, while the molar conductivities remain similar. As such, although the host-guest interaction dominates guest salt inclusion, the ion mobility appears strongly dependent on the basicity of the counterion.

2.2.4 Ionic conductivity of electrolyte grafted Mg₂(dobpdc). The similar conductivities of Mg(OPhCF₃)₂⊂**1** and Mg(TFSI)₂⊂**1**, despite the different nature and loading of the included salt, suggested to us that the interactions within the framework and transport processes for these guest electrolytes might be different enough to demonstrate a synergistic conductivity enhancement. While the nucleophilic electrolyte is strongly interacting with a single crystallite, ion transport between crystallites may be low. In contrast, the non-nucleophilic TFSI⁻ anion shows little or no preference for absorption in the framework. Upon soaking Mg(OPhCF₃)₂⊂**1** overnight in a solution of Mg(TFSI)₂, the inclusion of Mg(TFSI)₂ increased dramatically from 0.06 to 0.3 equivalents per formula unit. More importantly, the ionic conductivity increased by two orders of magnitude with respect to either of the component guest salts alone. The expanded analogue, Mg(OPhCF₃)₂ · Mg(TFSI)₂⊂**2**, also showed an increase in conductivity with respect to inclusion of only one of the salts, although in this case the increase was smaller, 0.1 mS cm⁻¹ to 0.25 mS cm⁻¹. These conductivity enhancements are likely explained by the relative increase in Mg(TFSI)₂ content in the mixed salt systems, rather than the two counterions together somehow offering a significant contribution to the total conductivity. The smaller increase in conductivity of Mg(TFSI)₂⊂**2** may be attributable to this material already having a relatively high ionic conductivity, and the only modest change in Mg(TFSI)₂ loading in the mixed salt phase. Importantly, the frameworks of **1** and **2** with dual guest salts show room temperature ionic conductivities approaching or greater than 0.1 mS cm⁻¹, which is already one-hundred times greater than that reported for any other crystalline material and greater than any other solid Mg²⁺ electrolyte.²⁰⁻²⁴ To the best of our knowledge, this is the only class of rigid

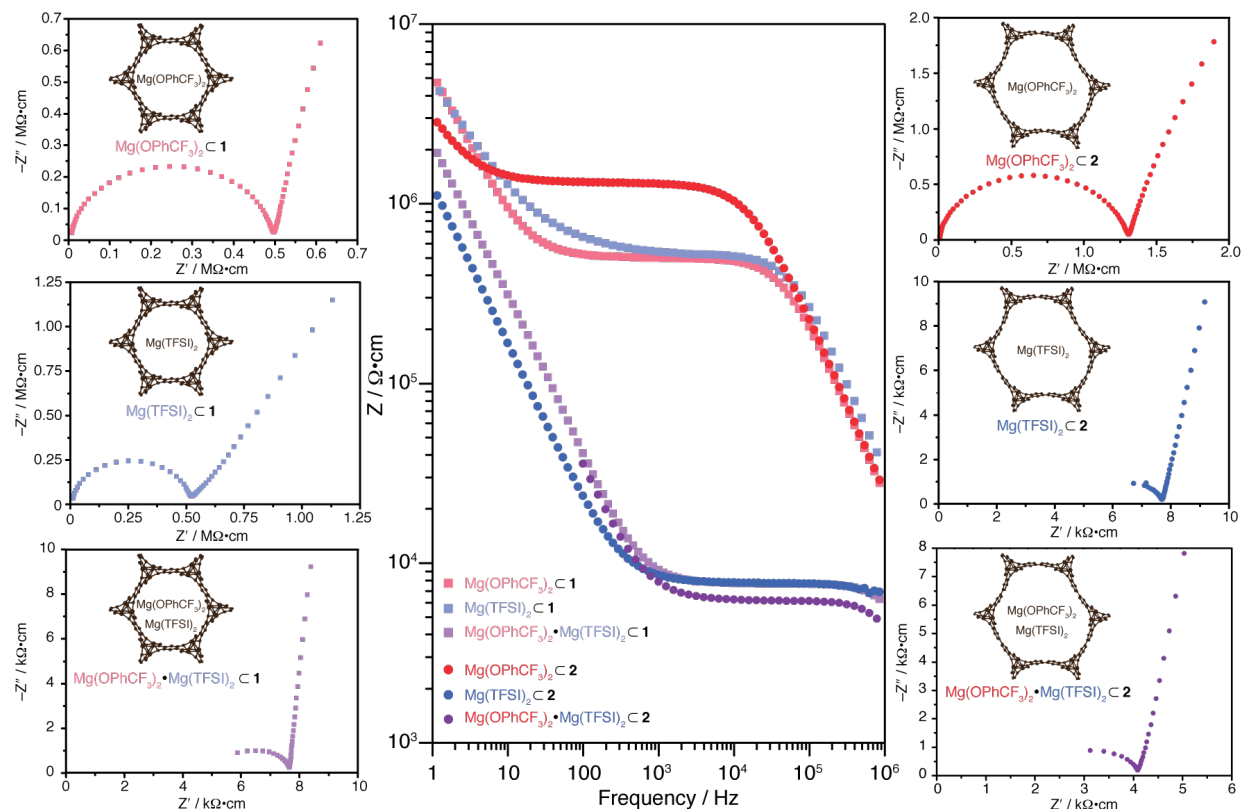


Figure 2.3. AC impedance spectra (1 MHz to 1 Hz) at 298 K. Center: Bode plot illustrating the bulk impedance as a plateau for $\text{Mg}(\text{OPhCF}_3)_2$ C 1 (light red), $\text{Mg}(\text{TFSI})_2$ C 1 (light blue), $\text{Mg}(\text{OPhCF}_3)_2 \cdot \text{Mg}(\text{TFSI})_2$ C 1 (light purple), $\text{Mg}(\text{OPhCF}_3)_2$ C 2 (dark red), $\text{Mg}(\text{TFSI})_2$ C 2 (dark blue), and $\text{Mg}(\text{OPhCF}_3)_2 \cdot \text{Mg}(\text{TFSI})_2$ C 2 (dark purple). Left: Nyquist plots for the host framework 1 and right: Nyquist plots for the host framework 2; colors match those in the Bode plot. The left most point in the Nyquist plots corresponds to an AC frequency of 1 MHz.

materials with ionic conductivities high enough for practical consideration as an electrolyte material in magnesium-based electrochemical cells.⁴⁰

2.2.5 Dependence of ionic conductivity with temperature. Activation energies were determined by fitting variable-temperature conductivity data to the Nernst–Einstein relation.⁴¹ The resulting values varied from 0.11 eV to 0.19 eV, which is within in the range of other fast ion conductors and MOF electrolytes.^{16,17,41} Ionic conductivity was found to have little dependence on the amount of solvent included in the pellet. This was evidenced by the conductivity typically increasing by less than 10–15% after saturating pressed pellets with excess triglyme, which presumably decreases contact impedance throughout the pellet. Interestingly, the materials reported here with conductivities on the order of 0.1 mS cm^{-1} maybe compared to polymer gels with similar solvent content. These MOF electrolytes are approximately 45–55 wt% solvent, as shown in **Figure S2.3** and **S2.4** by thermogravimetric analysis. Polymer gel electrolytes with comparable solvent content have demonstrated similar conductivities for $\text{Mg}(\text{TFSI})_2$.⁴² This is in spite of the fact that the pores in polymer gels are typically one or two orders of magnitude larger than the nanometer-scale pores of the MOF electrolytes discussed here, attesting to the advantages of using a well-defined and ordered pore structure for charge transport. MOFs may also double as mechanically robust

separators, and given the radically different methods by which MOFs are synthesized, new methods of cell construction and design may also be of technological interest.

2.2.6 Analysis of magnesium deposition by ac impedance spectroscopy.

Finally, the reversibility of magnesium deposition was probed by ac impedance spectroscopy in a symmetric, two electrode Mg|Mg(OPhCF₃)₂ · Mg(TFSI)₂·2|Mg cell. Shown in **Figure 2.4**, the high frequency feature matches the expected ionic conductivity through the bulk electrolyte. The multiple low frequency

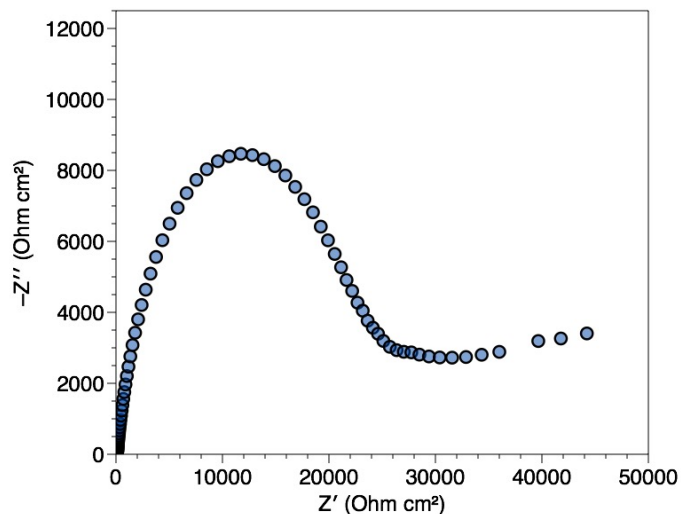


Figure 2.4. Nyquist plot of a Mg|Mg(OPhCF₃)₂ · Mg(TFSI)₂·2|Mg cell from 1 MHz to 0.01 Hz.

features, down to 0.01 Hz are tentatively assigned as charge transfer resistances for Mg deposition/dissolution. While the area normalized resistance is rather high and still capacitive at low frequency, high charge transfer resistances are commonly observed even at elevated temperatures for magnesium electrodes. In addition to the normally invoked passivation issues with magnesium electrolytes,³⁶ these solid electrolytes may display large contact resistances. That is, unlike the alkali metals, magnesium is very stiff and making a smooth homogenous contact with rough polycrystalline pellets is difficult, and could cause an overestimation of the charge transfer resistance. Variable temperature measurements indicated an Arrhenius temperature dependence with an activation energy of 0.43 eV significantly higher than any of the bulk ionic conductivities measured and more consistent with an electrochemical reaction.

2.3 Conclusions

A series of MOF-based magnesium electrolytes were prepared and their ionic conductivities assessed by AC impedance spectroscopy. By increasing pore size and tuning the anion basicity of guest electrolyte salts, conductivity values were found to vary over four orders of magnitude, and reaching values as high as 0.25 mS cm⁻¹. These frameworks can be considered rigid solid-state electrolyte alternatives to state-of-the-art gel electrolyte systems and may be of particular interest for developing new methods of cell construction and design for magnesium batteries. Although here only the pore size and the structure of the guest salt were varied, particle morphology, crystallite size, solvent polarity, and framework topology, amongst other parameters, are also expected to have a significant impact on the charge transport properties MOF electrolytes. Future work will focus on evaluating the performance of the new electrolytes in full electrochemical cells—importantly, preliminary results already show these materials to be stable against solid magnesium electrodes without passivation. We also seek to further improve the ionic conductivity and develop new methods for preparing solvent-free MOF electrolytes.

2.4 Experimental methods

2.4.1 General protocols. All reagents and solvents were commercially available and used without further purification. Powder X-ray diffraction data were collected using Cu K α ($\lambda = 1.5406 \text{ \AA}$) radiation source on a Bruker D8 Advance diffractometer. SEM was performed at the University of California Robert D. Ogg Electron Microscope Lab on a Hitachi S-5000 SEM.

2.4.2 Elemental analysis. Elemental analysis of carbon, hydrogen, and nitrogen and sulfur were obtained from the Microanalytical Laboratory of the University of California, Berkeley. Because of solvent volatility the elemental analysis often fit poorly with the data provided by ^1H NMR analysis; thus, stoichiometry determined from elemental analysis was determined by fitting $\text{Mg}(\text{TFSI})_2$ to the sulfur content, and then the content of triglyme was left as a free variable to fit carbon and hydrogen. Elemental analysis was further complicated since trace amounts of formate and dimethyl amine were observable by ^1H NMR believed to be charge balancing defect sites within $\text{Mg}_2(\text{dobdc})$ and $\text{Mg}_2(\text{dobpdc})$. In all cases the triglyme content was found to be less than what was determined from TGA or NMR as was expected.

2.4.3 Langmuir surface area measurements. Langmuir surface areas were measured by a volumetric method using a Micromeritics ASAP2020 instrument. A sample was transferred in an N_2 -filled glovebox to a pre-weighed analysis tube, capped with a transeal, evacuated and heated to $180 \text{ }^\circ\text{C}$ at $0.5 \text{ }^\circ\text{C}$ per minute until pressure stabilized at $11 \text{ }\mu\text{bar}$. N_2 isotherms at 77 K were measured in liquid nitrogen using UHP-grade gas sources.

2.4.4 Thermogravimetric analysis. TGA data were collected using a TA Instruments TGA Q5000. Linear temperature scans at $5 \text{ }^\circ\text{C}/\text{min}$ were completed under N_2 flow from room temperature to $300 \text{ }^\circ\text{C}$. At $300 \text{ }^\circ\text{C}$ the sample purge was switched to O_2 and the temperature ramp was continued to $600 \text{ }^\circ\text{C}$. The observed mass losses are given in **Figures S2.3** and **S2.4**.

2.4.5 Pellet preparation for ac impedance measurements. In an argon filled glove box, the powder electrolyte was dispensed into a Garolite spacer, inner diameter of 0.388 cm , $125 \text{ }\mu\text{m}$ in thickness, and was sandwiched between two polypropylene sheets. The loaded spacer was pressed between two stainless steel dyes polished to a mirror finish with a hydraulic press to a load of approximately $7,500 \text{ lbs}$. Sample thickness was measured following ac impedance data collection with a Mitutoyo Absolute thickness gauge accurate to $2 \text{ }\mu\text{m}$.

2.4.6 AC impedance measurements. Sample conductivity was characterized using a thermostatted custom-built test cell with stainless steel blocking electrodes polished to a mirror finish. With a Solartron 1260 frequency response analyzer, a Solartron 1296 dielectric interface and the SMART (v3.0.1) data acquisition and analysis program, ionic conductivity was characterized by ac impedance spectroscopy. All data was collected at 100 mV AC , a frequency sweep from 1 MHz to 100 or 1Hz , and a 1s integration time sampling 25 points per decade. The bulk conductivity was determined

from the right-hand minima of the semicircle observed at high frequency, R_{bulk} . The low frequency tail in the complex impedance plots was attributed cell polarization.

$$\sigma_{bulk} = \frac{l}{R_{bulk}A} \quad (2.1)$$

Bulk conductivity, in $S\text{ cm}^{-1}$, was calculated from **Equation 2.1**, where σ_{bulk} is the bulk conductivity, R_{bulk} is the real component at the right hand minima, l the sample thickness and A the sample area in contact with the electrode. Pseudo-activation energies were determined from the Nernst-Einstein relation, Equation 2.⁴¹

$$\sigma_{bulk} = \frac{\sigma_0}{T} e^{-\frac{E_A}{RT}} \quad (2.2)$$

In **Equation 2.2**, σ_0 is a pre-exponential factor, T is the temperature, E_A the pseudoactivation energy and R the ideal gas constant. The frequency response observed in the materials reported here mirrors that previously reported for lithium electrolytes in the same system.

2.4.7 Synthesis of Mg₂(dobdc). Mg₂(2,5-dioxidobenzene-1,4-dicarboxylate) was prepared by a method similar to that reported previously by Caskey et. al.²⁶ Since product formation was observed to initiate by nucleation on borosilicate glass, upon scaling it was necessary to maintain a glass surface area to volume ratio greater than or equal to that reported. To four 1-L borosilicate glass jars filled with 4-ml borosilicate glass scintillation vials, 5.858 g (29.60 mmol) of 2,5-dihydroxybenzene-1,4-dicarboxylic acid and 23.99 g (77.27 mmol) of Mg(NO₃)₂ · 9H₂O dissolved in 2600 mL of 15:1:1 DMF:EtOH:H₂O was added. The screw cap jars were sealed and heated to 120 °C for eight hours in a convection oven. Product was removed by sonication, then collected and dried via vacuum filtration. The dark orange powder was soaked in DMF at 100 °C for 4 days replacing the solution twice a day, then washed for 5 days in MeOH by soxhlet extraction. The powder was dried and heated to 180 °C at 10 μbar for 4 days. Langmuir surface area: 1845 m² g⁻¹. IR: 1577 (s), 1423 (s), 1371 (m), 1211 (s), 1120 (w), 1018 (w), 912 (w), 891 (m), 829 (s), 819 (s), 634 (w), 581 (m), 487 (w). PXRD is given in **Figure S2.1** and TGA in **Figure S2.3**. Proton NMR showed approximately 8 mol% formate and 3 mol% dimethylamine present in the material which are likely charge balancing ions at defect sites. Low concentrations of NMR inactive nitrates may also be present and also account for the small amount of excess nitrogen found by elemental analysis.

2.4.8 Mg₂(dobdc) ⊂ [0.05Mg(4-methylphenolate)₂ · 1.5triglyme]. Cresol (1.30 g, 12.0 mmol) was dissolved in 20 mL of anhydrous triethyleneglycoldimethylether (triglyme) in a flame dried 100-mL round bottom flask under N₂ flow. To the stirring solution, 8.57 mL (6.00 mmol) of 0.7 M magnesium bis(diisopropyl)amide in THF was added dropwise. After stirring for 2 hours the THF and diisopropylamine were removed by vacuum distillation. In a nitrogen filled glovebag, the resulting solution was transferred to a dry scintillation vial containing about 100 mg (0.5 mmol) of desolvated Mg₂(dobdc), sealed and heated to 80 °C for 7 days. The solution was decanted, replaced with 20 mL of anhydrous triglyme and sonicated. This was repeated two additional times. The

yellow-orange material was then filtered and dried by vacuum filtration affording a free-flowing powder. All electrolyte materials were washed similarly. The material's composition was determined by proton NMR. That is, 15 mg of the material was dissolved in a solution of 1 mL DMSO- d_6 and 20 μ L of 35 wt% DCl in D_2O and all other samples NMR samples were prepared similarly, **Figure S2.5**. PXRD, TGA and room temperature ac impedance data are given in the supporting figures. Elemental analysis: Calculated for $[Mg_2(dobdc) \cdot 0.05Mg(4\text{-methylphenolate})_2 \cdot 0.98\text{triglyme} \cdot 0.01\text{dimethylamine}]$ C: 47.3%, H: 5.52%, N: 0.14%; Found C: $45.2 \pm 0.3\%$, H: $5.70 \pm 0.04\%$, N: $0.16 \pm 0.1\%$.

2.4.9 $Mg_2(dobdc) \subset [0.07Mg(\text{phenolate})_2 \cdot 1.5\text{triglyme}]$. Phenol (1.130 g, 12.00 mmol) was dissolved in 20 mL of anhydrous triglyme in a flame dried 100-mL round bottom flask under N_2 flow. To the stirring solution, 8.57 mL (6.00 mmol) of 0.7 M magnesium bis(diisopropyl)amide in THF was added dropwise. After stirring for 2 hours the THF and diisopropylamine were removed by vacuum distillation. In a nitrogen filled glovebag, the resulting solution was transferred to a dry scintillation vial containing about 100 mg (0.5 mmol) of desolvated $Mg_2(dobdc)$, sealed and heated to 80 $^\circ C$ for 7 days. The dark yellow-orange material was collected, washed with 60 mL of anhydrous triglyme and dried by vacuum filtration affording a free-flowing powder. The material's composition was determined by proton NMR. PXRD and TGA and room temperature ac impedance data are also given in the supporting figures. Elemental analysis: Calculated for $[Mg_2(dobdc) \cdot 0.07Mg(\text{phenolate})_2 \cdot 0.96\text{triglyme} \cdot 0.01\text{dimethylamine}]$ C: 47.4%, H: 5.43%, N: 0.155%; Found: C: $45.2 \pm 0.3\%$, H: $5.70 \pm 0.04\%$, N: $0.155 \pm 0.005\%$.

2.4.10 $Mg_2(dobdc) \subset [0.06Mg(\text{bis}(\text{trifluoromethanesulfonyl})\text{imide})_2 \cdot 1.4\text{triglyme}]$. About 100 mg (0.5 mmol) of desolvated $Mg_2(dobdc)$ was soaked for 7 days in 20 mL of a 0.43 M solution of $Mg(\text{bis}(\text{trifluoromethanesulfonyl})\text{imide})_2$, $Mg(\text{TFSI})_2$, in triglyme at room temperature then collected, washed with 60 mL of triglyme and dried by vacuum filtration affording a dark orange free flowing powder. The TFSI^- content was estimated by elemental analysis and the amount of triglyme was determined by proton NMR. The NMR sample was prepared by dissolving about 15 mg of the material in a solution of 1 mL DMSO- d_6 and 20 μ L of 35 wt% DCl in D_2O , **Figure S2.5**. PXRD and TGA and room temperature ac impedance data are given in the supporting figures. Elemental analysis: Calculated for $[Mg_2(dobdc) \cdot 0.06Mg(\text{TFSI})_2 \cdot 1.43\text{triglyme} \cdot 0.01\text{dimethylamine}]$ C: 47.0%, H: 6.21%, N: 0.26%, S: 0.55%; Found: C: $46.31 \pm 0.04\%$, H: $6.32 \pm 0.01\%$, N: $0.2 \pm 0.0\%$, S: $0.55 \pm 0.0\%$.

2.4.11 $Mg_2(dobdc) \subset [0.39Mg(4\text{-trifluoromethylphenolate})_2 \cdot 6.0\text{triglyme}]$. 4-trifluoromethylphenol (1.94 g, 12.0 mmol) was dissolved in 20 mL of anhydrous triglyme in a flame dried 100-mL round bottom flask under N_2 flow. To the stirring solution, 8.57 mL (6.00 mmol) of 0.7 M magnesium bis(diisopropyl)amide in THF was added dropwise. After stirring for 2 hours the THF and diisopropylamine were removed by vacuum distillation. In a nitrogen-filled glovebag, the resulting solution was transferred to a dry scintillation vial containing about 100 mg (0.5 mmol) of

desolvated $\text{Mg}_2(\text{dobdc})$, sealed and heated to 80 °C for 7 days. The dark red-orange material was collected, washed with 60 mL of anhydrous triglyme and dried by vacuum filtration affording a free-flowing powder. The material's composition was determined by proton NMR. The larger amount of solvent present in this sample was attributed to absorption onto the significantly larger number of magnesium sites that may coordinate triglyme. As a control, conductivity was also measured on all samples once saturated with anhydrous triglyme. In every case only a small change in conductivity was observed. Conductivity and NMR of this sample are given in the supporting figures below.

2.4.12 $\text{Mg}_2(\text{dobdc}) \subset [0.31\text{Mg}(4\text{-trifluoromethylphenolate})_2 \cdot 0.30\text{Mg}(\text{TFSI})_2 \cdot 2.4\text{triglyme}]$.

The material described in **Section 2.4.11** was soaked for 12 hours in 20 mL of a 0.43 M solution of $\text{Mg}(\text{TFSI})_2$ in triglyme at room temperature then collected, washed with 60 mL of triglyme and dried by vacuum filtration affording a dark red-orange free flowing powder. The amount of triglyme and 4-trifluoromethylphenolate in the material was determined by proton NMR and the TFSI^- content was estimated from elemental analysis. PXRD and TGA and room temperature ac impedance data are given in the supporting figures. Elemental analysis: Calculated for $[\text{Mg}_2(\text{dobdc}) \cdot 0.31\text{Mg}(4\text{-trifluoromethylphenolate})_2 \cdot 0.30\text{Mg}(\text{TFSI})_2 \cdot 1.82\text{triglyme} \cdot 0.01\text{dimethylamine}]$ C: 45.3%, H: 5.90%, N: 0.56%, S 1.93%; Found: C: $43.46 \pm 0.05\%$, H: $6.24 \pm 0.11\%$, N: $0.63 \pm 0.03\%$, S: $1.92 \pm 0.01\%$.

2.4.13 Synthesis of $\text{Mg}_2(\text{dobpdc})$. 4,4'-Dihydroxybiphenyl-2,2'-dicarboxylic acid (0.962 g, 3.51 mmol) and $\text{Mg}(\text{NO}_3)_2 \cdot 9\text{H}_2\text{O}$ (2.249 g, 7.24 mmol) were dissolved in 19 mL MeOH and 16 mL DMF then distributed across three 20-mL screw-cap vials. The solution was heated to 120 °C for 24 hours. The phase was confirmed by PXRD and the material was desolvated as reported previously.²⁸

2.4.14 $\text{Mg}_2(\text{dobpdc}) \subset [0.22\text{Mg}(\text{TFSI})_2 \cdot 3.3\text{triglyme}]$. About 125 mg (0.4 mmol) of desolvated $\text{Mg}_2(\text{dobpdc})$ was soaked for 7 days in a 0.43 M solution of $\text{Mg}(\text{TFSI})_2$ in triglyme at room temperature then collected, washed with 30 mL of triglyme and dried by vacuum filtration affording a white free-flowing powder. The TFSI^- content was estimated by elemental analysis and the amount of triglyme by proton NMR. PXRD and TGA and room temperature ac impedance data are given in the supporting figures below. Elemental analysis: Calculated for $[\text{Mg}_2(\text{dobpdc}) \cdot 0.22\text{Mg}(\text{TFSI})_2 \cdot 2.78\text{triglyme}]$ C: 51.1%, 7.56%, N: 0.26%, S: 1.19%; Found: C: $51.4 \pm 0.2\%$, H: $7.42 \pm 0.07\%$, N: $0.23 \pm 0.03\%$, S: $1.19 \pm 0.11\%$.

2.4.15 $\text{Mg}_2(\text{dobpdc}) \subset [0.31\text{Mg}(4\text{-trifluoromethylphenolate})_2 \cdot 3.8\text{triglyme}]$. 4-trifluoromethylphenol (1.94 g, 12.0 mmol) was dissolved in 20 mL of anhydrous triglyme in a flame dried 100-mL round bottom flask under N_2 flow. To the stirring solution, 8.57 mL (6.00 mmol) of 0.7 M magnesium bis(diisopropyl)amide in THF was added dropwise. After stirring for 2 hours the THF and diisopropylamine were removed by vacuum distillation. In a nitrogen filled glovebag, the resulting solution was transferred to a dry scintillation vial containing about 125 mg (0.4 mmol) of desolvated $\text{Mg}_2(\text{dobpdc})$, sealed and heated to 80 °C for 7 days. The light red material was collected,

washed with 30 mL of anhydrous triglyme and dried by vacuum filtration affording a free-flowing powder. The material's composition was determined by proton NMR. PXRD and TGA and room temperature ac impedance data are given in the supporting figures below. Elemental analysis: Calculated for $[\text{Mg}_2(\text{dobpdc}) \cdot 0.31\text{Mg}(4\text{-trifluoromethylphenolate})_2 \cdot 2.64 \text{ triglyme} \cdot 0.05 \text{ dimethylamine}]$ C:52.19%, H:7.57%, N: 0.413%; Found: C: $53.42 \pm 0.14\%$, H: $7.38 \pm 0.52\%$, N: $0.445 \pm 0.03\%$.

2.4.16 $\text{Mg}_2(\text{dobpdc}) \subset [0.21\text{Mg}(4\text{-trifluoromethylphenolate})_2 \cdot 0.46\text{Mg}(\text{TFSI})_2 \cdot 4.8\text{triglyme}]$. The material described above was soaked for 12 hours in a 0.43 M solution of $\text{Mg}(\text{TFSI})_2$ in triglyme at room temperature then collected, washed with 20 mL of triglyme and dried by vacuum filtration affording a light red free-flowing powder. The amount of triglyme and 4-trifluoromethylphenolate in the material was determined by proton NMR and the TFSI^- content was determined by sulfur analysis. PXRD and TGA and room temperature ac impedance data are given in the supporting figures below. Elemental analysis: Calculated for $[\text{Mg}_2(\text{dobpdc}) \cdot 0.21 \text{ Mg}(4\text{-trifluoromethylphenolate})_2 \cdot 0.46\text{Mg}(\text{TFSI})_2 \cdot 3.07\text{triglyme}]$ C: 49.0%, H: 7.13%, N: 0.60%, S: 2.1%; Found: C: $49.4 \pm 0.4\%$, H: $7.10 \pm 0.14\%$, N: $0.56 \pm 0.05\%$, S: $2.1 \pm 0.3\%$.

2.5 Acknowledgements

Much of the work in this chapter was published with co-authors B.M. Wiers, R. Ameloot, and J. R. Long who helped with experiment design. This research was supported by the United States Department of Energy, Energy Efficiency and Renewable Energy, Hydrogen and Fuel Cell Program. R.A. thanks the Research Foundation Flanders (FWO – Vlaanderen) for a postdoctoral fellowship. We thank Mr. David Gygi for experimental assistance and Prof. Nitash Balsara for experimental assistance and helpful discussion.

2.6 Supporting figures and tables

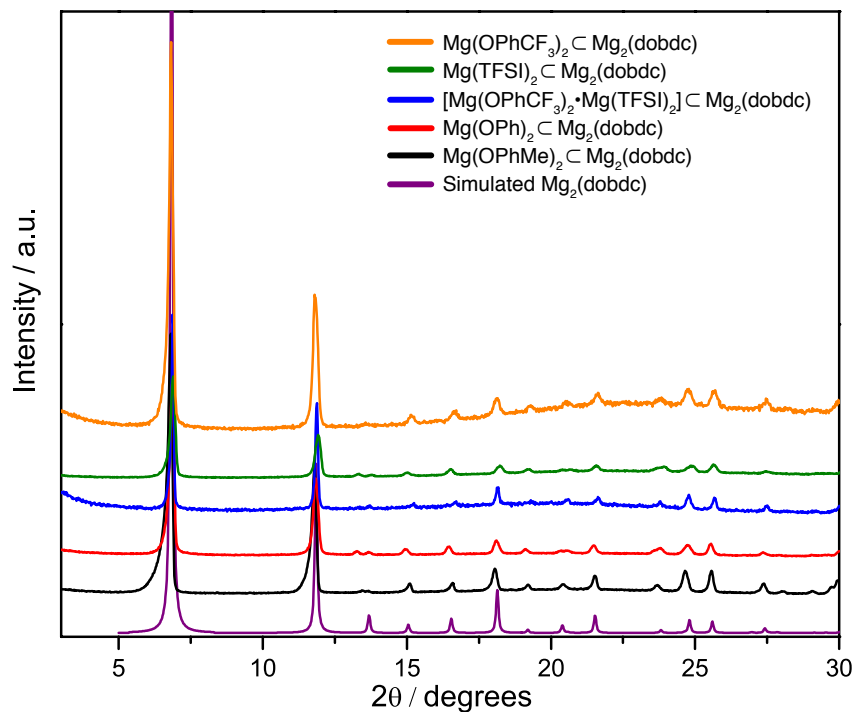


Figure S2.1. PXRD for materials containing $Mg_2(dobdc)$

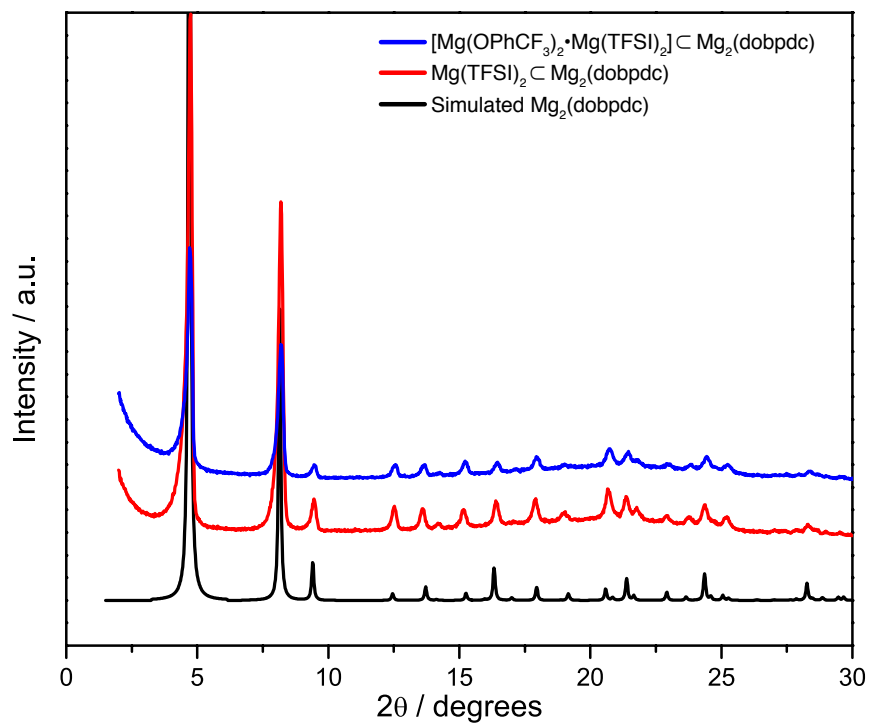


Figure S2.2 PXRD for materials containing $Mg_2(dobpdc)$

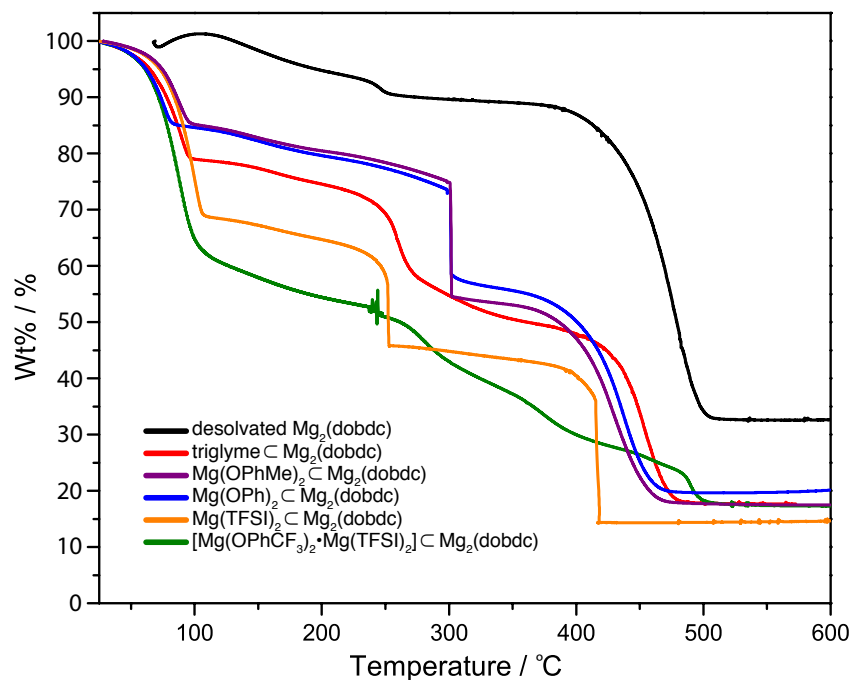


Figure S2.3. TGA for materials containing $Mg_2(dobdc)$

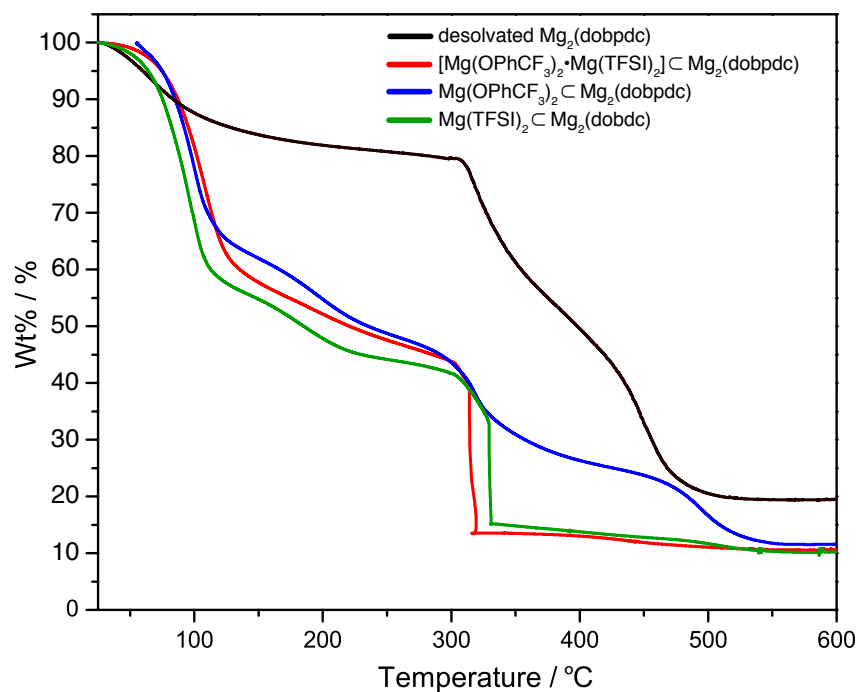


Figure S2.4. TGA for materials containing $Mg_2(dobpdc)$

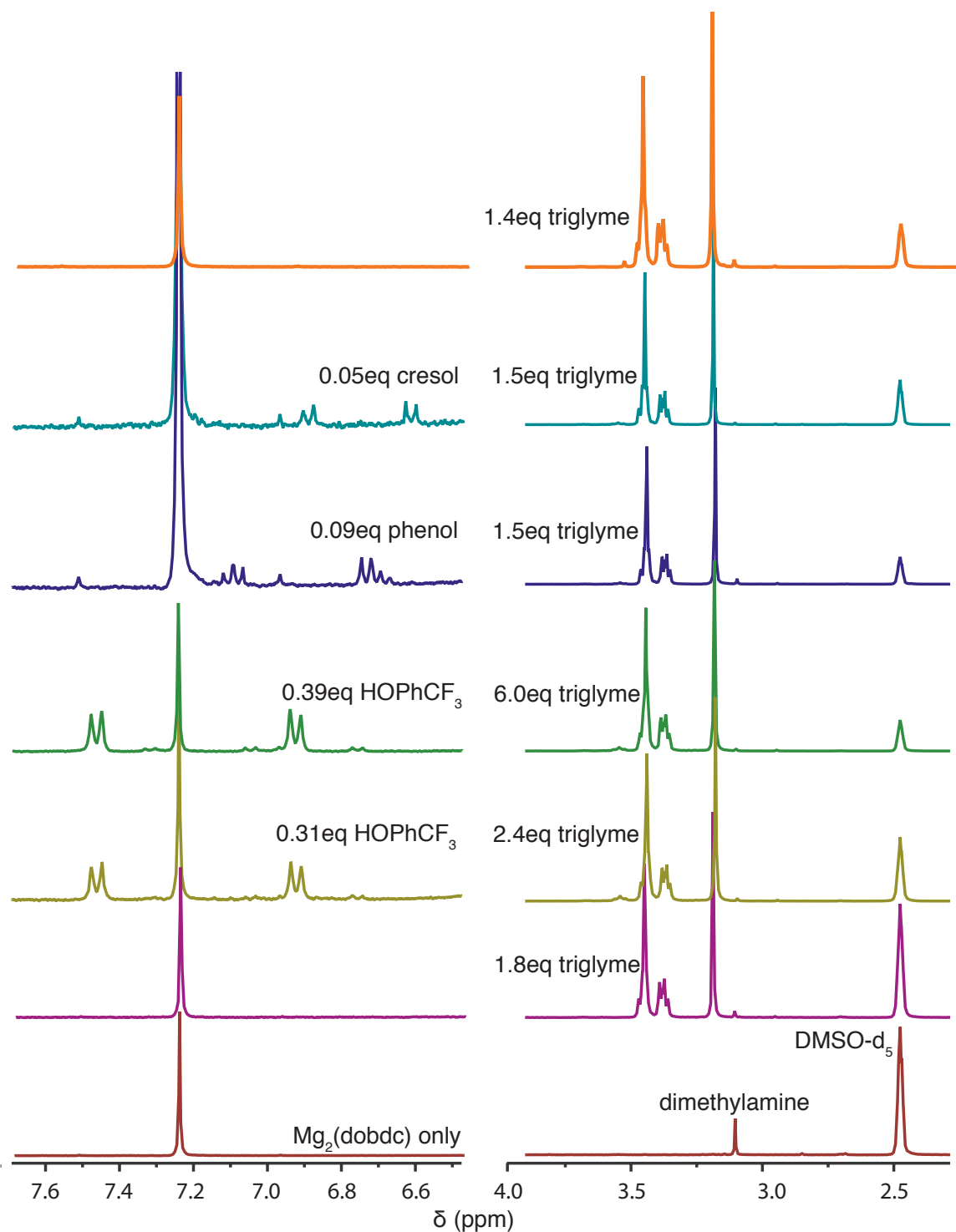


Figure S2.5. Selected regions of ^1H NMR (300 MHz) for materials containing $\text{Mg}_2(\text{dobdc})$. From the top: $\text{Mg}_2(\text{dobdc}) \cdot \text{Mg}(\text{TFSI})_2 \cdot \text{triglyme}$, $\text{Mg}_2(\text{dobdc}) \cdot \text{Mg}(\text{OPhMe})_2 \cdot \text{triglyme}$, $\text{Mg}_2(\text{dobdc}) \cdot \text{Mg}(\text{OPh})_2 \cdot \text{triglyme}$, $\text{Mg}_2(\text{dobdc}) \cdot \text{Mg}(\text{OPhCF}_3)_2 \cdot \text{triglyme}$, $\text{Mg}_2(\text{dobdc}) \cdot \text{Mg}(\text{OPhCF}_3)_2 \cdot \text{Mg}(\text{TFSI})_2 \cdot \text{triglyme}$, $\text{Mg}_2(\text{dobdc}) \cdot \text{triglyme}$, and desolvated $\text{Mg}_2(\text{dobdc})$

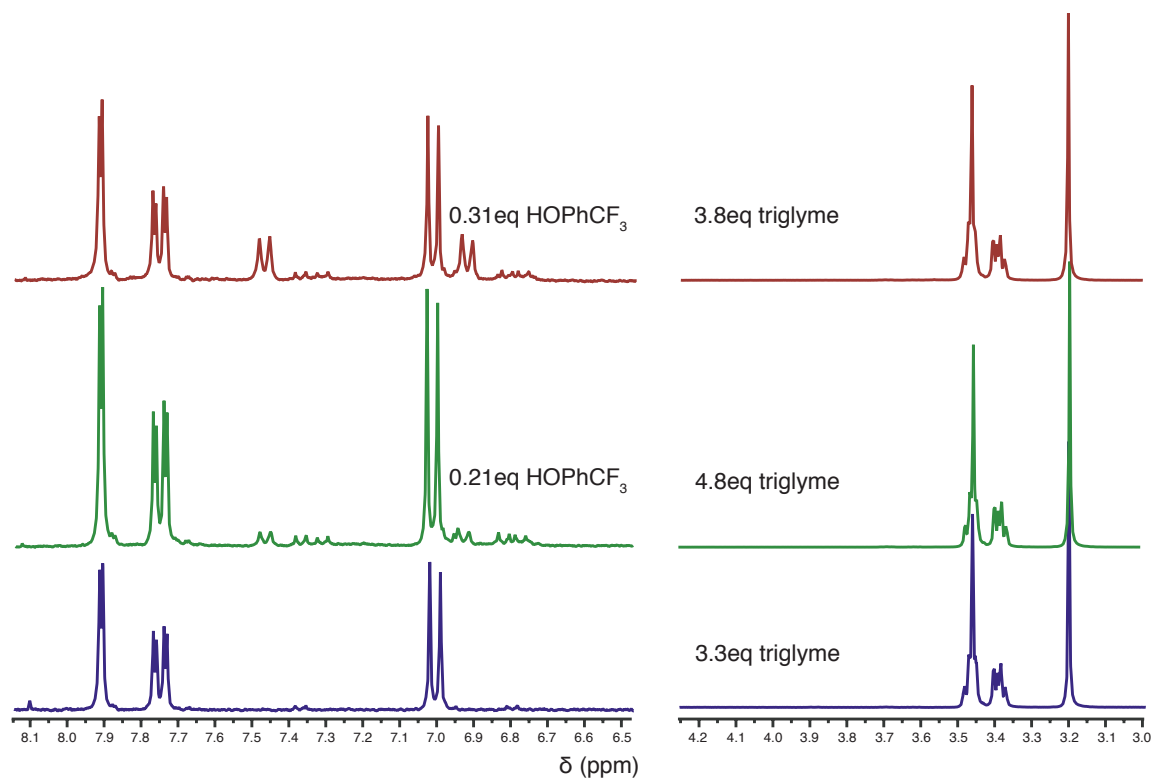


Figure S2.6. Selected regions of ^1H NMR (300 MHz) for materials containing $\text{Mg}_2(\text{dobpdc})$. From the top: $\text{Mg}(\text{OPhCF}_3)_2 \cdot \text{triglyme}$, $\text{Mg}(\text{TFSI})_2 \cdot \text{triglyme}$, and $\text{Mg}(\text{OPhCF}_3)_2 \cdot \text{Mg}(\text{TFSI})_2 \cdot \text{triglyme}$

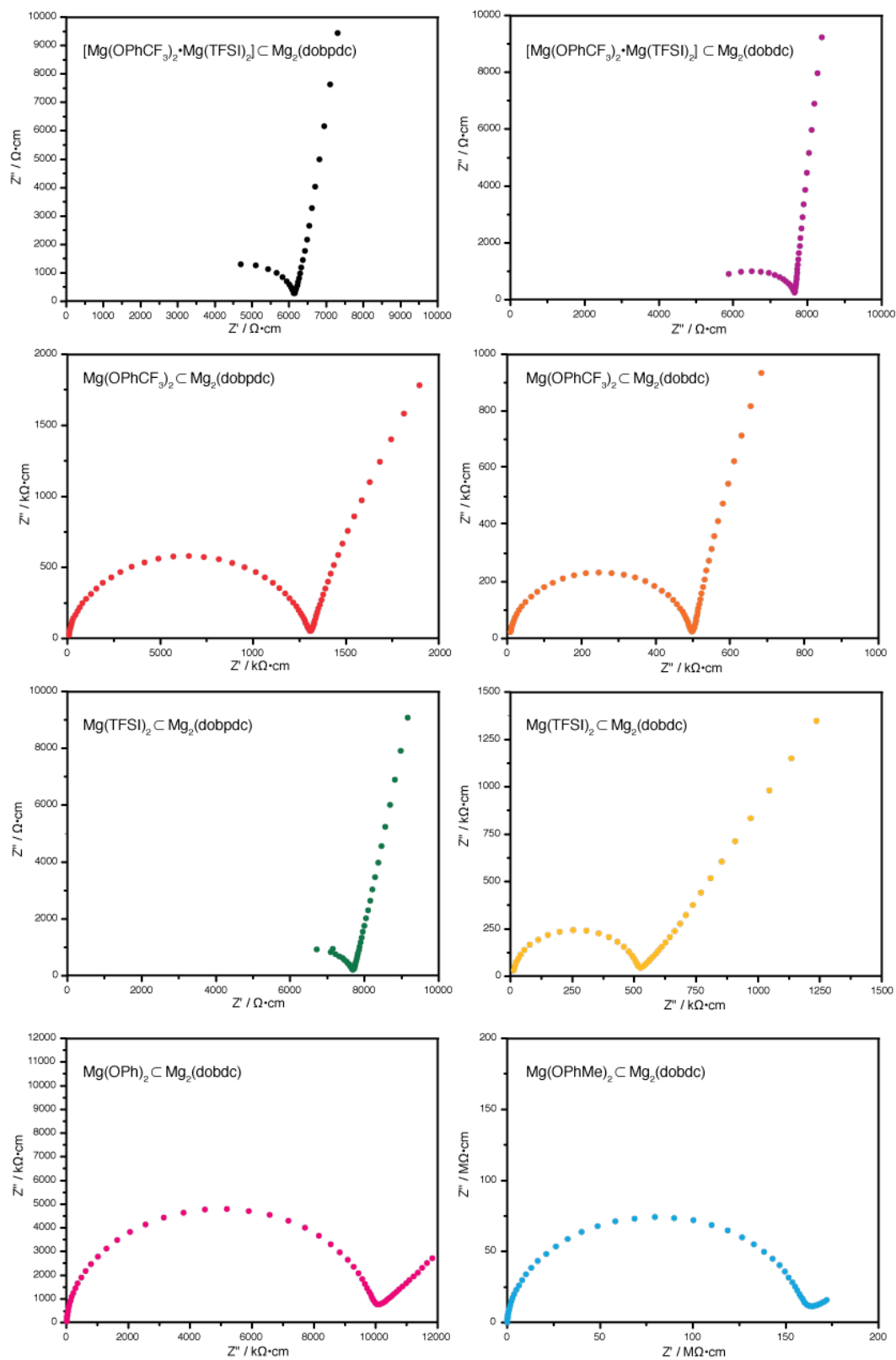


Figure S2.7. Room temperature Nyquist plots for the materials given in Table 2.1.

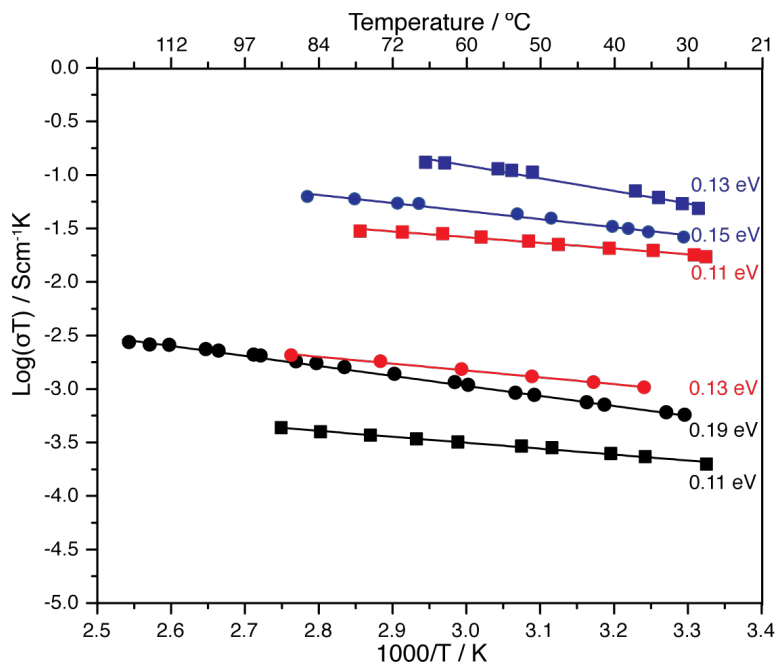


Figure S2.8. Temperature dependence on conductivity linearized using equation 2, pseudo-activation energies were determined from the slope. The host material $\text{Mg}_2(\text{dobdc})$ is depicted as circles and $\text{Mg}_2(\text{dobpdc})$ as squares. The guest species $\text{Mg}(\text{OPhCF}_3)_2$ is shown in black, $\text{Mg}(\text{TFSI})_2$ in red, and the materials containing both magnesium salts as guests are given in blue.

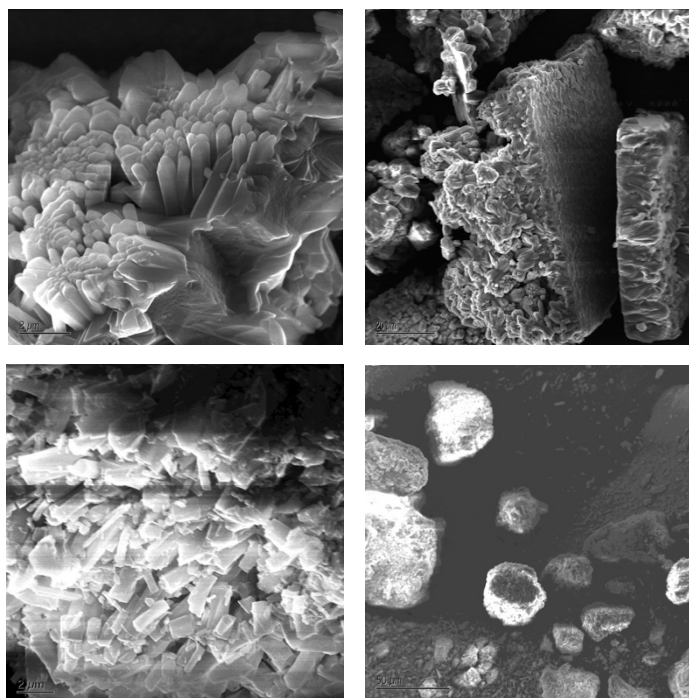


Figure S2.9. SEM images describing morphology of $\text{Mg}_2(\text{dobdc})$ (top two images) and $\text{Mg}_2(\text{dobpdc})$ (bottom two images). Scale bars read 2 μm (top left) 20 μm (top right), 2 μm bottom left, and 50 μm (bottom right).

2.7 References

- (1) “The pervasive chemistry of metal–organic frameworks” Long, J. R. and Yaghi, O. M. *Chem. Soc. Rev.* **2009**, *38*, 1213–1214.
- (2) “The chemistry and applications of metal-organic frameworks” Furukawa, H.; Cordova, K. E.; O’Keeffe, M.; and Yaghi, O. M. *Science* **2013**, *341*, 1230444.
- (3) “Systematic design of pore size and functionality in isorecticular MOFs and their application in methane storage” Eddaoudi, M.; Kim, J.; Rosi, N.; Vodak, D.; Wachter, J.; O’Keeffe, M.; and Yaghi, O. M. *Science* **2002**, *295*, 469–472.
- (4) “Hydrogen storage in microporous metal-organic frameworks” Rosi, N. L.; Eckert, J.; Eddaoudi, M.; Vodak, D. T.; Kim, J.; O’Keeffe, M.; and Yaghi, O. M. *Science* **2003**, *300*, 1127–1129.
- (5) “Postsynthetic modification of metal–organic frameworks” Wang, Z. and Cohen, S. M. *Chem. Soc. Rev.* **2009**, *38*, 1315–1329.
- (6) “Postsynthetic modification of metal–organic frameworks—a progress report” Tanabe, K. K. and Cohen, S. M. *Chem. Soc. Rev.* **2011**, *40*, 498–519.
- (7) “NMR studies on the diffusion of hydrocarbons on the metal-organic framework material MOF-5” Stallmach, F.; Gröger, S.; Künzel, V.; Kärger, J.; Yaghi, O. M.; Hesse, M.; and Müller, U. *Angew. Chem. Int. Edit. Engl.* **2006**, *45*, 2123–2126.
- (8) “Inclusion and dynamics of a polymer–Li salt complex in coordination nanochannels” Yanai, N.; Uemura, T.; Horike, S.; Shimomura, S.; and Kitagawa, S. *Chem. Commun.* **2011**, *47*, 1722–1724.
- (9) “Ionic liquid transported into metal–organic frameworks” Fujie, K. and Kitagawa, H. *Coord. Chem. Rev.* **2016**, *307*, 382–390.
- (10) “Lithium ion diffusion in a metal–organic framework mediated by an ionic liquid” Fujie, K.; Ikeda, R.; Otsubo, K.; Yamada, T.; and Kitagawa, H. *Chem. Mater.* **2015**, *27*, 7355–7361.
- (11) “Ion conductivity and transport by porous coordination polymers and metal-organic frameworks.” Horike, S.; Umeyama, D.; and Kitagawa, S. *Acc. Chem. Res.* **2013**, *46*, 2376–2384.
- (12) “Metal organic frameworks for electrochemical applications” Morozan, A. and Jaouen, F. *Energy Environ. Sci.* **2012**, *5*, 9269–9290.
- (13) “Proton conduction in metal–organic frameworks and related modularly built porous solids” Yoon, M.; Suh, K.; and Natarajan, S. *Angew. Chem. Int. Edit. Engl.* **2013**, *52*, 2688–2700.
- (14) “Anhydrous proton conduction at 150 °C in a crystalline metal–organic framework” Hurd, J. A.; Vaidhyanathan, R.; Thangadurai, V.; Ratcliffe, C. I.; Moudrakovski, I. L.; and Shimizu, G. K. H. *Nat. Chem.* **2009**, *1*, 705–710.
- (15) “One-dimensional imidazole aggregate in aluminium porous coordination polymers with high proton conductivity” Bureekaew, S.; Horike, S.; Higuchi, M.; Mizuno, M.; Kawamura, T.; Tanaka, D.; Yanai, N.; and Kitagawa, S. *Nat. Mater.* **2009**, *8*, 831–836.
- (16) “A solid lithium electrolyte via addition of lithium isopropoxide to a metal–organic framework with open metal sites” Wiers, B. M.; Foo, M.-L.; Balsara, N. P.; and Long, J. R. *J.*

- Am. Chem. Soc.* **2011**, *133*, 14522–14525.
- (17) “Ionic conductivity in the metal-organic framework UiO-66 by dehydration and insertion of lithium *tert*-butoxide” Ameloot, R.; Aubrey, M.; Wiers, B. M.; Gómora-Figueroa, A. P.; Patel, S. N.; Balsara, N. P.; and Long, J. R. *Chem. Eur. J.* **2013**, *19*, 5533–5536.
- (18) “Scandium/alkaline metal-organic frameworks: adsorptive properties and ionic conductivity” Cepeda, J.; Pérez-Yáñez, S.; Beobide, G.; Castillo, O.; Goikolea, E.; Aguesse, F.; Garrido, L.; Luque, A.; and Wright, P. A. *Chem. Mater.* **2016**, *28*, 2519–2528.
- (19) “Solid lithium electrolytes based on an organic molecular porous solid” Park, J. H.; Suh, K.; Rohman, M. R.; Hwang, W.; Yoon, M.; and Kim, K. *Chem. Commun.* **2015**, *51*, 9313–9316.
- (20) “Transport properties of the mineral vermiculite” Whittingham, M. S. *Solid State Ionics* **1989**, *32-33*, 344–349.
- (21) “Conductivity of mono- and divalent cations in the microporous zincosilicate VPI-9” McKeen, J. C. and Davis, M. E. *J. Phys. Chem. C* **2009**, *113*, 9870–9877.
- (22) “High ion conductivity in MgHf(WO₄)₃ solids with ordered structure: 1-D alignments of Mg²⁺ and Hf⁴⁺ ions” Omote, A.; Yotsuhashi, S.; Zenitani, Y.; and Yamada, Y. *J. Am. Ceram. Soc.* **2011**, *94*, 2285–2288.
- (23) “Ionic conductance of polymeric electrolytes consisting of magnesium salts dissolved in cross-linked polymer matrix with linear polyether” Yoshimoto, N.; Tomonaga, Y.; Ishikawa, M.; and Morita, M. *Electrochim. Acta* **2001**, *46*, 1195–1200.
- (24) “A novel inorganic solid state ion conductor for rechargeable Mg batteries” Higashi, S.; Miwa, K.; Aoki, M.; and Takechi, K. *Chem. Commun.* **2014**, *50*, 1320–1322.
- (25) “Magnesium ion dynamics in Mg(BH₄)_{2(1-x)}X_{2x} (X = Cl or AlH₄) from first-principles molecular dynamics simulations” Ikeshoji, T.; Tsuchida, E.; Takagi, S.; Matsuo, M.; and Orimo, S.-I. *RSC Adv.* **2014**, *4*, *3*, 1366–1370.
- (26) “Dramatic tuning of carbon dioxide uptake via metal substitution in a coordination polymer with cylindrical pores” Caskey, S. R.; Wong-Foy, A. G.; and Matzger, A. J. *J. Am. Chem. Soc.* **2008**, *130*, 10870–10871.
- (27) “Cooperative insertion of CO₂ in diamine-appended metal-organic frameworks” McDonald, T. M.; Mason, J. A.; Kong, X.; Bloch, E. D.; Gygi, D.; Dani, A.; Crocellà, V.; Giordanino, F.; Odoh, S. O.; Drisdell, W. S.; Vlasisavljevich, B.; Dzubak, A. L.; Poloni, R.; Schnell, S. K.; Planas, N.; Lee, K.; Pascal, T.; Wan, L. F.; Prendergast, D.; Neaton, J. B.; Smit, B.; Kortright, J. B.; Gagliardi, L.; Bordiga, S.; Reimer, J. A.; and Long, J. R. *Nature* **2015**, *519*, 303–308.
- (28) “Capture of carbon dioxide from air and flue gas in the alkylamine-appended metal-organic framework mmen-Mg₂(dobpdc)” McDonald, T. M.; Lee, W. R.; Mason, J. A.; Wiers, B. M.; Hong, C. S.; and Long, J. R. *J. Am. Chem. Soc.* **2012**, *134*, 7056–7065.
- (29) “Large-pore apertures in a series of metal-organic frameworks” Deng, H.; Grunder, S.; Cordova, K. E.; Valente, C.; Furukawa, H.; Hmadeh, M.; Gandara, F.; Whalley, A. C.; Liu, Z.; Asahina, S.; Kazumori H.; O’Keeffe M.; Terasaki O.; Stoddart J. F.; and Yaghi O. M. *Science* **2012**, *336*, 1018–1023.
- (30) “A novel electrolyte system without a grignard reagent for rechargeable magnesium batteries” Wang, F.-F.; Guo, Y. S.; Yang, J.; Nuli, Y.; and Hirano, S.-I. *Chem. Commun.* **2012**,

- 48, 10763–10765.
- (31) “Enhanced oxidative stability of non-grignard magnesium electrolytes through ligand modification” Nelson, E. G.; Kampf, J. W.; and Bartlett, B. M. *Chem. Commun.* **2014**, *50*, 5193–5195.
 - (32) “Fluorinated alkoxide-based magnesium-ion battery electrolytes that demonstrate Li-ion-battery-like high anodic stability and solution conductivity” Crowe, A. J.; Stringham, K. K.; and Bartlett, B. M. *ACS Appl. Mater. Interfaces* **2016**, *8*, 23060–23065.
 - (33) “A magnesium tetraphenylaluminate battery electrolyte exhibits a wide electrochemical potential window and reduces stainless steel corrosion” Nelson, E. G.; Brody, S. I.; Kampf, J. W.; and Bartlett, B. M. *J. Mater. Chem. A* **2014**, *2*, 18194–18198.
 - (34) “Prototype systems for rechargeable magnesium batteries” Aurbach, D.; Lu, Z.; Schechter, A.; Gofer, Y.; Gizbar, H.; Turgeman, R.; Cohen, Y.; Moshkovich, M.; and Levi, E. *Nature* **2000**, *407*, 724–727.
 - (35) “Structure and compatibility of a magnesium electrolyte with a sulphur cathode” Kim, H. S.; Arthur, T. S.; Allred, G. D.; Zajicek, J.; Newman, J. G.; Rodnyansky, A. E.; Oliver, A. G.; Boggess, W. C.; and Muldoon, J. *Nat. Commun.* **2011**, *2*, 427.
 - (36) “Electrolyte roadblocks to a magnesium rechargeable battery” Muldoon, J.; Bucur, C. B.; Oliver, A. G.; Sugimoto, T.; Matsui, M.; Kim, H. S.; Allred, G. D.; Zajicek, J.; and Kotani, Y. *Energy Environ. Sci.* **2012**, *5*, 5941–5950.
 - (37) “Electrolyte solutions for rechargeable magnesium batteries based on organomagnesium chloroaluminate complexes” Aurbach, D.; Gizbar, H.; Schechter, A.; Chusid, O.; Gottlieb, H. E.; Gofer, Y.; and Goldberg, I. *J. Electrochem. Soc.* **2002**, *149*, A115–A121.
 - (38) “Synthesis and structural study of a tetranuclear magnesium alkoxide: $[\text{Mg}_4(\text{M}_3, \eta^2\text{-OR})_2 (\mu^2, \eta^2\text{-OR})_4(\text{OR})_2]$ with $\text{OR-OCH}(\text{CH}_3)\text{CH}_2\text{OCH}_3$ ” Albaric, L.; Hovnanian, N.; Julbe, A.; Guizard, C.; Alvarez-Larena, A.; and Piniella, J. F. *Polyhedron* **1997**, *16*, 587–592.
 - (39) “Advanced batteries: materials science aspects” Huggins, R. A. *Springer Sciences and Business Media* **2010**, 1–491.
 - (40) “Electrolytes for solid-state lithium rechargeable batteries: recent advances and perspectives” Quartarone, E. and Mustarelli, P. *Chem. Soc. Rev.* **2011**, *40*, 2525–2540.
 - (41) “Physical techniques for the study of solid electrolytes” Linford, R. G. and Hackwood, S. *Chem. Rev.* **1981**, *81*, 327–364.
 - (42) “Rechargeable magnesium batteries with polymeric gel electrolytes containing magnesium salts” Yoshimoto, N.; Yakushiji, S.; Ishikawa, M.; and Morita, M. *Electrochim. Acta* **2003**, *48*, 2317–2322.

Chapter 3

Oxidative insertion of weakly coordinating anions in a metal-organic framework

3.1 Introduction

Underpinning a vast number of advanced materials, the intercalation reaction, a slipping of an ion or molecule through the galleries of a two-dimensional host lattice, and its more general three-dimensional analogue, the insertion reaction, allow the electronic properties of a host lattice to be dramatically altered.¹ In particular, reductive insertion has revolutionized rechargeable batteries. The general reaction mechanism is a simple one: a material with weakly interacting sheets, interconnected site vacancies, or tunnels accommodates a metal cation while a charge-balancing electron is transferred to the host lattice via a circuit.

Although insertion reactions are well-established for a plethora of metal cations, it is remarkably challenging to accomplish the same task with negative ions.² This difficulty is because electrochemically stable anions are large compared to metal cations; hence, their accommodation requires a much greater accessible volume. Indeed, inorganic materials that reversibly intercalate anions are rare, with the hydrotalcite structure type and graphite intercalation compounds largely making up the class.³⁻⁷ These materials are layered compounds with sheets that are easily separated. As such, the distance between the layers can increase to accommodate large guest species. In contrast, the implicit rigidity of a three-dimensional host lattice culminates in a dearth of topotactic anion insertion materials.

Of particular interest with respect to energy storage is the possible insertion of anions stable at strongly oxidizing potentials, such as tetrafluoroborate (BF_4^-), hexafluorophosphate (PF_6^-), and bis(trifluoromethylsulfonyl)imide (TFSI⁻). Unfortunately, the large ionic radii of these weakly coordinating anions necessitate substantial changes in the unit cell volume of the electrode material upon oxidative insertion. For graphite, 15, 16, and 20% increases in cell volume were observed upon intercalation of BF_4^- , PF_6^- , and TFSI⁻, respectively.⁸ Certain conducting organic polymers can not only be reversibly oxidized through a similar mechanism but also swell substantially upon insertion.⁹ In fact, this swelling phenomenon is of such sufficient magnitude that it has been leveraged to construct electrochemical actuators.^{10,11}

Metal-organic frameworks are hybrid materials with permanently porous structures that can be modified in a building block-like fashion.^{12,13} Because of the large pore sizes, they are also highly amenable to postsynthetic modification, which often requires the accommodation of large guest molecules.^{14,15} Over the past few years, the number of metal-organic framework semiconductors has increased rapidly.¹⁶⁻²⁰ Recently, it was shown that by selecting a framework structure with infinite

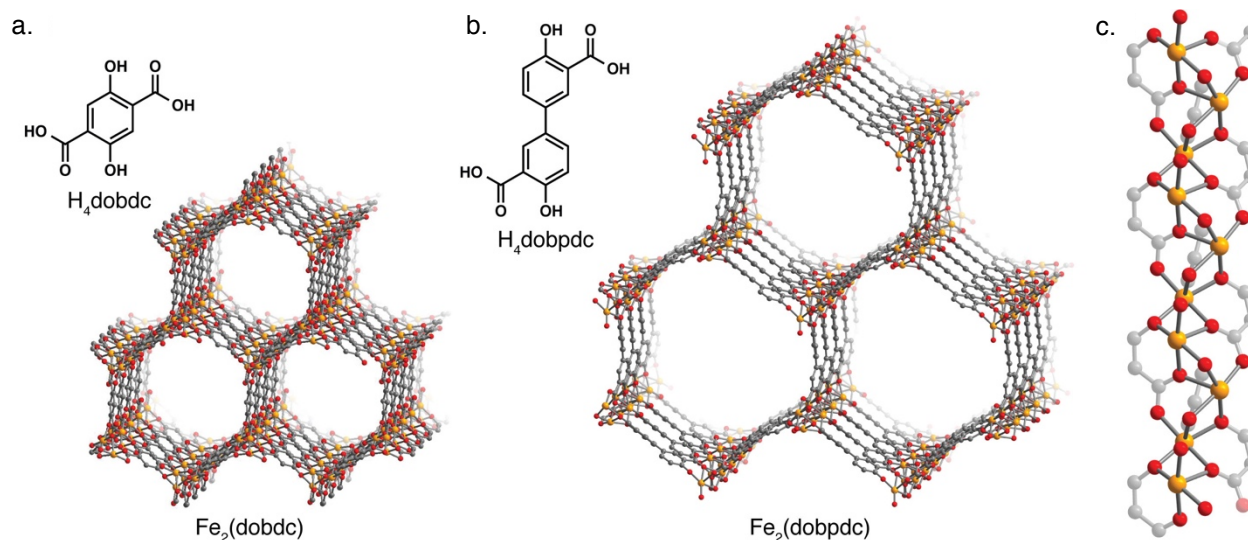


Figure 3.1. Structure of the framework (a) $Fe_2(dobdc)$ and (b) $Fe_2(dobpdc)$. (c) The structures are isorecticular and crystallize in a trigonal lattice with edge-sharing Fe(II) chains running parallel to the c axis. The desolvated structure is shown here for clarity. The pseudosquare pyramidal iron centers retain an open coordination site that points toward the center of the hexagonal pore. The longest distance across the channel for $Fe_2(dobdc)$ is 12 Å, and for $Fe_2(dobpdc)$, it is 21 Å.

chains of redox-active vanadium(IV) or iron(III) centers, a mixed-valence state could be engendered via reduction, thereby mediating electron diffusion, whereas the large pores facilitate concomitant cation insertion.²¹⁻²⁴ However, the specific energies reported in these previous studies were generally low or the materials were not found to be phase stable.²⁵⁻²⁷ At a glance, this is to be expected, given the size of the inert organic linkers that do not contribute to the total charge capacity of the material. In concert with the intrinsically low energy densities of porous electrodes, metal-organic frameworks have not yet proven promising as competitive battery electrodes. However, to our knowledge, the possible oxidative insertion of anions has not yet been investigated for this class of materials. Here, we demonstrate the efficacy of selected redox-active metal-organic frameworks for undergoing reversible anion insertion reactions with a high specific energy and utilize this capability in the construction of a dual-ion battery half-cell prototype.

3.2 Results and discussion

At least conceptually, it seems straightforward to design a metal-organic framework for an electrochemical anion insertion reaction. Toward this end, we sought a rigid three-dimensional framework with pores large enough to accommodate large ions; this encompasses the bulk of the metal-organic frameworks reported. What is rare yet most important, however, is a structural motif with short distances between redox-active metal centers that extends uninterrupted through the crystal. Because these metal centers contribute significantly to the valence band of the framework, judicious selection of a reversible redox manifold yields both a mode of charge storage and potentially substantial gains in electronic conductivity.²⁸ Lastly, the low gravimetric densities of redox sites must be addressed. The two most obvious solutions are to increase linker topology, and therefore the metal to linker ratio, and to install structural motifs on the ligands that also reversibly store charge.

With this in mind, one metal-organic framework in particular, $Fe_2(dobdc)$, ($dobdc^{4-} = 2,5-$

dioxidobenzene-1,4-dicarboxylate), presented itself, **Figure 3.1a**. Materials of this type are noteworthy for their remarkable gas sorption properties owing to their high density of gas-accessible binding sites at the metal ions.²⁹⁻³³ $\text{Fe}_2(\text{dobdc})$ is attractive from the molecular formula alone; its molar mass per metal ion is 57% greater than the similarly structured metal-organic-framework-based lithium insertion material $\text{Fe}(1,4\text{-benzenedicarboxylate})(\text{OH})_{0.8}(\text{F})_{0.2}$ and near identical to FePO_4 .²² The framework, shown in Figure 1a, has hexagonal channels with five-coordinate Fe^{2+} ions lining the vertices in infinite 1D chains of edge-sharing square pyramids.²⁹ When solvated, the iron centers are pseudo-octahedral. Similar phases are known to be redox-active and semiconducting.^{34,35} Because this material contains iron(II), unlike other iron insertion compounds, it must insert anions in order to access the $\text{Fe}^{\text{II/III}}$ couple.

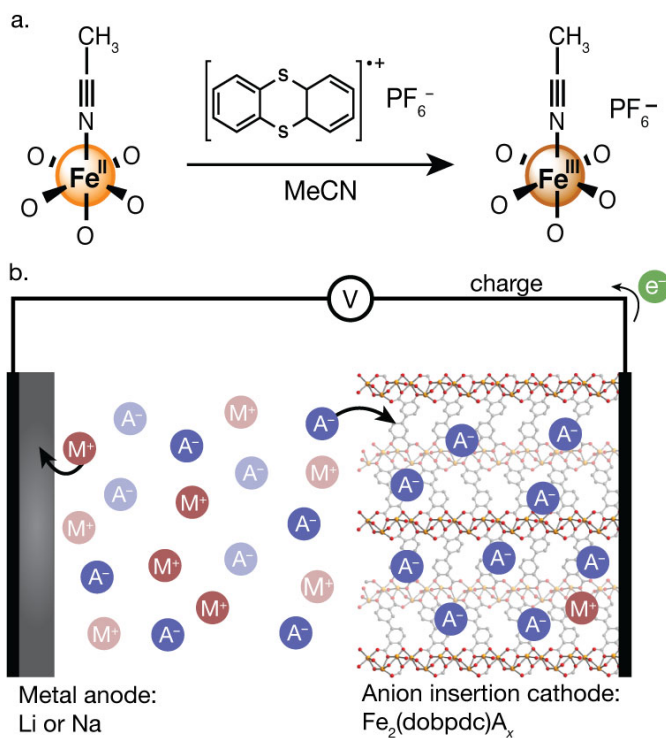


Figure 3.2. (a) Reaction scheme for postsynthetic oxidation of $\text{Fe}_2(\text{dobdc})$. Oxidation with thianthrenium hexafluorophosphate was carried out in acetonitrile. (b) Generalized schematic of how $\text{Fe}_2(\text{dobdc})$ operates in an electrochemical cell. In (b), A^- , can be BF_4^- , PF_6^- , bis(trifluoromethylsulfonyl) imide, or tetrakis-(perfluorophenyl)borate and cations, M^+ , can be lithium, sodium, or

3.2.1 Topotactic oxidative insertion in $\text{Fe}_2(\text{dobdc})$. By chemical oxidation with thianthrenium hexafluorophosphate (**Figure 3.2a**), a stoichiometric oxidation to the half-ferric phase $\text{Fe}_2(\text{dobdc})(\text{PF}_6)_{0.96} \cdot y\text{MeCN}$ ($y \approx 2.6$) was obtainable at room temperature. This stoichiometry was confirmed by ^{57}Fe Mössbauer spectroscopy and is further supported by a small contraction of the unit cell, which results from the smaller radius of the Fe^{3+} ion (**Figures S3.1 and S3.2**). Attempts at electrochemical oxidation were carried out, but only a much smaller fraction of the iron sites could be oxidized (**Figure S3.3**). Such a strong dependence on the reaction solvent results from solvent coordination to the iron sites, as discussed below. Nonetheless, the oxidation of $\text{Fe}_2(\text{dobdc})$ represents, to the best of our knowledge, the first topotactic oxidative insertion of a weakly coordinating anion and an exceptionally rare case of negative volume expansion upon topotactic oxidative insertion or epitaxial intercalation.

3.2.2 Chemical oxidation of $\text{Fe}_2(\text{dobdc})$. One convenient property of the $\text{M}_2(\text{dobdc})$ family is that the pore aperture can be systematically expanded with conservation of network topology and without the possibility of interpenetration.³⁶ **Figure 3.1b** shows one such framework constructed with the larger linker, 4,4'-dioxidobiphenyl-3,3'-dicarboxylate = dobpdc^{4-} , with the formula

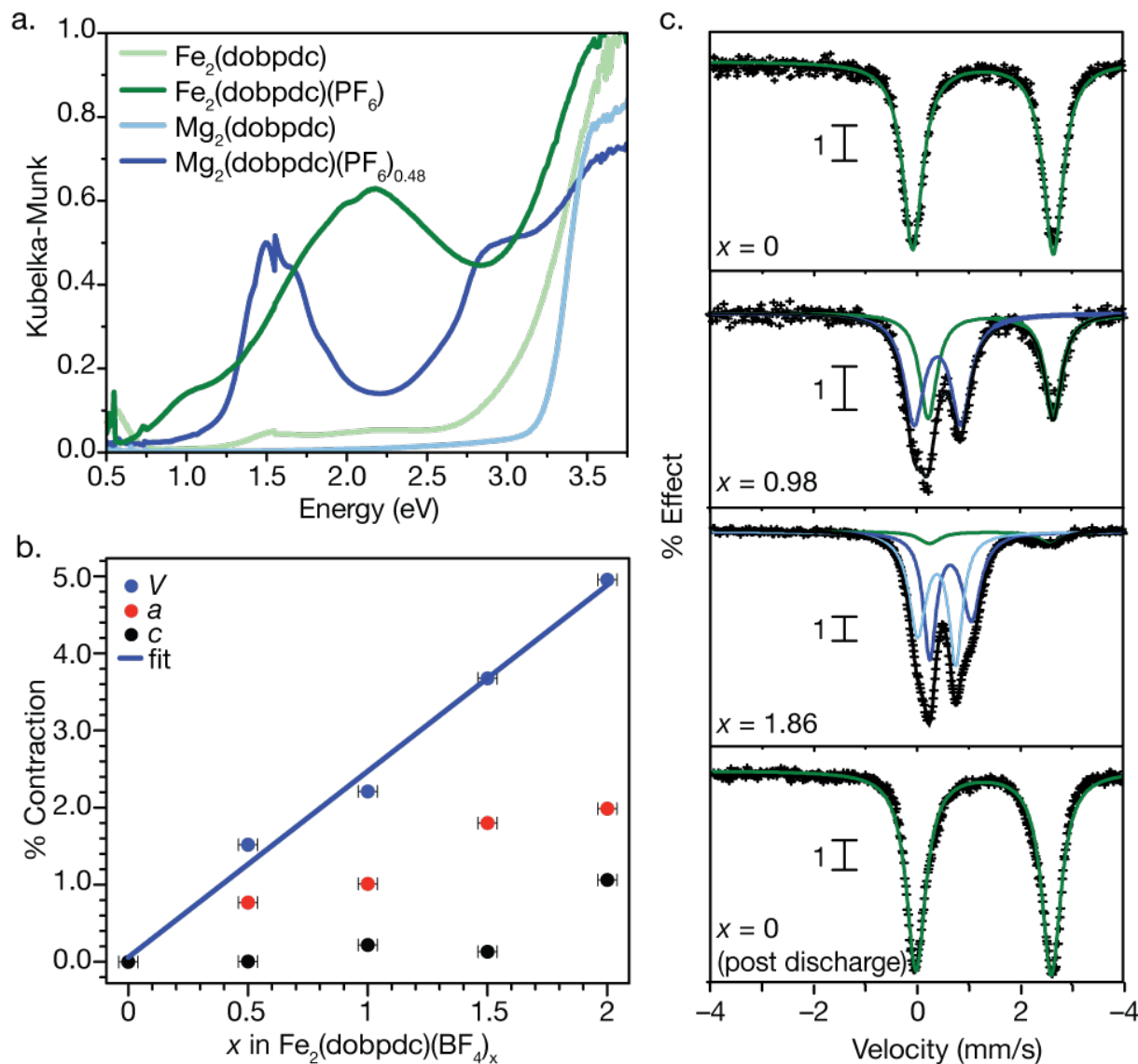


Figure 3.3. (a) NIR-*vis*-UV absorption spectrum for chemically oxidized samples, (b) unit cell parameters determined *ex situ* powder X-ray diffraction for electrochemically oxidized samples of Fe₂(dobpdc)(BF₄)_x, and (c) *ex situ* ⁵⁷Fe Mössbauer spectra for electrochemically oxidized samples of Fe₂(dobpdc)(BF₄)_x, experimental data (+), high-spin iron(II) (green), high-spin iron(III) (blue and light blue), and the fits (black). The values of *x* in b and c correspond to Fe₂(dobpdc)(BF₄)_x and were determined electrochemically. Samples were oxidized in three electrode electrochemical cells with lithium counter and reference electrodes and a 0.1 M LiBF₄ electrolyte in propylene carbonate.

Fe₂(dobpdc). This framework was synthesized previously in our laboratory.³⁷ With a crystallographic pore diameter ~50% larger than that of Fe₂(dobdc), even with solvent coordinated to the iron sites, a substantial void space remains at the center of the pore.

Chemically, it was found that this phase could be oxidized to Fe₂(dobpdc)(PF₆)_{1.56}·*y*MeCN (*y* ≈ 5.1) with two equivalents of thianthrenium hexafluorophosphate in acetonitrile (**Figure 3.2a**). The resulting material is electrochromic, with the color changing from pale green to a very dark blue upon partial oxidation. As depicted in **Figure 3.3a**, the diffuse reflectance UV-*vis*-NIR spectrum shows this as an appearance of a broad absorption band centered at 2.26 eV and extending down to

0.59 eV, indicative of a Robin-Day Class-II mixed-valence state.³⁸ More precisely the mixed valence state is best described as a polaron essentially localized on a single iron ion with a small barrier to thermally assisted charge hopping. This is in contrast to the all-ferrous starting material that only displayed weak d–d transitions and a ligand-centered transition above 2.93 eV.

Infinite chains of edge-sharing octahedra are a prevalent structural motif in mixed-valence iron minerals that display Class-II or Class-III behavior.³⁹ The nearest Fe···Fe distance of 3.04 Å in Fe₂(dobdc),²⁹ which should match that in the isostructural Fe₂(dobpdc), is the shortest of any metal-organic framework with infinite iron chains. Those that are the next closest are Fe^{III}(gallate)·2H₂O and Fe(bdc)(OH)_{0.8}(F)_{0.2}, possessing vertex-sharing octahedra.^{22,40}

Powder X-ray diffraction experiments confirmed a topotactic insertion and linear contraction of the unit cell with increasing oxidation, as shown in **Figure S3.12** and **Table S3.4**. No new peaks or large changes in intensity were observed upon oxidation. The relative change in unit cell volume was just ~5% and can be attributed to the smaller ionic radius of Fe³⁺ compared to that of Fe²⁺. The results suggest a random distribution of iron(II) and iron(III) centers in the host lattice upon oxidation and, similarly, a lack of order for the positions of the PF₆⁻ counterions within the channels. This leads us to suspect that the coordination environment at all of the iron sites is close to identical.

Iron-57 Mössbauer spectra collected at 100 K are consistent with discrete valences for the iron sites within Fe₂(dobpdc)(PF₆)_x (**Figure S3.4**). The spectrum of the initial all-ferrous compound, Fe₂(dobpdc), exhibits a single doublet with an isomer shift of $\delta = 1.297$ mm/s and a quadrupole splitting of $\Delta_E = 2.725$ mm/s, consistent with the presence of just one type of high-spin iron(II) center. Upon oxidation to the half-ferric material ($x = 1$) a new doublet emerges, with $\delta = 0.535$ mm/s and $\Delta_E = 0.626$ mm/s, matching those values expected for a high-spin iron(III) center. The relative area of this new doublet corresponds to the quantity of oxidant that was employed in the oxidation reaction, within mass error. Oxidation to $x = 2$ was attempted but did not go to completion, with 22% of the metal centers remaining as iron(II). As discussed below, this is likely because the oxidation potential of thianthrenium in acetonitrile is not high enough to achieve full oxidation. Unlike other compounds featuring edge-sharing mixed-valence iron oxide, no significant electron delocalization was detected by variable temperature Mössbauer spectroscopy experiments.³⁹

3.2.3 Electrochemical oxidation of Fe₂(dobpdc). Encouraged by the results of chemical oxidation suggesting charge mobility, electrochemical oxidation was attempted (**Figure 3.2b**). In a three-electrode Swagelok T-cell, a composite of Fe₂(dobpdc) with the conductive carbon Super P (30 wt %) and polyvinylidene difluoride (10 wt %) was dropcast onto a 0.5-inch diameter carbon cloth current collector. Lithium reference and counter electrodes were used to enable comparisons with previously reported materials. Specific capacities were determined from the mass of Fe₂(dobpdc) in the electrode. **Figure 3.6a** shows a charge-discharge curve for the composite in a 0.1 M electrolyte solution of lithium tetrafluoroborate in propylene carbonate collected at a rate of C/60. As the material is oxidized, the cell potential rises steadily. This increase is consistent with *ex situ* powder X-ray diffraction data (**Figure 3.3b**), which shows little change in the pattern except for a gradual shift of peaks to higher angles. Again, this results from a gradual contraction of the unit

cell, approaching what would be expected for the conversion of iron(II) to iron(III). No new diffraction peaks are apparent, and no significant changes in peak intensities arise. Accordingly, $\text{Fe}_2(\text{dobpdc})(\text{BF}_4)_x$ ($0 \leq x \leq 2$) can be considered to be a single phase.

This strong correlation between iron centers is not seen in other microporous iron-based electrodes, such as Prussian blue analogues or ferric metal-organic frameworks,

^{22,23,26,41,42} nor is it observed for the oxidative intercalation of graphite, where intercalation follows a series of phase changes, known as staging.^{43,44} The observation can be attributed to the particularly dense packing of iron centers at the vertices of the honeycomb lattice and the comparatively short distance between neighboring iron sites, as shown in **Table S3.3**. This also may be expected given the strong intrachain magnetic coupling reported previously for $\text{Fe}_2(\text{dobdc})$.⁴⁵

The ⁵⁷Fe Mössbauer spectra obtained *ex situ* for the electrochemically oxidized materials are similar to those obtained for chemically oxidized samples. As shown in **Figure 3.3c** and **Table S3.9**, discrepancies between the fractional oxidation states determined electrochemically and peak fits of the Mössbauer spectra are smaller than those for the chemically oxidized samples. Additionally, upon charging to an all-ferric state and discharging back to the all-ferrous form, the ferric doublet vanishes completely, and only the original ferrous signal is visible. This nicely confirms the reversibility of the oxidative electroinsertion reaction.

The open-circuit potentials for equilibrated samples of $\text{Fe}_2(\text{dobpdc})(\text{BF}_4)_x$ with $x = 0$ and $x = 2$ were observed to be 2.95 and 3.96 V vs Li^+/Li , respectively. The potential of the all-ferric phase is conspicuously high in comparison to that of ferric electrodes of similar structure. This can be attributed to the transformation of a neutral host lattice into a negatively charged lattice, as opposed to the situation for $\text{Fe}_2(\text{dobpdc})(\text{BF}_4)_x$, in which a cationic framework is reduced to a neutral one. Although the average discharge potential of $\text{Fe}_2(\text{dobpdc})(\text{BF}_4)_x$ is less than the 3.90 V of iron triplite, this strategy of increasing the redox potential of an iron-based electrode via charge cooperativity in a cationic host presents an alternative to the more general and popular inductive effect.⁴⁶ Integration of the discharge curve in **Figure 3.6a** yields a specific energy of 415 Wh/kg for $\text{Fe}_2(\text{dobpdc})(\text{BF}_4)_x$.⁴⁷ This is comparable to that of the outstanding lithium-insertion material LiFePO_4 (414 Wh/kg) and the graphite-intercalation compound $\text{C}_{20}(\text{TFSI})$ (397 Wh/kg).^{48,49} Although cycling in this electrolyte came with a small but steady decay in capacity, it is important to note that this is to our knowledge one of the only metal-organic frameworks that demonstrates a competitive specific energy. For the tetrafluoroborate anion in **Figure 3.6a**, the charge–discharge cycle is asymmetric, and we suspect that this anion may to some degree displace solvent at the iron center and interact more strongly with the host lattice than initially anticipated.

3.2.4 Ligand-centered redox activity. In principle, the quinoidal dobpdc^{4-} ligand may be expected to yield a delocalized radical anion upon oxidation to dobpdc^{3-} ; however, this species, present in

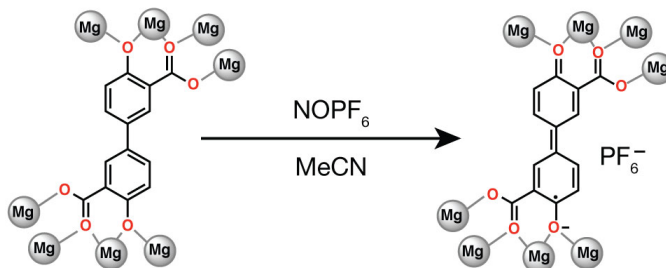


Figure 3.4. Postsynthetic oxidation of $\text{Mg}_2(\text{dobpdc})$ with nitronium hexafluorophosphate to yield an organic radical.

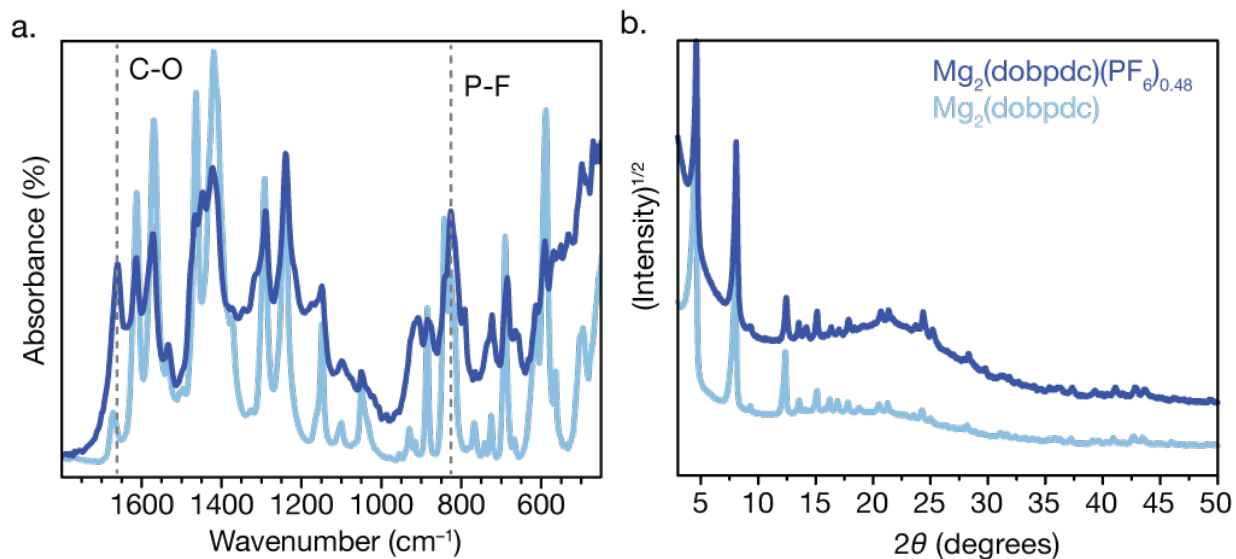


Figure 3.5. (a) Infrared spectra of $\text{Mg}_2(\text{dobpdc})$ (light blue) and $\text{Mg}_2(\text{dobpdc})(\text{PF}_6)_{0.48}$ (dark blue) revealed a new C–O stretch (1661 cm^{-1}) and a new P–F stretch (823 cm^{-1}) after oxidation. (b) Powder X-ray diffraction of $\text{Mg}_2(\text{dobpdc})$ (light blue) and $\text{Mg}_2(\text{dobpdc})(\text{PF}_6)_{0.48}$ (dark blue) show a 0.9% contraction in unit cell. The very broad feature at 20° originates from the borosilicate glass capillary used to exclude air from the sample.

$\text{Fe}_2(\text{dobpdc})\text{A}_x$ ($2 < x < 3$), was not cleanly accessible. Electrochemically, a second oxidation process was observed above 4.1 V vs Li/Li^+ , but was not reversible. Given the small size of tetrafluoroborate, 78 \AA^3 , the redox activity of the ligand should not be constrained by pore packing.⁵⁰ Likely, the diminished lattice enthalpy upon partial oxidation of the ligand renders the transformation irreversible.

The ligand radical itself is, however, clearly observable in the otherwise redox-inactive $\text{Mg}_2(\text{dobpdc})$ congener upon chemical oxidation with nitrosonium hexafluorophosphate (**Figure 3.4**). Addition of an acetonitrile solution of this oxidant results in an immediate color change of the solid from white to dark green, together with the evolution of bubbles from the solution. As shown in **Figure 3.3a**, the UV-*vis*-NIR spectrum of the resulting material, $\text{Mg}_2(\text{dobpdc})(\text{PF}_6)_{0.48}$, displays a new peak at 1.49 eV with a much narrower bandwidth than that observed for the $\text{Fe}^{\text{II/III}}$ intervalence charge-transfer band of $\text{Fe}_2(\text{dobpdc})(\text{PF}_6)$. This matches nicely with other reported oligophenyl quinone radical anions and is diagnostic of the formation of the semiquinoid radical.^{51,52}

By powder X-ray diffraction, a small contraction of just 0.9% in the unit cell volume is observed for $\text{Mg}_2(\text{dobpdc})(\text{PF}_6)_{0.48}$ (**Figure 3.5b** and **Table S3.7**). As shown in the structure in **Figure 3.1**, the long axis of the biphenyl linker runs nearly parallel to the *a*-axis of the unit cell, while the phenoxy–metal bonds lie along neither the *a*-axis nor the *c*-axis. Upon oxidation, the *a*-axis contracts as the bond order increases for the phenolic C–O and C–C bonds, bridging the two phenyl rings. The *c*-axis expands very slightly, as would be expected from a weakening of the phenolic Mg–O bonds arising from the less nucleophilic character of the oxidized ligand. In the infrared spectra shown in **Figure 3.5a**, a new intense C–O stretch is seen to emerge at 1661 cm^{-1} , consistent with oxidation of the dobpdc^{4-} ligand, as well as a P–F stretch at 827 cm^{-1} , confirming insertion of PF_6^- . Excitingly this confirms the first example of a semiquinoid stabilized within a metal-organic framework matrix,

and due to its highly reactive nature, has not been isolated by other methods. Attempts to oxidize $\text{Mg}_2(\text{dobpdc})(\text{PF}_6)_x$ to the quinone phase ($x = 2$) only resulted in amorphous orange powders.

3.2.5 Electrolyte dependence on oxidative insertion. The rigidity of the $\text{Fe}_2(\text{dobpdc})$ framework imposes a charge capacity curtailment that becomes more severe with increasing size of the counteranion, as reflected in the data shown in **Figure 3.6a**. With a lithium electrolyte solution containing BF_4^- (76 \AA^3), the material can be oxidized to $x = 2.49$. The larger TFSI^- (212 \AA^3) and tetrakis(perfluorophenyl)borate (BArF^- , 580 \AA^3) ions exhibit significantly reduced capacities, $x = 1.36$ and 0.60 equivalents, respectively. Interestingly, at 1.18 equivalents, PF_6^- (89 \AA^3) affords a lower charge capacity than TFSI^- , despite its smaller size. This may be the result of the coinsertion of neutral LiPF_6 or some otherwise convoluted ion pairing of the cation. Voltage hysteresis was smaller for the larger cations, the opposite of what would be expected if electrode polarization was caused by ion diffusivity. Rather, it is more suggestive of voltage polarization stemming from larger anions having a weaker electrostatic attraction to the cationic iron centers lining the framework channels. This would also explain the significantly higher equilibrium potentials observed for larger cations. A similar phenomenon has been reported for cationic graphite intercalation compounds, wherein larger anions result in significantly higher cell voltages.⁸ Given the same value of x in $\text{Fe}_2(\text{dobpdc})(\text{A})_x$, this also appears to be the case here.

To a first approximation, anion insertion materials should not be expected to display a dependence on the nature of the counteranion present in the electrolyte solution. The anion TFSI^- was selected for the superior solubility of its Li^+ , Na^+ , and K^+ salts in propylene carbonate and the reasonably high charge capacity already observed for the Li^+ salt. As shown in **Figure 3.6b**, the three salts gave rise to reversible oxidation reactions at similar potentials, and there is no clear trend in charge capacity. However, in a nanoporous electrode like $\text{Fe}_2(\text{dobpdc})(\text{TFSI})_x$, the reaction becomes convoluted. Instead of deinsertion of an anion from $\text{Fe}_2(\text{dobpdc})(\text{TFSI})_x$ upon discharge (formally the microscopic reverse of the oxidation reaction), a cation could instead be inserted for charge balance. We have previously found that the isostructural $\text{Mg}_2(\text{dobpdc})$ absorbs significant

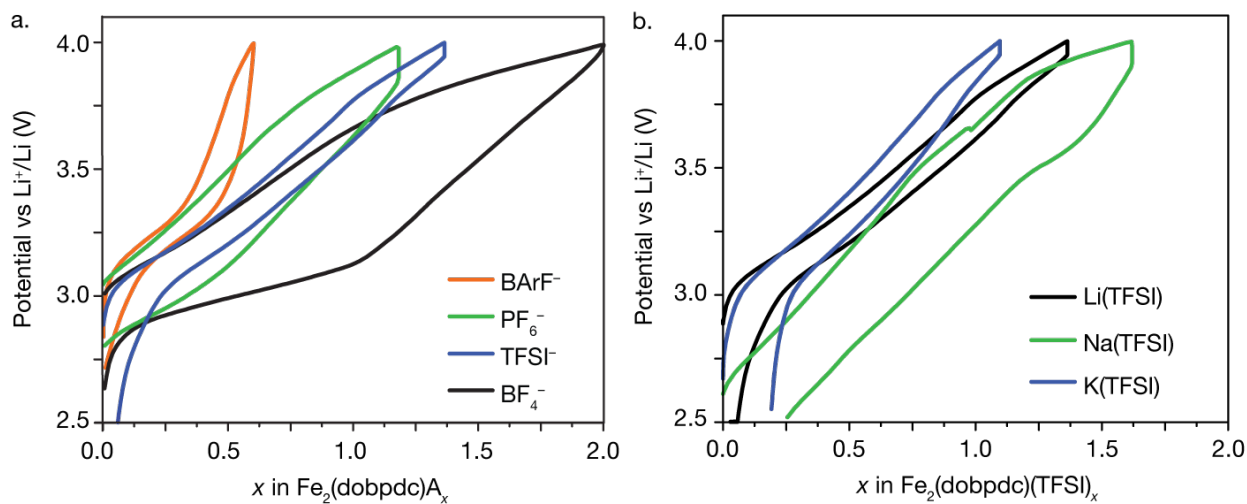


Figure 3.6. Charge–discharge dependencies on the (a) electrolyte anion, and (b) cation. All electrolyte solutions were 0.1 M in propylene carbonate (PC) for the anion and cation dependence experiments. All data was collected at a rate of C/60.

amounts of metal salts even without the driving force of oxidation.⁵³ The actual insertion mechanism likely involves some combination of these two scenarios. In fact, it is possible that metal-organic frameworks reported to electroinsert cations may in actuality have a similarly complex insertion mechanism.

The electrochemical insertion reaction was found to be more sensitive to solvent than to the inserted salt (**Figure 3.7c**). A set of 0.1 M LiBF₄ electrolyte solutions were prepared and tested using different solvents. Because every five-coordinate iron(II) center in the evacuated material will become

solvated upon introduction of the electrolyte solution, the pore volume is always occupied with more solvent than anions. The effect on cell performance was found to be dramatic. Dimethoxyethane (DME), which is not much larger than propylene carbonate (PC), displayed a massive voltage hysteresis and much reduced capacity. A solution of lithium tetrafluoroborate dissolved in the ionic liquid 1-butyl-3-methyl-imidazolium tetrafluoroborate showed a significantly lower equilibrium potential than for the all-ferrous Fe₂(dobpdc) compound as well as that for the oxidative sweep overall. In this electrolyte, the only available nucleophile is the charge-balancing tetrafluoroborate anion, which necessarily coordinates to the iron sites. With an inner sphere counterion, a lower cell potential would be expected. A postmortem analysis of the cell revealed significant electrolyte decomposition at the counter electrode and cycling was not possible. Most likely decomposition of BF₄⁻ is catalyzed upon coordination to iron. The solvent dependence on the charge–discharge curves for this material is complicated and unintuitive. Indeed, the solvation and conductance of ions in nanoconfined spaces remains a complex and still poorly understood phenomenon, one that electroactive metal-organic frameworks may be excellent candidates for elucidating.⁵⁴⁻⁵⁷

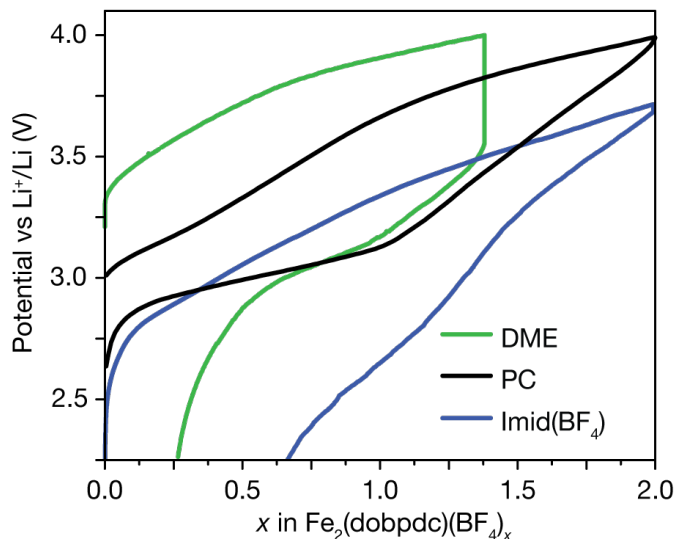


Figure 3.7. Charge–discharge dependence on the solvent. All solutions contained 0.1 M LiBF₄. All data was collected at a rate of C/60.

3.2.6 A prototype sodium half-cell. The search for new materials amenable for use in sodium batteries is a burgeoning field. Iron-based and certain organic-based electrode materials are of particular interest here, owing to the potential for reduced material costs and greater elemental abundance.⁵⁸ To our knowledge, metal-organic frameworks have not yet been considered for sodium batteries. Given the complex dependence of electrochemical performance with electrolyte and the low-lying quasireversible oxidation of the ligand, it was only after significant optimization that quality cycling conditions were obtained. With a sodium reference electrode, the potential limits were set to 3.65 V and 2.00 V. A previously vetted electrolyte consisting of 0.6 M NaPF₆ in a 30:70 ethylene carbonate/dimethyl carbonate (EC/DMC) mixture was ultimately found to perform well.⁵⁹

significantly

closer

iron–iron

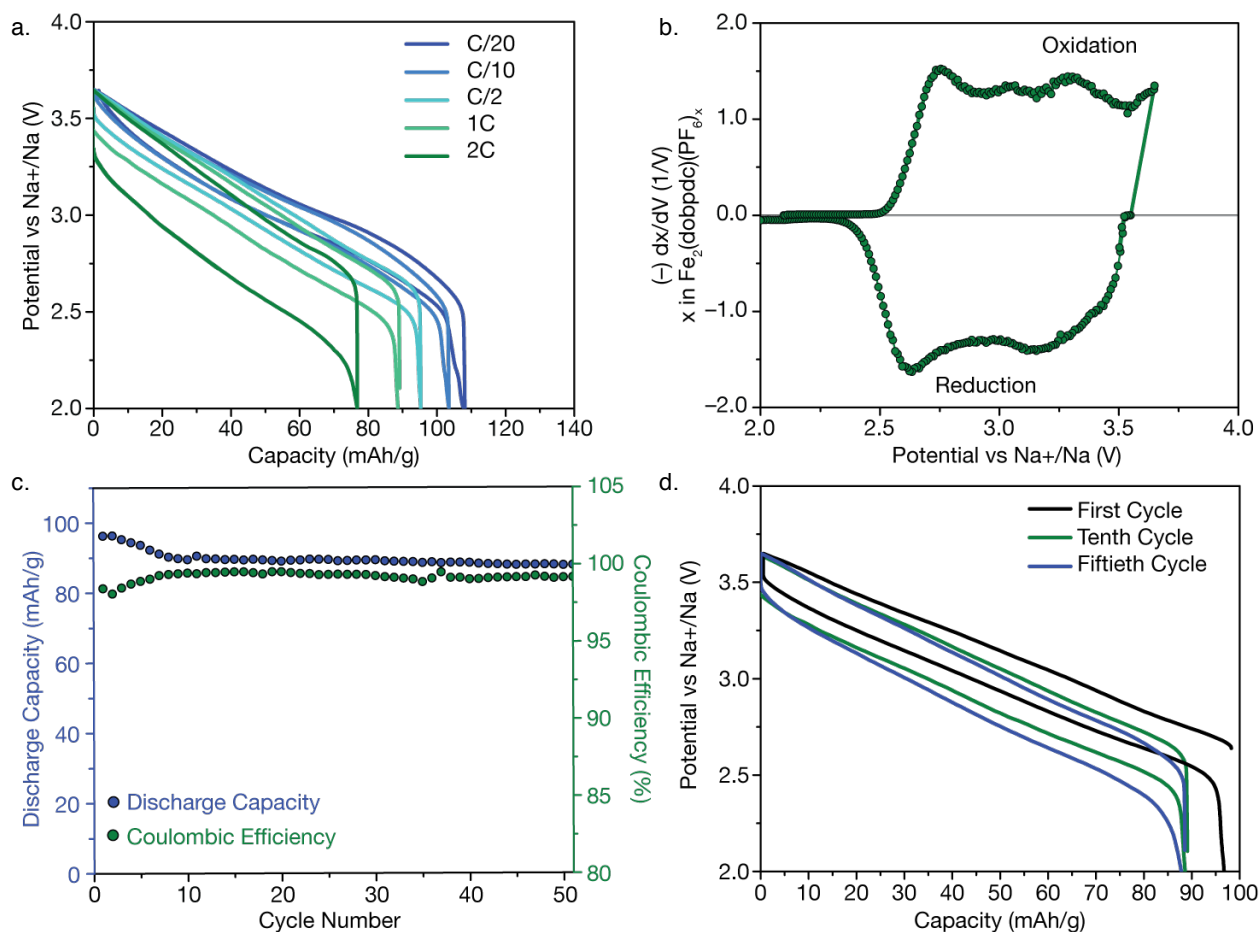


Figure 3.8. Half-cell performance of a prototype sodium battery with a 0.6 M NaPF₆ electrolyte in 30:70 EC/DMC. The theoretical capacity is 140 mAh g⁻¹. (a) Cycle rate dependence, (b) differential capacity plot after 49 cycles at 1 C, (c) change in capacity with cycle number at 1 C, and (d) discharge profiles at different points during cycling at 1 C.

The dependence of the charge/discharge rate upon capacity within the resulting battery construct is shown in **Figure 3.8a**. At a rate of C/2, 170 mV of voltage hysteresis occurs, which is gradually diminished at slower rates. Also at C/2, ~ 67% of the iron sites are reversibly oxidized, comparable to what was accessible in Li_xFe₂(bdc)(OH)_{0.8}F_{0.2} at a 40 h discharge rate.²² From comparison of the two framework structures, it is clear that the much larger pore size and contacts within Fe₂(dobpdc) are responsible for the faster kinetics. At C/20, the specific energy of the Fe₂(dobpdc) electrode is 316 Wh kg⁻¹; however, with such a large pore volume, the energy density is a relatively modest, 212 Wh L⁻¹.

Figure 3.8b displays the differential capacity as a function of potential versus Na⁺/Na for data collected at C/2 after 49 cycles. The oxidative sweep shows three broad peaks and the onset of a fourth tentatively attributed to partial ligand oxidation. The first peak matches the open-circuit potential of the pristine electrode at 2.75 V. The reductive sweep shows one very broad peak and a second sharper peak at 2.63 V juxtaposed to the initial oxidative peak. Although the coulombic efficiency of this cycle was greater than 99%, the peak asymmetry suggests that deinsertion is different from the insertion reaction which is possibly a result of changes in ion packing as the

concentration of PF_6^- increases or that the asymmetry of the reductive process is convoluted by simultaneous cation insertion and anion deinsertion.

The results from cycling the electrode at 1 C are shown in **Figure 3.8c**. After 10 cycles, the cell capacity plateaued at approximately 90 mAh g^{-1} , tenuously confirming long-term reversibility of PF_6^- insertion. Eventually, the material preferentially cycles between $0.58 < x < 1.92$. Previously, we reported ionic conductivity in a similar framework to be most strongly dependent upon the quantity of ions that can be absorbed.^{53,60} This observation is in agreement with the preference revealed here toward discharging at higher concentrations of PF_6^- . The change in the discharge profile between the 10th and the 50th cycle is indicative of slower electrode kinetics at high cycle numbers, whereas the total capacity remains the same (**Figure 3.8d**).

Figure 3.9 compares the discharge curve of $\text{Fe}_2(\text{dobpdc})(\text{PF}_6)_x$ to that of other metal-organic frameworks, sodium-inserting iron phosphates, and TFSI⁻-intercalated graphite at the slowest discharge rates reported.^{22,23,26,61-64} With the exception of graphite, all discharge curves plotted also store charge via an $\text{Fe}^{\text{II/III}}$ couple. This comparison reveals some striking differences for $\text{Fe}_2(\text{dobpdc})(\text{PF}_6)_x$ ($0.21 < x < 2$). First, its electrode potential decreases almost linearly with reduction, whereas other microporous electrodes, iron phosphate, and graphite show one or multiple plateaus. Second, the strong charge correlation upon charging yields an exceptionally high redox potential, higher than sodium Prussian white for 32% of the discharge. Indeed, the phases $\text{Fe}_2(\text{dobpdc})(\text{A})_x$ are unique in possessing very large pores yet a high linear density of redox-active metal centers that allow for this novel behavior. Finally, in comparison to graphite-intercalation electrodes, the operating potential is much lower. Similar to polymer electrodes, metal-organic frameworks that can insert anions may yield a large range of operating voltages. More broadly, postsynthetic oxidation of a host metal-organic framework, as demonstrated here, opens the door to more exotic electrochemical transformations and applications beyond energy storage.

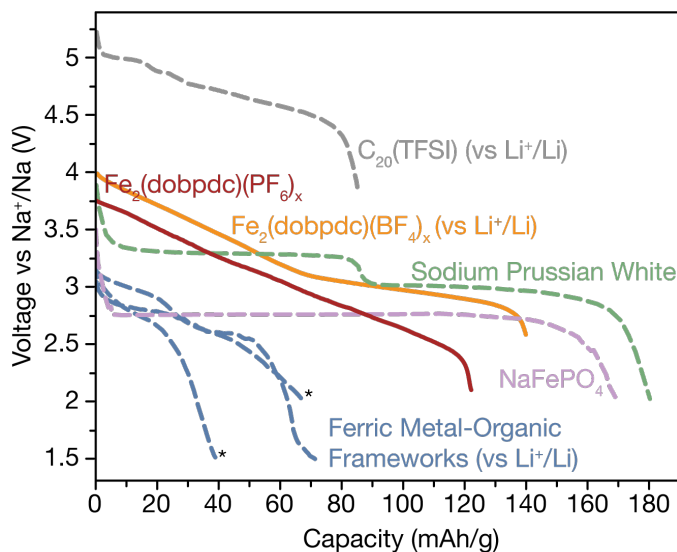


Figure 3.9. Comparison of $\text{Fe}_2(\text{dobpdc})(\text{PF}_6)_x$ discharge profile compared to those of other electrodes discharged at their maximum capacity. All materials shown store charge via an $\text{Fe}^{\text{II/III}}$ couple with the exception of $\text{C}_{20}(\text{TFSI})$. Reversible conditions were not reported for the starred curves. Discharge curves measured with a lithium reference were not rescaled.

3.3 Conclusions

The metal-organic frameworks $\text{Fe}_2(\text{dobdc})$ and $\text{Fe}_2(\text{dobpdc})$ were found to oxidatively insert weakly coordinating anions. The reactions proceed both chemically and electrochemically. Upon partial oxidation of $\text{Fe}_2(\text{dobpdc})$, the electronic properties of the material changed dramatically, as evidenced by the emergence of a strong intervalence charge-transfer band indicative of enhanced charge mobility. Powder X-ray diffraction, UV-*vis*-NIR spectroscopy, and coulombic titration all

afforded results consistent with classifying $\text{Fe}_2(\text{dobpdc})(\text{A})_x$, $0 < x < 2$ as a single phase. Redox activity of the analogous magnesium-based framework confirmed suspicions that a second, quasireversible oxidation at the quinoidal ligand was also accessible. Capacity fade with cycling and discrepancies in the integrated areas of ^{57}Fe Mössbauer spectra at high levels of oxidation are tentatively attributed to this ligand activation. Sodium half-cells were constructed and found to maintain a greater than 99% Faradaic efficiency over 50 redox cycles. The optimized capacity and voltage of this metal-organic framework resulted in an insertion electrode with specific energy more than double that of other iron-based metal-organic frameworks and comparable to that of graphite intercalation compounds.

3.4 Experimental methods

3.4.1 Electrochemical methods. The working electrodes were prepared in a dry, argon-filled glovebox from a composite of the evacuated metal-organic framework (60 wt %), Super P (30 wt %), and PVdF (10 wt %) suspended in THF. The suspension was dispersed with a horn sonicator, and the ink-like mixture was dropcast onto carbon cloth (Fuel Cell Earth) and heated to 180 °C for 3 h to remove residual THF. Because of the open metal sites and high surface area of the active material, mass loss was monitored periodically during the activation step in order to confirm full desolvation and to obtain an accurate mass. The electrode was compressed with a mechanical press and then transferred to a Swagelok union T-cell. Masses of active material typically ranged from 15 to 30 mg. The larger masses were used for *ex situ* iron-57 Mössbauer spectroscopy and powder X-ray diffraction measurements.

Electrochemical data were collected using a Bio-Logic VMP-3 Multipotentiostat/Galvanostat. All measurements were conducted inside a dry, argon-filled glovebox. Following cell assembly, the cell was left to relax until dV/dt dropped below 0.1 mV/h. Reported open circuit potentials were determined under the same limiting condition. Measurements reported were all collected under constant current conditions with potential and capacity limitations. All reported data had an oxidative capacity limitation of two equivalents as estimated from the mass of the evacuated framework. Over-reduction was not observed within the lower potential limits that were set.

3.4.2 Diffuse reflectance UV-visible-NIR spectroscopy. Samples were prepared in a dry, argon-filled glovebox by diluting the pure samples in PVdF (background subtracted). The sample was pelletized in a custom-built airtight cell with quartz windows and sealed. Spectra were collected on a Cary 5000 by Varian spectrophotometer equipped with a reflectance sphere.

3.4.3 FT-IR spectroscopy. Air- and water-free spectra were collected on a PerkinElmer Spectrum-400 FT-IR with an attenuated total reflectance accessory (Pike Technologies GladiATR) and equipped with a home-built, dry nitrogen-filled glovebag attachment.

3.4.4 Iron-57 mössbauer spectroscopy. Mössbauer spectra were collected at 100 K with a constant acceleration spectrometer and a rhodium matrix cobalt-57 source. The instrument was calibrated at 295 K with α -iron foil. The absorbers were composite electrodes (about 30 mg of active

material) with a carbon-cloth backing. Chemically oxidized sample contained a similar amount of sample diluted with boron nitride. All samples were prepared and sealed in an argon glovebox.

3.4.5 Powder X-ray diffraction. Diffraction data was collected on a Bruker D8 Advance diffractometer using Cu-K α ($\lambda = 1.5406 \text{ \AA}$) radiation. All data reported were collected inside 1 mm diameter glass capillaries with 0.01 mm thick walls (Charles Supper). Capillaries were packed inside a dry, argon-filled glovebox and then flame-sealed. Some data shows a weak, very broad feature that tapers off above 20° that originates from the glass capillary. Unit cells were determined by Le Bail refinement using the software package Topas (Bruker).

3.4.6 Chemical oxidation of Fe₂(2,5-dioxidobenzene-1,4-dicarboxylate). Fe₂(dobdc) and thianthrenium hexafluorophosphate (Th⁺PF₆⁻) were both prepared by previously reported procedures.^{29,65} In a dry, argon-filled glovebox, 24.3 mg (0.0795 mmol) of Fe₂(dobdc) was suspended in MeCN (~6 mL) and stirred vigorously in a 20-mL glass scintillation vial. In another vial, 28.7 mg (0.0794 mmol) of Th⁺PF₆⁻ was dissolved in ~4 mL of MeCN. To the stirring suspension, Th⁺PF₆⁻ was added dropwise. The vial was sealed and left to stir at room temperature for ~16 h. The black suspension was filtered to recover a free-flowing powder. Unit cell refinement and ⁵⁷Fe Mössbauer spectra with fits are reported in the supporting figures and tables. The chemical formula estimated from ⁵⁷Fe Mössbauer and the observed unit cell contraction is Fe₂(dobdc)(PF₆)_{0.96}·xMeCN.

3.4.7 Synthesis of Fe₂(4,4'-dioxidobiphenyl-3,3'-dicarboxylate)(PF₆)_{0.84}·5.1MeCN. The compound Fe₂(dobpdc) was prepared as previously reported.³⁷ In a dry, argon-filled glovebox, 22.9 mg (0.0600 mmol) of Fe₂(dobpdc) was suspended in ~6 mL of acetonitrile and stirred vigorously in a 20-mL glass scintillation vial. In another vial, 21.7 mg (0.0601 mmol) of TH⁺PF₆⁻ was dissolved in ~4 mL of acetonitrile. To the stirring suspension, TH⁺PF₆⁻ was added dropwise. The vial was sealed and left to stir at room temperature for about 16 h. The black suspension was filtered to recover a free-flowing powder. Unit cell refinements and ⁵⁷Fe Mössbauer spectra with fits are reported in the supporting figures and tables. Infrared (solid ATR) spectroscopy: 1654 (m), 1611 (s), 1547 (s), 1529 (s), 1462 (s), 1408 (s), 1371 (m), 1280 (m), 1226 (s), 1153 (m), 1104 (m), 1052 (m), 884 (m), 840 (s), 826 (s), 805 (s), 690 (s), 621 (m), 592 (s).

3.4.8 Synthesis of Fe₂(dobpdc)(PF₆)_{1.56}·~5.1MeCN. In a dry, argon-filled glovebox, 13.8 mg (0.0361 mmol) of Fe₂(dobpdc) was suspended in ~6 mL of acetonitrile and stirred vigorously in a 20-mL glass scintillation vial. In another vial, 26.0 mg (0.0719 mmol) of TH⁺PF₆⁻ was dissolved in ~4 mL of MeCN. To the stirring suspension, TH⁺PF₆⁻ was added dropwise. The vial was sealed and left to stir at room temperature for ~16 h. The black suspension was filtered to recover a free-flowing powder. The molecular formula was estimated from ⁵⁷Fe Mössbauer and the observed unit cell contraction. Infrared (solid ATR) spectroscopy: 1652 (m), 1610 (s), 1547 (s), 1523 (s), 1462 (s), 1406 (s), 1362 (m), 1280 (m), 1224 (m), 1154 (m), 1104 (m), 1052 (m), 884 (m), 839 (s), 805 (m), 691 (s), 621 (m), 593 (s).

3.4.9 Synthesis of $\text{Mg}_2(\text{dobpdc})(\text{PF}_6)_{0.48} \cdot \sim 5.1\text{MeCN}$. $\text{Mg}_2(\text{dobpdc})$ was prepared as previously reported.³⁷ In a dry, argon-filled glovebox, 50 mg (0.16 mmol) of $\text{Mg}_2(\text{dobpdc})$ was suspended in ~6 mL of acetonitrile and stirred vigorously in a 20-mL glass scintillation vial. In another vial, 27 mg (0.16 mmol) of NOPF_6 (Aldrich) was dissolved in ~4 mL of acetonitrile. To the stirring suspension, NOPF_6 was added dropwise. The powder turned from white to dark green immediately. The vial was sealed and left to stir at room temperature for ~16 h. The dark-green suspension was filtered to recover a free-flowing powder. Analytical: $\text{Mg}_2(\text{C}_{14}\text{H}_6\text{O}_6)(\text{PF}_6)_{0.48}(\text{C}_2\text{H}_3\text{N})_{5.1}$ calculated: C, 48.6, H, 3.59, N, 11.95; found: C, 48.63, H, 3.72, N, 11.93. Infrared (solid ATR) spectroscopy: 1661 (s), 1564 (s), 1573 (s), 1467 (s), 1448 (s), 1424 (s), 1291 (m), 1941 (s), 909 (m), 886 (m), 827 (s), 686 (m), 591 (m).

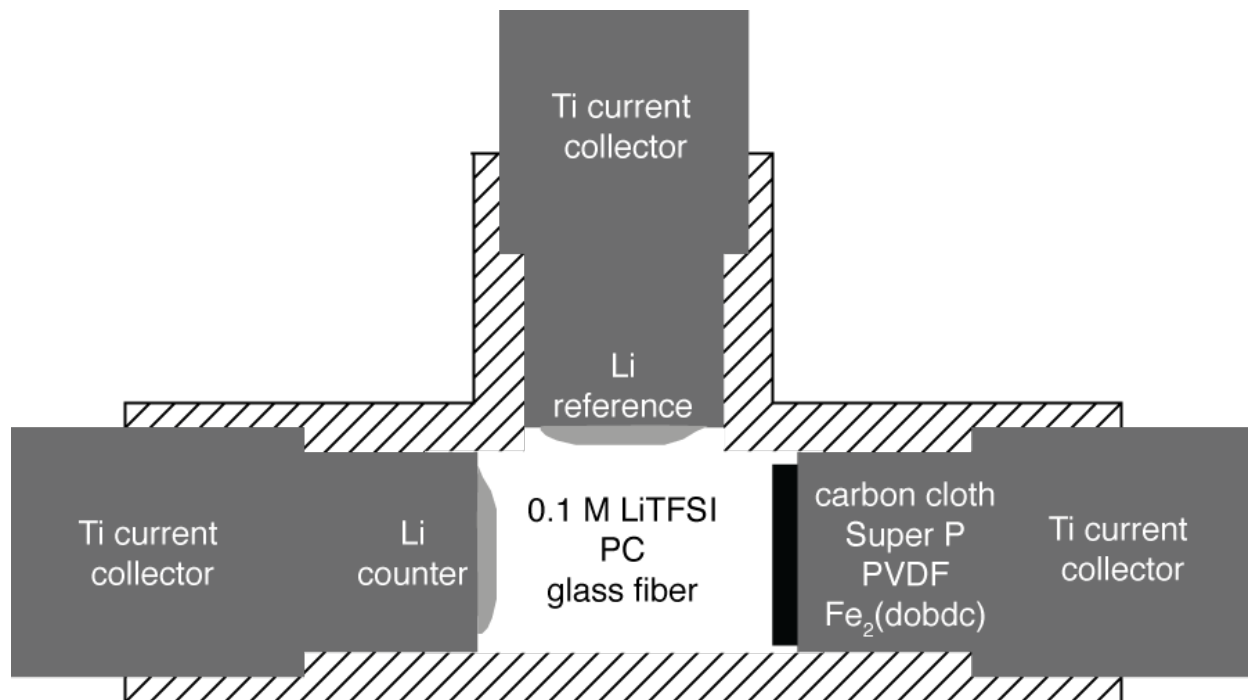
3.4.10 Calculation of Fe-Fe distances in metal-organic frameworks. All iron-iron distances were calculated from crystal information files (.cif) using the software Mercury in the CSD System software package by the Cambridge Crystallographic Data Centre. The structures $\text{Fe}_2(\text{dobdc})$, $\text{Fe}_2(\text{bdp})_3$, ferric gallate, Fe-Mil-53 (68), ilvaite and deerite can be found in the following references.^{29,39,40,66-68} Fe-Met-3 is a metal-triazolate framework with no structure file reported.⁶⁹ The reported space group was $\text{Fd}\bar{3}\text{-m}$ and the lattice parameter for the iron phase was 16.652(1). There were two distinct iron sites in the unit cell: 4-3m at (0,0,0) and 3m at (1/8, 1/8, 1/8). This is the nearest iron-iron distance in the unit cell and can be calculated using the pythagorean theorem to give 3.61 Å.

3.4.11 Calculation of anion sizes. Anion sizes were calculated from previously determined unit cells of their respective lithium salts.⁷⁰⁻⁷² The tetrakis(perfluorophenyl)borate salt of lithium is not known as a pure binary in the Cambridge Structural Database. The unit cell of the thallium salt was used instead which probably slightly overestimates the packing volume of this anion more so than the other anions.⁷³ The calculation was done by dividing the reported unit cell volume by the number of anions in the unit cell. This was taken to be an estimate of the densest packing of anions and their effective occupied volume in the $\text{Fe}_2(\text{dobpdc})$ pore.

3.5 Acknowledgements

This research was supported by the National Science Foundation under award no. DMR-1309066 and Arkema for fellowship support. I would also like to thank F. Grandjean for helpful discussion and guidance with modeling Mössbauer spectra.

3.6 Supporting schemes, figures, and tables



Scheme S3.1. Schematic of the electrochemical cell

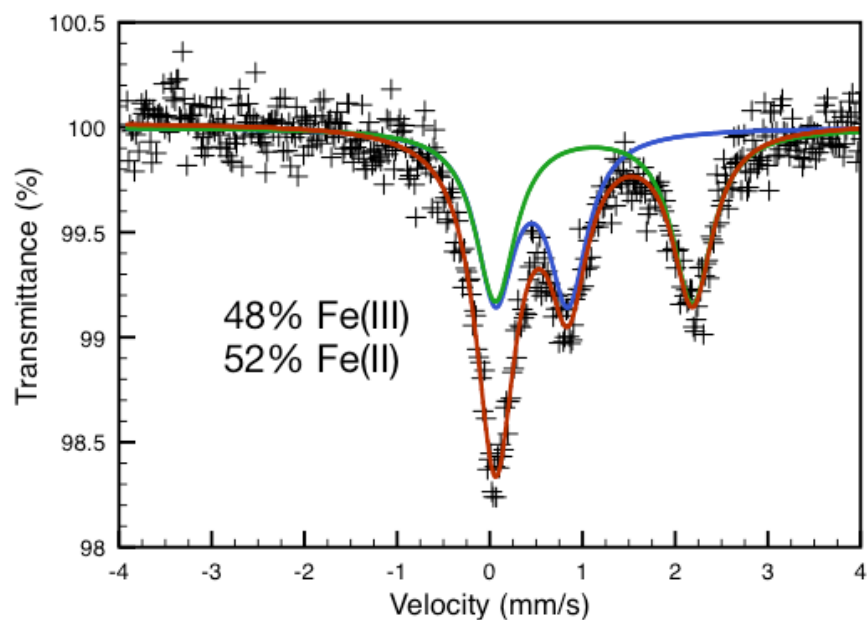


Figure S3.1. Fe-57 Mössbauer of $\text{Fe}_2(\text{dobdc})(\text{PF}_6)(\text{MeCN})_y$. Spectrum was collected at 100 K.

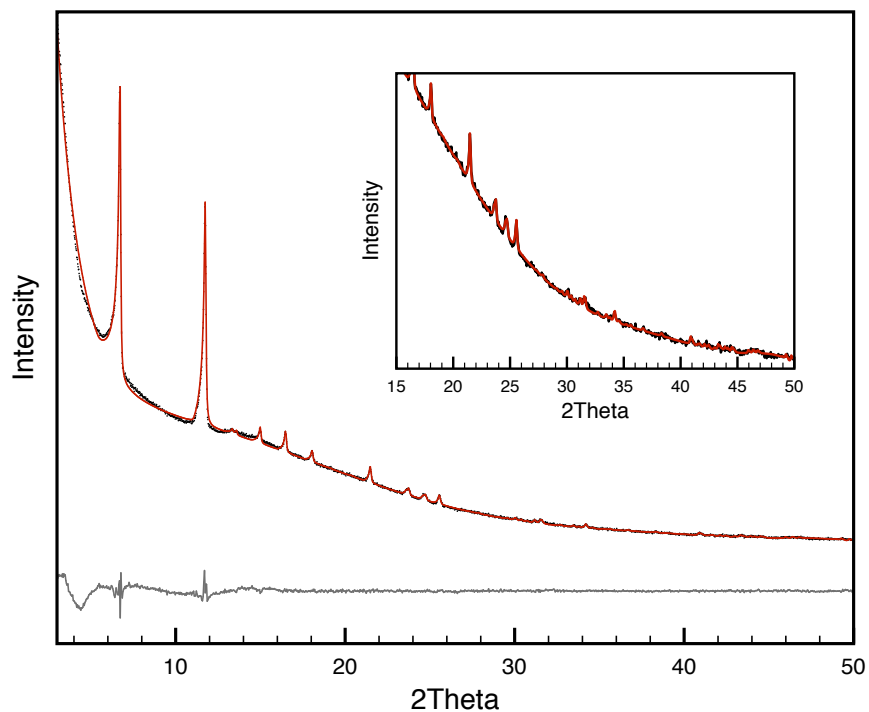


Figure S3.2. PXRD of $\text{Fe}_2(\text{dobdc})(\text{PF}_6)(\text{MeCN})_y$. Experimental data is in black, the Le Bail refined fit in red and the difference in grey. Inset shows the fit at high angle. No change in space group or new peaks are observed post oxidation.

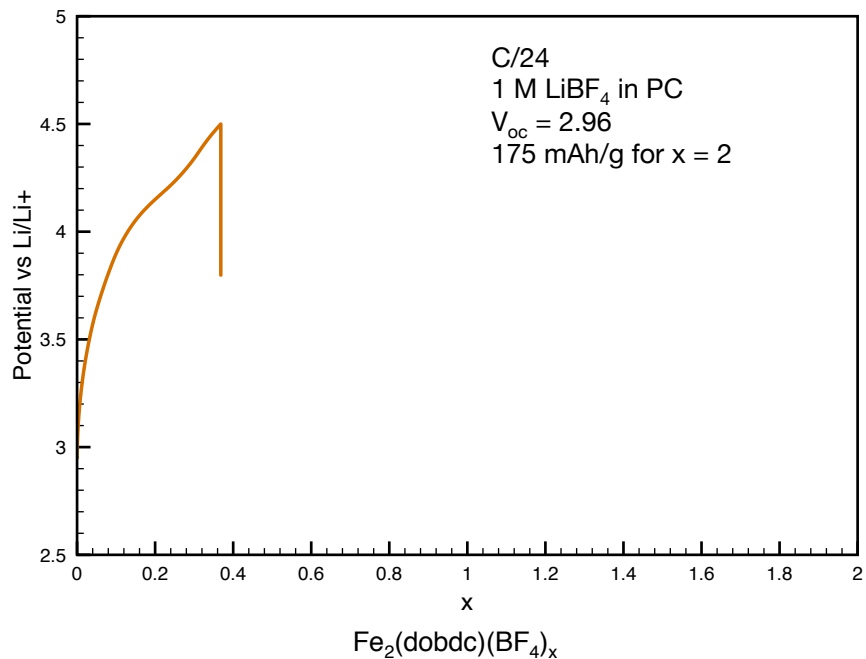


Figure S3.3. Electrochemical oxidation of Fe₂(dobdc) with a lithium reference and counter electrode. In addition to the massive hysteresis this oxidation was not reversible with a 4.5 V potential limit.

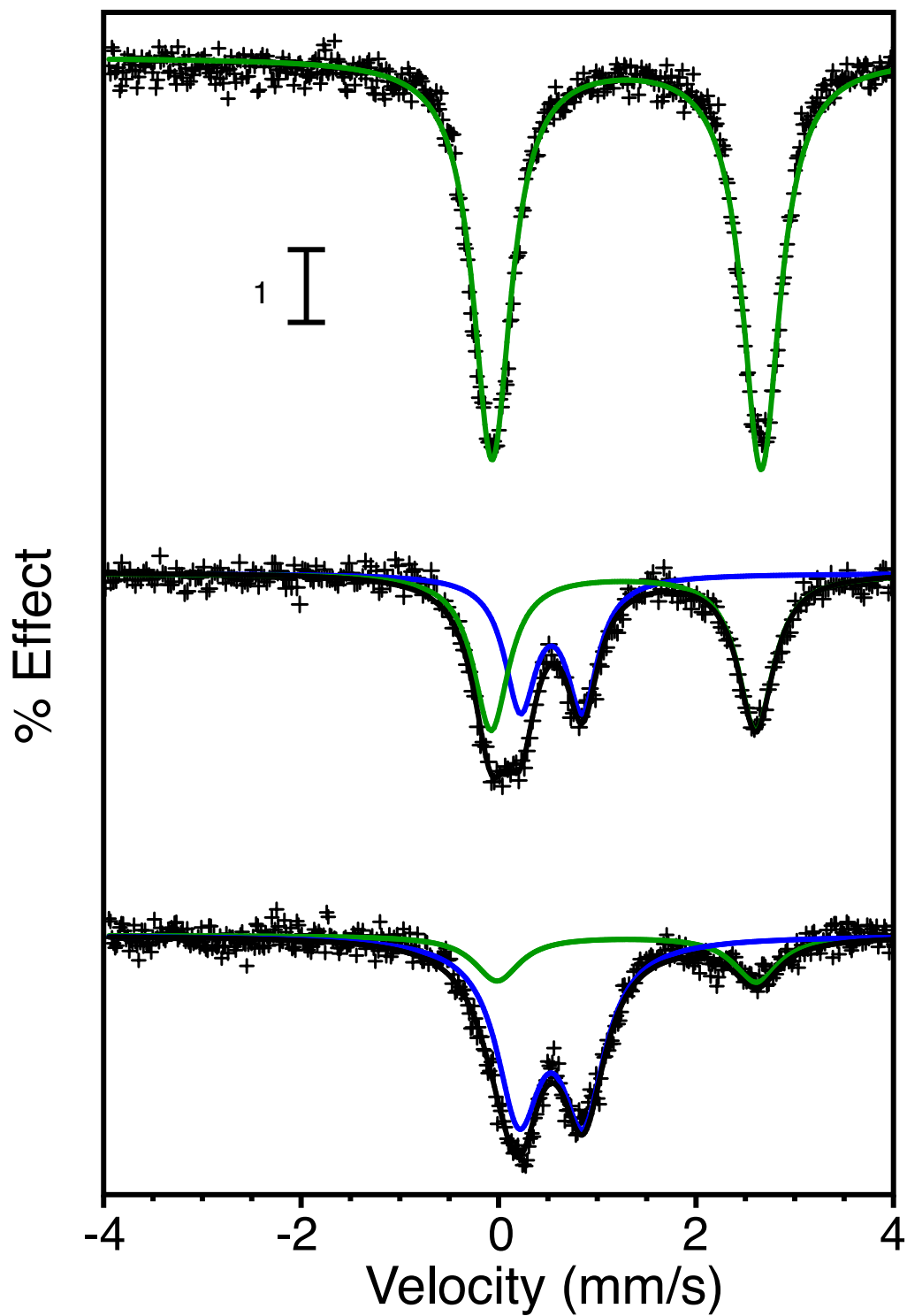


Figure S3.4. Fe-57 Mössbauer spectra before (top) and after chemical oxidation with one equivalent (middle) and two equivalents (bottom) of thianthrenium hexafluorophosphate. Graph elements are: experimental data (crosses), HS-Fe(II) (green), HS-Fe(III) (blue) and fit (black). Velocities are reported relative to the isomer shift of α -iron.

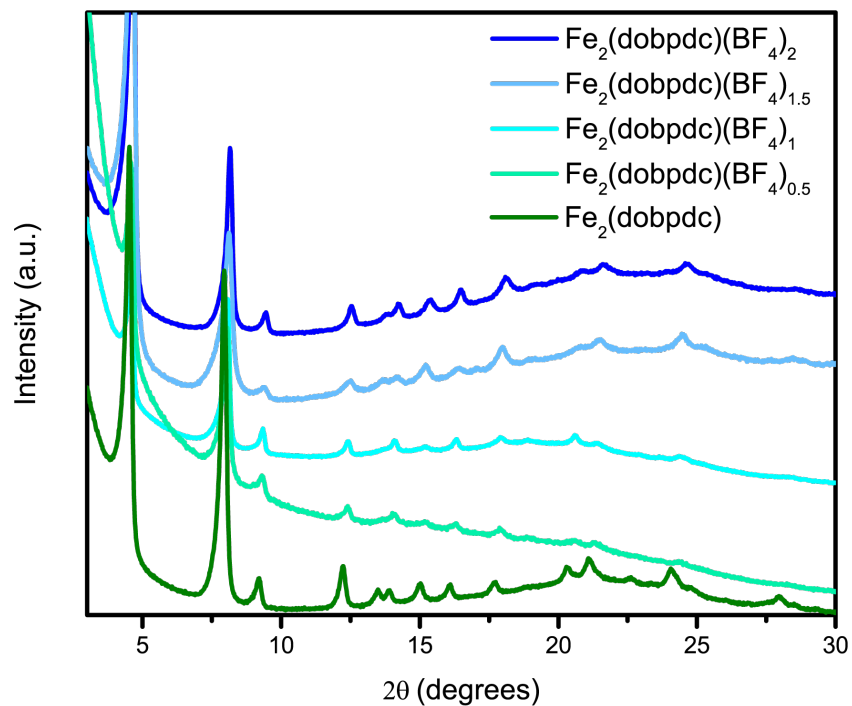


Figure S3.5. PXRDs of electrochemically prepared sample of $\text{Fe}_2(\text{dobpdc})(\text{BF}_4)_x$

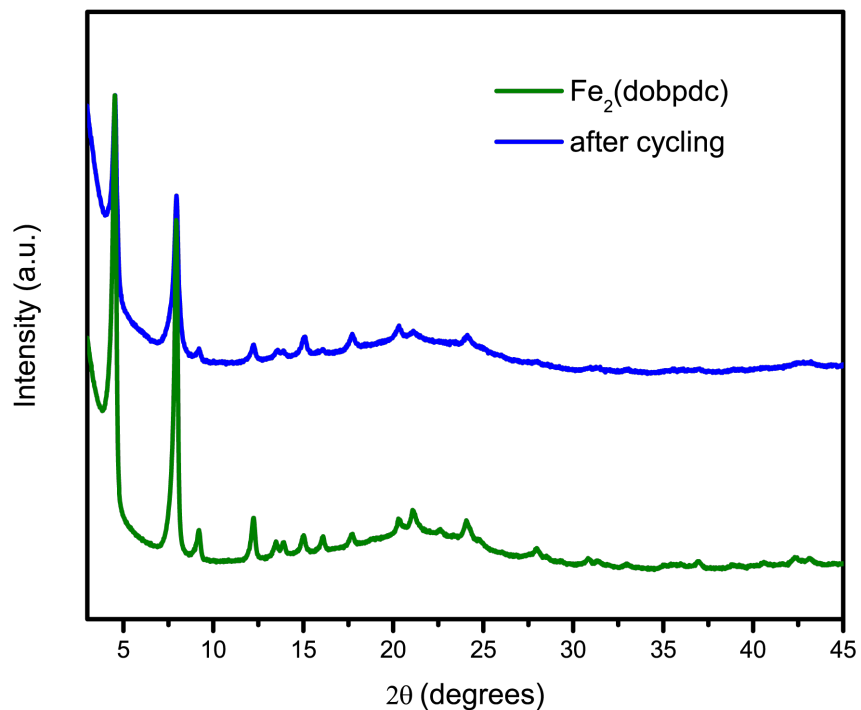


Figure S3.6. PXRD of $\text{Fe}_2(\text{dobpdc})(\text{PF}_6)_x$ before and after 50 cycles at 1 C in 0.6 M NaPF_6 in 30:70 EC:DEC with sodium reference and counter electrodes

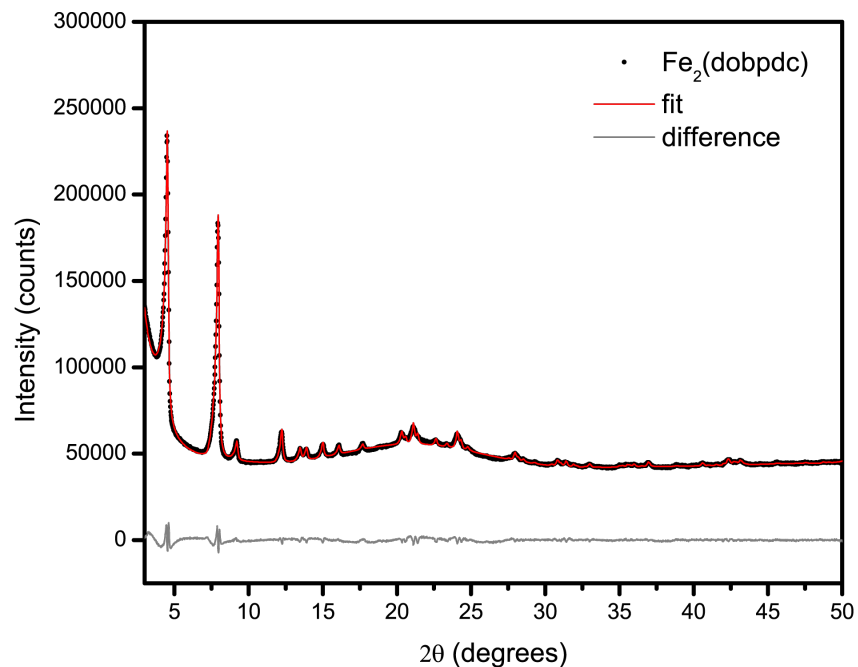


Figure S3.7. Le Bail refinement of Fe₂(dobpdc). The fit and difference are shown in red and grey. Experimental data is shown as black dots.

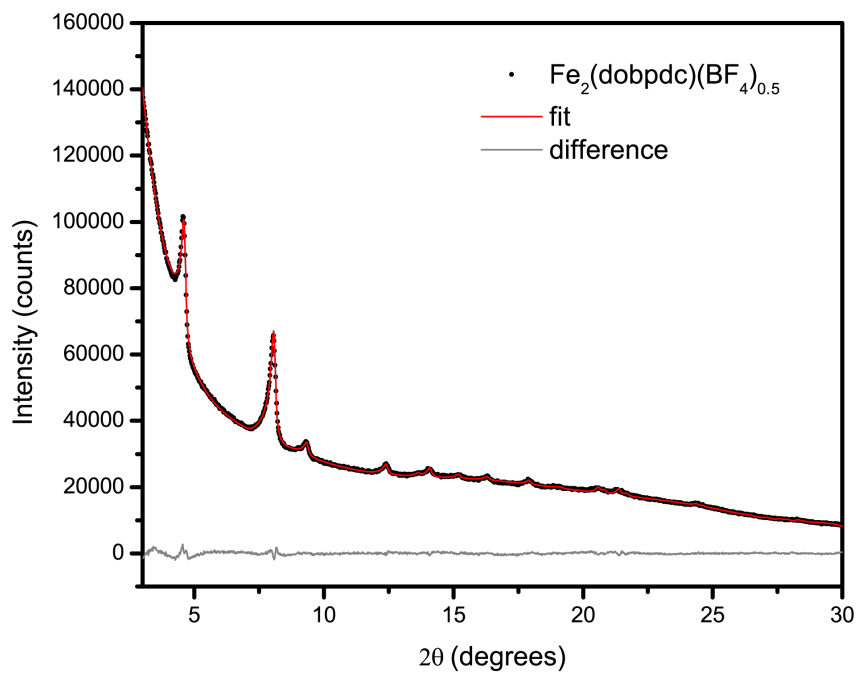


Figure S3.8. Le Bail refinement of electrochemically oxidized Fe₂(dobpdc)(BF₄)_{0.5}. The fit and difference are shown in red and grey. Experimental data is shown as black dots.

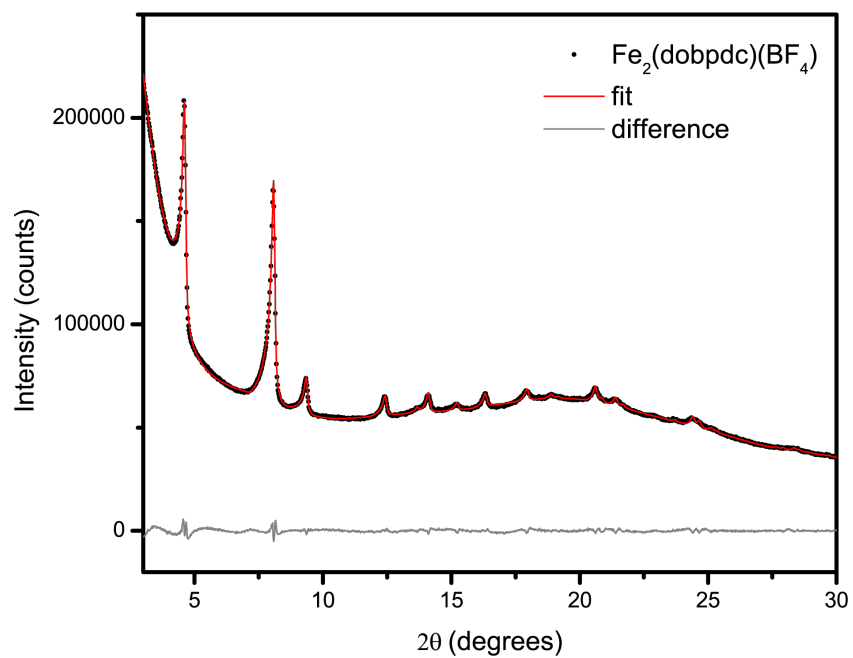


Figure S3.9. Le Bail refinement of electrochemically oxidized $\text{Fe}_2(\text{dobpdc})(\text{BF}_4)$. The fit and difference are shown in red and grey. Experimental data is shown as black dots.

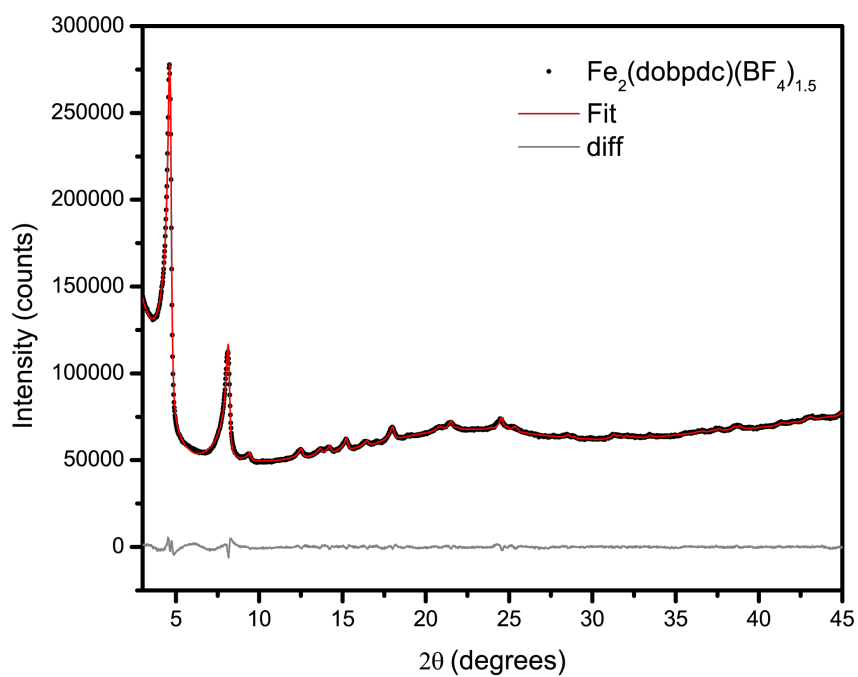


Figure S3.10. Le Bail refinement of electrochemically oxidized $\text{Fe}_2(\text{dobpdc})(\text{BF}_4)_{1.5}$. The fit and difference are shown in red and grey. Experimental data is shown as black dots.

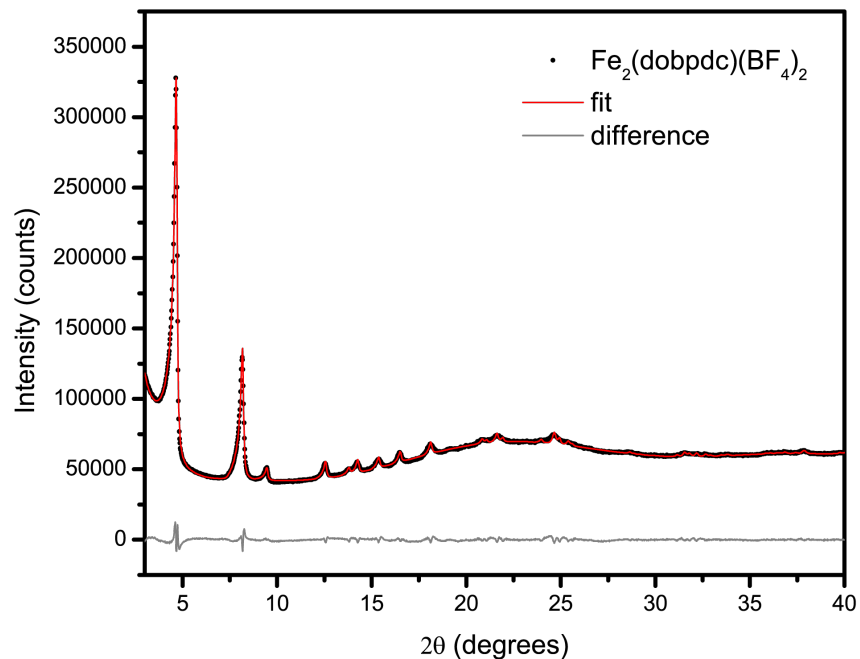


Figure S3.11. Le Bail refinement of electrochemically oxidized $\text{Fe}_2(\text{dobpdc})(\text{BF}_4)_2$. The fit and difference are shown in red and grey. Experimental data is shown as black dots.

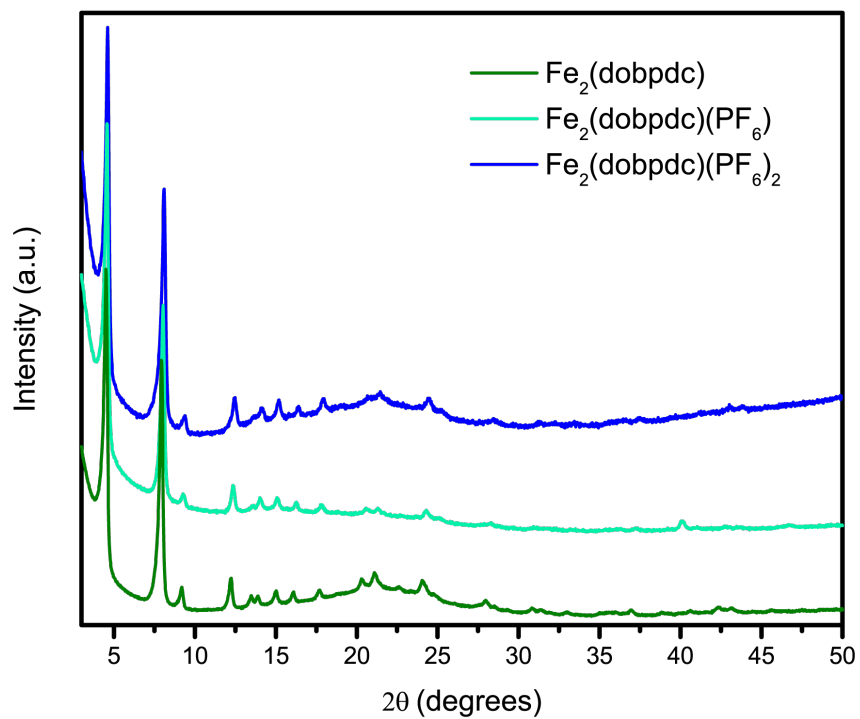


Figure S3.12. PXRDs of chemically oxidized samples of $\text{Fe}_2(\text{dobpdc})(\text{PF}_6)_x$

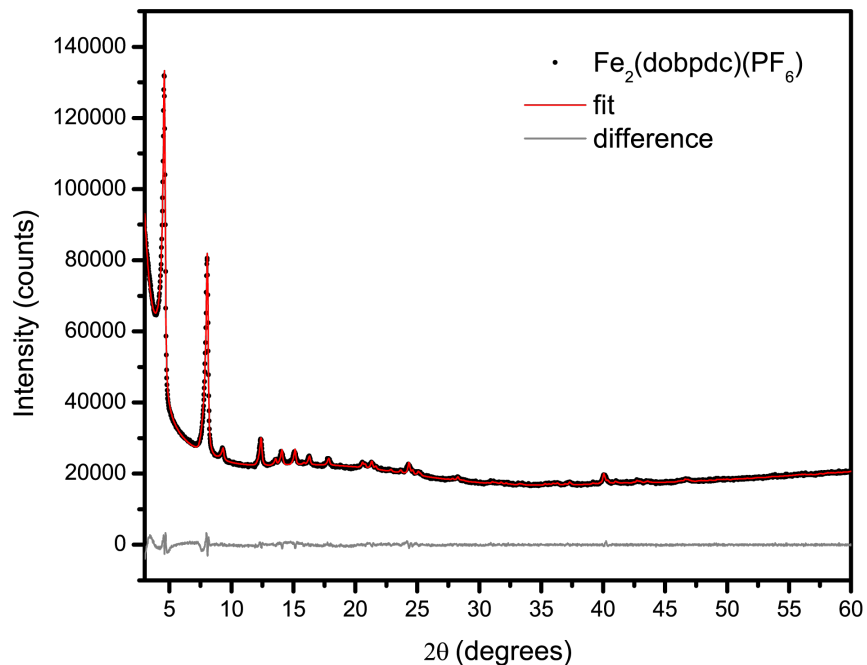


Figure S3.13. Le Bail refinement of chemically oxidized sample $\text{Fe}_2(\text{dobpdc})(\text{PF}_6)$. The fit and difference are shown in red and grey. Experimental data is shown as black dots.

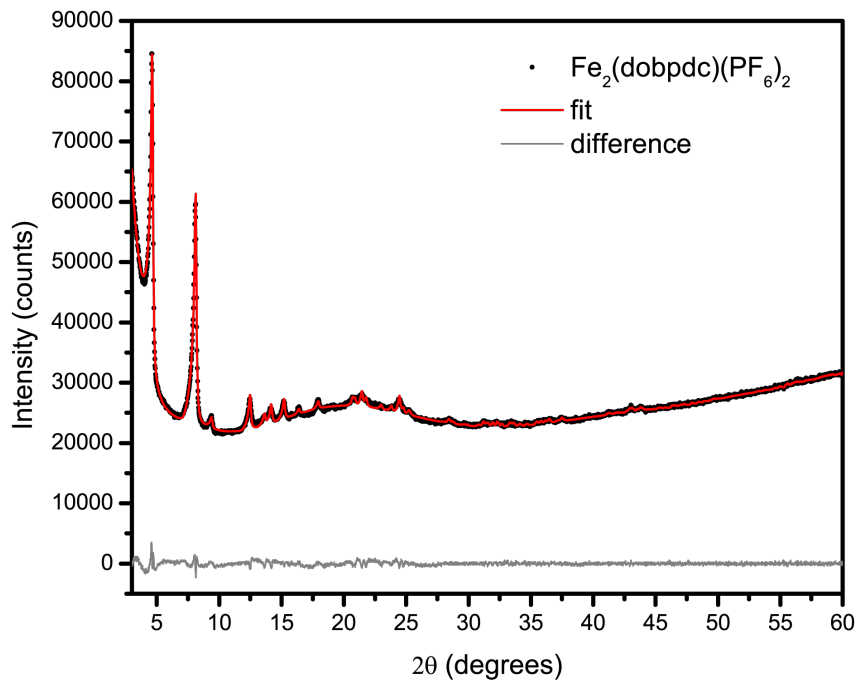


Figure S3.14. Le Bail refinement of chemically oxidized sample $\text{Fe}_2(\text{dobpdc})(\text{PF}_6)_2$. The fit and difference are shown in red and grey. Experimental data is shown as black dots.

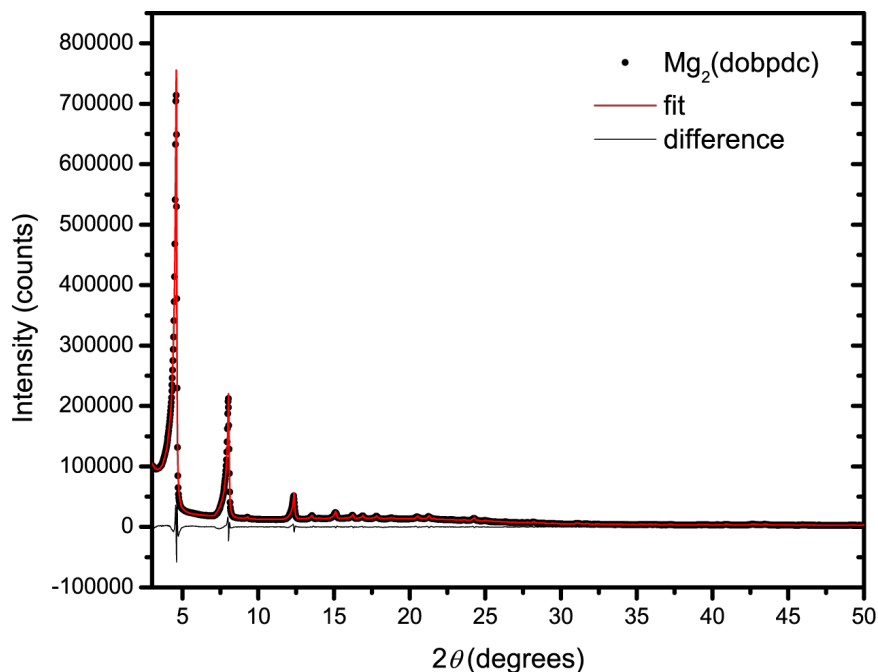


Figure S3.15. Le Bail refinement of $\text{Mg}_2(\text{dobpdc})$. The fit and difference are shown in red and grey. Experimental data is shown as black dots.

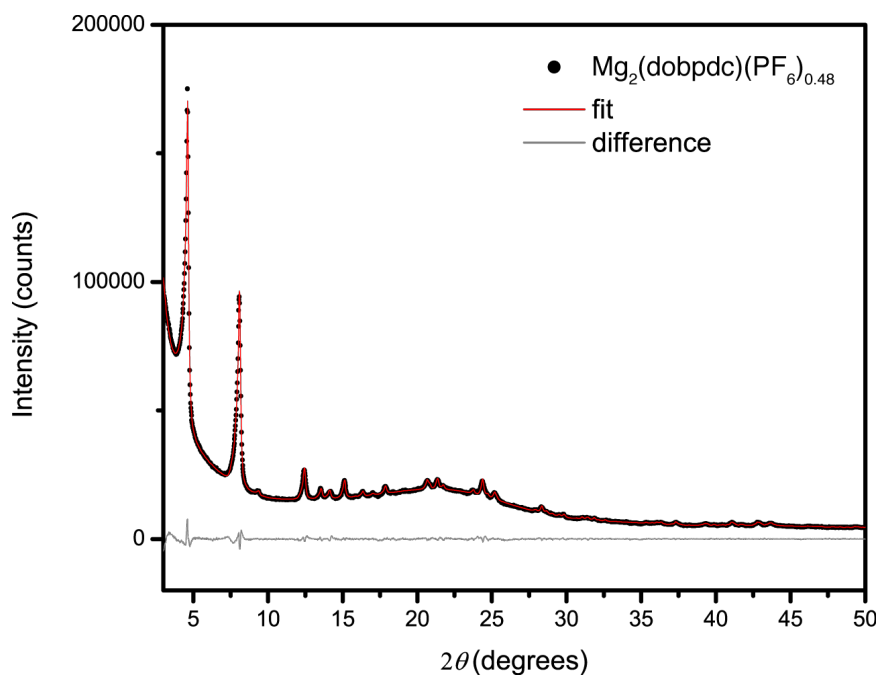


Figure S3.16. Le Bail refinement of chemically oxidized $\text{Mg}_2(\text{dobpdc})(\text{PF}_6)_{0.48}(\text{MeCN})_{5.1}$. The fit and difference are shown in red and grey. Experimental data is shown as black dots.

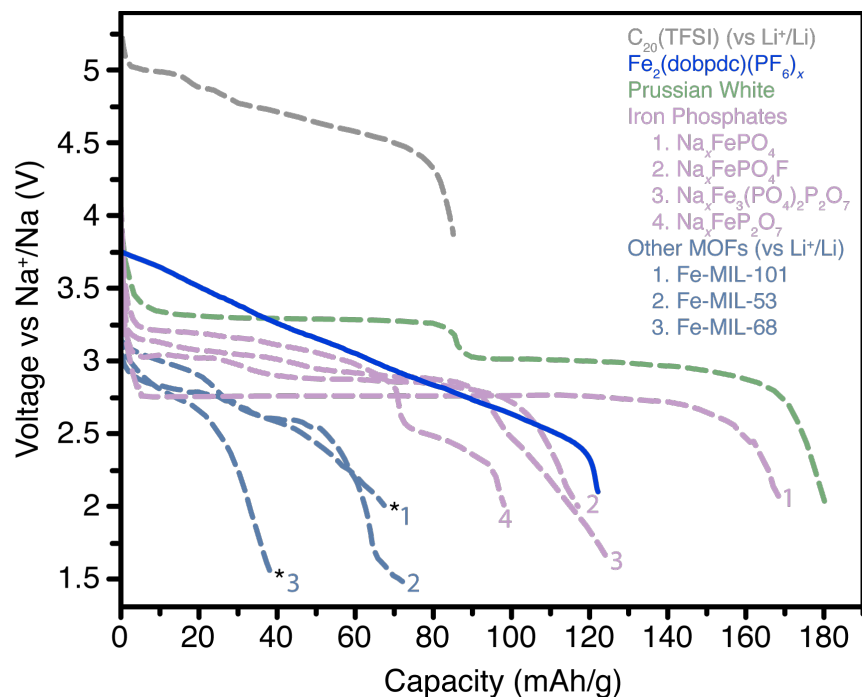


Figure S3.17. Battery summary with all discharge curves labeled. Data for these curves can be found in the references.^{22,23,26,61,62,74-76}

Table S3.1. ⁵⁷Fe Mössbauer fit parameters for chemically oxidized Fe₂(dobdc)(PF₆)•yMeCN. Displayed stoichiometry is as determined by the stoichiometry of the reaction.

Assignment	Fe ₂ (dobdc)(PF ₆)	
	HS-Fe(II)	HS-Fe(III)
δ	1.121	0.466
Δ _E	2.111	0.777
Γ	0.461	0.544
%	52.0	48.0

Table S3.2. Le Bail refined unit cells of Fe₂(dobdc) oxidized chemically. Dimensions are given in Ångstroms. Stoichiometry is as determined by the reagents added to the reaction. Unit cell parameters of the all ferrous phase were reported previously.²⁹

	Fe ₂ (dobdc)	Fe ₂ (dobdc)(PF ₆)
Space Group	R3	R3
α	26.098	25.808(3)
c	6.8512	6.875(2)
V	4041.2	3966(2)
r_{wp}		1.791
r_p		1.335

Table S3.3. Fe-Fe distances of selected minerals and iron based metal-organic frameworks with infinite chains of iron polyhedra (see experimental methods for details).

Framework	Fe-Fe distance (Å)
Fe-MOF-74	3.04
Fe-MIL-53 (68)	3.45
Fe-MET-3	3.61
Ferric Gallate	3.72
Fe ₂ (bdp) ₃	3.85
Ilvaite	2.83, 3.03, 3.01, 3.15, 3.25
Deerite	3.11-3.31 (9)

Table S3.4. Calculated anion volumes from the crystal structures of the binary salts. Only the thallium salt of tetrakis-(perfluorophenyl)borate has a known crystal structure without co-crystallized solvent. As such the anion volume may be over estimated.

Salt	Space Group	Z	Cell Volume (Å ³)	Volume per anion(Å ³)
LiBF ₄	P3 ₁ 2 ₁	3	228.02	76
LiPF ₆	R-3	3	266.65	88.88
LiTFSI	Pnaa	4	848.616	212.154
TIB(C ₆ F ₅) ₄	I34d	12	6962.4	580.2

Table S3.5. Le Bail refined unit cells of Fe₂(dobpdc) oxidized electrochemically. Dimensions are given in Ångstroms.

Phase (echem)	Fe ₂ (dobpdc)	Fe ₂ (dobpdc)(BF ₄) _{0.5}	Fe ₂ (dobpdc)(BF ₄) ₁	Fe ₂ (dobpdc)(BF ₄) _{1.5}	Fe ₂ (dobpdc)(BF ₄) ₂
space group	154	154	154	154	154
a	21.839(2)	21.580(5)	21.551(2)	21.357(4)	21.325(2)
c	6.925(1)	6.850(3)	6.835(2)	6.842(2)	6.7754(17)
V	2806.4(7)	2762(2)	2749.2(11)	2702.7(14)	2668.4(9)
r _{wp}	1.643	1.160	1.015	1.095	1.480
r _p	1.246	0.934	0.797	0.732	1.035

Table S3.6. Le Bail refined unit cells of $\text{Fe}_2(\text{dobpdc})$ oxidized chemically, stoichiometry was estimated from Mössbauer fits. Dimensions are given in Ångstroms.

Phase (chem)	$\text{Fe}_2(\text{dobpdc})$	$\text{Fe}_2(\text{dobpdc})(\text{PF}_6)_{0.84}$	$\text{Fe}_2(\text{dobpdc})(\text{PF}_6)_{1.56}$
space group	154	154	154
a	21.839(2)	21.573(2)	21.460(3)
c	6.925(1)	6.881(8)	6.860(1)
V	2806.4(7)	2773(4)	2736(1)
r_{wp}	1.643	1.415	1.122
r_{p}	1.246	1.045	0.846

Table S3.7. Le Bail refined unit cells of $\text{Mg}_2(\text{dobpdc})$ oxidized chemically. Dimensions are given in Ångstroms. Stoichiometry was estimated from elemental analysis.

Phase	$\text{Mg}_2(\text{dobpdc})$	$\text{Mg}_2(\text{dobpdc})(\text{PF}_6)_{0.48}$
space group	154	154
a	21.635(2)	21.5151(15)
c	6.890(1)	6.9031(7)
V	2793.1(8)	2767.4(6)
r_{wp}	4.607	1.894
r_{p}	2.687	1.45

Table S3.8. Fe-57 Mössbauer fit parameters for chemically oxidized samples. The stoichiometries displayed were determined from the stoichiometry of the reaction. Isomer shifts are reported relative to α -iron.

	Fe ₂ (dobpdc)	Fe ₂ (dobpdc)(PF ₆)		Fe ₂ (dobpdc)(PF ₆) ₂	
	HS-Fe(II)	HS-Fe(II)	HS-Fe(III)	HS-Fe(II)	HS-Fe(III)
δ (mm/s)	1.297	1.265	0.535	1.298	0.531
Δ_E (mm/s)	2.725	2.681	0.626	2.627	0.652
Γ (mm/s)	0.464	0.437	0.391	0.563	0.541
%	100	57	43	21.7	78.7

Table S3.9. Fe-57 Mössbauer fit parameters for electrochemically oxidized samples. The displayed stoichiometries were determined by current integration. Isomer shifts are reported relative to α -iron.

	Fe ₂ (dobpdc)	Fe ₂ (dobpdc)(BF ₄) ₁		Fe ₂ (dobpdc)(BF ₄) ₂			Fe ₂ (dobpdc) (post discharge)
	HS-Fe(II)	HS-Fe(II)	HS-Fe(III)	HS-Fe(II)	HS-Fe(III)	HS-Fe(III)	HS-Fe(II)
δ (mm/s)	1.297	1.286	0.536	1.270	0.552	0.507	1.300
Δ_E (mm/s)	2.725	2.718	0.641	2.65	1.051	0.508	2.622
Γ (mm/s)	0.464	0.481	0.383	0.41	0.397	0.325	0.454
% area	100	49.6	50.4	6.8	40.4	52.8	100

3.7 References

- (1) “Intercalation chemistry” Jacobson, A. J. and Nazar, L. F. *Encyclopedia of Inorganic and Bioinorganic Chemistry* **2011**, doi:10.1002/9781119951438.eibc0093.
- (2) “Mixed-conducting host structures into which either cations or anions can be inserted” Huggins, R. *Solid State Ionics* **1998**, 113-115, 533–544.
- (3) “The electrochemistry of black carbons” Besenhard, J. O. and Fritz, H. P. *Angew. Chem. Int. Edit. Engl.* **1983**, 22, 950–975.
- (4) “Intercalation chemistry of layered double hydroxides: recent developments and applications” Khan, A. I. and O’Hare, D. *J. Mater. Chem.* **2002**, 12, 3191–3198.
- (5) “Preparation of layered double hydroxides” He, J.; Wei, M.; Li, B.; Kang, Y.; Evans, D. G.; and Duan, X. *Layered Double Hydroxides* Springer Berlin Heidelberg, **2006**, Chapter 6, 89–119.
- (6) “Application of layered double hydroxides for removal of oxyanions: a review” Goh, K.-H.; Lim, T.-T.; and Dong, Z. *Water Res.* **2008**, 42, 1343–1368.
- (7) “Anion secondary batteries utilizing a reversible BF₄ insertion/extraction two-dimensional Si material” Nakano, H.; Sugiyama, Y.; Morishita, T.; Spencer, M. J. S.; Snook, I. K.; Kumai, Y.; and Okamoto, H. *J. Mater. Chem. A* **2014**, 2, 7588–7585.
- (8) “Graphite intercalation compounds with large fluoroanions” Katinonkul, W. and Lerner, M. M. *J. Fluorine Chem.* **2007**, 128, 332–335.
- (9) “Electrochemically active polymers for rechargeable batteries” Novák, P.; Müller, K.; Santhanam, K. S. V.; and Haas, O. *Chem. Rev.* **1997**, 97, 207–282.
- (10) “Conducting polymer artificial muscles” Baughman, R. H. *Synth. Met.* **1996**, 78, 339–353.
- (11) “Conjugated polymer actuators for biomedical applications” Smela, E. *Adv. Mater.* **2003**, 15, 481–494.
- (12) “Metal–organic frameworks (MOFs)” Zhou, H.-C. J. and Kitagawa, S. *Chem. Soc. Rev.* **2014**, 43, 5415–5418.
- (13) “The pervasive chemistry of metal–organic frameworks” Long, J. R. and Yaghi, O. M. *Chem. Soc. Rev.* **2009**, 38, 1213–1214.
- (14) “Postsynthetic modification of metal–organic frameworks—a progress report” Tanabe, K. K. and Cohen, S. M. *Chem. Soc. Rev.* **2011**, 40, 498–519.
- (15) “Postsynthetic modification of metal–organic frameworks” Wang, Z. and Cohen, S. M. *Chem. Soc. Rev.* **2009**, 38, 1315–16.
- (16) “Tunable electrical conductivity in metal-organic framework thin-film devices.” Talin, A. A.; Centrone, A.; Ford, A. C.; Foster, M. E.; Stavila, V.; Haney, P.; Kinney, R. A.; Szalai, V.; Gabaly, El, F.; Yoon, H. P.; Léonard, F.; and Allendorf, M. *Science* **2014**, 343, 66–69.
- (17) “Electrically conductive porous metal–organic frameworks” Sun, L.; Campbell, M. G.; and Dincă, M. *Angew. Chem. Int. Edit. Engl.* **2016**, 55, 3566–3579.
- (18) “Cation-dependent intrinsic electrical conductivity in isostructural tetrathiafulvalene-based microporous metal-organic frameworks.” Park, S. S.; Hontz, E. R.; Sun, L.; Hendon, C. H.; Walsh, A.; Van Voorhis, T.; and Dincă, M. *J. Am. Chem. Soc.* **2015**, 137, 1774–1777.
- (19) “High electrical conductivity in Ni₃(2,3,6,7,10,11-Hexamino-triphenylene)₂, a semiconducting

- metal-organic graphene analogue.” Sheberla, D.; Sun, L.; Blood-Forsythe, M. A.; Er, S.; Wade, C. R.; Brozek, C. K.; Aspuru-Guzik, A.; and Dincă, M. *J. Am. Chem. Soc.* **2014**, *136*, 8859–8862.
- (20) “New porous crystals of extended metal-catecholates” Hmadeh, M.; Lu, Z.; Liu, Z.; and Gandara, F. *Chem. Mater.* **2012**, *24*, 3511–3513.
- (21) “Exploration of vanadium benzenedicarboxylate as a cathode for rechargeable lithium batteries” Kaveevivitchai, W. and Jacobson, A. J. *J. Power Sources* **2015**, *278*, 265–273.
- (22) “Mixed-valence Li/Fe-based metal–organic frameworks with both reversible redox and sorption properties” Férey, G.; Millange, F.; Morcrette, M.; Serre, C.; Doublet, M.-L.; Grenèche, J.-M.; and Tarascon, J.-M. *Angew. Chem. Int. Ed.* **2007**, *46*, 3259–3263.
- (23) “Synthesis, structure, characterization, and redox properties of the porous MIL-68(Fe) solid” Fateeva, A.; Horcajada, P.; Devic, T.; Serre, C.; Marrot, J.; Grenèche, J.-M.; Morcrette, M.; Tarascon, J.-M.; Maurin, G.; and Férey, G. *Eur. J. Inorg. Chem.* **2010**, 3789–3794. DOI: 10.1002/ejic.201000486.
- (24) “Reduction of a metal–organic framework by an organometallic complex: magnetic properties and structure of the inclusion compound $[(\eta^5\text{-C}_5\text{H}_5)_2\text{Co}]_{0.5}\text{@MIL-47(V)}$ ” Meilikhov, M.; Yussenko, K.; Torrisi, A.; Jee, B.; Mellot Draznieks, C.; Pöpl, A.; and Fischer, R. A. *Angew. Chem. Int. Edit. Engl.* **2010**, *49*, 6212–6215.
- (25) “Monitoring the solid-state electrochemistry of Cu(2,7-AQDC) (AQDC = anthraquinone dicarboxylate) in a lithium battery: coexistence of metal and ligand redox activities in a metal–organic framework” Zhang, Z.; Yoshikawa, H.; and Awaga, K. *J. Am. Chem. Soc.* **2014**, *136*, 16112–16115.
- (26) “MIL-101(Fe) as a lithium-ion battery electrode material: a relaxation and intercalation mechanism during lithium insertion” Shin, J.; Kim, M.; Cirera, J.; Chen, S.; Halder, G. J.; Yersak, T. A.; Paesani, F.; Cohen, S. M.; and Meng, Y. S. *J. Mater. Chem. A* **2015**, *3*, 4738–4744.
- (27) “Metal-organic frameworks for electrochemical applications” Morozan, A. and Jaouen, F. *Energy Environ. Sci.* **2012**, *5*, 9269–9290.
- (28) “Polarons, bipolarons, and solitons in conducting polymers” Bredas, J. L. and Street, G. B. *Acc. Chem. Res.* **1985**, *18*, 309–315.
- (29) “Selective binding of O₂ Over N₂ in a redox–active metal–organic framework with open iron(II) coordination sites” Bloch, E. D.; Murray, L. J.; Queen, W. L.; Chavan, S.; Maximoff, S. N.; Bigi, J. P.; Krishna, R.; Peterson, V. K.; Grandjean, F.; Long, G. J.; Smit, B.; Bordiga, S.; Brown, C. M.; Long, J. R. *J. Am. Chem. Soc.* **2011**, *133*, 14814–14822.
- (30) “Dramatic tuning of carbon dioxide uptake via metal substitution in a coordination polymer with cylindrical pores” Caskey, S. R.; Wong-Foy, A. G.; and Matzger, A. J. *J. Am. Chem. Soc.* **2008**, *130*, 10870–10871.
- (31) “Rod packings and metal–organic frameworks constructed from rod-shaped secondary building units” Rosi, N. L.; Kim, J.; Eddaoudi, M.; Chen, B.; O’Keeffe, M.; and Yaghi, O. M. **2005**, *127*, 1504–1518.
- (32) “Synthesis of a honeycomb-like Cu-based metal–organic framework and its carbon dioxide

- adsorption behaviour” Sanz, R.; Martínez, F.; Orcajo, G.; Wojtas, L.; and Briones, D. *Dalton Trans.* **2013**, *42*, 2392–2398.
- (33) “Enhanced H₂ adsorption in isostructural metal–organic frameworks with open metal sites: strong dependence of the binding strength on metal ions” Zhou, W.; Wu, H.; and Yildirim, T. *J. Am. Chem. Soc.* **2008**, *130*, 15268–15269.
- (34) “Million-fold electrical conductivity enhancement in Fe₂(debdc) versus Mn₂(debdc) (E = S, O).” Sun, L.; Hendon, C. H.; Minier, M. A.; Walsh, A.; and Dincă, M. *J. Am. Chem. Soc.* **2015**, *137*, 6164–6167.
- (35) “Ligand redox non-innocence in the stoichiometric oxidation of Mn₂(2,5-dioxidoterephthalate) (Mn-MOF-74)” Cozzolino, A. F.; Brozek, C. K.; Palmer, R. D.; Yano, J.; Li, M.; and Dincă, M. *J. Am. Chem. Soc.* **2014**, *136*, 3334–3337.
- (36) “Large-pore apertures in a series of metal-organic frameworks” Deng, H.; Grunder, S.; Cordova, K. E.; Valente, C.; Furukawa, H.; Hmadeh, M.; Gandara, F.; Whalley, A. C.; Liu, Z.; Asahina, S.; Kazumori H.; O’Keeffe M.; Terasaki O.; Stoddart J. F.; and Yaghi O. M. *Science* **2012**, *336*, 1018–1023.
- (37) “Cooperative insertion of CO₂ in diamine-appended metal-organic frameworks” McDonald, T. M.; Mason, J. A.; Kong, X.; Bloch, E. D.; Gygi, D.; Dani, A.; Crocellà, V.; Giordanino, F.; Odoh, S. O.; Drisdell, W. S.; Vlasisavljevich, B.; Dzubak, A. L.; Poloni, R.; Schnell, S. K.; Planas, N.; Lee, K.; Pascal, T.; Wan, L. F.; Prendergast, D.; Neaton, J. B.; Smit, B.; Kortright, J. B.; Gagliardi, L.; Bordiga, S.; Reimer, J. A.; and Long, J. R. *Nature* **2015**, *519*, 303–308.
- (38) “Mixed valence chemistry. a survey and classification” Robin, M. B. and Day, P. *Adv. Inorg. Chem. Radiochem.* **1968**, *10*, 247–422.
- (39) “Intervalence transitions in mixed-valence minerals of iron and titanium” Burns, R. G. *Annu. Rev. Earth Planet. Sci.* **1981**, *9*, 345–383.
- (40) “Fe(III), Mn(II), Co(II), and Ni(II) 3,4,5-trihydroxybenzoate (gallate) dihydrates; a new family of hybrid framework materials” Feller, R. K. and Cheetham, A. K. *Solid State Sciences* **2006**, *8*, 1121–1125.
- (41) “Reversible multivalent (monovalent, divalent, trivalent) ion insertion in open framework materials” Wang, R. Y.; Shyam, B.; Stone, K. H.; Weker, J. N.; Pasta, M.; Lee, H.-W.; Toney, M. F.; and Cui, Y. *Adv. Energy Mater.* **2015**, *5*, 1401869. doi:10.1002/aenm.201401869.
- (42) “Prussian blue: a new framework of electrode materials for sodium batteries” Lu, Y.; Wang, L.; Cheng, J.; and Goodenough, J. B. *Chem. Commun.* **2012**, *48*, 6544–6546.
- (43) “Insertion des ions PF₆⁻, AsF₆⁻ et SbF₆⁻ dans le graphite par methode electrochimique. Caracterisation des produits obtenus” Jobert, A.; Touzain, P.; and Bonnetain, L. *Carbon* **1981**, *19*, 193–198.
- (44) “Electrochemical intercalation of PF₆ into graphite” Dahn, J. R.; and Seel J. A. *J. Electrochem. Soc.* **2000**, *147*, 892–898.
- (45) “Single-ion magnetic anisotropy and isotropic magnetic couplings in the metal–organic framework Fe₂(dobdc)” Maurice, R.; Verma, P.; Zadrozny, J. M.; Luo, S.; Borycz, J.; Long, J. R.; Truhlar, D. G.; and Gagliardi, L. *Inorg. Chem.* **2013**, *52*, 9379–9389.
- (46) “A 3.90 V iron-based fluorosulphate material for lithium-ion batteries crystallizing in the

- triplite structure” Barpanda, P. *Nat. Mater.* **2011**, *10*, 772–779.
- (47) Given the large number of anions and fluctuations in solvation states for the compounds reported herein, all charge capacities were calculated using the mass of host lattice only in order to make chemically meaningful comparisons. because this diverges from normal convention, all literature values reported here were recalculated from the original discharge curves using the mass of the host lattice and not the mass of the reactants in the electrochemical reaction.
- (48) “Dual-ion cells based on anion intercalation into graphite from ionic liquid-based electrolytes” Placke, T.; Bieker, P.; Lux, S. F.; Fromm, O.; Meyer, H.-W.; Passerini, S.; and Winter, M. *Z. Phys. Chem.* **2012**, *226*, 391–407.
- (49) “Phospho-olivines as positive-electrode materials for rechargeable lithium batteries” Padhi, A. K.; Nanjundaswamy, K. S.; and Goodenough, J. B. *J. Electrochem. Soc.* **1997**, *144*, 1188–1194.
- (50) Volumes of anions were estimated from the cell volumes of their lithium salts. These values are tabulated with citations in Table S3.4.
- (51) “Charge localization in a 17-bond mixed-valence quinone radical anion” Nelsen, S. F.; Weaver, M. N.; and Telo, J. P. *J. Phys. Chem. A* **2007**, *111*, 10993–10997.
- (52) “Organic mixed valence” Hankache, J. and Wenger, O. S. *Chem. Rev.* **2011**, *111*, 5138–5178.
- (53) “Metal–organic frameworks as solid magnesium electrolytes” Aubrey, M. L.; Ameloot, R.; Wiers, B. M.; and Long, J. R. *Energy Environ. Sci.* **2014**, *7*, 667–671.
- (54) “In situ NMR spectroscopy of supercapacitors: insight into the charge storage mechanism” Wang, H.; Forse, A. C.; Griffin, J. M.; Trease, N. M.; Trognko, L.; Taberna, P.-L.; Simon, P.; and Grey, C. P. *J. Am. Chem. Soc.* **2013**, *135*, 18968–18980.
- (55) “Ion exclusion by sub-2-nm carbon nanotube pores.” Fornasiero, F.; Park, H. G.; Holt, J. K.; Stadermann, M.; Grigoropoulos, C. P.; Noy, A.; and Bakajin, O. *Proc. Natl. Acad. Sci. U.S.A.* **2008**, *105*, 17250–17255.
- (56) “Infiltration of electrolytes in molecular-sized nanopores” Liu, L.; Chen, X.; Lu, W.; Han, A.; and Qiao, Y. *Phys. Rev. Lett.* **2009**, *102*, 184501–4.
- (57) “Quantized ionic conductance in nanopores” Zwolak, M.; Lagerqvist, J.; and Di Ventra, M. *Phys. Rev. Lett.* **2009**, *103*, 128102–4.
- (58) “Towards greener and more sustainable batteries for electrical energy storage” Larcher, D. and Tarascon, J.-M. *Nat. Chem.* **2014**, *7*, 19–29.
- (59) “Electrochemical stability of non-aqueous electrolytes for sodium-ion batteries and their compatibility with $\text{Na}_{0.7}\text{CoO}_2$ ” Bhide, A.; Hofmann, J.; Dürr, A. K.; Janek, J.; and Adelhelm, P. *Phys. Chem. Chem. Phys.* **2014**, *16*, 1987–1998.
- (60) “A solid lithium electrolyte via addition of lithium isopropoxide to a metal–organic framework with open metal sites” Wiers, B. M.; Foo, M.-L.; Balsara, N. P.; and Long, J. R. *J. Am. Chem. Soc.* **2011**, *133*, 14522–14525.
- (61) “Rhombohedral prussian white as cathode for rechargeable sodium-ion batteries” Wang, L.; Song, J.; Qiao, R.; Wray, L. A.; Hossain, M. A.; Chuang, Y.-D.; Yang, W.; Lu, Y.; Evans, D.; Lee, J.-J.; Vail, S.; Zhao, X.; Nishijima, M.; Kakimoto, S.; and Goodenough, J. B. *J. Am.*

- Chem. Soc.* **2015**, *137*, 2548–2554.
- (62) “Reversible NaFePO₄ electrode for sodium secondary batteries” Oh, S.-M.; Myung, S.-T.; Hassoun, J.; Scrosati, B.; and Sun, Y.-K. *Electrochem. Commun.* **2012**, *22*, 149–152.
- (63) “Influence of graphite characteristics on the electrochemical intercalation of bis(trifluoromethanesulfonyl) imide anions into a graphite-based cathode” Placke, T.; Rothermel, S.; Fromm, O.; Meister, P.; Lux, S. F.; Huesker, J.; Meyer, H.-W.; and Winter, M. *J. Electrochem. Soc.* **2013**, *160*, A1979–A1991.
- (64) Individual discharge curves are labeled in the Figure S3.17 with the specific phase transformation and corresponding citation.
- (65) “Preparation of solid thianthrene cation radical tetrafluoroborate” Boduszek, B. and Shine, H. J. *J. Org. Chem.* **1988**, *53*, 5142–5143.
- (66) “Mixed valence of iron in minerals with cation clusters” Amthauer, G. and Rossman, G. R. *Phys. Chem. Miner.* **1984**, *11*, 37–51.
- (67) “Separation of hexane isomers in a metal-organic framework with triangular channels.” Herm, Z. R.; Wiers, B. M.; Mason, J. A.; van Baten, J. M.; Hudson, M. R.; Zajdel, P.; Brown, C. M.; Masciocchi, N.; Krishna, R.; and Long, J. R. *Science* **2013**, *340*, 960–964.
- (68) “Functionalization in flexible porous solids: effects on the pore opening and the host–guest interactions” Devic, T.; Horcajada, P.; Serre, C.; Salles, F.; Maurin, G.; Moulin, B.; Heurtaux, D.; Clet, G.; Vimont, A.; Grenèche, J.-M.; et al. *J. Am. Chem. Soc.* **2009**, *132*, *3*, 1127–1136.
- (69) “Porous, conductive metal-triazolates and their structural elucidation by the charge-flipping method.” Gándara, F.; Uribe-Romo, F. J.; Britt, D. K.; Furukawa, H.; Lei, L.; Cheng, R.; Duan, X.; O’Keeffe, M.; and Yaghi, O. M. *Chem. Eur. J.* **2012**, *18*, 10595–10601.
- (70) “Anomalously large formula unit volume and its effect on the thermal behavior of LiBF₄” Kazuhiko Matsumoto; Rika Hagiwara; Zoran Mazej; Evgeny Goreshnik, A.; and Žemva, B. *J. Phys. Chem. B* **2006**, *110*, 2138–2141.
- (71) “Die Kristallstrukturen von Li[PF₆] und Li[AsF₆]: Zur Kristallchemie von Verbindungen A[E^VF₆] / The Crystal Structures of Li[PF₆] and Li[AsF₆]: On the Crystal Chemistry of Compounds A[E^VF₆]” Röhr, C.; and Kniep, R.; *Z.Naturforsch. B* **1994**, *49b*, 650–654.
- (72) “Structure of LiN(CF₃SO₂)₂, a novel salt for electrochemistry” Nowinski, J. L.; Lightfoot, P.; and Bruce, P. G. *J. Mater. Chem.* **1994**, *4*, 1579–1580.
- (73) “Thallium tetrakis(pentafluorophenyl)borate” Parvez, M.; Piers, W. E.; and Ghesner, I. *Acta Crystallographica* **2005**, *E61*, m1801–m1803. doi:10.1107/S1600536805025808.
- (74) “Na₂FeP₂O₇: a safe cathode for rechargeable sodium-ion batteries” Barpanda, P.; Liu, G.; Ling, C. D.; Tamaru, M.; Avdeev, M.; Chung, S.-C.; Yamada, Y.; and Yamada, A. *Chem. Mater.* **2013**, *25*, 3480–3487.
- (75) “Room-temperature stationary sodium-ion batteries for large-scale electric energy storage” Pan, H.; Hu, Y.-S.; and Chen, L. *Energy Environ. Sci.* **2013**, *6*, 2338–2360.
- (76) “Synthesis and electrode performance of carbon coated Na₂FePO₄F for rechargeable Na batteries” Kawabe, Y.; Yabuuchi, N.; Kajiyama, M.; Fukuhara, N.; Inamasu, T.; Okuyama, R.; Nakai, I.; and Komaba, S. *Electrochem. Commun.* **2011**, *13*, 1225–1228.

Chapter 4

Interrogation of charge transport in metal-organic frameworks by gas sorption

4.1 Introduction

Metal-organic frameworks have garnered much attention due to their fantastic structural diversity and potential as component materials in gas sorption and separation-based applications.¹⁻⁶ However, it is the inherent modularity of these metal-organic hybrid materials that yields an unprecedented level of control and specificity in crystal engineering. In addition to superior performance in existing technologies, a key advantage of metal-organic frameworks over traditional porous solids is the potential amalgamation of disparate functionalities. That is, the hybrid nature of these framework materials make it easier and more intuitive to produce multifunctional materials that can potentially enable new technologies not possible with zeolite or activated carbons.^{7,8}

Traditional porous crystals, such as zeolites, derive their permanent porosity from their of open network structures stabilized by particularly strong sigma-bond networks between oxyanions donors and oxophilic cations like Zr^{4+} , Si^{4+} , Al^{3+} , Mg^{2+} and Zn^{2+} . However, unlike zeolites, the chemistry of metal-organic frameworks is not constrained to these highly localized interactions, making emergent long range and cooperative effects more accessible.⁹⁻¹³ In fact, the diversity of possible structures derived from molecular coordination chemistry and organic synthesis has yielded a whole host of new phenomena difficult to replicate in other materials. One curious property to emerge from the new chemistry of MOFs is bulk electrical conductivity.¹⁴

This combination of crystallinity, permanent porosity, and bulk electrical conductivity yield a truly unique set of material properties. Mastery of charge transport in porous crystals may result in new technologies including energy storage,^{15,16} gas sensing,^{17,18} electrocatalysis,¹⁹⁻²¹ and field gated gas sorption.²² However, the number of porous conductive frameworks is relatively small and the state of research remains nascent. While several strategies for engendering bulk conductivity in metal-organic frameworks have been proposed, many of these are difficult to control or predict like serendipitous pi-stacking or close sulfur-sulfur contacts.²³ Extremely high conductivities and charge mobilities have been observed in lamellar pi-d conjugated coordination solids. However, most of these are non-porous and the few that are lack the diverse surface chemistry that distinguish metal-organic frameworks from materials like activated carbons.²⁴⁻²⁷ Techniques like redox doping, while widely applicable to a host of metal-organic framework chemistries, usually sacrifice surface area for bulk conductivity.^{28,29}

Much of this apparent difficulty in obtaining metal-organic frameworks with both desirable charge transport and interesting host-guest interactions stems from persistent lack of understanding of general design principles for the synthesis of high surface area, conductive frameworks. Likewise, much of the underlying processes that determine or limit transport in porous crystals remains poorly

understood. Furthermore, while there have been a number of breakthrough reports on the dependence of solvents and volatile organic guest species on charge transport, linking these changes to specific host-guest interactions has not yet been possible.³⁰⁻³³

One strategy to better elucidate the mechanics of conductivity and the link between charge transport, surface chemistry, and host-guest interactions is to leverage the permanent porosity of metal-organic frameworks. That is, the interrogation of transport in a metal-organic framework within a typical gas sorption experiment may be an easily implemented mode of precisely modulating conductivity via inclusion of gaseous probe molecules. Under such pure component isothermal conditions, changes in conductance may be related to guest specific lattice interactions. Currently, such measurements are difficult or impossible with technology driven chemresistive sensing experiments where transport modulation is derived from a substitution reaction.^{31,33} Further, by measuring conductivity during a standard gas sorption measurement, conductivity-composition profiles may be readily determined and the conductivity of precisely determined phase composition reported.

To this end, the previously reported conductive metal-organic framework Cu[Ni(pdt)₂] was selected as a case study, **Figure 4.1**.³⁴ This particular phase is notable for being the first permanently porous conductive metal-organic framework, and more recently for its ability to selectively adsorb

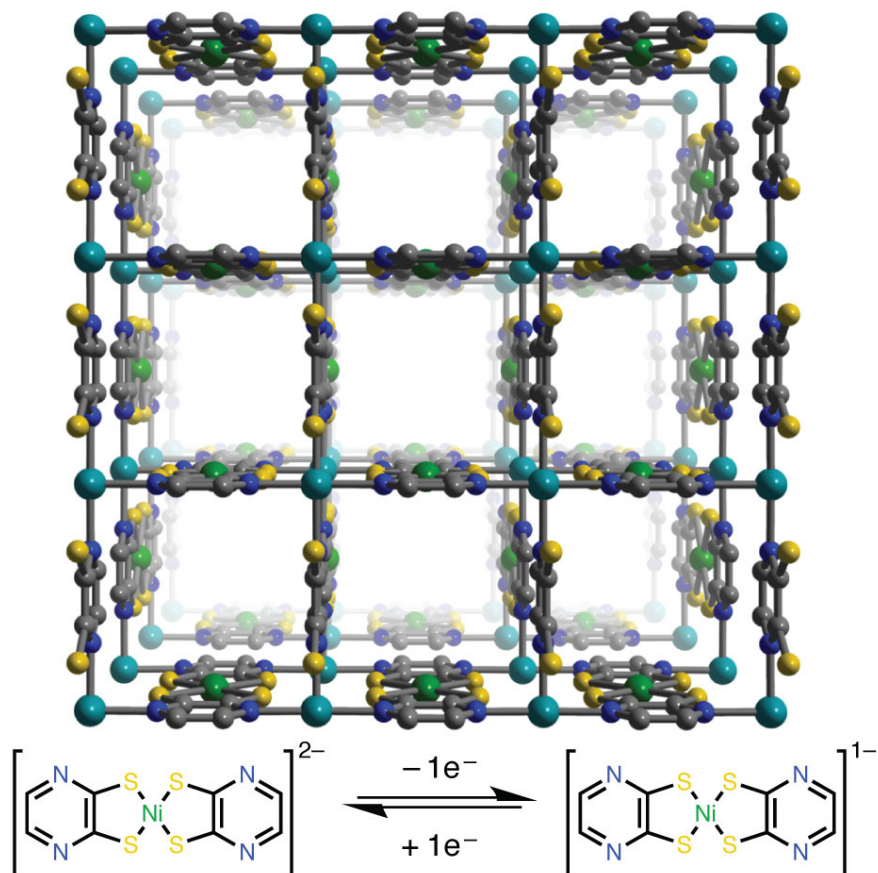


Figure 4.1. A portion of the crystal structure of Cu[Ni(pdt)₂] (top). Copper is shown in teal, nickel in green, sulfur in yellow, nitrogen in blue, carbon in grey and hydrogen in white. The one-dimensional pore structure is directed into the page. Bond-angle structure of the Ni(pdt)₂ subunit and the reaction scheme from which the charge carrier density of this material originates (bottom).

and efficiently separate light hydrocarbons.³⁵ Importantly, among all porous metal-organic frameworks Cu[Ni(pdt)₂] is a very rare example of a framework with both significant conductivity and desirable gas sorption properties stemming from a unique surface chemistry.³⁶

4.2 Results and discussion

The structure of Cu[Ni(pdt)₂], **Figure 4.1**, forms a three-dimensional lattice of square planar nickel pyrazine-1,2-dithiolate units networked by octahedral copper ions to yield a one-dimensional pore system. While the structure is anisotropic, significant conductivity along all three axes may be expected given the similarity in coordination environments and connectivity. The Ni(pdt)₂ units are redox active and can potentially interact strongly with guests at the valence states primarily centered within the Ni-S π -*d* manifold. Notably, similar Ni(pdt)₂ congeners in solution have also been found to interact strongly with unsaturated hydrocarbons.³⁷ Further, fractional oxidation of this subunit in Cu[Ni(pdt)₂] increases the bulk conductivity by a factor of one-thousand, suggesting that the potential binding site is also the primary source of carriers for charge transport.³⁴

4.2.1 Hopping transport in Cu[Ni(pdt)₂]. Slight modification of the original Cu[Ni(pdt)₂] synthesis afforded a material with higher purity and comparable surface area (Langmuir: 426 m² g⁻¹). Remarkably, by a two-contact, pressed pellet measurement, the conductivity was found to be about twenty times higher (2.6 μ S cm⁻¹) than previously reported. However, it should be noted that variances of an order of magnitude in conductivity may result from differences in pellet preparation and measurement conditions.³⁰ Nonetheless, the simultaneous optimization of gas sorption and conductivity with the same sample was encouraging. By ac impedance spectroscopy, **Figure 4.2**, a single Debye type relaxation mode was observed with a well-defined time constant. In view of these results, bulk transport in Cu[Ni(pdt)₂] is best described as charge hopping, likely between mid-gap states localized on individual Ni(pdt)₂ units.³⁸ It cannot as of yet be ruled out whether quantities of oxidized Ni(pdt)₂ undetectable by analytical methods are responsible for hopping transport given the relatively low conductivity of $\sim 1 \mu$ S cm⁻¹.

In order to determine the effect of solvation state on conductivity, the activated phase was exposed to acetonitrile vapor (the synthesis solvent) at room temperature for 12 hours. Remarkably, the conductivity decreased by a factor of nearly two hundred-fold to 0.015 μ S cm⁻¹, with no apparent loss in crystallinity. This value matches nicely with that of the synthesized phase originally reported as Cu[Ni(pdt)₂] $\cdot n$ MeCN. Changes in conductivity upon exposure to similar volatile organic

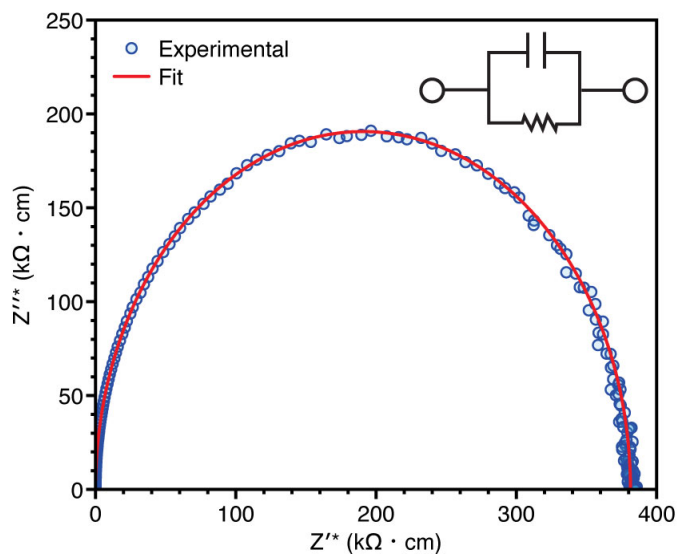


Figure 4.2. Nyquist impedance plot of Cu[Ni(pdt)₂] from 1 MHz to 0.01 Hz with a 100 mV sinus amplitude and fit to a model circuit (inset) representative of Debye type relaxation or bulk hopping transport through the sample.

compounds in other conductive MOFs are normally much smaller though reports are still scarce.^{30,31} This extreme sensitivity to a volatile organic compound encouraged us to probe the structure with other guest species that typically interact much less strongly with porous materials, i.e. gases.

4.2.2 Transport modulation by gas sorption. To this end, a conductivity cell that could be directly attached to a Micromeritics 3-flex gas sorption analyzer was constructed. A simplified diagram is shown in **Figure 4.3**. An OCR to Swagelok fitting was attached to a two-way Swagelok valve followed by an expansion to a 1/2 inch tube diameter. The conductivity cell was attached at the bottom of the apparatus with a union tee. In order to ensure a vacuum tight seal capable of maintaining pressures less than 0.1 μ bar, the cables attached to the cell were threaded through small section of 1/2-inch diameter tubing at the bottom of the cell and the tubing was then filled with a solventless high vacuum epoxy.

While this setup can support any number of conductivity measurement geometries, given the relatively low conductivity of activated $\text{Cu}[\text{Ni}(\text{pdt})_2]$, a two-contact method was sufficient. To accomplish this, a printed circuit board with copper leads was fabricated with two long, parallel leads separated by 152 μm . A thin pellet, (50–100 μm) of $\text{Cu}[\text{Ni}(\text{pdt})_2]$ was pressed between the two copper rails using a mechanical press in an argon glovebox. The Swagelok cell was sealed and the valve closed to prevent exposure to air with transfer to the gas sorption analyzer.

The conductivity of $\text{Cu}[\text{Ni}(\text{pdt})_2]$ was measured at room temperature with a variety of gases under one bar relative to vacuum. Dinitrogen, helium, argon, and methane all resulted only small changes in conductivity (about a 1% enhancement or less for all three). Further, no immediate step in conductance was observable for any of these gases. Any slight shift that occurred was over several minutes and was likely the result of a change in pressure rather than an interaction with the analyte. With such a small response, especially compared to the saturated acetonitrile phase, the signal-to-noise level was unfortunately too low (< 1) to obtain accurate data for these gases. However, considering that this particular framework binds these gases only very weakly and that the capacity at one bar is very small, a small change in transport is to be expected.

4.2.3 Isothermal response of hydrocarbons at equilibrium. In contrast, this framework does display significant absorption of certain hydrocarbons, like ethylene, ethane and propane. For these

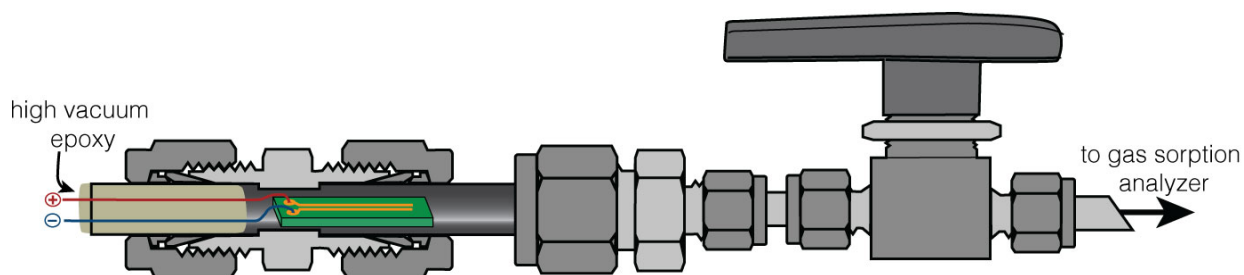


Figure 4.3. Schematic of conductivity cell for *in situ* transport measurements on a gas sorption analyzer. A pressed pellet of the polycrystalline sample is embedded between the two copper rails on the green the circuit board and the resistance of the closed circuit measured.

gases, the change in conductivity is significant. **Figure S4.8**, shows the raw, transient changes in conductance at constant voltage upon ethylene dosing. Subsequent evacuation back to 0.1 μ bar showed a facile return to the original baseline and confirmed the reversibility of the response. Notably, the dose-evacuation cycles could be performed very quickly with the change in conductance stabilizing after only about ten seconds.

The room temperature conductivity of $(C_xH_y)_nCu[Ni(pdt)_2]$ was determined at equilibrium as a function of pressure for propane ($x, y = 3, 8$), ethane ($x, y = 2, 6$), and ethylene ($x, y = 2, 4$), **Figure 4.4**. While ethylene adsorption and change in conductivity are the steepest at low pressure, both ethane and propane display a larger relative conductivity at 1 bar and greater average sensitivities over the entire pressure range. With all three gaseous probe molecules, a monotonic increase in conductivity with pressure was observed, reminiscent of a Type I adsorption isotherm. Thus, while entirely empirical, all three isotherms could be tentatively modeled with excellent agreement with an equation identical in form to the Langmuir-Freundlich relation. This may imply that the change in conductivity correlates strongly with the quantity of gas adsorbed.

In comparison to the adsorption isotherms, the relative curvature of the conductivity-pressure relation also matches closely, as shown in **Figure 4.4a**. Given the extremely small amount of material used in the conductivity measurements, the isotherms shown here were collected with a larger quantity of material from the same sample batch, and were measured by methods established previously.³⁹ The ethylene gas sorption isotherm is the steepest, however, the trend for saturation capacity is the reverse of the trend for conductivity. Ethylene, being the smallest and most strongly adsorbed also displays the greatest capacity near 1 bar, while ethane and propane showed lower capacities. This is expected given the larger molecular volumes of ethane and propane. However, the underlying reasons for why charge transport is less sensitive to more strongly interacting guests with higher concentrations is less clear.

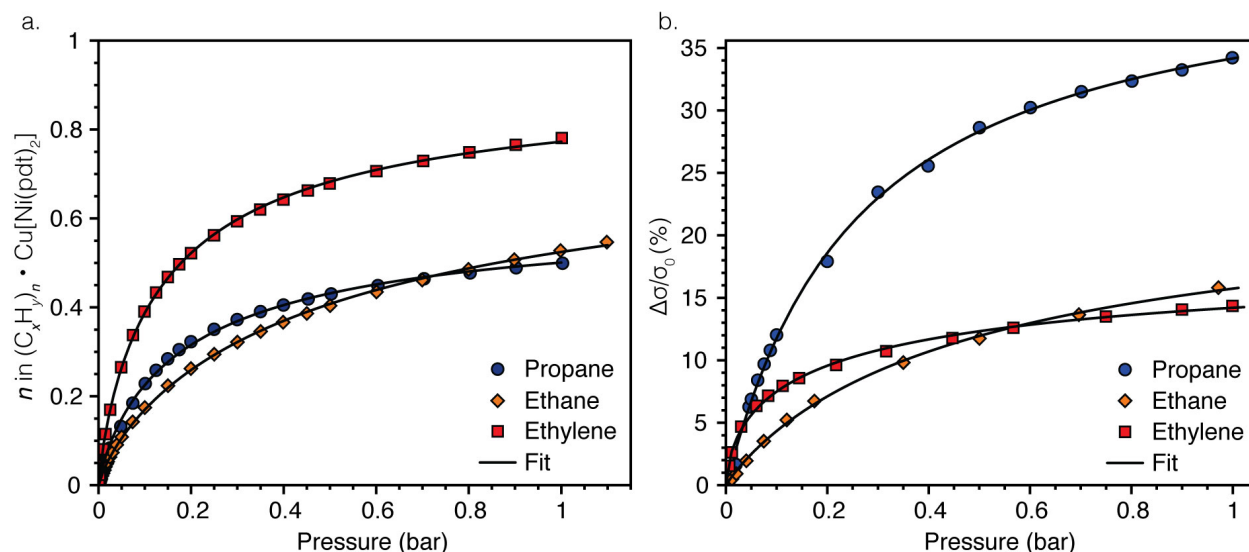


Figure 4.4. Room temperature gas adsorption isotherms (a) and room temperature conductivity isotherms as a function of absolute pressure (b) for propane (blue circles), ethane (orange diamonds), and ethylene (red squares). Empirical fits to the data are given in black and are identical in form to the Langmuir-Freundlich equation. Gas adsorption was measured on the same sample batch independently with a larger sample mass.

4.2.4 Conductivity-composition profiles. Perhaps a better way to consider the change in conductance of these gases upon gas sorption is not as a function of pressure but rather phase composition. By modeling both isotherms, points of equivalent pressure were interpolated to yield the equilibrium conductivity-composition profiles as shown in **Figure 4.5**. From this, a more intuitive relationship emerges. First, a near linear dependence of conductivity with respect to equivalents of gas adsorbed was observed, especially in the high-pressure limit. Calculating the slopes of these curves with a simple linear fit, allowed for an approximation of the materials' sensitivity to each gas to be determined. Conductivity is least sensitive the amount of ethylene present in the pores. This is surprising considering that it has the greatest adsorption enthalpy and thus interacts most strongly with the host lattice at the Ni(pdt)₂ centers. This is additionally evidenced by powder neutron diffraction where ethylene was found to crystallographically ordered at cryogenic temperatures.⁴⁰ By slope analysis, ethane is about 1.9 times more sensitive to the amount of guest included compared to ethylene; propane is 4.7 times more sensitive than ethylene.

It does not appear that the strength of interaction (enthalpy of adsorption) is responsible for the changes in conductance. This is not unreasonable considering charge transport, while a steady state measurement, is an intrinsically dynamic effect; especially in the case of the hopping transport that is observed here. Instead of modulating the frontier band edges, guest molecules in (C_xH_y)_nCu[Ni(pdt)₂] should be considered as scattering agents, colliding with the pore walls and thus creating new vibrational excited states that are not present in the evacuated phase (*n* = 0). One explanation for the different sensitivities for different gases is mutual polarization, which is largely responsible for the band structure and transport properties of undoped semiconductors.⁴¹ Since the host lattice itself is unchanged with gas sorption, the polarizabilities of the guests themselves may be compared directed. The trend is correct ($\alpha_{\text{propane}} > \alpha_{\text{ethane}} > \alpha_{\text{ethylene}}$), but the polarizabilities of ethane and ethylene are very similar (44 and 42.5 · 10²⁵ cm³ respectively) while that of propane is significantly larger, 63 · 10²⁵ cm³.⁴² Accordingly, this may not be the best description of enhanced hopping transport in this material.

The most important host guest interaction is one that effectively reduces the thermal barrier to hopping transport. As such, it may be expected that sensitivity the included guest scales with the canonical ensemble of allowable states available to transfer heat to the host lattice. This capacity to transfer heat is, to a first approximation, the standard entropy of each guest at room temperature. **Figure S4.9** plots the gas phase entropy as a function of sensitivity, to show a linear correlation.⁴³ This result further supports an

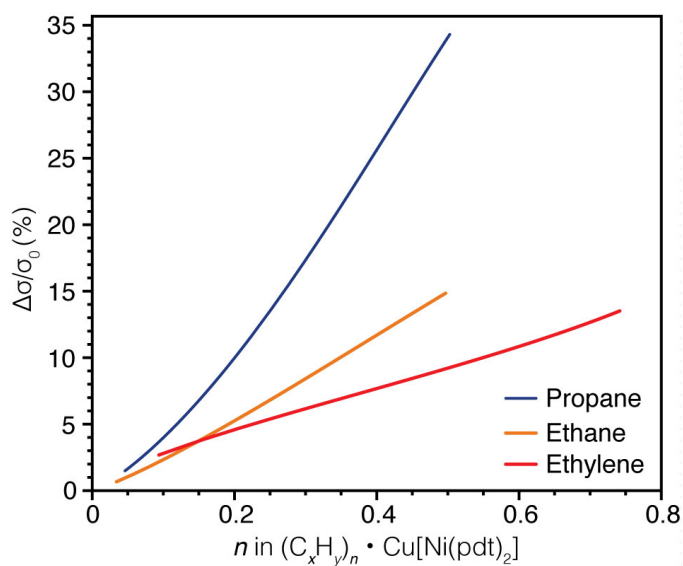


Figure 4.5. Conductivity-composition profiles in the phase (C_xH_y)_nCu[Ni(pdt)₂] for propane (x = 3, y = 8), ethane (x = 2, y = 6) and ethylene (x = 2, y = 4).

intrinsic hopping transport mechanism in $\text{Cu}[\text{Ni}(\text{pdt})_2]$, and is the first example relating specific host-guest interactions in a metal-organic framework and fundamental thermodynamic properties to emergent charge transport phenomena. The ability to probe and understand how local host-guest interactions affect bulk transport by direct measurement is exceptionally difficult, and use of gaseous probes, as shown here, presents a simple alternative for doing so in porous crystals.

4.2.5 Kinetic analysis of guest binding and charge transport upon dosing.

Both the quantity of adsorbed gas and the change in conductivity were determined as a function of time, enabling a kinetic analysis of the chemresistive effect to be compared to the equilibration of the bulk crystal, **Figures S4.10–S4.12**.

The rate of adsorption for all the gases suggests a combination of rate limiting effects. Over very short times (less than one minute) gas sorption was limited by a combination of diffusion and gas conduction through the manifold that was difficult to model. Over longer time intervals, the rate of adsorption corresponded nicely with equilibration kinetics for a reversible adsorption-desorption process, **Figure S4.13**.⁴⁴ In contrast to the equilibration of the bulk composition, the chemresistive effect was fast. In fact, much of the saturation kinetics are masked by gas conduction through the manifold in the first few seconds after dosing. This is confirmed with dosing at higher pressures, where a gas conduction induced echo effect is observed in the first few seconds, **Figures S4.11 and S4.12**. Over the entire time allotted for equilibration, the change in conductivity consistently saturated faster than the bulk host-guest inclusion at all pressures.

There are two explanations for the observed rate of chemresistive response. One is that conductivity is measured directly on the sample being probed while pressure equilibration is determined far away and requires the transmittance of pressure changes through several feet of manifold. This is evidenced by the time difference with respect to the echo effect, which was seen in the first few seconds by conductivity, but not until much later by the pressure transducer. The other difference is that conductivity in the pressed pellet likely limited by intercrystalline contact resistances. This effect is broadly claimed for pressed pellet conductivity measurements, but is seldom confirmed experimentally.³⁰ Conductivity through a single crystal is expected to be much higher than between crystals, and can differ by several orders of magnitude. Additionally, a small decrease in resistance at crystal contacts can cause a significant change in the bulk resistance of the samples, while a comparable effect within a single crystal is masked. This mechanism is illustrated in

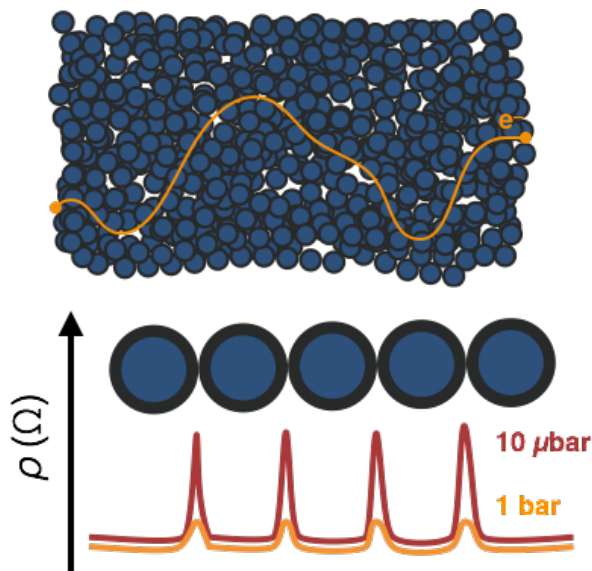


Figure 4.6. Illustration of a bulk electron path through a pressed pellet conducting through both bulk crystallite and across interparticle contacts (top). A one-dimensional model plotting the relative resistivity both within and between neighboring crystallites (bottom). Both intracrystallite and intercrystallite resistivity decrease with gas adsorption but intercrystallite contacts decrease more.

Figure 4.6. A similar mechanism is invoked in chemresistive gas sensors made with sintered metal-oxide active materials, where more energetic grain boundaries and interparticle contacts are believed to be most sensitive.⁴⁵

4.3 Conclusions

A simple adaptation of a standard gas sorption analyzer was constructed, allowing the *in situ* determination of conductivity as a function of pressure and gaseous analyte. The change in conductivity of Cu[Ni(pdt)₂] was found to increase almost linearly with the quantity of hydrocarbon absorbed, and the relative sensitivity correlated strongly with the gas phase entropy of the included guest. Notably, the chemiresistivity of Cu[Ni(pdt)₂] is non-responsive for other gases like CO₂, O₂, N₂, Ar, and He. Further, for hopping conductors like Cu[Ni(pdt)₂], it was found that the included guests essentially act as scattering centers that thermally excite charge carriers and increase bulk conductivity. Additionally, chemiresistivity in this framework was remarkably fast and confirmed that the single crystal conductivity of Cu[Ni(pdt)₂] is likely significantly greater than the conductivity between crystallites that appears to be transport limiting. Most significantly, the method described herein is simple and uses the evacuated framework of a known and well defined composition. As such, this method can serve as a standard for characterizing transport and its modulation upon gas or vapor dosing since it allows the direct determination of conductivity-composition profiles, unlike in more practical gas sensing apparatuses. Moving forward, other investigations of host guest interactions will be performed, including gas phase redox doping, partial charge transfer reactivity, the continued search for band-like surface polarization effects, and studies on the effects of ion transport with vapor dosing by ac impedance methods.

4.4 Experimental methods

4.4.1 General procedures and measurements. The synthesis of Na₂[Ni(pdt)₂] was completed according to the literature procedure.³⁴ Diffraction data were collected using a Bruker AXS D8 Advance diffractometer with the generator set at 40 kV and 40 mA; samples were loaded onto zero-background sample holders. Elemental analysis was obtained from the Microanalytical Laboratory at the University of California, Berkeley.

4.4.2 Modified synthesis of Cu[Ni(pdt)₂]. The synthesis of Cu[Ni(pdt)₂] was adapted from a previous report.³⁴ A flask was charged with 270 mL acetonitrile and sparged with dry N₂ for 30 min. Na₂[Ni(pdt)₂] (0.630 g, 1.62 mmol) was added and the solution was stirred. A separate flask was charged with 75 mL of acetonitrile, sparged with dry N₂ for 30 min, and CuI (0.309 g, 1.62 mmol) was added. While under positive nitrogenous atmosphere, the CuI solution was slowly added to the solution of Na₂[Ni(pdt)₂] via a syringe, rapidly precipitating Cu[Ni(pdt)₂] as a black solid. The resulting solid was filtered on 0.22- μ m nylon filter paper in air and activated overnight at 90 °C under high vacuum on a Micromeritics ASAP 2420 instrument equipped with a turbo pump, yielding 0.453 g of the framework (68.8% yield). Powder diffraction pattern is shown in **Figure S4.1** and the isotherm used to calculate the Langmuir surface area is given in **Figure S4.2**. Elemental

Analysis for Cu[Ni(pdt)₂]: calcd C 23.63%, H 0.99%, N 13.78%, S 31.54%; found: C 22.92%, H 1.05%, N 13.74%, S 30.43%.

4.4.3 Gas adsorption measurements. Low-pressure gas adsorption data between 0 and 1.1 bar were measured using a Micromeritics 3Flex instrument. Samples consisting of Cu[Ni(pdt)₂] powder were loaded into a pre-weighed tube, and heated at 90 °C overnight. The mass of the activated sample was used as the basis for the adsorption measurements. After an adsorption isotherm was measured, the sample was reactivated at 90 °C before measuring a subsequent adsorption isotherm.

4.4.4 Ac impedance measurements. In an argon filled glovebox, the activated Cu[Ni(pdt)₂] was pressed into a pellet inside a 2-contact PEEK screw cell as previously reported.⁴⁶ The ac electronic conductivity of Cu[Ni(pdt)₂] was determined using a Bio-Logic VMP-3 multipotentiostat equipped with an impedance analyzer between the frequencies 1 MHz and 0.01 Hz, a sinus amplitude of 100 mV and dc bias voltage of 0 mV. The observed spectrum was ohmic with dc bias voltage (**Figure S4.3**), linear with sinus amplitude (**Figure S4.4**), causal/time invariant as confirmed by calculation of the Kramers-Kronig transform (**Figure S4.5**), and matched closely to what would be expected for a single Debye type relaxation process with a well-defined time constant (**Figures 4.2, S4.6, S4.7**).⁴⁷

4.4.5 Time resolved gas sorption and *in situ* conductivity measurements. Conductivity and gas sorption were measured as a function of time using the conductivity cell shown in **Figure 4.3**. A short ~3-inch piece of stock 1/2-inch stainless steel tubing was cut, deburred and fitted with Swagelok ferrules. Printed circuit board arrays were designed using the free computer aided design software package PBC123 and submitted to rapid prototyping service Sunstone Circuits for fabrication. The arrays consisted of sets of two vias and two 1-oz copper rails spaced by a 0.152 μm gap printed on a standard FR-4 base. Individual sets of rails were hand cut to fit within the 1/2-inch OD tubing and silver coated copper conductors were soldered in place. The board was then threaded through the pre-cut tubing and the bottom two thirds of the tube was filled with a solventless high vacuum expox (TorrSeal® or Hysol 1C) such that the board was fully exposed above the end of the tube with the ferrules attached. The adapter for the Micromeritics 3-Flex consisted on a 1/2-inch union, a 1/2-inch to 1/4-inch reducing coupling, a two-way Swagelok ball valve and a 1/4-inch Swagelok to OCR adapter (not shown in **Figure 4.3**).

The circuit board and adapter were transferred to an argon-filled glovebox. A pellet of Cu[Ni(pdt)₂] powder was prepared on top of the two copper rails using a mechanical press with thicknesses typically on the order of 50 μm to 100 μm. The circuit board was attached to the union on the adapter and sealed in the glovebox. The entire apparatus was then transferred under argon to the analysis port on the gas sorption analyzer. After ~3 hours of cycling between 1 bar and <1 μbar of helium the cell was left under vacuum to stabilize.

The cables connected to the samples were attached with banana plugs to a Bio-Logic SP-200 6-lead potentiostat that was used as a precision source-meter. The potentiostat, measurement cell and gas sorption analyzer were all set to a common ground to reduce noise. For a typical experiment, currents of 1 μA to 10 μA were applied and the voltage response measured with 0.5 second time

resolution. After the voltage response stabilized, a gas sorption isotherm was measured. Given the low mass of sample in the pellet the mass error for these isotherms was relatively large in comparison to the methods described in **Section 4.5.3** where a much larger sample mass was used. An exemplary raw data set is given in **Figure S4.14** showing clearly resolved steps between pressure points. The standard deviation of the baseline noise was about 0.7 mV. Signal to noise ratios were about three for the first pressure point in **Figure S4.14** and greater than 10 for all subsequent pressure points.

Rate of adsorption data was extracted directly from the 3Flex gas sorption analyzer using the PuTTY client to access the raw data transmitted from the instrument with 0.5 second time resolution. Detailed specifics for accessing this data via ethernet connection are instrument dependent and available from Micromeritics by request.

4.5 Acknowledgements

This research was supported by the National Science Foundation under award no. DMR-1309066. I would like to also thank Matt Kapelewski and Jonathan Melville for supplying the Cu[Ni(pdt)₂] sample.

4.6 Supporting figures

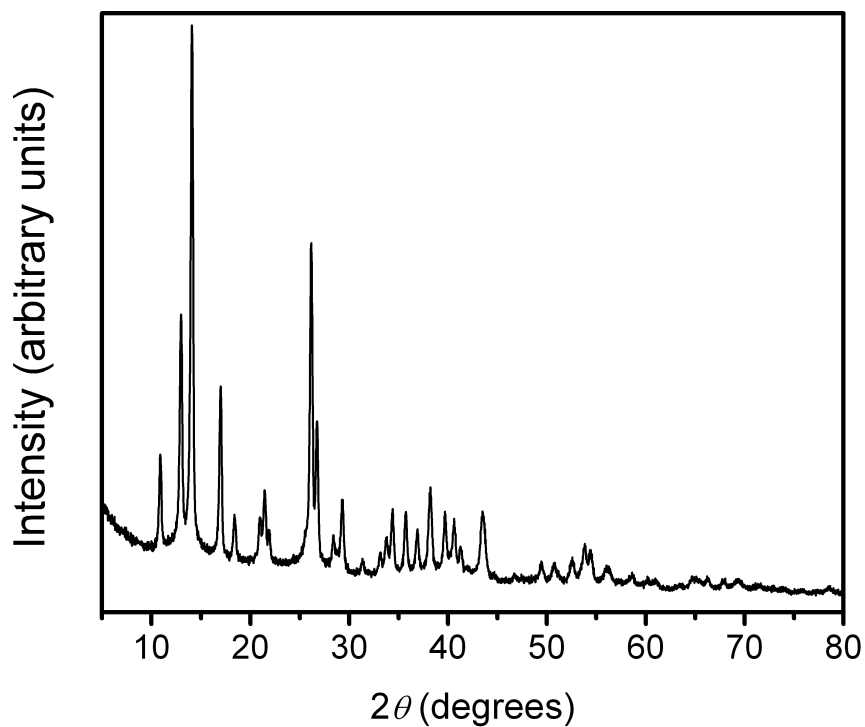


Figure S4.1. The powder X-ray diffraction pattern of Cu[Ni(pdt)₂] synthesized using the modified literature procedure.

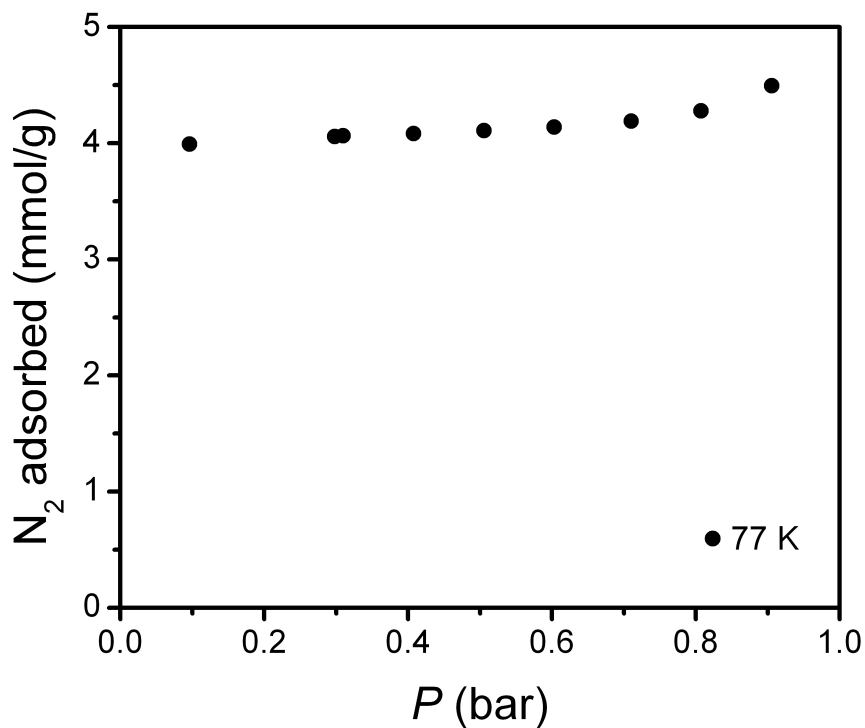


Figure S4.2. The 77 K N₂ adsorption isotherm of Cu[Ni(pdt)₂] used to calculate the Langmuir surface area of 426 m²/g.

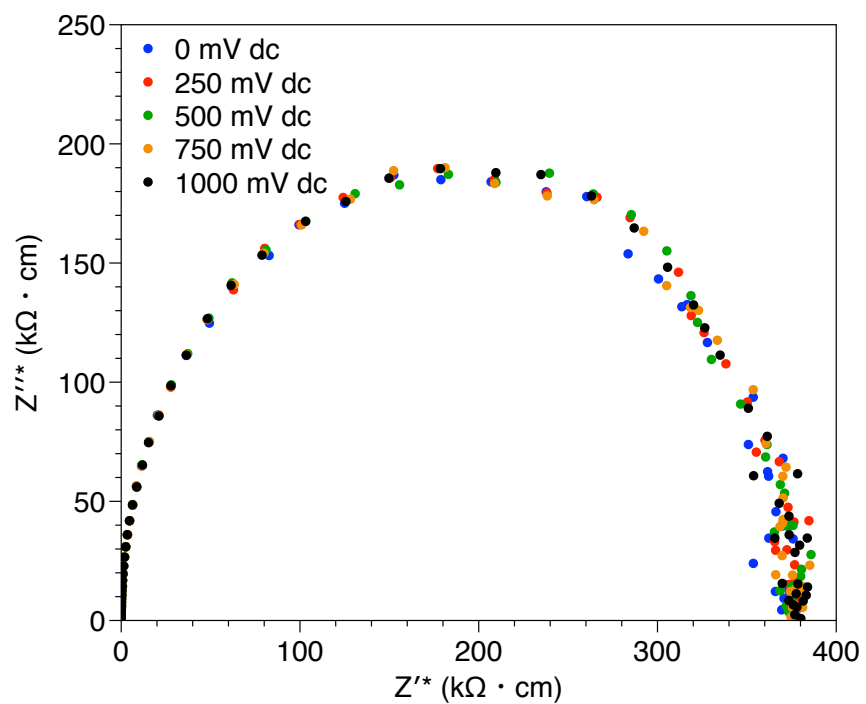


Figure S4.3. Dc field invariance of Nyquist plots of $\text{Cu}[\text{Ni}(\text{pdt})_2]$ between 1 MHz and 0.01 Hz confirm ohmic conductivity.

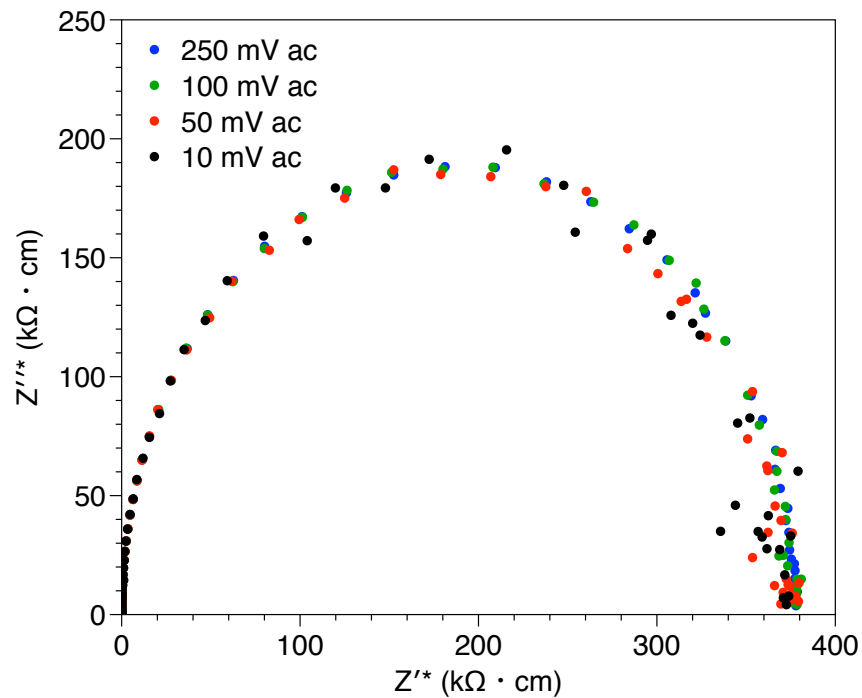


Figure S4.4. Ac field invariance of Nyquist plots of $Cu[Ni(pdt)_2]$ between 1 MHz and 0.01 Hz confirm linearity with sinus amplitude and validate the 100 mV sinus amplitude data potted in Figure 2 of the main text.

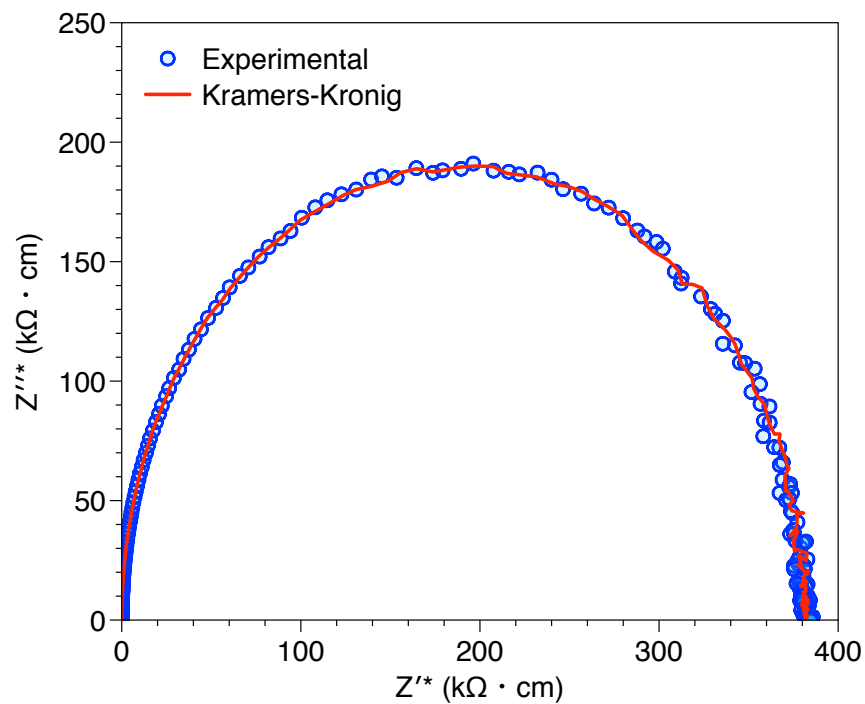


Figure S4.5. Kramers-Kronig transform of Nyquist plot for $Cu[Ni(pdt)_2]$ between 1 MHz and 0.01 Hz with 100 mV sinus amplitude and 0 mV dc field confirms linearity and time invariance.

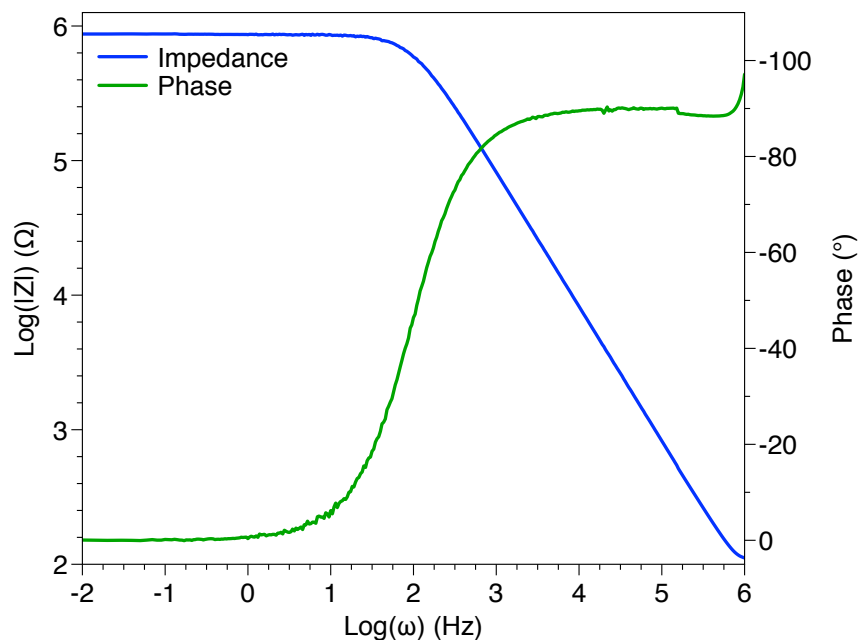


Figure S4.6. Bode impedance plot and phase dependence of Cu[Ni(pdt)₂] between 1 MHz and 0.01 Hz.

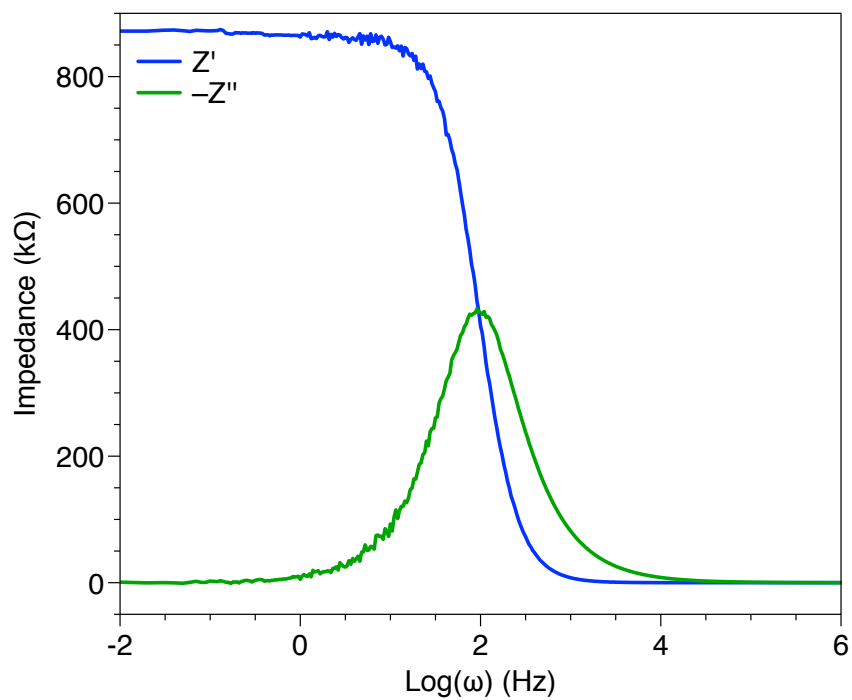


Figure S4.7. Real (Z') and imaginary (Z'') bode plots of Cu[Ni(pdt)₂] between 1 MHz and 0.01 Hz.

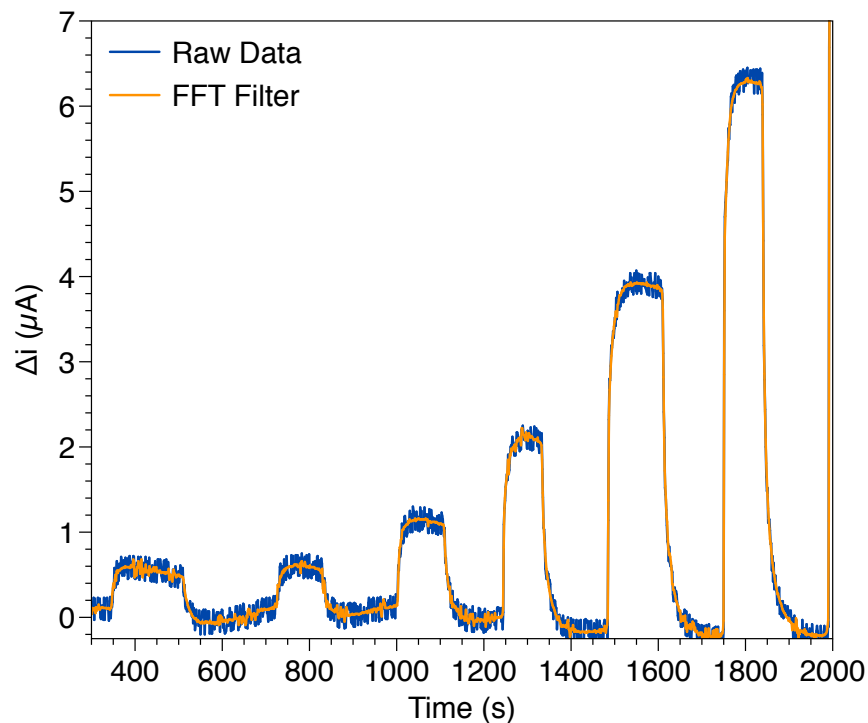


Figure S4.8. Time dependent change in current upon pump dose cycles of ethylene at different pressures between 0.5 mbar and 8 mbar. Raw data was collected with 0.25 s resolution (blue) and a 1 Hz low pass FFT filter was applied to enhance the signal to noise ratio.

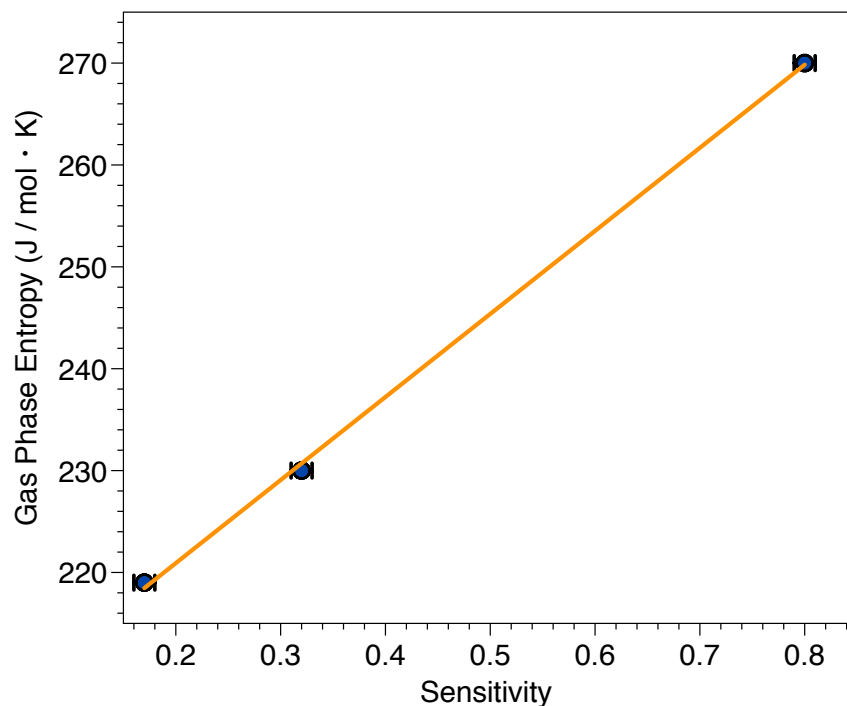


Figure S4.9. Correlation of sensitivity to guest inclusion and gas phase entropy. Correlation coefficient ($r^2 = 0.9995$), slope = $81.5 \text{ J mol}^{-1} \text{ K}^{-1}$, intercept = $204.61 \text{ J mol}^{-1} \text{ K}^{-1}$.

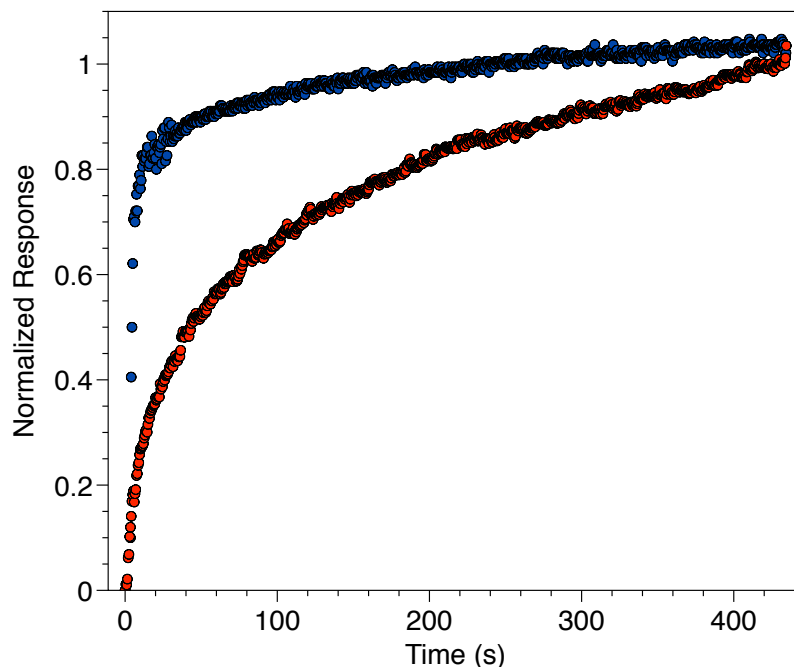


Figure S4.10. Kinetic analysis of gas adsorbed (red) and change in conductivity (blue) normalized to the final measured value when the equilibration conditions set by the gas sorption analyzer were satisfied. The absolute equilibrium pressure step was between 19 and 45 mbar.

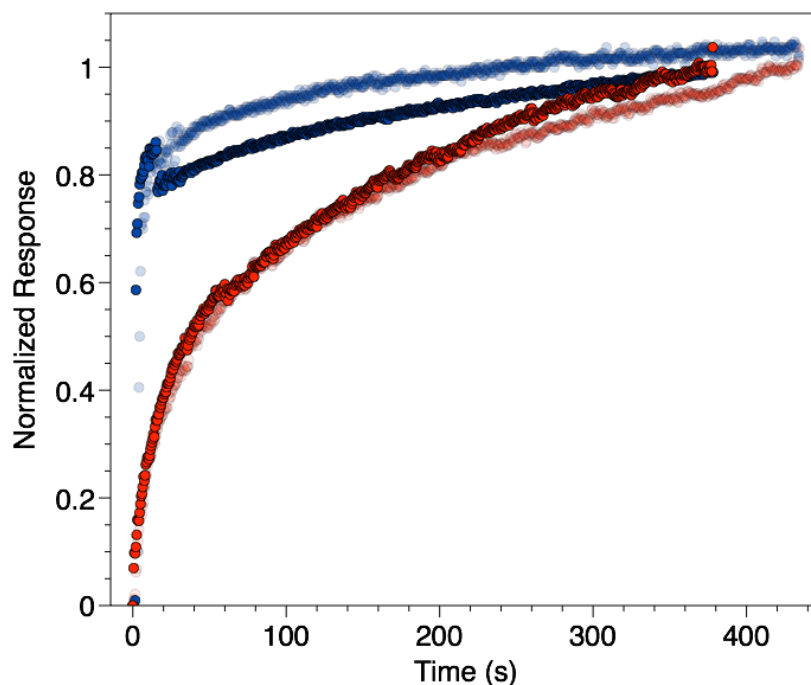


Figure S4.11. Kinetic analysis of gas adsorbed (red) and change in conductivity (blue) normalized to the final measured value when the equilibration conditions set by the gas sorption analyzer were satisfied. The absolute equilibrium pressure step was between 200 and 300 mbar. Data from **Figure S4.10** is plotted in the background for reference.

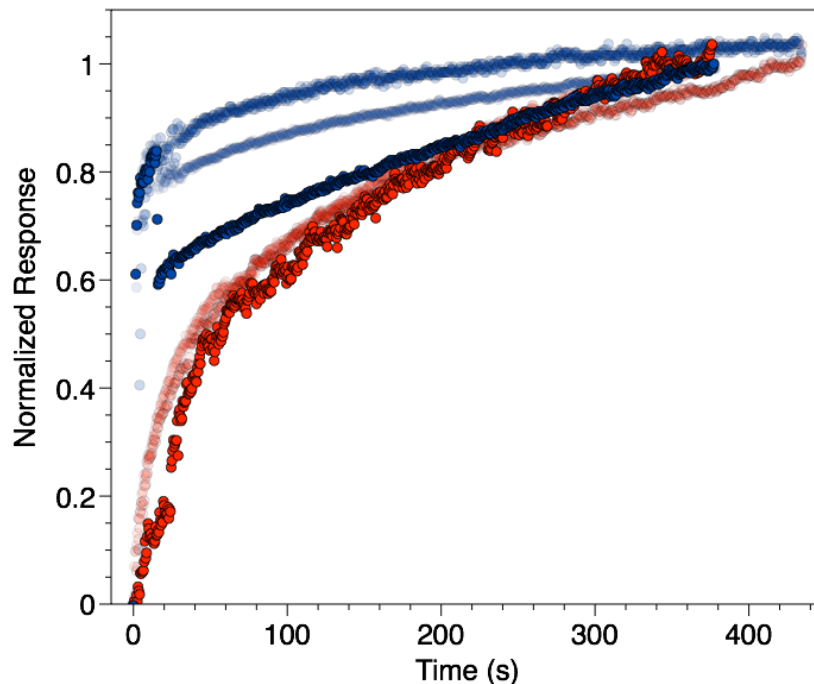


Figure S4.12. Kinetic analysis of gas adsorbed (red) and change in conductivity (blue) normalized to the final measured value when the equilibration conditions set by the gas sorption analyzer were satisfied. The absolute equilibrium pressure step was between 500 and 600 mbar. Data from **Figure S4.10** and **Figure S4.11** is plotted in the background for reference.

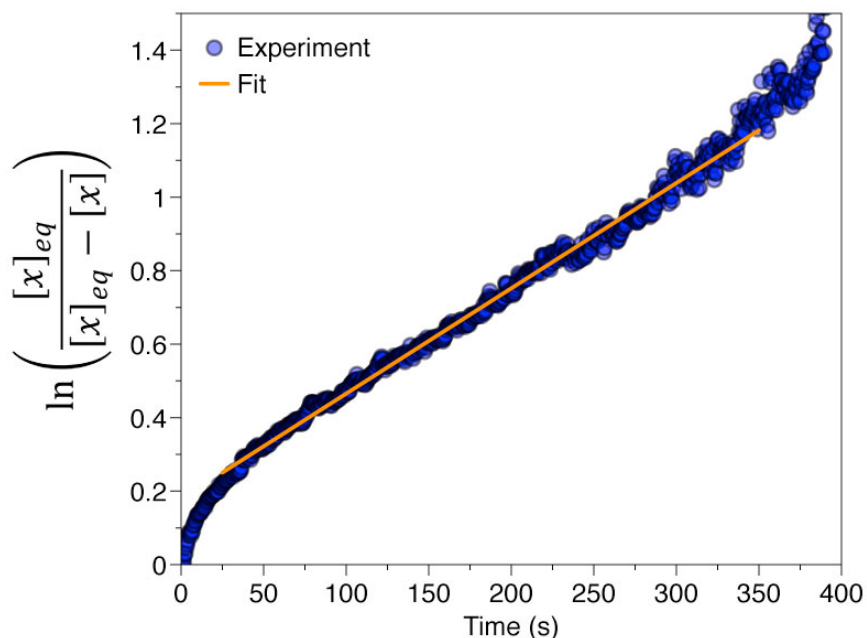


Figure S4.13. linearized rate of adsorption curve from **Figure S4.10** with respect to an equilibrium kinetic model. Deviation from linearity at short times is due to mass transport while that at times approaching equilibrium is due to the sensitivity of the model to noise very near equilibrium. The slope of the linear regime is equal to the sum of the forward and reverse rate constants.

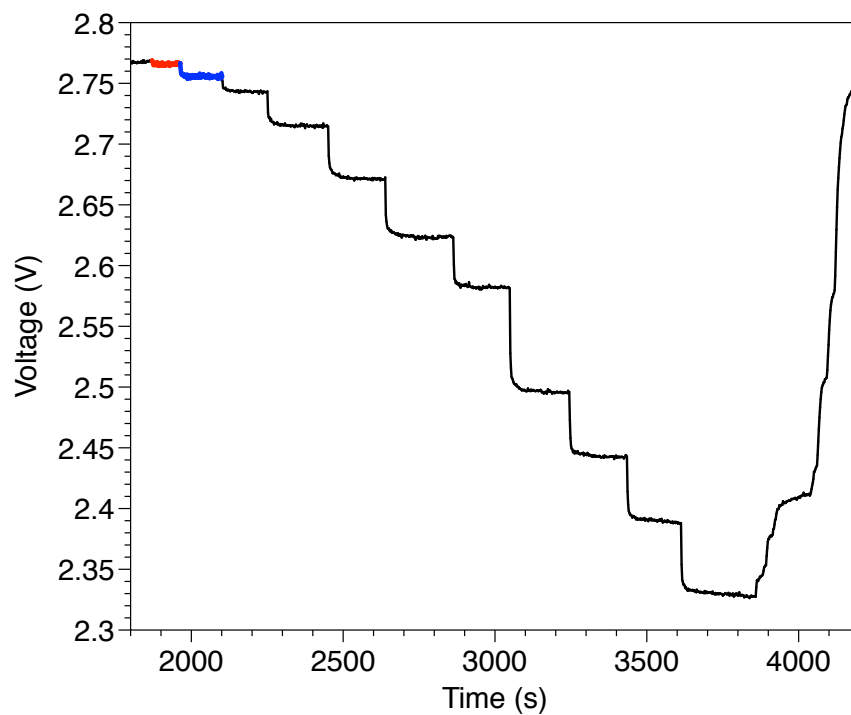


Figure S4.14. Typical time-resolved conductivity data during the collection of an ethane isotherm. The first two pressure steps are highlighted in red and blue. The large anomaly at 3900 s is due to stepwise evacuation of the cell post-isotherm measurement.

4.7 References

- (1) “The chemistry and applications of metal-organic frameworks” Furukawa, H.; Cordova, K. E.; O’Keeffe, M.; and Yaghi, O. M. *Science* **2013**, *341*, 1230444.
- (2) “Hydrogen storage in metal-organic frameworks” Murray, L. J.; Dincă, M.; and Long, J. R. *Chem. Soc. Rev.* **2009**, *38*, 1294–1314.
- (3) “CO₂/CH₄, CH₄/H₂ and CO₂/CH₄/H₂ separations at high pressures using Mg₂(dobdc)” Herm, Z. R.; Krishna, R.; and Long, J. R. *Microporous Mesoporous Mater.* **2012**, *151*, 481–487.
- (4) “Carbon dioxide capture in metal-organic frameworks.” Sumida, K.; Rogow, D. L.; Mason, J. A.; McDonald, T. M.; Bloch, E. D.; Herm, Z. R.; Bae, T.-H.; and Long, J. R. *Chem. Rev.* **2012**, *112*, 724–781.
- (5) “The pervasive chemistry of metal-organic frameworks” Long, J. R. and Yaghi, O. M. *Chem. Soc. Rev.* **2009**, *38*, 1213–1214.
- (6) “Metal-organic frameworks (MOFs)” Zhou, H.-C. J. and Kitagawa, S. *Chem. Soc. Rev.* **2014**, *43*, 5415–5418.
- (7) “Multifunctional metal-organic frameworks: from academia to industrial applications” Silva, P.; Vilela, S. M. F.; João P. C. Tomé; and Paz, F. A. A. *Chem. Soc. Rev.* **2015**, *44*, 6774–6803.
- (8) “Emerging multifunctional metal-organic framework materials” Li, B.; Wen, H. M.; Cui, Y.; Zhou, W.; Qian, G.; and Chen, B. *Adv. Mater.* **2016**, *28*, 8819–8860.
- (9) “Cooperative insertion of CO₂ in diamine-appended metal-organic frameworks” McDonald, T. M.; Mason, J. A.; Kong, X.; Bloch, E. D.; Gygi, D.; Dani, A.; Crocellà, V.; Giordanino, F.; Odoh, S. O.; Drisdell, W. S.; Vlaisavljevich, B.; Dzubak, A. L.; Poloni, R.; Schnell, S. K.; Planas, N.; Lee, K.; Pascal, T.; Wan, L. F.; Prendergast, D.; Neaton, J. B.; Smit, B.; Kortright, J. B.; Gagliardi, L.; Bordiga, S.; Reimer, J. A.; and Long, J. R. *Nature* **2015**, *519*, 303–308.
- (10) “Methane storage in flexible metal-organic frameworks with intrinsic thermal management” Mason, J. A.; Oktawiec, J.; Taylor, M. K.; Hudson, M. R.; Rodriguez, J.; Bachman, J. E.; Gonzalez, M. I.; Cervellino, A.; Guagliardi, A.; Brown, C. M.; Llewellyn, P. L.; Masciocchi, N.; and Long, J. R. *Nature* **2015**, *527*, 357–361.
- (11) “Magnetic metal-organic frameworks” Kurmoo, M. *Chem. Soc. Rev.* **2009**, *38*, 1353–1379.
- (12) “Flexible metal-organic frameworks” Schneemann, A.; Bon, V.; Schwedler, I.; Senkovska, I.; Kaskel, S.; and Fischer, R. A. *Chem. Soc. Rev.* **2014**, *43*, 6062–6096.
- (13) “Large breathing effects in three-dimensional porous hybrid matter: facts, analyses, rules and consequences” Férey, G. and Serre, C. *Chem. Soc. Rev.* **2009**, *38*, 1380–1399.
- (14) “Electrically conductive porous metal-organic frameworks” Sun, L.; Campbell, M. G.; and Dincă, M. *Angew. Chem. Int. Edit. Engl.* **2016**, *55*, 3566–3579.
- (15) “Metal-organic frameworks for electrochemical applications” Morozan, A. and Jaouen, F. *Energy Environ. Sci.* **2012**, *5*, 9269–9290.
- (16) “Metal-organic frameworks as cathode materials for Li–O₂ batteries” Wu, D.; Guo, Z.; Yin, X.; Pang, Q.; Tu, B.; Zhang, L.; Wang, Y. G.; and Li, Q. *Adv. Mater.* **2014**, *26*, 3258–3262.
- (17) “Metal-organic framework materials as chemical sensors” Kreno, L. E.; Leong, K.; Farha, O. K.; Allendorf, M.; Van Duyne, R. P.; and Hupp, J. T. *Chem. Rev.* **2011**, *112*, 1105–1125.

- (18) “Chemical sensors based on metal-organic frameworks” Yi, F. Y.; Chen, D.; Wu, M. K.; Han, L.; and Jiang, H. L. *ChemPlusChem* **2016**, *81*, 675–690.
- (19) “Metal-organic frameworks for electrocatalytic reduction of carbon dioxide” Kornienko, N.; Zhao, Y.; Kley, C. S.; Zhu, C.; Kim, D.; Lin, S.; Chang, C. J.; Yaghi, O. M.; and Yang, P. *J. Am. Chem. Soc.* **2015**, *137*, 14129–14135.
- (20) “Fe-porphyrin-based metal–organic framework films as high-surface concentration, heterogeneous catalysts for electrochemical reduction of CO₂” Hod, I.; Sampson, M. D.; Deria, P.; Kubiak, C. P.; Farha, O. K.; and Hupp, J. T. *ACS Catal.* **2015**, *5*, 6302–6309.
- (21) “Ultrastable polymolybdate-based metal-organic frameworks as highly active electrocatalysts for hydrogen generation from water” Qin, J.-S.; Du, D.-Y.; Guan, W.; Bo, X.-J.; Li, Y.-F.; Guo, L.-P.; Su, Z.-M.; Wang, Y.-Y.; Lan, Y.-Q.; and Zhou, H.-C. *J. Am. Chem. Soc.* **2015**, *137*, 7169–7177.
- (22) “Adsorption of gas molecules on monolayer MoS₂ and effect of applied electric field” Yue, Q.; Shao, Z.; Chang, S.; and Li, J. *Nanoscale Res. Lett.* **2013**, *8*, 425.
- (23) “Cation-dependent intrinsic electrical conductivity in isostructural tetrathiafulvalene-based microporous metal-organic frameworks.” Park, S. S.; Hontz, E. R.; Sun, L.; Hendon, C. H.; Walsh, A.; Van Voorhis, T.; and Dincă, M. *J. Am. Chem. Soc.* **2015**, *137*, 1774–1777.
- (24) “High electrical conductivity in Ni₃(2,3,6,7,10,11-Hexaiminotriphenylene)₂, a semiconducting metal-organic graphene analogue.” Sheberla, D.; Sun, L.; Blood-Forsythe, M. A.; Er, S.; Wade, C. R.; Brozek, C. K.; Aspuru-Guzik, A.; and Dincă, M. *J. Am. Chem. Soc.* **2014**, *136*, 8859–8862.
- (25) “A two-dimensional π -*d* conjugated coordination polymer with extremely high electrical conductivity and ambipolar transport behaviour.” Huang, X.; Sheng, P.; Tu, Z.; Zhang, F.; Wang, J.; Geng, H.; Zou, Y.; Di, C.-A.; Yi, Y.; Sun, Y.; et al. *Nat. Commun.* **2015**, *6*, 7408.
- (26) “New porous crystals of extended metal-catecholates” Hmadeh, M.; Lu, Z.; Liu, Z.; and Gandara, F. *Chem. Mater.* **2012**, *24*, 3511–3513.
- (27) “Pi-conjugated nickel bis(dithiolene) complex nanosheet” Kambe, T.; Sakamoto, R.; Hoshiko, K.; Takada, K.; Miyachi, M.; Ryu, J.-H.; Sasaki, S.; Kim, J.; Nakazato, K.; Takata, M.; and Nishihara, H. *J. Am. Chem. Soc.* **2013**, *135*, 2462–2465.
- (28) “Iodine release and recovery, influence of polyiodide anions on electrical conductivity and nonlinear optical activity in an interdigitated and interpenetrated bipillared-bilayer metal-organic framework” Yin, Z.; Wang, Q.-X.; and Zeng, M.-H. *J. Am. Chem. Soc.* **2012**, *134*, 4857–4863.
- (29) “Porous, conductive metal-triazolates and their structural elucidation by the charge-flipping method.” Gándara, F.; Uribe-Romo, F. J.; Britt, D. K.; Furukawa, H.; Lei, L.; Cheng, R.; Duan, X.; O’Keeffe, M.; and Yaghi, O. M. *Chem. Eur. J.* **2012**, *18*, 10595–10601.
- (30) “Measuring and reporting electrical conductivity in metal-organic frameworks: Cd₂(tftfb) as a case study” Sun, L.; Park, S. S.; Sheberla, D.; and Dincă, M. *J. Am. Chem. Soc.* **2016**, *138*, 14772–14782.
- (31) “Chemiresistive sensor arrays from conductive 2D metal-organic frameworks” Campbell, M. G.; Liu, S. F.; Swager, T. M.; and Dincă, M. *J. Am. Chem. Soc.* **2015**, *137*, 13780–13783.

- (32) “Cu₃(hexaiminotriphenylene)₂: an electrically conductive 2D metal-organic framework for chemiresistive sensing” Campbell, M. G.; Sheberla, D.; Liu, S. F.; Swager, T. M.; and Dincă, M. *Angew. Chem. Int. Edit. Engl.* **2015**, *54*, 4349–4352.
- (33) “Metal-organic frameworks for sensing applications in the gas phase” Achmann, S.; Hagen, G.; Kita, J.; Malkowsky, I.; Kiener, C.; and Moos, R. *Sensors* **2009**, *9*, 1574-1589.
- (34) “Conductivity, doping, and redox chemistry of a microporous dithiolene-based metal-organic framework” Kobayashi, Y.; Jacobs, B.; Allendorf, M. D.; and Long, J. R. **2010**, *22*, 4120–4122.
- (35) “Kapelewski, M. *Personal Communication* November 2016.”
- (36) “Electron mobility as a function of reduction in a conductive metal-organic framework” Wiers, B. M.; Long, J. R.; Andrews, S. C.; Sakurai, T.; Aubrey, M. L.; Yu, C. J.; Mason, J. A.; Baeg, J.-O.; Grandjean, F.; Long, G. J.; Seki, S.; Neaton, J.; Yang, P.; and Long, J. R. *In Review* **2016**.
- (37) “Toward separation and purification of olefins using dithiolene complexes: an electrochemical approach” Wang, K. and Stiefel, E. I. *Science* **2001**, *291*, 106–109.
- (38) “One-dimensional metals: Conjugated Polymers, Organic Crystals, Carbon Nanotubes and Graphene” Roth, S.; and Carroll, D. *John Wiley & Sons* **2015**, 1–49.
- (39) “Hydrocarbon separations in a metal-organic framework with open iron(II) coordination sites” Bloch, E. D.; Queen, W. L.; Krishna, R.; Zadrozny, J. M.; Brown, C. M.; and Long, J. R. *Science* **2012**, *335*, 1606–1610.
- (40) “Kapelewski, M; and Brown, C. *Personal Communication* November 2016.”
- (41) “The transition to the metallic state” Edwards, P. P. and Sienko, M. J. *Acc. Chem. Res.* **1982**, *15*, 87–93.
- (42) “Selective gas adsorption and separation in metal-organic frameworks” Li, J.-R.; Kuppler, R. J.; and Zhou, H.-C. *Chem. Soc. Rev.* **2009**, *38*, 1477–1504.
- (43) “Estimation of the thermodynamic properties of hydrocarbons at 298.15 K” Domalski, E. S. and Hearing, E. D. *J. Phys. Chem. Ref. Dat.* **1988**, *17*, 1637–1678.
- (44) “Modern physical organic chemistry” Anslyn, E. V. and Dougherty, D. A. *University Science Books* **2006**.
- (45) “Grain size effects on gas sensitivity of porous SnO₂-based elements” Xu, C.; Tamaki, J.; Miura, N.; and Yamazoe, N. *Sensors and Actuators B: Chemical* **1991**, *3*, 147–155.
- (46) “Electronic conductivity, ferrimagnetic ordering, and reductive insertion mediated by organic mixed-valence in a ferric semiquinoid metal-organic framework” Darago, L. E.; Aubrey, M. L.; Yu, C. J.; Gonzalez, M. I.; and Long, J. R. *J. Am. Chem. Soc.* **2015**, *137*, 15703–15711.
- (47) “Fundamentals of Impedance Spectroscopy” Macdonald, J. R. and Johnson, W. B. *in Impedance Spectroscopy: Theory, Experiment and Applications* **2005**, *2nd Ed.*, 1–26.